Optimization of nanoporous materials formulations for NOx capture by ab initio molecular modeling

Giannis Karamanis

▶ To cite this version:

Giannis Karamanis. Optimization of nanoporous materials formulations for NOx capture by ab initio molecular modeling. Chemical Sciences. Université de Lorraine, 2023. English. NNT : 2023LORR0193 . tel-04628654

HAL Id: tel-04628654
https://hal.univ-lorraine.fr/tel-04628654v1

Submitted on 24 Jan 2025

École Doctorale : C2MP - CHIMIE MECANIQUE MATERIAUX PHYSIQUE

Thèse

Présentée et soutenue publiquement pour l'obtention du titre de

DOCTEUR DE l'UNIVERSITE DE LORRAINE

Mention : Chimie

par **Ioannis KARAMANIS**

OPTIMIZATION OF NANOPOROUS MATERIALS FORMULATIONS FOR NO$_X$ CAPTURE BY AB INITIO MOLECULAR MODELING

20 Juillet 2023

Membres du jury :

Directeur de thèse	Michael BADAWI	Professeur, Université de Lorraine, Saint-Avold
Co-encadrant	Hubert MONNIER	Responsable d'études, Institut National de Recherche et de Sécurité, Nancy
Rapporteurs	Tomáš BUCKO	Professeur, Comenius University, Bratislava
	Céline CHIZALLET	Ingénieure IFPEN, Lyon
Examinateur	Jérôme TRIOLET	Directeur Adjoint des Applications, Institut National de Recherche et de Sécurité, Paris
Président du jury	Andreea PASC	Professeure, Université de Lorraine, Nancy

Resume

People working in closed spaces with limited ventilation, are exposed to harmful NO_x (NO and NO_2) and CO pollutants, emitted by diesel exhaust fumes. Vehicles in construction sites often work discontinuously, being systematically subjected to *cold starts*; the latter refers to the action of starting an engine (the temperature is low, hence cold start). As a result, the catalysts which need high temperatures (> 200 °C) to deal with NO_x abatement efficiently, remain inactive for long periods. The topic of this dissertation is to screen a big number of materials using periodic density functional theory (DFT) and choose the most appropriate molecular trap, primarily for NO_x and secondarily for CO. The complexity of the problem is enhanced by the high concentration of steam in the exhaust fumes, which competes with NO_x for the adsorption sites of the traps. This study is part of bigger effort towards the improvement of the working conditions led by *Institut National de Recherche et de Sécurité* (INRS).

In this work we used periodic density functional theory to assess the low temperature NO_x and CO trapping capabilities of several porous materials. The interaction energy between the porous materials and the gases NO, NO_2, and CO is compared with the one between the porous materials and the inhibiting H_2O and CO_2, and their difference determines the selectivity of the material. Also, Bader theory is used to calculate charge transfers that occur during the adsorptions. Intramolecular bond elongation of the gases during the adsorption is used as an indication of whether the gases will further react, forming potential hazardous by-products. Based on these tools, we screen the suitability of several transition metals incorporated in various zeolitic and amorphous silica structures. Cu^+ promoted faujasites Y and X were selective and bond elongation analysis suggested that there no further reaction can be triggered. Fe^{2+} promoted faujasites were exceptionally selective but the bond elongation was significant. On the contrary, chabazite and mordenite supporting Fe^{2+} were found to be thermodynamically selective towards NO_x in most of the cases, without provoking strong bond elongation during adsorption. Finally, all of the clusters Fe_{13}, Co_{13}, Ni_{13} and Cu_{13} were found to be selective towards NO_x and CO, while incorporated onto amorphous silica surfaces. Further calculations are needed to provide evidence associated with the formation of byproducts.

Keywords

NO, NO_2, water, CO, porous materials, zeolites, DFT, thermodynamic selectivity, low temperature, occupational diseases, diesel exhaust gas

Contents

Résumé général de la thèse

1 - CONTEXTE DE LA THESE

Il a été prouvé que le monoxyde d’azote (NO), le dioxyde d’azote (NO_2) et le monoxyde de carbone (CO) sont toxiques et nocifs pour l'homme. Présents sous forme gazeuse dans l’atmosphère, ils sont générés essentiellement par des opérations de combustion, notamment l’échappement des moteurs thermiques diesel. En France, c’est près de 800 000 salariés qui s’estiment exposés aux émissions diesel considérées comme la première source d’exposition à un produit cancérigène. La concentration de ces gaz dans l’atmosphère se trouve renforcée dans certaines situations de confinement du fait de l’absence de ventilation naturelle. Enfin, s’il existe des solutions techniques qui utilisent la catalyse telles que la réduction catalytique sélective (SCR) pour les oxydes d’azote (NO_x), elles ne sont efficaces qu’à haute température, supérieure à 200°C. Leur efficacité pour la réduction des NOx devient limitée sur les engins de chantier fonctionnant de manière discontinue et donc soumis à plusieurs démarrages à froid. Par ailleurs, lorsqu'on cherche à piéger les NOx et le CO, il faut aussi tenir compte des autres espèces présentes en grande quantité dans les gaz d'échappement, comme l'eau qu’il n’est pas souhaitable de piéger sous peine de saturer l’adsorbant trop rapidement. Ainsi, l’adsorbant proposé doit être sélectif : il doit piéger les NOx et le CO sans retenir l'eau.

2 - OBJECTIFS

Les tendances actuelles visant à réduire l'empreinte carbone des activités sur les chantiers de construction impliquent l'utilisation de moteurs électriques alimentés par des batteries, ce qui pourrait constituer une solution à long terme à ces émissions. Par exemple, certaines entreprises ont réussi à électrifier une pelleteuse malgré ses besoins énergétiques élevés (Caterpillar : 26 tonnes 300 kWh - Liebherr : e-dumper 700 kWh). Ce changement de source d'énergie nécessite le développement de batteries de taille significative. Une autre alternative au diesel est l'hydrogène, qui a été adoptée par le groupe Toyota pour ses engins de manutention. Cependant, les moteurs à source d'énergie alternative ne seront commercialisés qu'à partir de 2030, voire 2035 (Volvo Trucks, Caterpillar). Ainsi, compte tenu des difficultés liées à l'utilisation de l'électricité pour alimenter des engins de chantier relativement gourmands en énergie, les alternatives au moteur diesel ne devraient se développer qu'à relativement long terme (20-30 ans). C'est dans ce contexte que l'étude présentée vise à développer un procédé d'adsorption des NOx et du CO, pour les véhicules non routiers grâce à un adsorbant efficace. Le procédé serait placé en sortie d'échappement du véhicule. La cartouche de granulés adsorbants doit alors être périodiquement changée car elle fonctionne en mode cumulatif, par un procédé de physisorption. Le système est par conséquent régénéré hors du véhicule, en différé dans le temps : les NOx pourront été réduit en azote à partir d'un réacteur catalytique du même type que celui dont sont équipés les véhicules légers fonctionnant au diesel (Figure 1). Le principe retenu est basé sur la physisorption de gaz par un adsorbant. Une sélection de matériaux comme les zéolithes, avec les propriétés requises a été effectuée à partir de calculs de modélisation moléculaire. L'objectif a été ensuite de synthétiser les adsorbants les plus prometteurs.

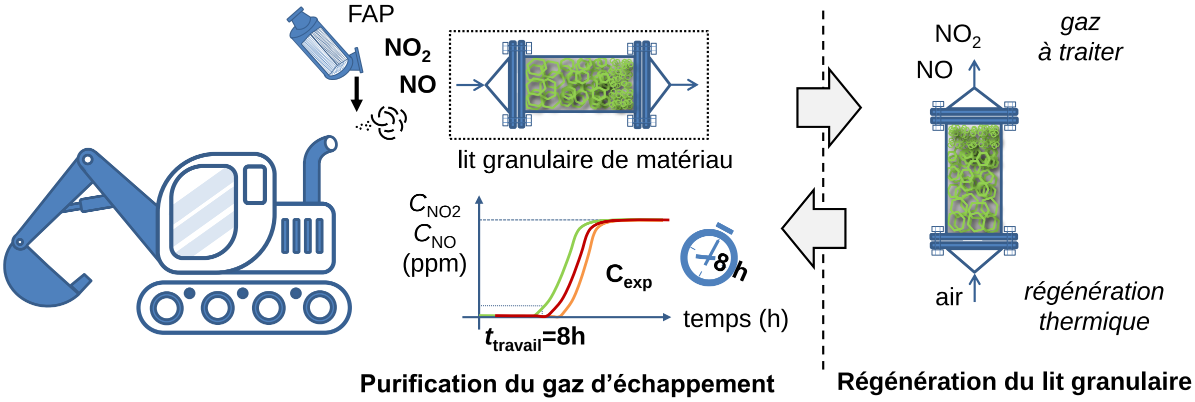

Figure 1 : Schéma simplifié du procédé - Un FAP est nécessaire pour piéger les particules de suie - les courbes de couleur représentent les concentrations de CO, NO et de NO_2.

3 - MODELISATION MOLECULAIRE- CRIBLAGE

L'identification par des calculs théoriques de modélisation moléculaire est très utilisée en dépollution automobile. Il s'agit d'étudier le comportement de matériaux cristallins pour permettre une adsorption maximale du CO et des NO_x. L'objectif est aussi d'investiguer l'influence des « inhibiteurs » comme l'eau sur la sélectivité des matériaux testés. Les calculs théoriques ont été menés avec la méthode DFT. Ils ont été effectués avec le code de calcul VASP dont dispose l'Université de Lorraine. Les forces de dispersion de Van der Waal ont été prises en compte pour obtenir une description correcte des interactions entre le matériau et les molécules gazeuses. Concrètement, il s'agit de déterminer le changement de longueur de liaison des composés au moment de l'adsorption ainsi que l'enthalpie d'adsorption *ab initio* entre le milieu adsorbant et le(s) composé(s) gazeux. La connaissance du changement de la taille des liaisons permet de comprendre les phénomènes chimiques qui se produisent en co-adsorption. Les modèles utilisés et les calculs menés ont l'obligation de caractériser la nature du milieu et de représenter la structure du système chimique sans que le nombre d'atomes soit pharaonique. Si la structure solide est cristalline, le modèle peut s'intéresser à une maille d'atomes représentative, limitant ainsi le nombre d'atomes dans le calcul (Figure 2). C'est le cas des zéolithes dont le squelette est connu.

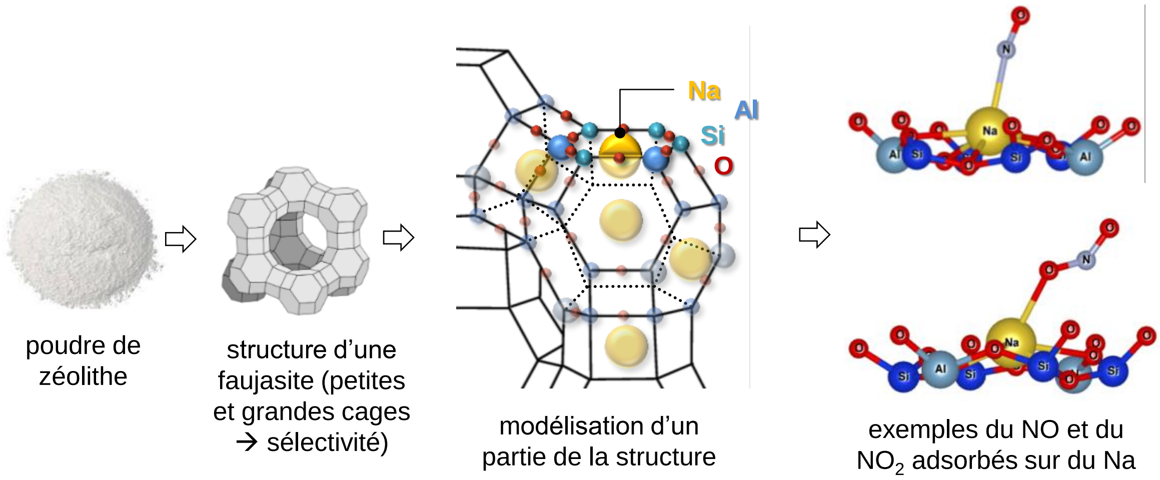

poudre de zéolithe

structure d'une faujasite (petites et grandes cages → sélectivité)

modélisation d'un partie de la structure

exemples du NO et du NO_2 adsorbés sur du Na

Figure 2 : Schématisation du calcul de modélisation moléculaire par DFT – code VASP – cas d'une zéolithe faujasite

4 - PRINCIPAUX RESULTATS

Trois types de zéolithes ont été étudiés : les faujasites, la mordénite et la chabazite. La faujasite a fait l'objet de nombreuses investigations car elle a la caractéristique de pouvoir échanger relativement facilement son cation compensateur de charge : sept cations monovalents et neuf cations divalents ont été testés. Par ailleurs, il est possible d'étudier l'influence du rapport Si/Al car là aussi, il est facile de se procurer dans le commerce des faujasites à différents rapports. Trois rapports Si/Al ont été étudiés : 47 ; 2,43 (zéolithe Y) et 1,4 (zéolithe X). Ensuite, lorsqu'un cation nous a semblé être un bon candidat, il a été étudié au sein d'une mordénite et du chabazite qui offrent une structure et des tailles de pores intéressants pour notre étude.

Etude des cations monovalents sur une faujasite

La Figure 3 montrent les énergies d'interaction, $E_{int.}$, calculées par DFT pour les sept cations monovalents et les trois rapports Si/Al. Pour les structures avec Si/Al = 47, tous les cations alcalins présentent une énergie beaucoup plus importante pour l'eau que pour les NOx (Figure 3a). En revanche, le cuivre montre une affinité plus élevée pour NO que pour l'eau avec une différence d'énergie de 31,5 kJ/mol.

Pour les structures Y avec Si/Al = 2,43 (Figure 3b), tous les atomes alcalins donnent une interaction plus forte avec H_2O qu'avec les NOx. Avec le cuivre, l'énergie d'interaction est beaucoup plus élevée pour NO et NO_2 que pour l'eau avec des différences à 37 et 42 kJ/mol, respectivement. La littérature rapporte des résultats similaires pour tous ces cations. Avec l'argent, NO a une énergie supérieure à l'eau alors que l'énergie du NO_2 se situe bien en dessous.

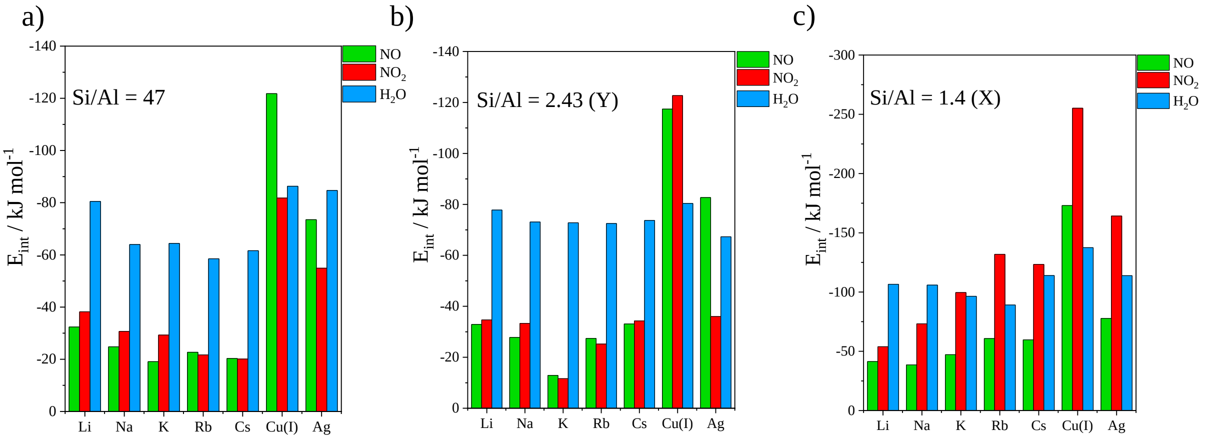

Figure 3 : Energies d'interaction calculées par DFT pour NO, NO_2 et H_2O sur des faujasites constituées d'un cation monovalent (a) Si/Al = 47, (b) la faujasite Y, Si/Al = 2,43 et (c) la faujasite X, Si/Al = 1,4 – $T \rightarrow 0°C$.

Un exemple de configurations d'adsorption est illustré sur la Figure 4 avec respectivement, le NO_2 (Figure 4a) et l'eau (Figure 4b) adsorbés sur le cation cuivre. NO_2 forme une liaison avec une longueur de 1,88 Å, tandis que l'eau se situe à 1,93 Å, avec tout de même une liaison hydrogène de 1,75 Å. Plus la distance de liaison est courte et plus l'affinité est forte. Ainsi malgré une double accroche de l'eau grâce à sa liaison hydrogène, celui-ci à une affinité inférieure au NO_2. L'adsorption du NO est donc plus stable avec le cuivre comme cation que celle de l'eau. Le cuivre (I) semble être un bon candidat.

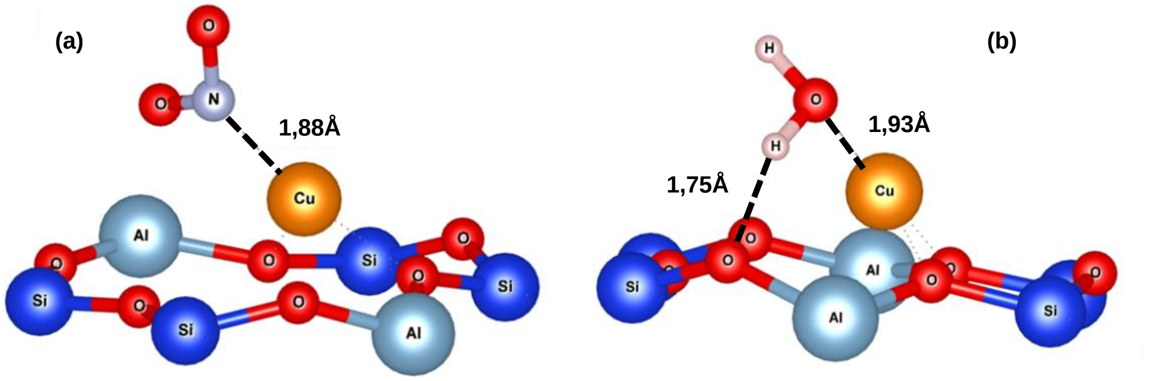

Figure 4 : Exemples de configurations d'adsorption identifiées avec le cuivre dans la faujasite Y(Si/Al=2,43) avec (a) NO_2 et (b) H_2O.

Pour la structure X (Si/Al = 1,4), le cuivre apparait à nouveau très sélectif et efficace pour l'adsorption des NOx (Figure 3c). De plus, les énergies augmentent globalement fortement par rapport aux résultats obtenus avec des rapports plus faibles. Cette observation se retrouve avec l'eau et les cations alcalins. Elle s'explique par l'augmentation du nombre de cations dans la structure (égal au nombre d'atomes d'aluminium). Ainsi, l'adsorption des molécules de gaz peuvent former une seconde liaison avec un second cation suffisamment proche. Cela est possible grâce aux atomes d'hydrogène pour l'eau et au doublet électronique des atomes d'oxygène pour les NOx.

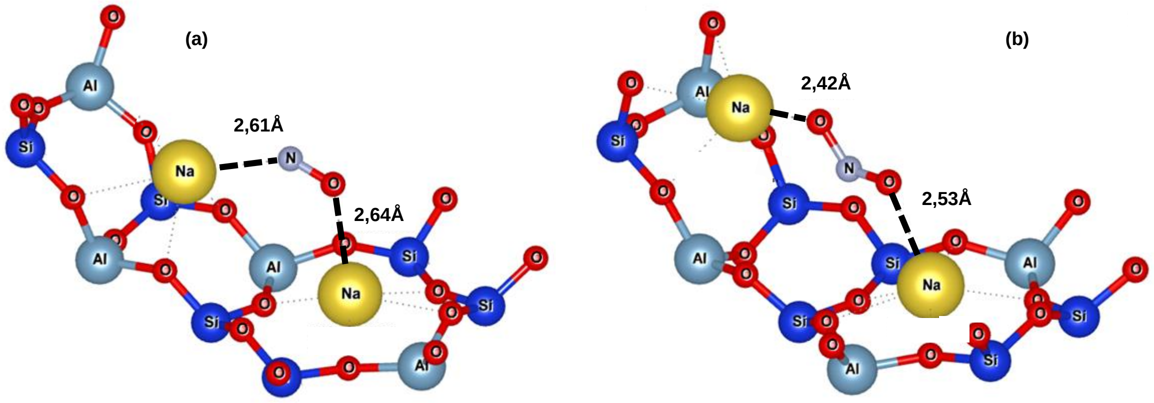

Figure 5 : Configurations d'adsorption avec la faujasite X (Si/Al=1,4) au sodium Na, (a) NO et (b), NO_2 – Exemple d'une double accroche qui explique l'augmentation de stabilité de l'adsorption

En résumé, la structure X (Si/Al=1,4) propose des énergies nettement supérieures aux autres configurations. Pour autant, l'écart nécessaire entre les énergies obtenues avec les gaz cibles et l'eau n'augmente pas tant que ça par rapport à la structure Y (Si/Al=2,43). Par ailleurs, il est primordial de garder à l’esprit que la régénération sera d’autant plus difficile à réaliser que les enthalpies seront importantes. En ce qui concerne l’argent, il propose des affinités intéressantes avec certains gaz en fonction du rapport Si/Al. Enfin, le résultat important est la grande différence observée avec le cuivre entre les NOx et l’eau. La sélectivité est présente aussi bien avec les zéolites Y que X.

Etude des cations divalents sur une faujasite

Les énergies d’interaction déterminées pour NO, NO_2 et l'eau sur des faujasites de cations divalents sont illustrées sur la Figure 6abc.

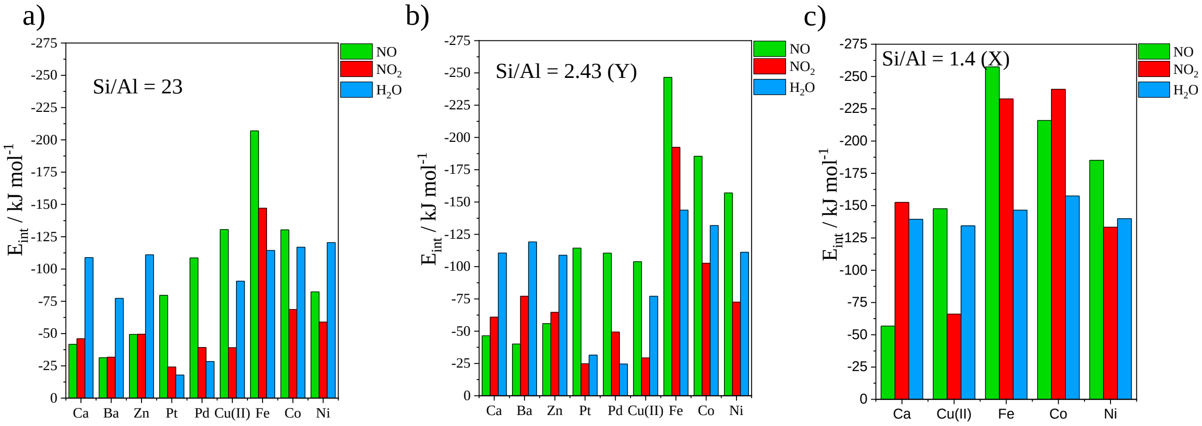

Figure 6 : Energies d’interaction calculées par DFT pour NO, NO_2 et H_2O sur de la faujasite échangée avec des cations divalent –(a) Si/Al = 23 ; (b) : Si/Al = 2,43 (Y) et (c) Si/Al=1,4 (X) – $T \rightarrow 0°C$.

Pour un rapport Si/Al =23, les zéolites échangées avec le platine (Pt) et palladium (Pd) montrent une forte affinité pour NO et NO_2, et une affinité beaucoup plus faible pour l'eau (Figure 6a). En revanche, les cations alcalino-terreux (Ca, Ba) et Zn montrent une affinité plus forte pour l'eau que pour les NOx. Enfin, les autres métaux (Cu(II), Fe(II), Co(II) et Ni(II)) ont une préférence pour le NO mais manifestent une faible affinité pour le NO_2. Lorsque le rapport Si/Al diminue et tend vers 2,43 (Figure 6b), les alcalino-terreux et le zinc se comportent toujours comme des cations hydrophiles. Pt et Pd restent exceptionnellement sélectifs et efficaces pour l'adsorption de NOx vis à vis de l’eau. Le fer semble également être sélectif envers le NO et le NO_2, avec des énergies de liaison dépassant celles de l'eau. Enfin, Co et Ni sont apparus comme de bons candidats pour l'adsorption du NO. Ces résultats ont été corroborés par la littérature.

Un exemple de configuration atomique sur la zéolite Y (Si/Al=2,43) avec le fer permet d’observer que le NO et le NO_2 ont été adsorbés approximativement à la même distance du cation compensateur de charge, à 1,67 Å et 1,68 Å, respectivement (Figure 7a et b), beaucoup plus près que l'eau qui est restée à 1,98 Å (Figure 7c).

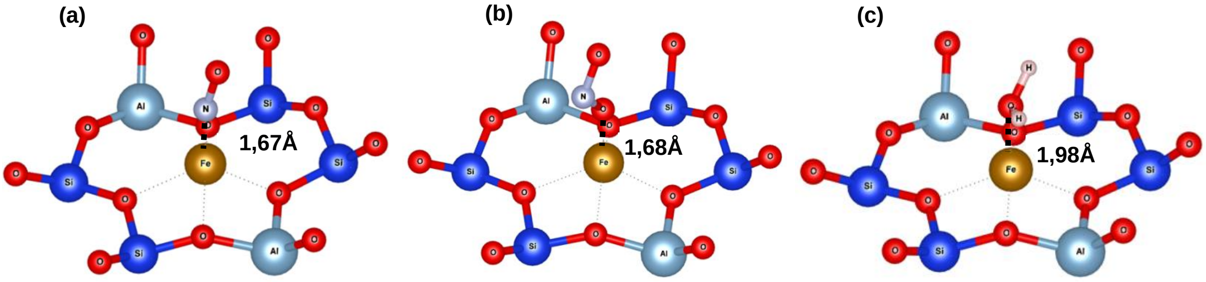

Figure 7 : Configurations atomiques de (a) NO, (b) NO_2 et (c) H_2O sur une faujasite Y (Si/Al=2,43) au fer – distances interatomiques entre les gaz et le cation compensateur de charge.

Ce résultat confirme ceux obtenus pour les énergies : le fer a une plus grande affinité pour les NOx que pour l'eau. Il est à noter que, contrairement aux résultats obtenus avec les cations monovalents, aucune liaison hydrogène ne se forme avec H_2O lorsqu'elle s’adsorbe sur des cations divalents.

Pour la zéolithe X (Si/Al=1,4), les valeurs des énergies d’interaction sont globalement plus élevées qu’avec des rapports plus faibles. Pour autant, la sélectivité n’est pas au rendez-vous sauf pour le fer et le cobalt. Enfin, le nickel confirme sa tendance à adsorber moins l'eau que NO. Par ailleurs, il semble pertinent d'indiquer que l'adsorption croisée (avec deux cations) se produit rarement sur les cations divalents. Ce phénomène qui est présent avec des cations monovalents, n’a jamais été observé lors des calculs effectués sur des cations divalents (Figure 5). Cependant, si le fer apparait comme le meilleur candidat pour adsorber les NOx en présence d’humidité, il est nécessaire de la synthétiser. Ce travail s’effectue le plus souvent à partir d’une zéolite au sodium qui subit un échange cationique. Au final, il n’est pas rare d’obtenir une zéolithe qui contiennent les deux cations car l’échange est rarement total (

Figure 8).

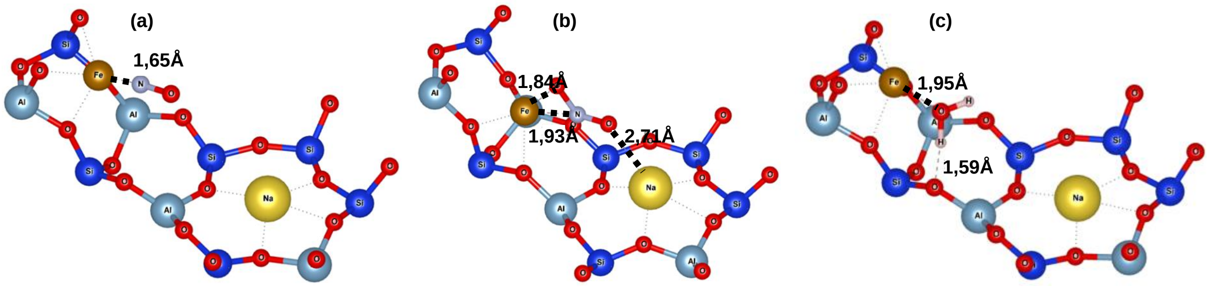

Figure 8 : Modes d'adsorption de (a) NO, (b) NO_2 et (c) H_2O sur une faujasite X (Si/Al=1,4 - Figure 6c) qui contient du fer et du sodium comme cation compensateur de charge - étude des adsorptions croisées.

La

Figure 8 a met en évidence une liaison étroite à 1,65 Å entre NO et le fer sans liaison avec le sodium. L'ordre de grandeur est quasiment identique à celui rencontré avec uniquement le fer (Figure 7a). NO_2 est, quant à lui, adsorbé par le fer grâce à ses deux atomes N et O avec des distances de 1,93 et 1,84 Å, respectivement, gardant aussi son deuxième oxygène à 2,71 Å de Na (

Figure 8b). L'adsorption semble plus robuste qu'avec uniquement le fer, ce qui est de bon augure pour la suite. L'eau forme une liaison avec le fer, avec une longueur de 1,95 Å (

Figure 8c) qui est bien plus longue que celle des NOx. Cependant, l'interaction de l'eau avec la charpente de la zéolithe a été renforcée par une liaison hydrogène de 1,59 Å.

Conclusion

Afin d'extraire les meilleures structures en fonction de leur sélectivité thermodynamique entre les NOx et l'eau, les différences d'énergies d'interaction H_2O-NO d'une part et H_2O- NO_2 d'autre part, pour les faujasites X et Y, ont été rassemblées dans la Figure 9. Le carré supérieur droit correspond aux matériaux les plus sélectifs. Il s'agit des faujasites Cu(I)Y, PtY, PdY, FeY, Cu(I)X, FeX et CoX. Par ailleurs, quelques soient les gaz, les énergies d'interaction sont presque toujours plus élevées pour les zéolites X que pour les zéolites Y (

Figure 3bc et Figure 6bc). Cette observation remet en question la faisabilité de la régénération de la zéolithe. En effet, l'adsorption est un phénomène exothermique. Ainsi, la désorption a besoin d'autant plus d'énergie que l'adsorption est forte. Or, pour garantir une stabilité de la structure cristalline, il n’est pas possible de chauffer au-delà de 500°C pour certaines zéolithes, bien moins pour d’autres. De plus, la zéolite X est connue pour être beaucoup plus hydrophile que la zéolite Y et plus fragile. Par conséquent, les faujasites Y sont à préférer aux X.

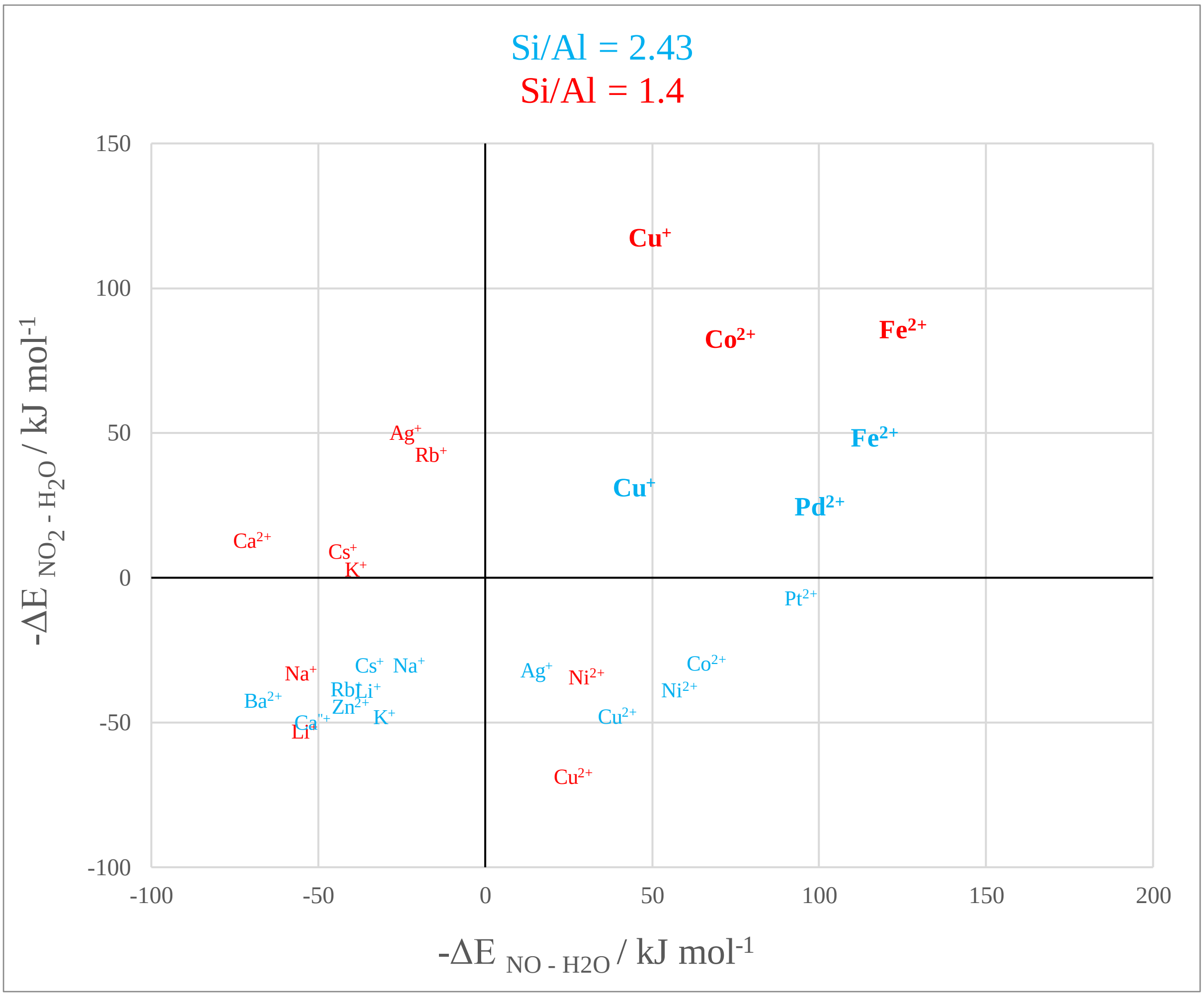

Figure 9 : Criblage DFT des cations mono et divalents au sein de la faujasite avec les rapports Si/Al de 2,43 (Y) et 1,4 (X) – Différence d’enthalpie entre l’eau et NO et entre l’eau et NO_2.

Au final, Cu^+, Pt^{2+}, Pd^{2+} et Fe^{2+} sont apparus comme les cations les plus intéressants. Le platine et le palladium présentent une sélectivité supérieure aux autres métaux. Cependant, leur coût, les ressources minières et leur enthalpies très élevées interdisent leur utilisation pour nos besoins. En revanche, Cu^+ et Fe^{2+} sont très bon marché, abondants, et leur sélectivité est plutôt bonne, surtout celle du fer. Par conséquent, Cu^+ et Fe^{2+} incorporés sur de la faujasite Y sont les candidats les plus appropriés pour notre application. Enfin, si le cuivre(II), le nickel et l’argent n’offre pas les mêmes garanties que le fer et le cuivre(I), ils ne sont pas écartés car ils semblent prometteurs notamment avec le NO. L’utilisation d’un mélange de zéolithes peut être approprié pour l’utilisation recherchée.

Le fer au sein de la Chabazite et de la Mordenite

Les énergies d'interaction du NO, du NO_2, du CO, du CO_2 et de H_2O avec la chabazite et la mordénite supportant le Fe^{2+} avec différents rapports Si/Al ont été calculées par DFT sur la base d'un PBE+D2+U statique à 0 K et d'une dynamique moléculaire ab-initio de pointe à 297 K. Des calculs à configuration unique ont d'abord été effectués. Les ensembles de rapports Si/Al de {11, 5, 3} et {23, 11, 5} ont été choisis pour la chabazite et la mordénite, respectivement. Les deux matériaux présentent une préférence thermodynamique pour le NO et le NO_2 par rapport à H_2O et au CO_2. Les simulations de dynamique moléculaire à 300 K pour Si/Al = 3 avec Fe-chabazite montrent une adsorption notable de NO, NO_2 et CO sur le Fer, même en présence de molécules d'eau. La fonction de distribution radiale a été utilisée pour décrire l'effet de la vapeur sur l'accroche de NO, NO_2 et CO sur le métal de transition. La co-adsorption du CO_2 a été négligée dans notre étude en raison de sa faible énergie d'interaction. L'allongement de la liaison après l'adsorption a été étudié pour tenir compte de la régénération de la zéolithe du substrat. À cet égard, les charges de Bader et les différences de densité de charge ont été calculées pour rationaliser les élongations. Plus important encore, les faibles rapports Si/Al améliorent l'affinité pour le NO et le NO_2 et favorisent la régénération.

En conclusion, la méthodologie développée dans ce travail a permis de prédire les énergies d'interaction pour piéger le CO et les NOx en présence d'eau et de CO_2 afin de traiter les gaz d'échappement diesel. Le fer a été identifié comme un cation compensateur de charge intéressant de par son efficacité d'adsorption et de désorption mais aussi par son coût industriel au regard de celui du platine, par exemple. Cependant, des expériences (à l'équilibre et dynamiques) doivent être menées pour s'assurer que le Fe-MOR et le Fe CHA soient de bons candidats pour répondre aux problèmes de santé au travail.

5 - DISCUSSION ET CONCLUSIONS

L'objectif de ce projet a été d'évaluer la capacité de matériaux à séparer le NO, le NO_2 et le CO d'un flux gazeux riche en eau et en dioxyde de carbone. La séparation est basée sur l'affinité plus forte qu'ont ces gaz toxiques pour l'Homme pour les matériaux poreux. Les approches statiques et dynamiques moléculaires de la théorie de la fonctionnelle de la densité ont été mises en œuvre au niveau théorique PBE. La fonction D2 de Grimme est utilisée pour traiter les corrections de dispersion. La méthodologie mise en œuvre pour étudier l'adsorption des NOx en présence d'eau a montré tout l'intérêt de la modélisation moléculaire pour mener à bien un criblage sur de nombreuses faujasites et extraire les candidats d'intérêt. Concrètement, ce travail a montré que l'utilisation du cuivre (I) et du fer (II) comme cations compensateur de charge sur des faujasites permettaient une adsorption plus importante des NOx. Les investigations sur les équilibres thermodynamiques et le comportement d'un lit granulaire en dynamique se poursuivent actuellement à l'INRS dans le cadre du programme ANR NOA (ANR-20-CE08-0024) dont l'INRS est coordinateur. Enfin, de premières investigations menées sur des silices amorphes et des matériaux carbonés à base de tanin de mimosa nous amènent à poursuivre dans cette voie. En effet, l'utilisation de ces matériaux ont montré une grande affinité pour les gaz ciblés. Ce travail doit se poursuivre. Les résultats devront être comparés à ceux obtenus avec les zéolithes et des expériences en présence d'humidité et de mélange en dynamiques devront être programmées.

Enfin, d'autres situations de travail où des oxydes d'azotes sont présents dans l'atmosphère pourront être étudiées et améliorées. Citons, les atmosphères des usines de formation d'acide nitrique, les postes de soudage et de décapage où les taux d'humidité sont bien inférieurs de ceux rencontrés dans un échappement diesel.

6 - ACRONYMES

a : Surface spécifique de l'adsorbant (m2/kg).
ACGIH : Association Advancing Occupational and Environmental Health
ANR: Agence nationale de la recherche
BET : Brunauer, Emmett et Teller
BJH : Barret-Joyner-Halenda (m)
BTP : Bâtiments et Travaux Publics
C : Concentration volumique (mol/m^3)
Calc : Calcination
d : Longueur de la liaison ou diamètre de pores (m)
D6R : Double 6-membered ring
DFT : Density Functional Theory
DN : Diamétre Nominal (m)
DRX : Diffraction Des Rayons X
E : Energie d'interaction (J/mol)
Ech : Echange

EGR : Exhaust Gas Recirculation
Ent : Entrée
ET : Etude Transversale
F : Débit total du gaz (m3/s)
FAP : Filtre à Particules
FRC : Flow Regulator Controller
FTIR : Spectroscopie Infrarouge à Transformée de Fourier
i : Indice pour « Espèce gazeuse »
ICP OES : Spectroscopie d'émission de plasma à couplage inductif
IJL : Institut Jean Lamour (Université de Lorraine – CNRS)
int : Indice pour « interaction »
IUPAC : International Union of Pure and Applied Chemistry
IZA : International Zeolite Association
m : Masse (kg)
NOA : Nitrogen Oxydes Adsorption
NOx : NO et NO_2
o : Indice pour “initial”
P : Pression, Pa
PBE : Perdew Burke Ernzerhof
ppm : Partie par million
q : Quantité adsorbée (mol/kg ou g/kg)
Q_v : Débit volumique (m^3/s)
R : Constante des gaz parfaits (R=8,315 J/mol K)
RH : Humidité relative
sat : Indice pour « saturation »
SCR : Selective Catalytic Reduction
STP : Standard Temperature Pression
T : Température (K)
t : Temps (s)
UL : Université de Lorraine
VASP : Vienna Ab Initio Simulation Package
X : zéolithe dont le rapport Si/Al <2
Y : zéolithe dont le rapport Si/Al >2
Z : Hauteur du lit granulaire (m)

ZPVE : Zero Point Vibrational Energy

ΔH_{ads} : Enthalpie d’adsorption (J/mol)

F_{HK} : fonctionnelle de la densité de Hohenberg et Kohn

ρ : densité électronique

General Introduction

Quantum chemistry, a modern scientific subdiscipline and a powerful tool in the equipage of human against the countdown he has set to himself by defying the laws that govern life from its beginning to its termination. Dating approximately 100 years, depending on the point that one wishes to set the starting line, albeit probably it has to be the paper of Heitler and London of 1927 on the explanation of stability of hydrogen, quantum chemistry has been forged through the presence of never-ending dilemmas and endeavours. Between chemist's intuitional approach with pictorial structural representations and physicist's persistence to deduction of chemistry to a pure quantum mechanical application, between rigorous mathematical treatments and semi-empirical approaches, which have no other origin than the simple fact that the Schrodinger equation could not provide analytic solutions except from hydrogen and helium. As the introduction of group theory made the study of atoms with polyelectronic valences reasonable, the goal was to produce any results with strong correlation to known chemical facts (like the proof of stability of chemical compounds known by the chemists), introducing thus a system of "rules", and setting the ground for the mathematical treatment of complex chemical problems.

Today, it is rather clear that quantum chemistry not only has been proven capable of produce results with quantitative value but has reached the potential of replacing experiments of high cost or danger. Ab-initio treatments of large molecules have been rendered possible, within the introduction of approximations and the utilization of electronic computers. Starting from the investigation of numbered atoms in gas phase, now, even the vastness of sold surfaces and porous materials are in the microscope of the theoretician under the premise of the periodicity of fundamental structural units.

This work, although of humble content compared to the state-of-the-art, is another triumph of quantum chemistry and its fervorous supporters, who brought about its practicality for the confrontation even of singular chemical problems. The thermodynamic separation primarily of NO and NO_2, and secondarily of CO, out of H_2O is currently explored in the grounds of limiting the diesel emissions permitted to be released in the environment. The project takes interest of low temperature conditions, where the currently applied diesel catalysts are unable to neutralize NO_x emissions with significant performances, putting the health of workers in the vicinity in jeopardy, which is especially problematic in the case of non-road vehicles working with many cold starts. The capture of those air pollutants is a step towards the amelioration of working conditions, a program led by institut national de recherche et de sécurité (INRS).

This investigation is a combination of theoretical modelling on gas adsorption in porous materials and experimental validation of selected samples. The modelling is done using periodic density functional theory (DFT) at the Perdew-Burke-Ernzerhof (PBE) level of theory, making single-configuration and molecular dynamics considerations. Various zeolitic structures and cations are tested and the most appropriate are further analysed for the nature of interactions and the co-adsorption of several gases at the same time. The breakthrough curves carried out assess the performance of selected zeolites on the selective capture of NO_x and CO in realistic conditions.

This unfolding of the current dissertation follows in 6 chapters. The first one the state-of-the-art, presents the problem at hand in a thorough manner, so that a non-specialist can comprehend its nature and the progress achieved, and be prepared for the heart of the investigation. The second chapter summarizes the extensive list of theoretical tools and considerations made, to reach results of quantitative import. The rest of the chapters will be analysed in individual paragraphs as they comprise the very core of this endeavour.

The third chapter is made up of the most extensive and demanding part of this work, which is the screening of a series of monovalent and divalent cations, promoting the large pored faujasite. Grimme's correction scheme, D2, was employed to handle the imperfectly represented by DFT, dispersion forces. The well-known self-interaction originated over-localization of transition metal d-electrons was treated with Hubbard's potential, utilizing values generated in the literature for similar systems. This screening was complemented with Bader charge transfer analyses and their 3-D corresponding representations, charge density differences, crediting the assumption that the separation of NO_x from H_2O has to be based on the π-backdonation, which results from the substantially different electronic configuration characteristics of the molecular species. Finally, the inclination of the adsorbed gases for further chemical reactions during their trapping, which might lead to unwanted by-products, is assessed by the bond-length disturbances occurring as a result of the trapping itself. This work has been accepted for publication from the journal "Molecular Systems Design & Engineering" with the doi, 10.1039/D3ME00044C.

The fourth chapter refers to the investigation of alternative zeolitic structures, for the selective adsorption of NO_x and CO against H_2O, employing the most prominent cation as came out of chapter 3. Small pored chabazite and large-pored mordenite are explored with static DFT, harvesting once more optimistic results. Molecular dynamics were utilized only after, for low silica chabazite, to verify the selectivity of the structure, and test the inhibiting potential of water towards the capture of NO_x and CO by co-adsorption simulations.

In the fifth chapter amorphous silica is tested, representing also the medium pored category, for the thermodynamic preference of NO_x against H_2O. Previously proven cation is assessed in isolated and stable cluster form, in realistic amorphous silica surfaces with single configuration calculations. Once more optimistic results were produced regarding the selectivity.

1. State of the art

The purpose of this chapter is to summarise scientific advancements on "*optimization of nanoporous materials formulations for NO_x capture by ab initio molecular modelling*". The present chapter is an introduction, that can help a non-specialist reader to get familiar to the topic and reach the core of the work, which is in the results. The "skeleton" of the chapter is defined by the dissertation title since the chapter progressively defines and describes every term of the dissertation title.

1.1 NO_x air pollutants

NO_x is currently used as an abbreviation for NO and NO_2 molecular substances, whose trace gases affect atmospheric chemistry, air quality, human health, and climate. Although NO_x are not major greenhouse gases, they can affect the latter's concentration through complex chemical processes.[1] Anthropogenic sources of NO_x include biomass burning, fossil fuel and biofuel combustion and N-fertilized soil emissions[1,2]. The partitioning of each NO_x source in a particular region can be analysed with big scale top-down measurements.

Regarding human health, repeated exposure of asthmatic and allergic individuals to ambient NO_2, has been shown to enhance asthmatic response.[3] Moreover, long-term exposure to particulate matter and NO_2 (both present in car exhausts gases) has been linked to the development of heart failure[4].

From an environmental viewpoint, NO_x have a significant impact on the atmospheric chemistry. NO, gets oxidized in the atmosphere forming NO_2, the latter being **the only source of tropospheric O_3**[5]. Ozone is a major air pollutant, being itself a greenhouse gas, but also a precursor of radical OH, which determines the atmospheric lifetime of other gaseous pollutants as methane, volatile organic compounds (VOCs) and carbon monoxide.[5]

1.2 Measures to limit NO_x emissions

According to European Environment Agency[6], in 2011, the most significant sources of NO_x, were road transport (41%), energy production and distribution (23%) and the commercial, institutional and household sectors (13%). Furthermore, a decrease of 44% in NO_x emissions had been observed since 1990, mainly in the road transport sector. This reduction was achieved despite the increase in activity in this sector, mainly thanks to fitting *three-way catalysts* (TWC) to spark ignition engines.

Diesel engines exhibit several benefits compared to spark-ignition ones, but their environmental impact has prevented them from being the exclusive choice. On the one hand, they present better thermodynamic efficiency and limited CO_2 emissions. On the other hand, they release more NO_x and particulate matter than gasoline engines. Euro stage VI regulation published in 2014 by the European union has set a series of new ceilings concerning exhaust gases, according to which, NO_x fumes cannot exceed the limit of 80 mg/km[7]. This is a decrease of 56% from the previous regulation (Euro V). As TWC need stoichiometric amounts of oxygen, or less, they can be implemented in gasoline engines, but not in diesel, where oxygen is present in excess. An alternative solution had to be applied by companies in order to reduce NO_x emissions.

Exhaust gas recirculation (EGR) is a procedure where, the exhaust gas, instead of being released in the environment, is rather reinjected in the cylinder. Three major effects have been suggested to explain the impact of EGR on NO_x reduction, given that increasing the temperature of the combustion flame, the concentration of NO_x produced is also increased: 1) the intake oxygen concentration is decreased by replacing part of it with recirculated gas. Limited oxygen availability in the cylinder increases mixing time and results in a lower flame temperature (*dilution effect*); 2) the addition of recirculated CO_2 and water vapour in the engine cylinder increases the heat capacity of the in-cylinder charge (*thermal effect*), leading to lower flame temperature during the combustion process; 3) the endothermic dissociation of carbon dioxide and water vapour lowers the flame temperature (*chemical effect*) and hence reduces NO_x emissions.[8] The significance of these 3 effects has been studied, and there is an agreement on the statement that the chemical effect is the least important. The rest have both been proposed as dominant, though the last results suggest the dilution effect as the strongest.[8–10] The trade-off to be paid is the increase in particulate matter emissions and unburned hydrocarbons as well as deterioration in engine power output and fuel economy.[10] 80-90% of NO_x reduction was attributed to the dilution effect, and equal was the increase of particulate matter emission.

NO_x storage reduction (NSR) is another method allowing the reduction of NO_x fumes. NSR working conditions comprise two phases, and a proposed mechanism for its activity is given below: Initially, during the *lean phase* (~ 60-90 s), produced NO_x are trapped in the form of nitrates or nitrites on the surface of a catalyst. Next, during the *fuel rich phase* (~ 3-5 s), trapped nitrates are reduced firstly to nitrites and secondly to isocyanate/cyanate species, which finally

react with residual nitrates to give N_2. Dedicated experiments have shown that excess O_2 can oxidize NCO species to nitrites, and further to nitrates, hence explaining the required fuel rich period. A representative catalyst used for this reactions is Pt-BaO/Al_2O_3, and the reducing agent can be H_2, CO, C_3H_6 and others, with H_2 being the most efficient among them for NO_x traps.[11] NSR catalysts are very effective for NO_x conversion at specific temperature ranges; Pt-K/Al_2O_3 was measured to yield 80% NO_x conversion at 300 °C, and almost 100% at 500 °. However, the efficiency of this system falls to 60% at higher temperatures and never regains its initial potential.[12] Furthermore, NSR catalysts suffer from many other drawbacks, like carbon deposition on Pt sites, sulphur poisoning and thermal degradation, the latter occurring during sulphur de-poisoning. Other metals have been proposed for replacing Ba, such as K which improves reaction kinetics. Alternative precious metals, to the exceedingly expensive Pt, were also proposed, like Pd and Rh. Nonetheless, the cost is still high and plenty of issues remain.

Selective catalytic reduction (SCR) is an alternative solution for reducing NO_x emissions from diesel engine exhausts. It was first applied to thermal power plants in Japan. Ammonia is the most used reducing agent for the selective NO_x reduction to harmless N_2 and H_2O. The most employed catalyst is V_2O_5-WO_3TiO_2, owing to its excellent activity, selectivity and working life. Its efficiency can reach almost 100% NO_x conversion.[13] Two overall reactions occur in the process are as follows:

$$4NO + 4NH_3 + O_2 \rightarrow 4N_2 + 6H_2O \tag{1.1}$$

$$2NO_2 + 4NH_3 + O_2 \rightarrow 3N_2 + 6H_2O \tag{1.2}$$

A solution of urea (32.5) and high purity water (distilled water) known as AdBlue is usually used as a source of ammonia.[14] Although SCR is widely used in NO_x neutralization, it may give undesired reactions under various conditions. 1) Reactions (1.3) and (1.4) occur when NO_2 concentration dominates in NO_x emissions; 2) excess O_2 can oxidize ammonia to NO and N_2; 3) reaction (1.5) occurs above 450 °C; 4) reaction (1.6) occurs below 200 °C, leading to the production of ammonium nitrates which can be deposited on the catalyst active sites, temporally deactivating it. In addition, reactions (1.7) and (1.8) occur below 200 °C, producing sulphates which are also deposited on the catalyst, hindering its functionality. The catalyst regeneration occurs above 500 °C, restoring its activity.[14]

$$8NO_2 + 6NH_3 \rightarrow 7N_2O + 9H_2O \tag{1.3}$$

$$4NO_2 + 4NH_3 + O_2 \rightarrow 4N_2O + 6H_2O \tag{1.4}$$

$$2NH_3 + O_2 \rightarrow N_2O + 6H_2O \tag{1.5}$$

$$2NH_3 + 2NO_2 + H_2O \rightarrow NH_4NO_3 + NH_4NO_2 \tag{1.6}$$

$$2NH_3 + SO_3 + H_2O \rightarrow (NH_4)_2SO_4 \tag{1.7}$$

$$NH_3 + SO_3 + H_2O \rightarrow NH_4HSO_4 \tag{1.8}$$

On the other hand, V_2O_5-WO_3TiO_2 is only efficient between 300 and 400 °C and the loss of V during the preparation of the catalyst and operation is hazardous to the environment and to human health.[15] The issue of the narrow temperature range can be addressed with the replacement of part of V with Ce and other metals, which at the same time are not so harmful when released. Apart from that, a typical diesel emission control system using SCR also includes a diesel particulate filter (DPF) which may expose the SCF catalyst to temperatures > 650 °C during its regeneration. Traditional V-based catalysts do not remain active at these temperatures due to the phase transformation of TiO_2 support.

Current pollution control legislations have set up guidelines for imposing a complex treatment of diesel exhaust gases (Figure 1.1), as follows: Once exhaust gases leave the engine, they flow through the *diesel oxidation catalyst* (DOC), followed by the *diesel particulate filter* (DPF). DOC oxidizes hydrocarbons and CO, and partially NO to NO_2, which helps SCR present after DPF and requiring equal amounts of NO and NO_2 for its activity. DPF filters particulate matter present in exhaust gas. SRC chamber performs NO_x neutralization in DPF outstream, mixed with urea before SCR. However, SCR catalysts, are inefficient at low temperatures (< 200 °C), which concerns heavy duty vehicles discontinuously working, and systematically remaining in the low temperature range. Hence, additional gas exhaust treatments, and mainly NO_x treatments are required for such vehicles. This is the subject of next parts of the present chapter.

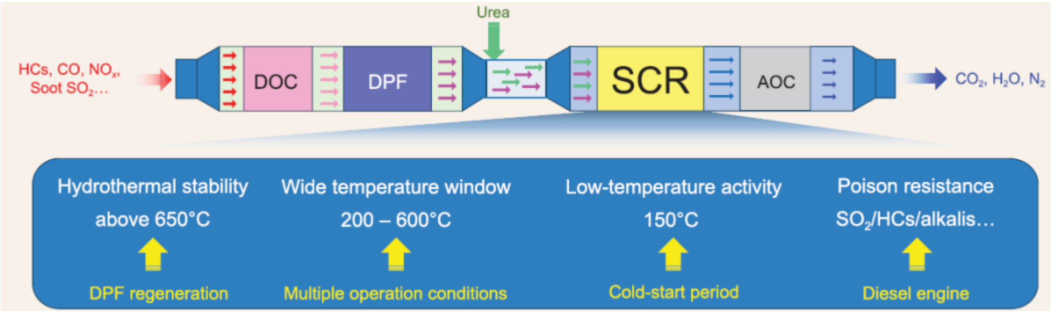

Figure 1.1: [16] Processing of exhaust gases from the moment they leave the engine till the point they are released in the air. This set-up belongs to a commercial model.

1.3 NO_x removal in diesel exhaust through adsorption

To dive into adsorption, which is a molecular scale phenomenon, it is suitable to introduce here some key definitions. Adsorption is the adhesion of atoms, ions or molecules from a gas, liquid or dissolved solid to a surface.[17] According to the kind of bonding between adsorbent and adsorbate, two categories of adsorption can be considered as follows: (1) Physical adsorption or physisorption, involving physical interactions between the adsorbate and the adsorbent, and (2) chemical adsorption or chemisorption, involving chemical reactions between them.

NO_x adsorption has been investigated for the development of cheap processes of NO_x removal in diesel exhaust gas. Indeed, high specific area adsorbents like porous materials can be used to separate molecules that differ a) structurally (size and/or shape), b) chemically (functionality) and c) electronically (polarizability). These properties can be used for selectively capturing NO_x in diesel exhaust gases. Separation and adsorption of gas molecules present, such as NO_x and its competitors CO_2, CO and water can be performed through various mechanisms as follows: a) A thermodynamic (enthalpic)-driven mechanism based on the adsorbent affinity that varies for the various gases present in the mixture. On this basis, *adsorption enthalpy* is defined as *the heat released when an adsorbate binds on the adsorbent surface*; b) kinetics-driven mechanism, based on gas diffusivity limited by the porous material, depending on pores opening and molecular characteristics; c) entropy-based separation, where the size/shape of the adsorbent allows efficient packing of the target-molecule, securing its crossing; iv) molecular sieving, where the absorbent pores allow full exclusion of a molecule in the mixture. Modelized materials have to be efficient and also very selective NO_x adsorbents, for avoiding inhibition by molecules (water, CO_2,…) present in diesel exhaust gas at much higher concentration than NO_x (NO_x concentration is about 350–1000 ppm while H_2O content is about 10%[18,19]). For capturing NO_x in exhaust gases, the thermodynamic mechanism has been selected, because water and NO_x have very different electronic structures, but similar sizes.

The adsorption capacity or storage capacity is the maximum amount of adsorbate per unit mass (or volume) of adsorbent at a certain temperature. To ensure the maximum efficiency for a trap, the capacity must be just enough to support the expected amount of pollutant gas. The adsorption rate defined as, how fast the gas adsorbs on the surface is highly dependent on gas diffusion in the present work. This is because kinetics play a decisive role in the determination of the efficiency of a passive NO_x adsorbent (see 1.4 for definition), the latter being a non-isolated system, where the time scale of the process is only a few seconds. Adsorbent regeneration is absolutely required for a passive NO_x adsorbent, as it determines its reusability. It is accomplished by gas desorption, with increasing the temperature up to a value high enough for the gas kinetic energy to overcome the gas attractive force to the adsorbent surface. Regeneration is performed by a committed process, like a *temperature programmed gas desorption*, or naturally by fully exploiting altering conditions of the experiment.

Experimentally, adsorption processes are investigated with determining adsorption isotherms, describing the amount of adsorbate on the adsorbent as a function of the pressure (concerning gases) or concentration (concerning liquids) at a constant temperature. Isotherms have been modelized using various mathematical models (Langmuir, Sips, Dubinin-Astakhov, Toth, …) to explain the way adsorption takes place. One of the most famous models, named after Langmuir, describes adsorption as a reversible process where solely one molecule of adsorbate (behaving as an ideal gas) adsorbs at an adsorption site, leading to several equations describing the process. Figure 1.2 depicts experimental isotherm data and various correlation models (Woo et al., 2021).[20]

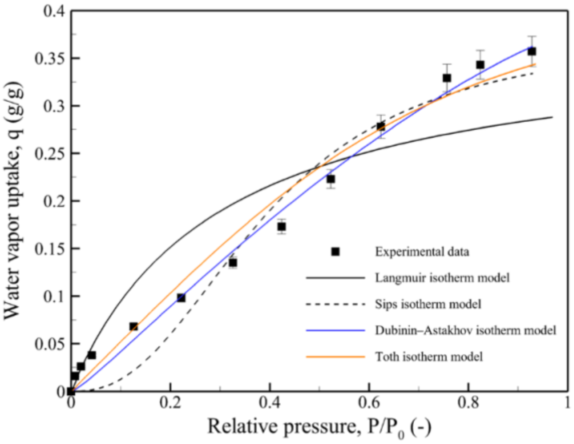

Figure 1.2: Water vapor adsorption on silica gel; various phenomenological models are compared based on their fitting to the experimental data[20].

Adsorption is also studied by determining the breakthrough curve which shows the variation with time, of the outlet gas concentration, after gas flow through a trap. The trap hosts gas molecules until saturation. Then, the outlet gas concentration becomes equal to the inlet concentration, after the appearance of a small peak, called *roll-up*, a phenomenon occurring in multi-component adsorption processes.[21] Breakthrough curves are shown in Figures 1.3a and 1.3b. The green area representing the time window where gas adsorbs to the trap, allows the determination of the trapped gas amount. The blue area existing only in 1.3b represents the rollup, where for a short period of time, the outlet gas concentration is higher than the inlet concentration.

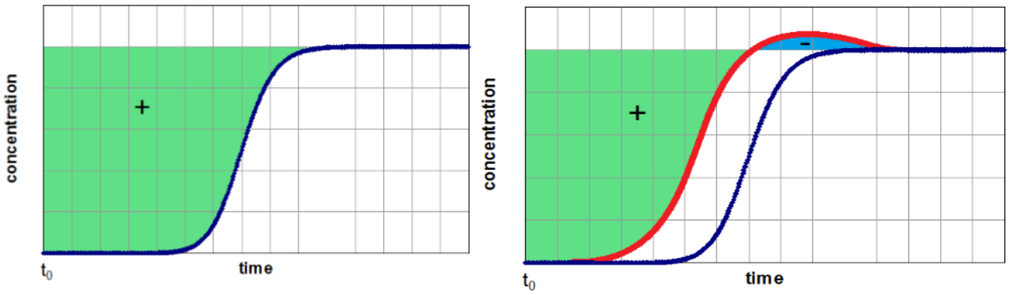

Figure 1.3: Representations of [22] a) a simple breakthrough curve on the left, and b) a breakthrough curve with a roll-up on the right.

1.4 Cold starts and passive NO_x adsorbents

Since catalytic technology is a promising solution for high temperature (>200 °C) NO_x adsorption, effort is made to reach these conditions with limited NO_x release while the engine temperature is lower than 200°C. The *cold start* corresponds to starting a vehicle's engine at ambient temperature. While a TWC component can quickly reach its operating temperature[23], diesel vehicles suffer from extended warm-up periods[24,25]. For resolving this problem, a component called *passive NO_x adsorber* (PNA) is introduced in the vehicle for NO_x trapping at low temperatures, followed by NO_x release at higher temperatures (Figure 1.4). The idea of PNA is old, according to numerous patents published in the past[26–28]. However, the actual lowering of acceptable NO_x emission levels has led to reconsider this technology. Moreover, one major NO_x abatement technology that followed PNA, is the *cold start concept* (CSC)[19,29] catalyst, which not only stores NO_x until the temperature is high enough, but also starts catalysing NO_x conversion to N_2, enabling even better performances.

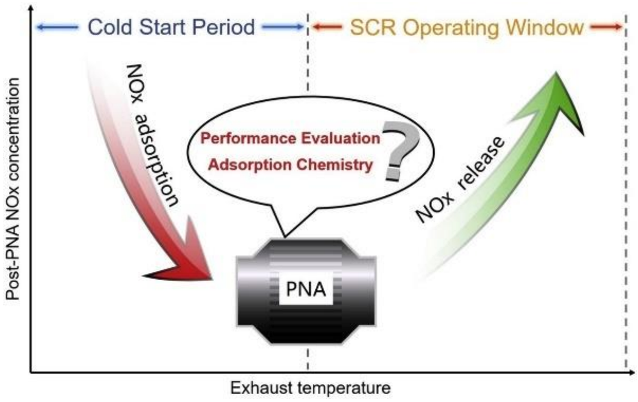

Figure 1.4: A graphical representation of PNA device.[30]

The effectiveness of these catalysts has been tested by Chen et al[19]. DOC, PNA and CSC have been compared by considering their NO_x abatement efficiency on a realistic gas stream with NO at 200 ppm and 80 °C. This comparison has shown persuasive results for the CSC and – to a lesser extent – for the PNA. The choice of NO as the only NO_x species in the feed has been decided, considering that NO is the major gas that reaches SCR during cold starts[30]. Figure 1.5 indicates that, approximately 120 ppm NO leak from PNA, but only 40 ppm from CSC, showing 40 and 80 % efficiency, respectively. The time window of 100 seconds is considered as the time required to reach high temperatures in the engine. The main drawback of this technology is the high material cost due to the use of expensive Pt and Pd.

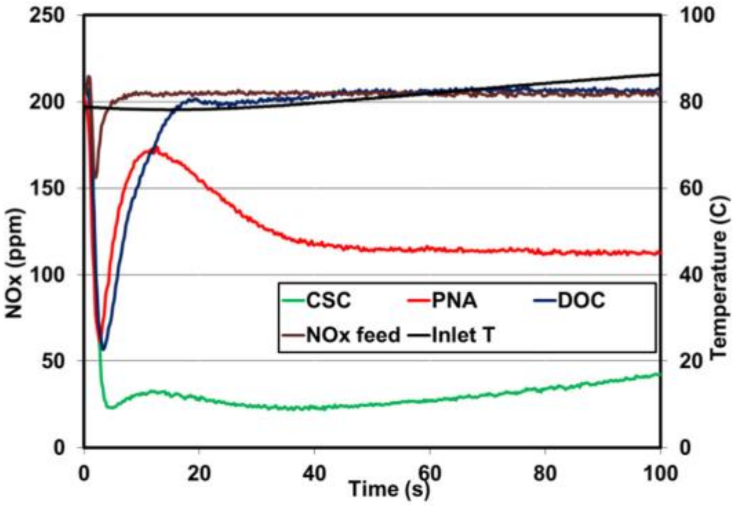

Figure 1.5: Breakthrough curves depicting the exposition of CSC, PNA and DOC to NOx feed of 200 ppm at 80 °C. [19] Both PNA and CSC show great NOx limiting potential.

Gu et al.[30] used a series of criteria to assess the effectiveness of a PNA: a) Low temperature NO_x storage capacity, b) rate of NO_x adsorption, c) NO_x desorption temperature, d) real exhaust compatibility, e) degradation resistance and f) cost. Clearly, NO_x storage capacity dictates the amount of PNA required to trap low-temperature NO_x emissions. The adsorption rate is a significant parameter, as it determines whether gases will be adsorbed or not, in the limited time during which they are in contact with the PNA. NO_x desorption temperature must be compatible with the trap regeneration mechanism. Ideally, it must be just higher than the SCR operating temperature. Real exhaust compatibility refers to the trap adaptability to the actual process conditions. Namely, the trap must be effective and selective and chemically inert in the process conditions. Both the desorption temperature and the real exhaust compatibility are strongly associated to the degradation resistance. As mentioned before, real exhaust conditions in SCR involve temperatures > 650 °C, as well as high steam concentrations, causing thermal aging. In addition, sulphur oxides present are also responsible for sulphur poisoning. Both these key features cause alterations to the storage capacity and the desorption temperature range of the PNA, damaging its performance over time. Finally, precious metals are up to date imperative for the construction of PNA and CSC materials, causing their cost to skyrocket. Thus, further investigations are needed, for mass-production of viable materials.

PNA's potential has been reported in several publications. Crocker et al.[31] published an article reporting the performance of a PNA using combinations of Ce and Zn oxides, supporting Pt and Pd. They observed formation of Pt and Pd particles of 2 nm. Moreover, they showed that adding Ce into ZrO_2 results in improved adsorption capacity in the temperature range of 80-160 °C. On the other hand, the addition of Ce was related to increased nitrites production which can be oxidized to stable nitrates, during NO_x adsorption. Regarding the cations, Pd reduced the PNA storage efficiency, but also improved the low temperature NO_x desorption, associated with a lower production of nitrates, in comparison with Pt. To ensure balanced results, the authors attempted a mix between the Ce and Zn, Pt and Pd. These findings are summarized in Figures 1.6 & 1.7.

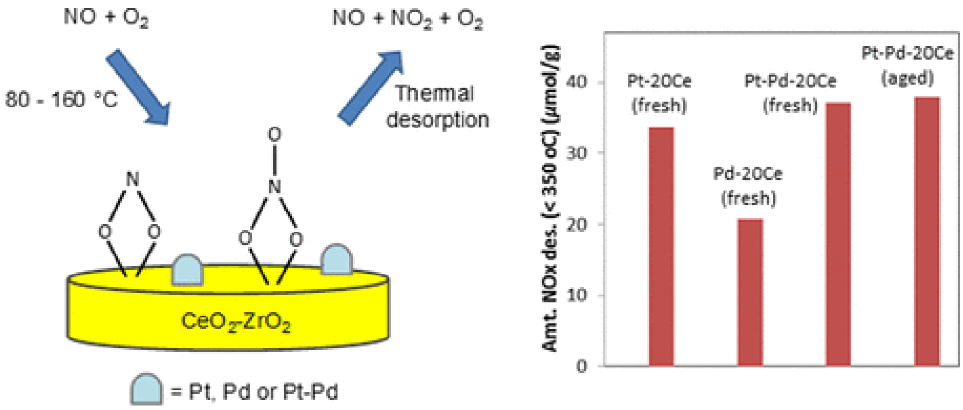

Figures 1.6 & 1.7: Figure 1.6 on the left depicts graphically a CeO_2-ZrO_2 based PNA, supporting Pt or Pd. Figure 1.7 on the right shows the amount of NO_x desorbed below 350°C for fresh Pt, Pd and Pt-Pd supporting PNA, as well as aged Pt-Pd supporting PNA.[31]

In another study, Crocker et al.[32] used Pd promoted mixed WO_3 with ZrO_2, for the low-temperature capture of NO_x. They reported that 95% of the trapped NO_x had been released by thermal ramping to 350 °C. They also identified that during co-feeding of CO, increased NO_x capacity was observed for Pd-W-Zr.

Judging these materials by the aforementioned criteria we observe really promising results. Low temperature NO_x storage capacity appears satisfying, since up to 80% of NO_x were reduced. The rate of adsorption appeared also suitable. The desorption temperature is tuneable by changing the compensating cation and the support composition. However, poor resistance to sulphur poisoning was observed for CeO_2 based catalysts [33]. CeO_2 sulphur aging leads to a decreased surface area, and to the production of $Ce(SO_4)_2$ which prevents the trap regeneration[33,34].

Transition metal promoted zeolites have also been tested for low temperature NO_x storage. Chen et al.[35] reported high storage efficiency in diesel engine-like gas feed for Pd exchanged BEA, MFI, CHA and CeO_2, as illustrated in Figures 1.8 & 1.9. Furthermore, they observed high sulphur poisoning resistance for all zeolites as shown in Figure 1.9. In another study Ryou et al.[36] showed that hydrothermal treatment of Pd promoted SSZ-13 enhanced the low-temperature passive NO adsorption performance below 120 °C, by converting PdO species to Pd^{2+}. They proved this conversion by NO_x desorption peaks at 250 and 400 °C, by diffuse reflectance infrared Fourier transform spectroscopy (DRIFT) (Figure 1.10). They also compared samples synthesised with different ion employing methods: Incipient wetness impregnating method (IWI), wet impregnation (WET), ion exchange (ION), solid-state ion exchange (S-S).

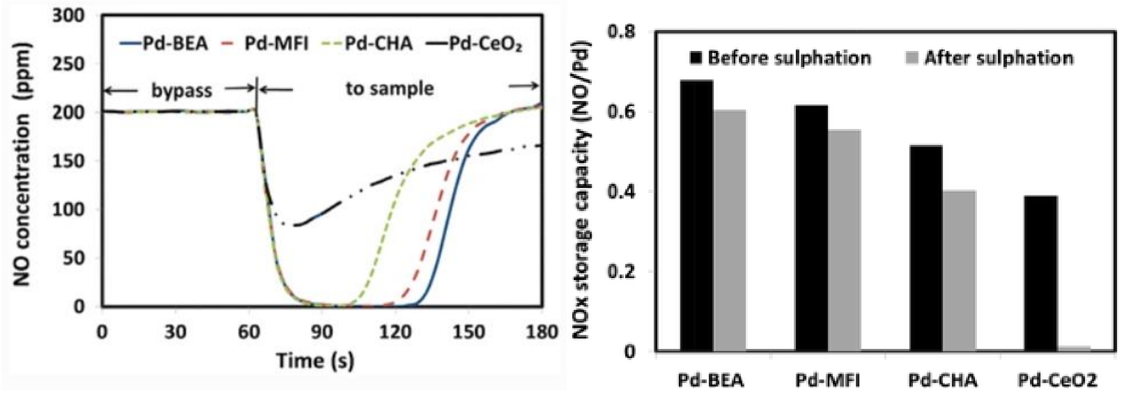

Figures 1.8 & 1.9: Figure 1.8 on the left is a breakthrough-kind curve, showing how NO outlet concentration is reduced when the feed passes through a corresponding PNA. Figure 1.9 compares the performances of different PNAs before and after sulphur poissoning[35]

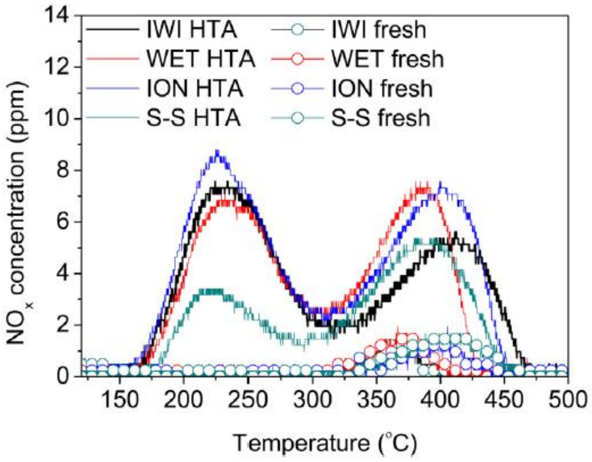

Figure 1.10: A comparison of hydrothermally aged and fresh samples synthesised with different methods, as came out of desorption curves.[36]

A crucial characteristic of the PNA quality is the amount of NO_x trapped per adsorption site. For this purpose, Gu and Epling defined the ratio NO_x to PGM (platinum group metals). Comparing the efficiencies of other bibliographic results, they showed that for a loading equal or lower to $\sim 1 wt.\%$, zeolite supported Pd is associated with high ratios. The efficiency of the catalyst has also been associated with the quantity $\mu mol\ of\ NO_x\ /\ g\ catalyst$.[37] *The measure*

NO_x/PGM can give a hint to the most cost-efficient PNA possible – with the approximation that the total cost of the catalyst is determined by the metal – but not necessarily the most effective. Naturally, for a much cheaper metal, where the cost of the ion impregnating method and the cost of the substrate itself are comparable to it, NO_x/metal ratio would be far less important. Figure 1.11 illustrates the potential of PGM/NOx as a cost-efficiency measure[36–39].

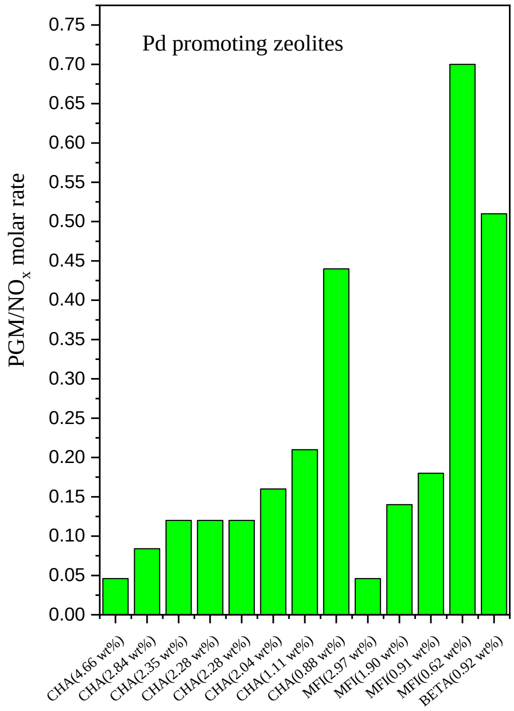

Figure 1.11: A collection of bibliographic results on the zeolites chabazite, MFI and BETA, exchanged with Pd are used for the calculation of PGM/NO_x molar ratio, an index reflecting the cost-efficiency of the PNA.

All of the criteria given above have been respected for the zeolites tested apart from the low-cost. These materials have been experimentally found to effectively trap NO_x. However, only little has been said about the influence of the various gases present in diesel exhaust, during NO_x capture. N_2 is a neutral gas which has no impact on NO_x capture. O_2 has a negligible effect[40]. CO_2 present in diesel exhaust has been reported to reduce the PNA capacity of $Pd/Ce/Al_2O_3$ but had not any impact on the PNA capacity of Pd promoted zeolite[41]. H_2O has also been reported to severely suppress the PNA efficiency of Pd-zeolite materials by Zhang et al.[39], but CO promotes NO_x capture.

1.5 Metal-organic frameworks

Another category of porous materials, whose members have shown great potential as separating agents, consists of the *metal-organic frameworks* (MOF). These relatively newly discovered materials, have attracted great attention due to their excellent efficiency in gas separation.[42] In fact, zeolites, which have been widely used for similar applications, do not offer absolute flexibility regarding the tuning of their pore sizes and shapes, forbidding their utilization in cases that very precise pore structures are desired. More specifically, scientists have come up with a classification of the separation difficulty, called *level of complexity*, which groups a mixture of gas/vapour separation systems based on the average difference in kinetic diameter. Ultra-microporous MOFs address exactly this issue, offering the possibility for very fine tuning of the porous size, shape and functionality.

MOFs have been investigated for their low temperature deNO_x potential in the past. Shanshan Shang et al.[43] studied the adsorption of NO_2 in ambient temperatures, in dry and wet conditions. They reported promising behaviour for the MOFs they used, with wet conditions almost doubling the adsorption capacity of their best candidate. In another study Gopalsamy et al.[44] tested UiO-66, as support for various divalent metals, using periodic DFT and grand canonical Monte Carlo simulations. They showed that this MOF has excellent behaviour when it contains Fe^{II}, which is a far cheaper alternative to Pt and Pd. S. Jensen et al.[45] performed a combination of synthesis, spectroscopy and ab initio modelling of several metal containing MOF-74 structures, and showed that Ti-MOF-74 adsorbs NO with much higher affinity than water.

1.6 Zeolites

Up to this point, the suitability of zeolites as PNA has been pointed out. Several zeolites with different three-dimensional structures, varying in pore shape, size and Si/Al ratio, can be produced for interesting applications in adsorption and catalysis chemistry. They have high boiling points, and don’t get burned, they resist high pressures, they are not soluble in water and other inorganic solvents, they do not get oxidized in air, and they are not reactive. Being able to exchange cations, they exhibit flexible affinity for polar molecules such as water, they have very high surface area, shape selectivity, as well as relatively low cost.

Regarding their microscopic structure, zeolites are aluminosilicate materials comprising cavities (often called pores), occupied by large ions and water molecules both of which have considerable freedom of movement, permitting ion-exchange and reversible dehydration. Al and Si atoms occupy 4-connected vertices of a three-dimensional nets and oxygen atoms occupy 2-connected positions between the 4-connected vertices.

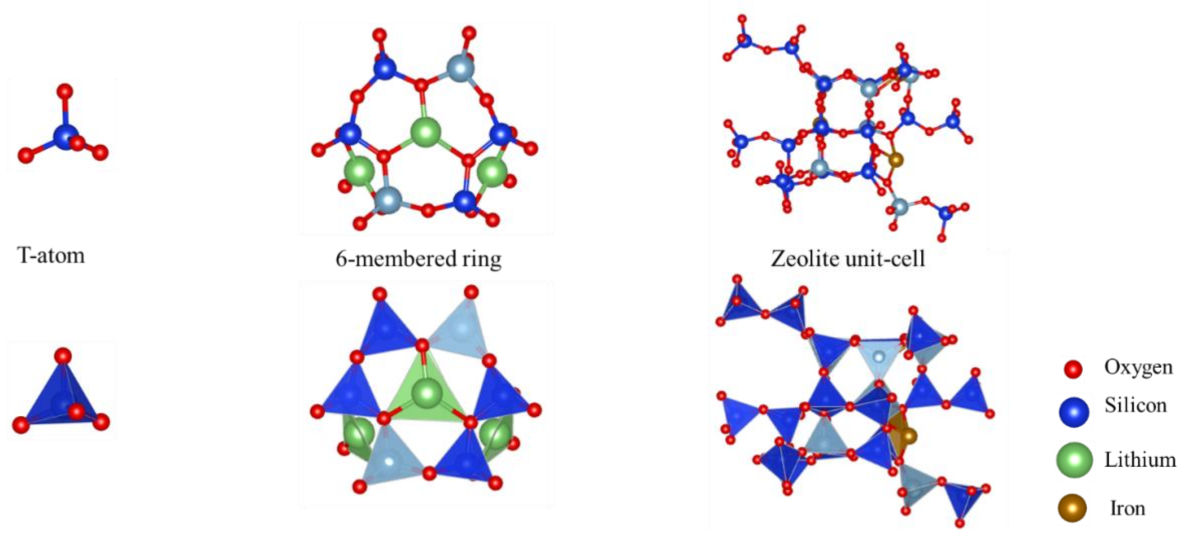

Figure 1.12: Two different representations of small zeolitic structures are presented. One with ball and stick and one with polyhedral prisms, focusing on the bond-coordination of the atoms in the structure.

Thus, each tetrahedral (T) vertex is surrounded by four oxygen positions, and each oxygen is chemically bonded to two (Si, Al) atoms in T sites.[46] The replacement of each Si with Al is followed by electron deficit which is compensated by the introduction of a metal in the vicinity. As shown in Figure 1.12 tetrahedral-coordinated Si and Al atoms are surrounded by O atoms, which when placed in space create micro-arrangements, like 6-membered rings (6MR), and depending on their further ordering give rise to various zeolites. When these unit cells are repeated in three-dimensions they create perfect macroscopic crystals.

Zeolites are divided into groups according to their aperture size. The latter is measured based on the T atoms that a pore (or ring) contains. If a ring contains n T atoms it is a *n-membered ring or n-MR*. We categorize zeolites whose largest apertures are 8-MR (like chabazite) as small-pore, those with 10-MR (like MFI) as medium-pore, those with 12-MR (like faujasite) as large pore and those with $>$ 12-MR as ultra-large pore.[16] Their pore-size, can affect in several ways their application as PNA. The most used cation for low temperature NO_x adsorption has been Pd due to the selectivity, efficiency and regenerability it offers to the material. However, its implementation in small-pore zeolites is limited[36–38], as the majorly used ion-exchange method, is heavily inhibited. In fact, in small pore zeolites, Pd has been observed to mainly form clusters in the surface of the supporter. Additionally, the Pd-based chemical species that are formed, are strongly influenced by the Si/Al ratio. Smaller Si/Al ratios mean that Al atoms will be probably far from each other, disfavouring the formation of Pd^{2+}.[38,47] On the other hand, Chen et al.[35] showed that the desorption temperature of the gases is inversely proportional to the pore size, by comparing BEA, MFI and CHA, as representatives of large, medium and small-pored zeolites, respectively. They proposed that a combination of zeolites can help with the rational design of a PNA, adjusting the desorption temperature window. Zheng et al. ended up to the same conclusions using Pd promoted MFI and CHA.[39] In the aforementioned study, Chen et al. revealed a very interesting trend: Whereas in the large pore zeolite BEA, the temperature rise disfavours PNA capacity, this is mitigated for the middle sized pores of MFI, and even inversed in the case of small-pored chabazite, validating the exploration of zeolites represented by different pore sizes.

1.6.1 Faujasite

Faujasite (FAU) is a three-dimensional network belonging to the large-pore materials. It is consisted of three important building units, the sodalite cage, the supercage and the double six-membered ring (D6R) prism. The supercage consists of 12-MRs which do not appear in the D6R or in the sodalite cage.

The D6R is consisted of 2 six-membered rings, where the Si atoms of the two rings are bridged through an O atom forming a second type of ring: a 4-membered one. The sodalite cage is constructed of eight hexagonal windows linked with 4-membered ones. The opening of the sodalite cage is not sufficient for most of the molecules to pass through, but for very small ones like dihydrogen[48], except on higher gas loadings[49,50]. On the contrary, supercage gives access to bigger molecules as well. Figure 1.13 is a representation of a pure silica faujasite (for simplicity no Al atoms, and hence, no cations are introduced in the framework), having labelled the fundamental structural units. The rhombohedral boundaries enclose the periodically repeated volume.

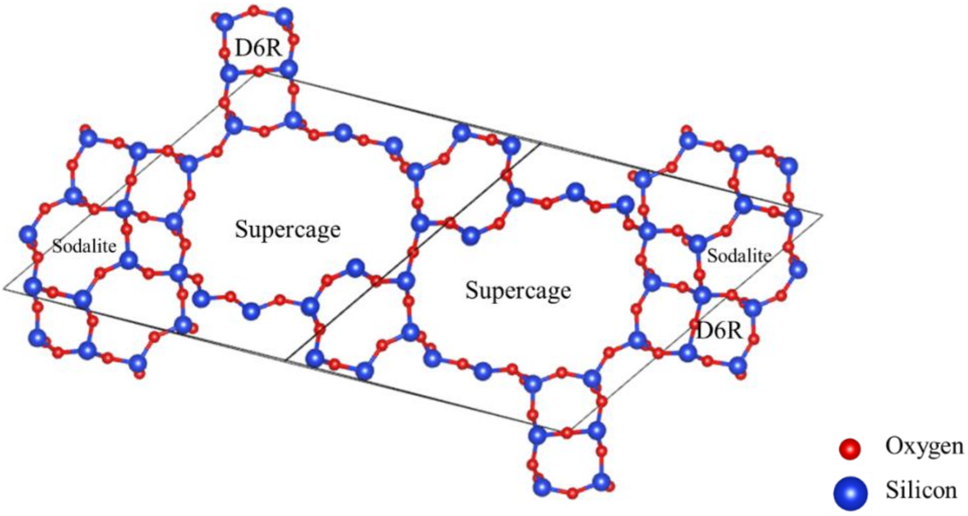

Figure 1.13: A pure silica faujasite. The fundamental structural units are underlined by labels.

Another basic structural property is the place that metals can occupy within the framework of FAU. There have been identified several positions for the distribution of metals in the framework of FAU, associated with different binding energies, with the stabler positions having higher priority. These positions are defined as *adsorption sites* and their occupation is dependent on the Si/Al ratio. Higher Si/Al ratios translate to larger cation loadings. Only when all the stable adsorption sites have been saturated, can the less stable host cations. Consequently, between two faujasite structures with different Si/Al ratios, like X (Si/Al = 1-1.5) and Y (Si/Al > 2), there are different cationic distributions, with different gas-trapping properties, owing to the difference in electron configuration of the hosted cations. Further discussion on faujasite's structural details will be given in chapter 3.

1.6.2 Chabazite

Chabazite (CHA) is a small-pore zeolite. It is consisted of D6Rs similarly to FAU, which are connected by 8MRs. A supercage is also formed as shown in Figure 1.14. This structure is characterized by Si/Al = 11 and is embedded with divalent Fe in the most stable location (the 6-MR). Chabazite has been investigated in the past for the separation of CO_2 from N_2, due to the π-backdonation interaction of the gases with the compensating metals.[51] Differently from water, NO_x have the potential to receive electron charge through their LUMO. Consequently, π-backdonation is supposed to favour the low-temperature NO_x separation from H_2O.

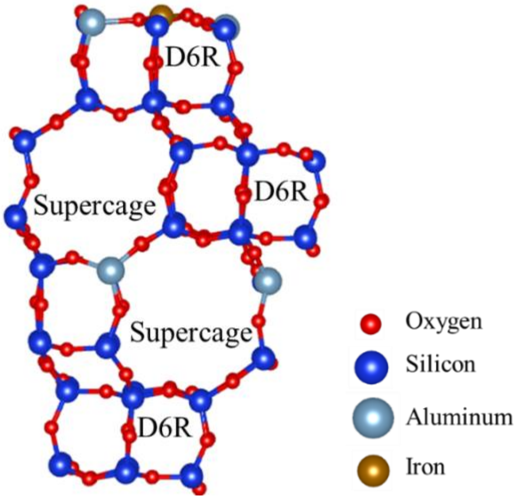

Figure 1.14: A representation of chabazite with Si/Al = 11, with the basic structural units noted with labels.

Lowering the Si/Al ratio of CHA results in structural distortions, complicating the synthesis of crystals[52,53]. Chabazite shares many structural properties with FAU, being itself a zeolite. Its aluminosilicate framework can host metal cations in 6- and 8- membered rings, with 6MR cations being the most stable[54–57]. The Al and Si distribution during the synthesis is highly random[52].

Chabazite has been widely investigated as PNA in many works, some of which have already been mentioned. More structural properties will be presented in chapter 4.

1.6.3 Mordenite

Mordenite (MOR) is a large pore zeolite, with channels as cavities. Figure 1.15 depicts the main structural units of MOR. We can identify three different kinds of channels, the side channel (SC), the side pocket (SP) and the main channel (MC)[58,59]. As easily obvious from the figure, MC contains 12-MRs, SC contains 8MRs, and SP contains 5-MR, which are extended “infinitely” in the z dimension. The Si/Al ratio of 5 has been implemented in this figure and the cations are placed in the main channel, which permits crossing to all the molecules of interest. The inner main channel is also illustrated in the right side of Figure 1.15.

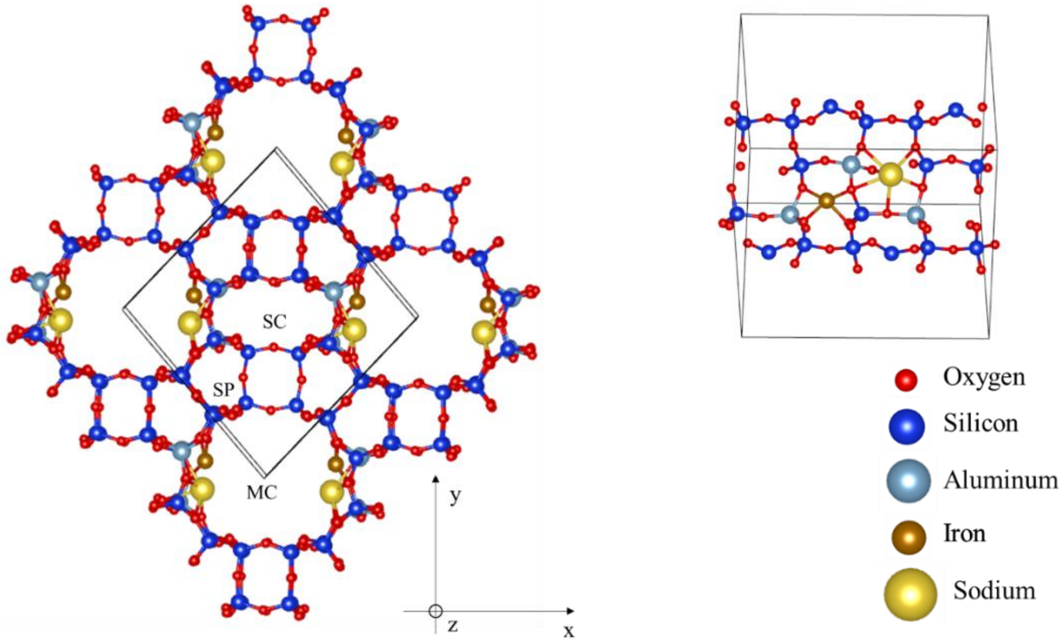

Figure 1.15: Mordenite structure with its channels denoted by labels. The inner rhombus contains the unit cell, which, when periodically repeated, forms a perfect crystal. The interior of the main channel is also depicted in the right side.

Mordenite has been tested in the past as PNA. Porta et al.[60] tested several Pd promoted zeolites in presence and absence of humidity. MOR showed strong low-temperature NO_x capture in the absence of water. The latter's presence had serious inhibiting effects on NO_x capture. Co-MOR was also tested among other zeolites by Zhang et al.[61] as PNA, showing high ability to trap NO_x in the temperature window of 273-523 K. As the introduction of cations with a valency of 2 like Pd^{2+} requires a significantly dense net of Al, the Si/Al ratio has to be as low as possible. Van laak et al. managed to improve the porosity of low silica mordenite (Si/Al = 5.7 – 10) with alkaline treatment[62]. Other studies have also verified the synthesis of mordenite with similar and higher silica content[63,64]. Further details on the structure and the stability of mordenite will be given in chapter 4.

1.6.4 Amorphous silica

Amorphous silica is one of the most widely used supports for transition metals combining high mechanical resistance, selectivity for chemical modification and dielectric strength[65–69]. The aperture sizes of amorphous silica are characterized by distributions as it does not have a standard periodic form. Its pore size distributions place it into the medium pore category[70–72]. Amorphous silica, as chabazite, having smaller pore openings than mordenite and faujasite, limit the diffusion of the adsorbed gases in their interior.[73–75].

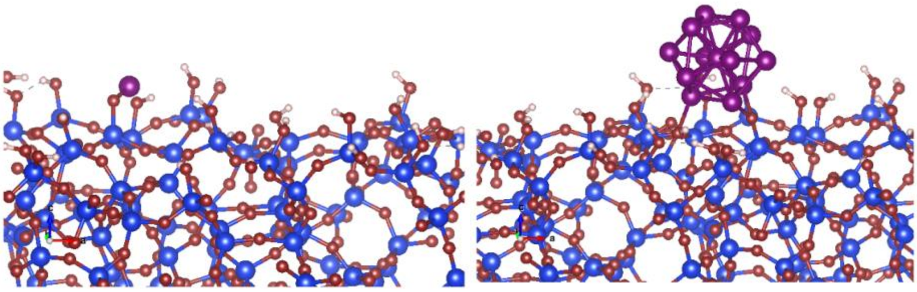

Figure 1.16: Monomer Co grafting on the left and cluster in the right, on amorphous silica surface[65].

The grafting of transition metals on the amorphous silica surfaces is possible in the form of monomers, dimers, or clusters. Gueddida et al[65] investigated the energetics of different conformations of Co, Ni, and Cu on amorphous silica. Figure 1.16 depicts monomer Co grafted on the left and a 13-atom cluster grafted on the right. Among the cluster sizes, there are "magic numbers", with particularly high stability. Icosahedral clusters tend to be particularly stable[76–78]. Weijun et al.[77] studied the stability of Ni clusters up to 40 atoms and reported a series of characteristically stable species in the series, as noted in Figure 1.17. Among these clusters, the ones with $n = 13, 19, 23$ and 26 are icosahedrical and all of them appear to be much more stable than their direct neighbours.

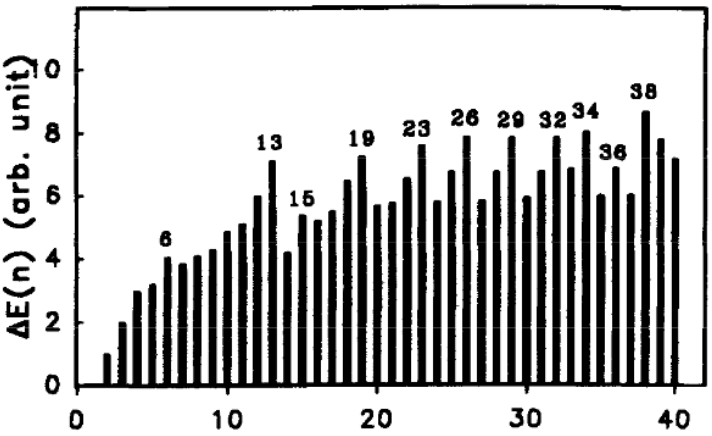

Figure 1.17: The energy difference $\Delta E = E(n) - E(n-1)$ between the species with $n \leq 40$ for Ni clusters.

The stability of the cationic grafting on the surface depends also on the – OH group density of the surface. Zhuravlev[80] synthesised various kinds of amorphous silica materials (silica gels, aerogels and porous glasses) differing in production conditions, surface area and pore size distributions. They showed that the surface – OH density is a physicochemical constant for a fully hydroxylated surface and at a constant temperature of vacuum treatment, it doesn't depend on the type of silica, resulting always around 4.9 OH/nm^2. In another work Blin end Carteret investigated the influence of hydrothermal treatment on the silanol (Si-OH) group density[79]. They showed that passing from a treatment of 80 to 180 °C, the surface undergoes condensation, losing pore ordering and increasing its silanol density. The concentration of silanol groups increases from 3.5 – 4 OH/nm^2 to 5 – 6.5 OH/nm^2. Gueddida et al[65,81] used similar – OH densities to study physicochemical properties of amorphous silica surfaces at a molecular level.

To sum up, a series of materials with tuning abilities is implemented for the selective adsorption of NO_x and CO among other diesel gases. Several structural properties of zeolites and amorphous silica-based materials are presented. Their previously studied de-NO_x capabilities are given and the purpose of this work is illustrated through the needs of the application. Currently, we use density functional theory to screen several adsorbent candidates. The most promising among them will be synthesized and studied experimentally, to verify their applicability, with adsorption isotherms and breakthrough curves.

2. Methodology

In computational chemistry theoretical models are implemented to simulate systems. Generally, the more sophisticated the computational tools, the bigger the computational cost. A compromise has thus to be made between the cost and the accuracy of the calculation. Naturally, the size of the system enhances its complexity and increases the computational cost. Modern advances in computer science have made possible the theoretical simulation of various kind of molecular systems; from clusters of several atoms to large aggregations, even materials of macroscopic sizes, made up of microscopic, repeated unit cells.

2.1 Introduction

Solving the Schrödinger equation, one can predict the time evolution of a given system:

$$\boldsymbol{H}\psi = -i\hbar\frac{\partial\psi}{\partial t} \tag{2.1}$$

H is the *Hamiltonian operator*, ħ is the reduced Planck's constant, and the solution of this equation, ψ, is the wavefunction, dependent on time, and space distribution of the particles. When we study an isolated molecular system that is not perturbed by any external potential, (2.1) reduces to its time independent form, giving us the energy of the state where the system is located:

$$\boldsymbol{H}\psi = E\psi \tag{2.2}$$

E is the energy of the system.

There are quantum mechanical methods that are based on *ab initio* investigations, or others that embody known parameters to accelerate the procedure, called *semi-empirical*. Also, if the size of the system renders the computational cost of the ab initio and semi-empirical methods unrealistic, *molecular dynamics*, can be implemented to shed some light into these cases, although properties calculated this way have limited accuracy. However, for large materials, not only there is no substitute for molecular dynamics, but also, for certain properties, it is adequate.

An essential step towards the solution of the Schrödinger equation for molecules is the Born-Oppenheimer approximation, where the coupling between the motions of nuclei and electrons is neglected. This allows the electronic part to be solved with the nuclear positions as parameters, and the resulting potential energy surface (PES) formed, is used to calculate the nuclear motion.

In order to study many-body systems, further approximations have to be made. In the *independent particle* model, the motion of one electron is considered independent of the positions of the other electrons. The interaction in this scheme is, either neglected, or taken in an average fashion. The famous *Hartree-Fock* model (HF) has been built based on the second principle. In the HF model, each electron is described by an orbital, and the total wavefunction is the product of all the orbitals. Due to the fermionic nature of the electrons, the wavefunction must be antisymmetric, which can be easily achieved by arranging the orbitals in a Slater determinant.

$$\Phi_{SD} = \frac{1}{\sqrt{N!}} \begin{vmatrix} \varphi_1(1) & \varphi_2(1) & \dots & \varphi_N(1) \\ \varphi_1(2) & \varphi_2(2) & \dots & \varphi_N(2) \\ \vdots & \vdots & \ddots & \vdots \\ \varphi_1(N) & \varphi_2(N) & \dots & \varphi_N(N) \end{vmatrix} \tag{2.3}$$

In $\varphi_i(j)$, i accounts for the state and j accounts for the electron. N is the total number of electrons of the given system. Expanding the orbitals in a basis set, one can acquire the orbitals by calculating the contribution of each basis element using the variational principle.

HF method, apart from being a very basic – nonetheless reliable – method itself, is used as a starting point for constructing other theoretical models. Ab initio methods of higher accuracy use multi-determinant wavefunctions enabling inclusion of electron correlation and approaching the exact solution of Schrödinger equation systematically. A different methodology uses previously obtained parameters, skipping therefore some parts of the calculations, leading to the formation of semi-empirical methods; less exact, physically incorrect, but quite faster than ab initio methods. *Density functional theory* in the Kohn-Sham version can be considered as an improvement of HF where the many-body effect of electrons is modelled as a function of the electron density. Although DFT provides improved results in comparison to HF with approximately the same computational cost, there is no possibility for systematic improvement.

2.2 Periodic systems

Periodic systems can be described as a periodic *unit cell* being repeated to form an infinite system. There is not further partition of the unit cell that can be used itself as a unit cell. The repetition of a unit cell in space which spans the crystal is called a *lattice*. For a given systems there are several possible unit cells like shown in Figure 2.1. A *primitive cell* contains only one lattice point and is the smallest possible cell. If there is a point at the edge of the cell and thus shared with another cell, it is counted half. In the same spirit if a point is in the corner of a cube and shared by eight cells it is counted as 1/8.

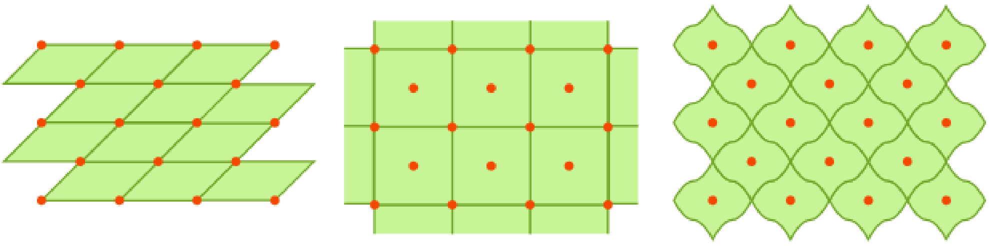

Figure 2.1: Different unit cells for a 2-D lattice[82].

There is a special type of primitive cells called *Wigner-Seitz cell* of a lattice point, defined as the volume that encloses all points in space that are closer to the lattice point of reference than to any other lattice point. It is drawn in two steps: a) connect a reference lattice point with its neighbouring ones through line segments, and b) bringing perpendicular lines passing exactly from the middle of these segments. These perpendicular lines enclose the Wigner-Seitz primitive cell as shown in Figure 2.2. Figure 2.3 also offers a summary of what has already been defined as a primitive unit cell, a Wigner-Seitz unit cell and a non-primitive cell.

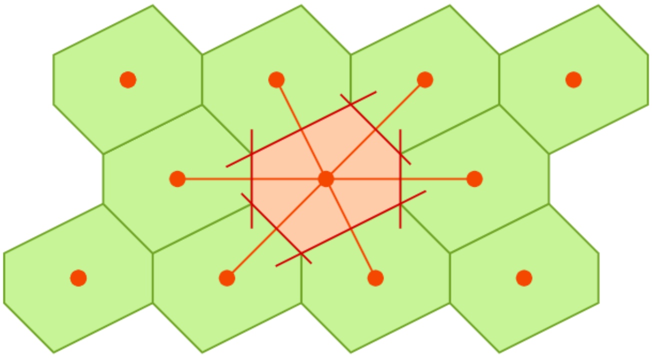

Figure 2.2: The orange area represents the Wigner-Seitz cell, shaped after connecting the perpendicular lines crossing the linear segments that connect neighbouring lattice points at the middle[82].

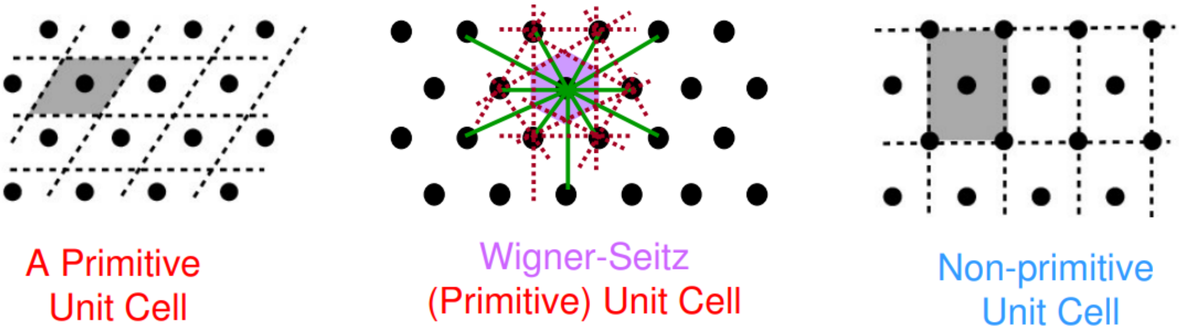

Figure 2.3: A representation and comparison of a primitive cell, a Wigner-Seitz unit cell and a non-primitive cell.

There are one-, two- and three-dimensional systems, e.g., polymers, surfaces and crystals. The unit cell in three dimensions can be characterized by three vectors, called *lattice vectors*, $\boldsymbol{a_1}$, $\boldsymbol{a_2}$, and $\boldsymbol{a_3}$ spanning in the physical space, with the length and angles between them defining the shape. The combination of the unit cell, with the positions of the atoms in it, result in the *Bravais lattice*; there are seven different unit cells and 14 Bravais lattices. The periodic system can be generated by translation of the Bravais lattice by lattice vectors $\boldsymbol{t}$.

Apart from the real space there is the need to introduce another one called the *reciprocal space* and define the periodic systems again in those constructions. The reciprocal cell can be defined by three vectors, called *reciprocal lattice vectors*, $\boldsymbol{b_1}$, $\boldsymbol{b_2}$ and $\boldsymbol{b_3}$ derived by the direct cell vectors, satisfying the orthonormality condition $\boldsymbol{a_i}\boldsymbol{b_j} = 2\pi\delta_{ij}$.

$$\boldsymbol{b_1} = 2\pi \frac{\boldsymbol{a_2} \times \boldsymbol{a_3}}{V} \quad \boldsymbol{b_2} = 2\pi \frac{\boldsymbol{a_3} \times \boldsymbol{a_1}}{V} \quad \boldsymbol{b_3} = 2\pi \frac{\boldsymbol{a_1} \times \boldsymbol{a_2}}{V} \tag{2.4}$$

In the case of a cubic cell with side length L the reciprocal space cube would have side length equal to $2\pi/L$. The primitive cell of the reciprocal lattice in the momentum space (which is the case if we assume that the real space is the position space) is called the *Brillouin zone*. The centre of the Brillouin zone is called the *gamma point*. It is easy to imagine that it is the one shown with red dots in Figure 2.2, if we assume this lattice to belong to the reciprocal space. In reciprocal space we use the symbol k to denote vectors as we use r for the real space. So, the gamma point should be the one with $k = (0,0,0)$. Although in solid state theory k points are used to define vectors in reciprocal space, in the language of electronic structure theory, we use k-points as sampling for the first Brillouin zone of the material, namely the lattice point closest to the gamma point.

There can be solutions to Schrödinger’s equation for different k-points, and to calculate the eigenvalue of an observable one must integrate over the possible k, as would be the case with r in the real space. For example, the energy of a particular state E would be:

$$E = \int E(k)dk \tag{2.5},$$

where $E(k)$ the energy for a given k (the integral is actually in three dimensions). However, since the eigenvalues to Schrödinger’s equations change slowly with k values, it is possible to replace the integral with a grid of k points:

$$E = \sum\nolimits_{k=1} w(k)E(k) \tag{2.6},$$

where $w(k)$ is a weight.

The size of k-points sampling depends on several factors: a) The length of the cell parameters which, as already mentioned is inversely proportional to the length of the reciprocal space cell parameters is also inversely proportional to the k-point sampling size. This happens because the smaller the reciprocal space cell the more often the phase of the wavefunction in the reciprocal space changes, thus the smaller the requisite k-point sampling. b) Whether the system is periodic or not; in case it isn’t 1 k-point is a valid approximation. c) The band gap of the system. The prediction of the Fermi level becomes tricky in conductors, raising the requiring k-points sample size, at least for an accurate calculation. For illustrative reasons, a set of visual examples in 2- and 3D are provided in Figure 2.4, to show how a change in real space lattice vectors affects the reciprocal space lattice vector analogues.

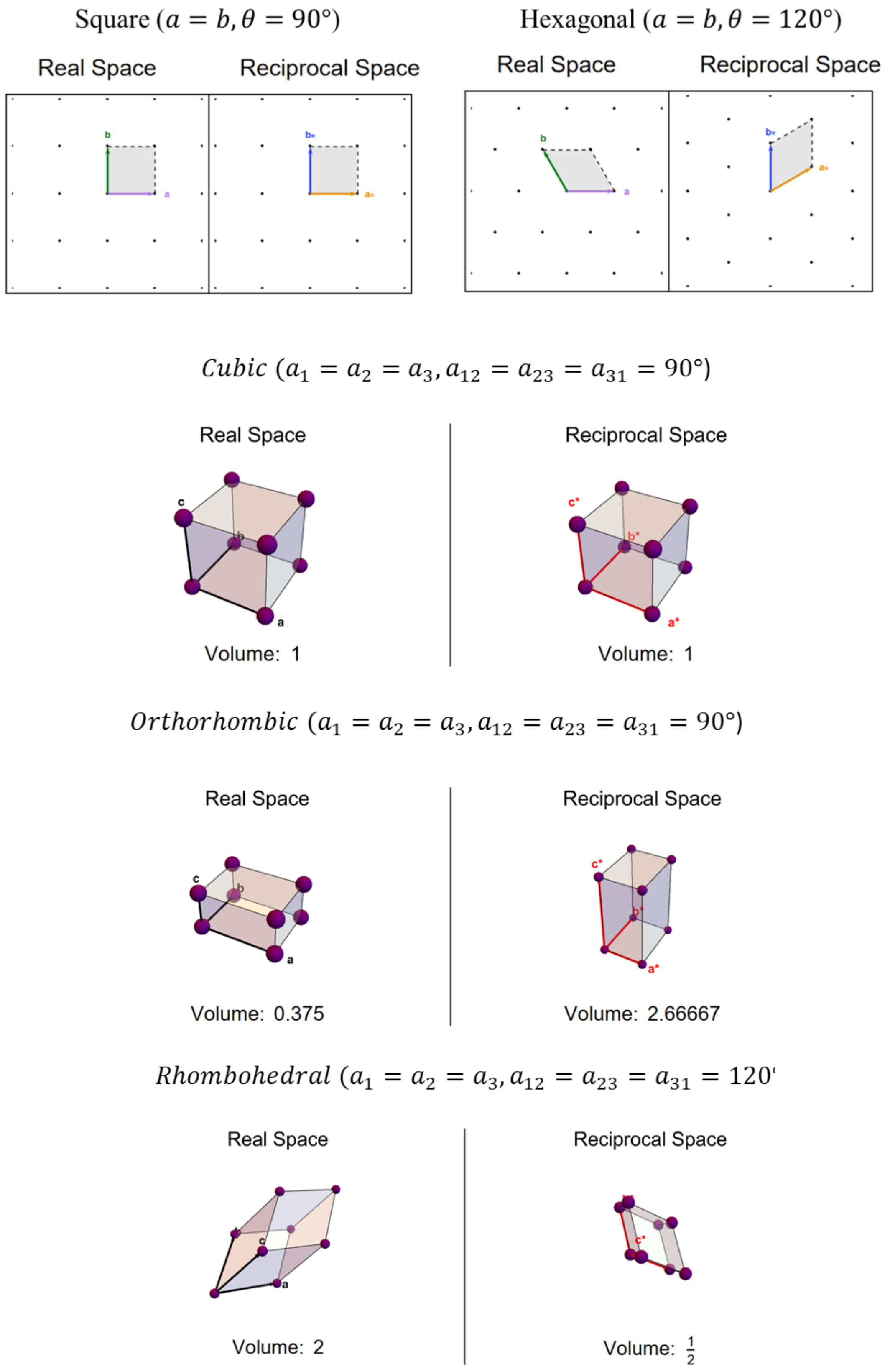

Figure 2.4: Square and hexagonal real space lattice unit cells are given.

2.3 Block's theorem

The square of the wave function, the electron density, must display the same periodicity as the nuclei of the system. According to Block's theorem, the wave function of the system is quasi-periodic, namely, equivalent cell positions are related with a complex phase factor involving the lattice vector $\boldsymbol{t}$ and a vector in the reciprocal space:

$$\rho(\boldsymbol{r}+\boldsymbol{t}) = \rho(\boldsymbol{r}) => \psi(\boldsymbol{r}) = e^{-i\boldsymbol{kt}}\,\psi(\boldsymbol{t}+\boldsymbol{r}) \tag{2.7}$$

Alternatively stated, the Bloch theorem indicates that a crystalline orbital ψ for the nth band in the unit cell can be written as a wave-like part and a cell-periodic part called a Bloch orbital φ:

$$\psi_{n,k}(\boldsymbol{r}) = e^{i\boldsymbol{kr}}\varphi_n(\boldsymbol{r}) \tag{2.8}$$

The block orbital can be expanded into a basis set of plane wave functions χ^{PW}:

$$\varphi_n(\boldsymbol{r}) = \sum_{a}^{M_{basis}} c_{na}\chi_a^{PW}(\boldsymbol{r}) \tag{2.9a}$$

$$\psi_{n,k}(\boldsymbol{r}) = e^{i\boldsymbol{kr}} \sum_{a}^{M_{basis}} c_{na}\chi_a^{PW}(\boldsymbol{r}) \tag{2.9b}$$

The problem has now been transformed from treating an infinite number of orbitals to only treating those within the unit cell. The problem can equally be solved in the reciprocal space within the Brillouin zone. For a system with M_{basis} functions, the variation problem can be written as a matrix equation like the Roothan-Hall equations (see Annex).

$$\boldsymbol{F^kC^k} = \boldsymbol{S^kC^k\varepsilon^k} \tag{2.10}$$

The solutions are continuous as a function of $\boldsymbol{k}$ and provide a range of energies called a *band* with the total energy per unit cell being calculated by integrating over $\boldsymbol{k}$ space. The variation with $\boldsymbol{k}$ is slow for non-metallic systems, and the integration can be done numerically by including relatively few points as mentioned before. For a given value of $\boldsymbol{k}$, the solution of this equation provides M_{basis} orbitals. The aufbau principle (in the ground state of an atom or ion, the lowest energy levels are filled first) holds for periodic systems as well, and the equivalent of the *higher occupied molecular orbital* (HOMO) (see Annex) for molecular systems is the Fermi energy level in periodic systems. The Homo-Lumo (Lumo stands for *lowest unoccupied molecular orbital*) gap for the molecular systems, namely the energy difference between the highest occupied and the lowest unoccupied molecular orbital, has the equivalent *band gap* in periodic systems. Systems with band gap equal to zero are metallic, while those with finite band gap are either insulators or semi-conductors, depending on whether the band gap is large or small compared to the thermal energy kT.

For a plane wave basis, the construction of energy matrix can be done using fast Fourier transformation (FFT) methods for switching between the real and reciprocal space. FFT methods have a big advantage concerning the scaling of the computational cost.

2.4 Pseudopotentials

When atoms get close to form solids the inner electrons stick close to nuclei in a deep potential well and remain unchained under most circumstances[83]. At the same time, they neutralize the nuclear charge as much as -1 each. Because they are so inert their participation in the formation of bonds is minimal.

On the contrary, valence electrons are much more active, they form bonds, get ionized conduct electricity in metals etc. In metals they even travel the whole solid almost like a plane wave. In covalent and ionic solids, they are not as free but roughly maintain this general behaviour.

Thus, one can state that we may remove core electrons and nuclei from the picture and deal only with the active valence electrons. This is called the *frozen core approximation*, and in this picture the nuclear charge is largely screened by the core electrons having much less effect on the valence electrons. This approximation cuts increasingly big computational load as we go down on the periodic table.

In addition to the treatment of the core to save resources we can now pseudize the valence electrons. Indeed, when valence wave functions pass through the highly localized core region they oscillate rapidly producing wiggles to be orthogonal to the core states. These kind of wave functions with many nodes are very difficult to express simply and create computational issues.

The frozen core approximation sets the stage to remove these – useless now – nodes, since there are no lower-lying electrons than the valence ones, for them to be orthogonal with. It is now possible to “soften” both the wave functions of the valence electrons and their potentials with ions. This procedure is termed as *pseudation*. The standard pseudation steps are as follows:

1) Select an atom as a reference state to formulate the atomic pseudopotential (PP), which will be applied in different environments and many-atom systems.
2) Calculate the exact all-electron (AE) potential, wave function, and energy by DFT. We precalculate them for the core electrons and keep them frozen for the rest of the calculations.
3) Choose a proper r_c of the atom and make the core part $(r < r_c)$ of the wave function nodeless and smooth. At $r = r_c$ make the first and second derivatives of pseudo- and AE wave functions equal.
4) At $r > r_c$ make the pseudo and AE wave functions exactly the same, since the AE wave function in this area has decisive behaviour for the chemistry of the system. Figure 4 summarizes the steps in a graphical example.
5) Make the eigenvalues (energies) of the smooth pseudo and original AE wave functions the same.
6) Generate a PP from the pseudo wave function and the valence electron density and parameterize it in spherical functions (like Gaussian) to use.

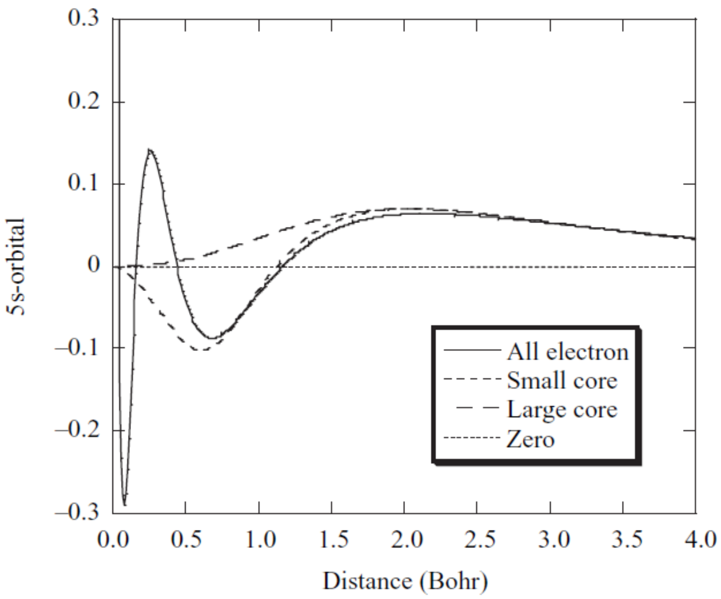

Figure 2.5: The 5s Ag orbital with either an all-electron, large-, or small-core pseudopotential. The difference of large core (11 electrons considered explicitly), and small core (19 electrons considered explicitly) has to do with the size of the frozen core[84].

There exist different categories of pseudopotentials. Throughout this work we use *ultrasoft* PPs and *projected-augmented wave* potentials (PAW). Accounting for ultrasoft PPs, apart from the elimination of radial nodes, the position of the peak is shifted to further distances with reduced peak height. They give the benefit of convergence using only a small number of plane waves as a basis, but naturally they don't recover the full charge density, rather the valency electron composed one. As for PAW, it aims for both the efficiency of the PP and the accuracy of the AE potential. It maps both core and parts of valence wave functions with two separate descriptions. The valence part ψ_{inter} is represented with the plane wave expansion, whereas the ψ_{core} of the core part is projected on a radial grid at the atom centre. After the additive augmentation of these two terms, the overlapping part, ψ_{net}, is trimmed off to make the final wave function, ψ_{PAW}, very close to the AE wave function:

$$\psi_{PAW} = \psi_{inter} + \psi_{core} - \psi_{net} \tag{2.11}$$

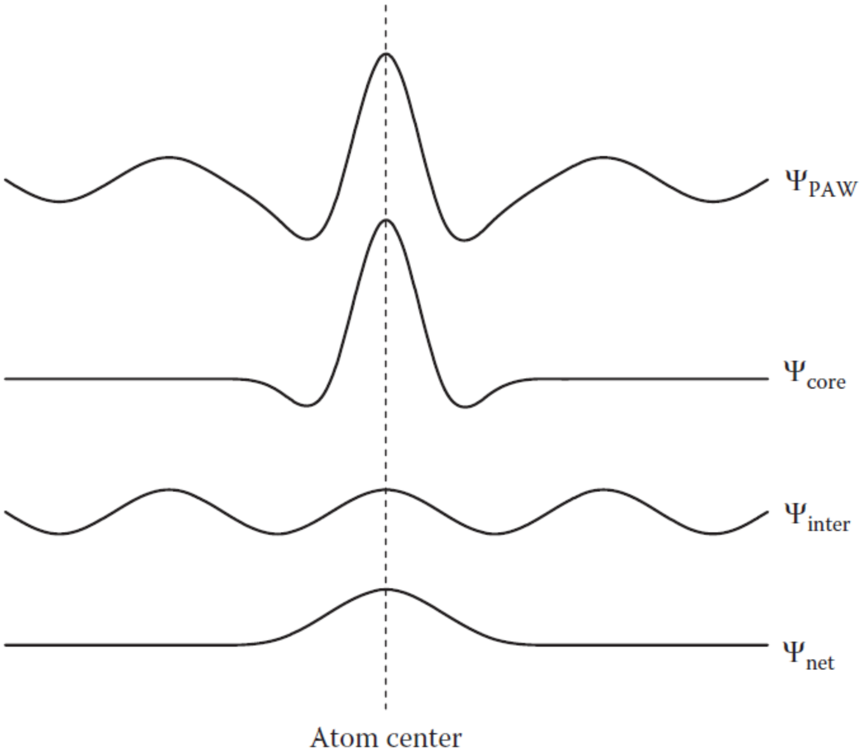

Figure 2.6: The PAW pseudopotential depicted, composed of the linear composition of $\psi_{inter} + \psi_{core} - \psi_{net}$.

2.5 Density functional theory

In order to calculate the electron correlation with wavefunction methods we may use various techniques, like configuration interaction (using multi-determinant wavefunction), perturbation theory e.t.c. These methods can give very accurate results and they can also be improved systematically. However, they can only be used in small systems because of the computational cost. For the presentation of the density functional theory, references to Hartree-Fock will be made, which is analysed further through the annex.

In principle, density functional theory (DFT) wants to treat the problem of the system using just its electron density. This idea became a possibility when Hohenberg and Kohn[85] proved that the ground state electronic energy is determined completely by the electron density ρ. Stated otherwise, there is a one-one correspondence between the electronic energy of a system and the density. This is really important because a wavefunction method has to deal with $3N$ spatial coordinates plus the N spin coordinates. The electron density is the square of the wavefunction integrated over $N-1$ electron coordinates and each spin density depends only on the three spatial coordinates, independent of the number of electrons. While the complexity of a wavefunction increases exponentially with the number of electrons, the electron density has the same number of variables independent of the system size. The problem is that the energy functional (a mathematical tool that maps a function on a number) of the density is not known.

Early attempts were made to construct such kind of functionals, but their performance was poor. They were focused on mimicking the wavefunction methods at dividing the energy functional into kinetic $T[\rho]$, nucleus-electron attraction $E_{ne}[\rho]$ and electron-electron repulsion $E_{ee}[\rho]$ functionals, with the nucleus-nucleus interaction being a constant in the Born-Oppenheimer approximation. In addition, the $E_{ee}[\rho]$ is further divided into exchange $K[\rho]$ and $J[\rho]$ Coulomb functionals, implicitly including electron correlation.

$$E_{ne}[\rho] = -\sum_{\alpha}^{N_{nuclei}} \frac{\int Z_{\alpha}(\boldsymbol{R}_{\alpha})\,\rho(\boldsymbol{r})}{|\boldsymbol{R}_{\alpha} - \boldsymbol{r}|} d\boldsymbol{r} \qquad (2.12a)$$

$$J[\rho] = \frac{1}{2}\int\int \frac{\rho(\boldsymbol{r})\rho(\boldsymbol{r}')}{|\boldsymbol{r}-\boldsymbol{r}'|} d\boldsymbol{r} \tag{2.12b}$$

Early attempts of deducing functionals for the kinetic and exchange energies considered a uniform electron gas, where it may be shown that $T[\rho]$ and $K[\rho]$ are given as:

$$T_{HF}[\rho] = C_F \int \rho^{\frac{5}{3}}(\boldsymbol{r}) d\boldsymbol{r} \tag{2.13a}$$

$$K_D[\rho] = -C_x \int \rho^{\frac{4}{3}}(\boldsymbol{r}) d\boldsymbol{r} \tag{2.13b}$$

$$C_F = \frac{3}{10}(3\pi^2)^{\frac{2}{3}} \tag{2.13c}$$

$$C_x = \frac{3}{4}\left(\frac{3}{\pi}\right)^{\frac{1}{3}} \tag{2.13d}$$

The energy functional $E_{TF}[\rho] = T_{TF}[\rho] + E_{ne}[\rho] + J[\rho]$ is known as Thomas-Fermi (TF) theory, while inclusion of the $K_D[\rho]$ exchange part constitutes the Thomas-Fermi-Dirac (TFD) model.

The assumption of a uniform electron gas is fair for the valence electrons in certain metallic (periodic) systems, but poor for atoms and molecules. A serious flaw from a chemical point of view is it that neither TF nor TFD theories predict bonding: molecules do not exist.

The kinetic and exchange functional can be improved by making the electron density non-uniform. This can be done by the inclusion higher order terms of a Taylor expansion of electron density, namely with the inclusion of terms dependent on the derivatives of the electron density. This addition will insert inhomogeneity into the electronic gas creating the potential for a chemical bond formation. The same strategy can be followed for the exchange energy functional. The addition of these gradient correction terms will improve the performance of the Thomas-Fermi results. However, after the inclusion of the first correction (dependent on the first derivative) the results do not converge, and the accuracy of the methods up to that point are not sufficient to the point that they can replace the wavefunction methods.

2.6 Kohn-Sham Theory

The reason why DFT is so popular today is the introduction of orbitals as suggested by Kohn and Sham[86] in 1965. Orbitals will of course bring back the 3N dimensional problem that we tried to avoid using the electron density. In fact, Kohn-Sham DFT is closely related to HF method sharing identical formulas for kinetic, nuclear-electron attraction and Coulomb electron-electron repulsion energies.

The procedure starts by considering a system where the electron-electron interaction is initially neglected. We may show it by considering the Hamiltonian:

$$\boldsymbol{H}_\lambda = \boldsymbol{T} + \boldsymbol{V}_{ext}(\lambda) + \lambda \boldsymbol{V}_{ee} \tag{2.14}$$

If λ is set equal to one, then V_{ext}, has to be equal to the electron-nucleus potential. If λ is set equal to zero, then the electrons of the system do not interact at all. All the intermediate values represent the partially interacting system. In case $\lambda = 0$, since the electrons do not interact, the exact solution to Schrödinger's equation is given by a single Slater determinant, composed of orbitals φ_i, and the kinetic energy functional is given as:

$$T_S = \sum_i^{N_{elec}} \left\langle \varphi_i \middle| -\frac{1}{2}\nabla^2 \middle| \varphi_i \right\rangle \tag{2.15}$$

Where the subscript S denotes that the wavefunction is a Slater determinant. The non-interaction picture is only an approximation and so, (2.14) is only an approximation.

Since the single Slater determinant forces the excited states to be unoccupied, the missing kinetic energy can be attributed there. We remember that the excited states are also unoccupied in the case of a Hartree-Fock single determinant wave function, so we can state that part of the correlation energy that was missing in there, is now found inside the missing (correlation) kinetic energy.

In Kohn-Sham theory we calculate the kinetic energy for the non-interacting problem. In HF the missing correlation energy is $\sim 1\%$, just a small percentage. The same holds for the correlation kinetic energy in DFT, which is included now, into an exchange-correlation term (the parts that are **not** already known from HF). A general DFT expression can be written as:

$$E_{DFT}[\rho] = T_S[\rho] + E_{ne}[\rho] + J[\rho] + E_{xc}[\rho] \tag{2.16}$$

By equating E_{DFT} with the exact energy:

$$E_{xc}[\rho] = (T[\rho] - T_S[\rho]) + (E_{ee}[\rho] - J[\rho]) \tag{2.17}$$

The first parenthesis contains the correlation kinetic energy, while the second, the potential correlation and exchange energies.

While the orbital-free DFT tries to produce kinetic and exchange functionals, Kohn-Sham DFT wants to produce exchange-correlation functionals. For that reason, Kohn-Sham DFT is much less sensitive to errors, as the exchange-correlation energy is roughly a factor of 10 smaller than the kinetic energy. Although Kohn-Sham theory is not a 3-dimensional problem anymore, it is an independent particle model (we have to solve one-electron equations), and consequently, much simpler than the many-body problem that the wavefunction methods have to face in order to calculate the electron correlation.

2.7 Remarks on the treatment of the energy terms in DFT

The exchange energy has by far the biggest contribution to the exchange-correlation functional. This could encourage someone to calculate the exchange energy exactly from the formula known from Hartree-Fock and approximate the rest, minimizing the potential error. However, this method does not yield accurate results because the exchange and correlation energies are given in a different way by the two theories. In fact, even if the formulas for the calculation of the energy in DFT are the same, we use Kohn-Sham orbitals. In HF, the exchange potential is non-local, in contrast to DFT, where it only depends on its close vicinity; the treatment of an inhomogeneous density becomes even qualitatively possible, only when the gradient of the density is considered. The correlation energy behaves in the same spirit. Both have a short- and a long-range part (in terms of the distance between two electrons). The long-range part in wave mechanics coming from the multi-reference wavefunction is the static one, while the short-range correlation is the dynamical correlation. The long-range part of the correlation energy in wave mechanics effectively cancels the delocalized part of the exchange energy. In DFT the long-range cancellation should be built inside the exchange-correlation functional. Thus, calculating the exchange energy in a HF way, and the correlation by DFT we lose the cancellation. Modern methods have tried to address this problem by separating the correlation functional into short and long-range and use HF for the exchange.

A quantitative presentation of these matters can be given in terms of probability *holes*. If the electrons did not have spin or charge, the probability of finding one at a given position would be independent of the position of a second electron. The electron pair density would then be given by their product of the two one-electron densities ρ_1 with a proper normalization factor:

$$\rho_2^{indep}(\boldsymbol{r}_1,\boldsymbol{r}_2) = \frac{N_{elec}-1}{N_{elec}}\rho_1(\boldsymbol{r}_1)\rho_1(\boldsymbol{r}_2) = \left(1-\frac{1}{N_{elec}}\right)\rho_1(\boldsymbol{r}_1)\rho_1(\boldsymbol{r}_2) \tag{2.18}$$

Since electrons have spin and charge there is a reduced probability of finding an electron near another electron. We can write it formally as a condition probability factor $h_{xc}(\boldsymbol{r}_1,\boldsymbol{r}_2)$, that includes the $1/N_{elec}$ self-interacting factor:

$$\rho_2(\boldsymbol{r}_1,\boldsymbol{r}_2) = \rho_1(\boldsymbol{r}_1)\rho_1(\boldsymbol{r}_2) + \rho_1(\boldsymbol{r}_1)h_{xc}(\boldsymbol{r}_1,\boldsymbol{r}_2) \tag{2.19}$$

The reduced probability is called the exchange-correlation hole, and it can be written in terms of ρ_2 and ρ_1 by solving (2.18):

$$h_{xc}(\boldsymbol{r}_1,\boldsymbol{r}_2) = \frac{\rho_2(\boldsymbol{r}_1,\boldsymbol{r}_2)}{\rho_1(\boldsymbol{r}_1)} - \rho(\boldsymbol{r}_2) \tag{2.20}$$

The exchange-correlation hole expresses the reduced probability of locating electron 2 in position $\boldsymbol{r}_2$ when the electron 1 is at position $\boldsymbol{r}_1$. The exchange part of h_{xc} is called the *Fermi hole* and the dynamical correlation gives rise to the *Coulomb hole*. Since the exchange only occurs between electrons of the same spin, the total hole can also be written in terms of individual spin contributors.

$$h_{xc} = h_x + h_c \tag{2.21a}$$

$$h_x = h_x^{\alpha\alpha} + h_x^{\beta\beta} \tag{2.21b}$$

$$h_c = h_c^{\alpha\alpha} + h_c^{\beta\beta} + h_c^{\alpha\beta} \tag{2.21c}$$

The integral of the exchange-correlation hole over the space of r_2 equals -1. The fermi hole also integrates to -1, leaving the Coulomb hole with 0. The fermi hole describes a static reduction to the probability of finding an electron close to another, while the Coulomb hole reduces the probability of finding one electron close to another but increases the probability of finding it in longer distances.

It is customary to separate E_{xc} into two parts, the exchange (E_x) and correlation (E_c) part. This is reasonable based on the discussion on the holes, although only the combined functional has a physical meaning. Writing it down formally:

$$E_{xc}[\rho] = E_x[\rho] + E_c[\rho] = \int \rho(\boldsymbol{r})\varepsilon_x[\rho(\boldsymbol{r})]\, d\boldsymbol{r} + \int \rho(\boldsymbol{r})\varepsilon_c[\rho(\boldsymbol{r})]\, d\boldsymbol{r} \qquad (2.22)$$

The exchange energy by definition involves electrons with the same spin. Thus, we may separate the densities originating from different spins as ρ_α and ρ_β. Then the individual exchange and correlation energies will be written in terms of the separated densities.

$$E_x[\rho] = E_x^{\alpha}[\rho_\alpha] + E_x^{\beta}[\rho_\beta] \qquad (2.23a)$$

$$E_c[\rho] = E_c^{\alpha\alpha}[\rho_\alpha] + E_c^{\beta\beta}[\rho_\beta] + E_c^{\alpha\beta}[\rho_\alpha, \rho_\beta] \qquad (2.23b)$$

A closely related phenomenon is the self-interaction term. In DFT, even a one-electron system has a self-repulsion. In HF this is treated automatically by the cancellation of the diagonal terms of the Coulomb and exchange matrices. In DFT, there must be a part in the exchange functional, which is equal to the negative of the self-interaction Coulomb energy. In this view, the self-interaction correction is a major part of the exchange energy, while the rest corresponds to the quantum mechanical correction to the electron-electron repulsion, arising from the antisymmetry of the wavefunction, being comparable to the coulombic part. However, such a partitioning is not invariant under a unitary transformation of the occupied orbitals. This error cancellation is not guaranteed in DFT and not many functionals have managed to produce self-interaction free results.

2.8 Local Density Approximation

In *Local density approximation* (LDA), the electron density is treated locally, as a uniform electron gas, namely it is a slowly varying function. Using Dirac's formula (2.13):

$$E_x^{LDA}[\rho] = -C_x \int \rho^{\frac{4}{3}}(\boldsymbol{r})\, d\boldsymbol{r} \qquad (2.24a)$$

$$\varepsilon_x^{LDA} = -C_x \rho^{\frac{1}{3}} \qquad (2.25b)$$

In the more general case, where the density originating from spin α is not the same as that from β, LDA is replaced with *Local Spin Density Approximation* (LSDA):

$$E_x^{LSDA}[\rho] = -2^{\frac{1}{3}}C_x \int \left(\rho_\alpha^{\frac{4}{3}} + \rho_\beta^{\frac{4}{3}}\right) d\boldsymbol{r} \tag{2.26}$$

The LSDA method is an exact DFT method for the case of uniform electron gas except for small differences arising from correlation energy. For molecular systems LSDA underestimates the exchange energy by 10%, an error bigger than the correlation energy itself. Electron correlation is also underestimated by a factor close to 2, and consequently bond strengths are overestimated often by $\sim 100\ kJ/mol$. LSDA is useful for the description of extended systems, as metals, where the approximation of a slowly varying electron density is quite valid.

2.9 Gradient Corrected methods

An improvement over the LDA is made by adding the derivative of the electron density as variable. That way, the electron gas becomes inhomogeneous, and the description of chemical bonds becomes qualitatively possible. The first order correction to the exchange energy in terms of the derivative of the density is given as:

$$K_2[\rho] = -\frac{5}{216}(3\pi^5)^{-\frac{1}{3}} \int \frac{|\nabla \rho(\boldsymbol{r})|^2}{\rho^{\frac{4}{3}}(\boldsymbol{r})} d\boldsymbol{r} \tag{2.27}$$

The corresponding quantity for the correlation correction often makes the correlation energy positive. A straightforward inclusion of these first order corrections harvests worse results than LSDA because with the inclusion of the derivative of the density we lost some very important for our functionals, properties. This is, the integral of the Fermi and Coulomb holes no more equal -1 and 0, respectively.

In *Generalized Gradient Approximation* (GGA) methods, the first derivative is included with the constraint that the integrals of the Fermi and Coulomb holes are equal to the required values. The *Pedrew-Burke-Ernzerhof* (PBE)[87] functional is a refinement of older GGA methods. The exchange part is written as an enhancement factor multiplied onto the LSDA functional. The x variable introduced below is dimensionless.

$$\varepsilon_x^{PBE} = \varepsilon_x^{LDA} F(x) \tag{2.28a}$$

$$F(x) = 1 + a - \frac{a}{1 + bx^2} \tag{2.28b}$$

$$x = \frac{|\nabla \rho|}{\rho^{4/3}} \tag{2.28c}$$

The correlation part is similarly written as an enhancement factor added to the LSDA functional, where the t variable is linked to x by means of a spin polarization function.

$$\varepsilon_c^{PBE} = \varepsilon_c^{LDA} + H(t) \tag{2.29a}$$

$$H(t) = cf_3^3 \ln\left[1 + dt^2\left(\frac{1 + At^2}{1 + At^2 + A^2t^4}\right)\right] \tag{2.29b}$$

$$A = d\left[\exp\left(-\frac{\varepsilon_c^{LDA}}{cf_3^3}\right) - 1\right]^{-1} \tag{2.29c}$$

$$f_3(\zeta) = \frac{1}{2}\left[(1+\zeta)^{\frac{2}{3}} + (1-\zeta)^{\frac{2}{3}}\right] \tag{2.29d}$$

$$t = \left[2(3\pi^3)^{\frac{1}{3}} f_3\right]^{-1} x \tag{2.29e}$$

$$\zeta = \frac{\rho_\alpha - \rho_\beta}{\rho_\alpha + \rho_\beta} \tag{2.29f}$$

The a, b, c and d parameters are non-empirical, i.e., they are not obtained by fitting to experimental fitting to experimental data, but derived by some conditions that are needed to be satisfied (like the integrals of the holes, aforementioned). ζ is a spin polarization function, its denominator existing for normalizing purposes. The PBE functional will be used throughout this work.

2.10 Van Der Waals corrections

A main issue of DFTs is that they fail to describe vdW forces correctly. Thus, various methods have been introduced in order to include them as a correction. These methods can be mainly classified by the way they compute the energy corrections and whether they include this energy in the SCF procedure or not.[88]

The case which will interest us is *D2*, a damped atom-pairwise dispersion correction of the form C_6R^{-6}, combined with the PBE density functional[89]. In this scheme the dispersion correction is added after the self-consistent procedure. Its formula is written as:

$$E_{disp} = -s_6 \sum_{i=1}^{N-1} \sum_{j=i+1}^{N} \frac{C_6^{ij}}{R_{ij}^2} f_{dmp}(R_{ij}) \tag{2.30}$$

s_6 is a factor that depends on the density functional used, C_6^{ij} is the dispersion coefficient and is dependent on the two atoms that are treated, R_{ij}, the interatomic distance. A straightforward implementation of this method would present issues by double-counting the short- and intermediate-range interactions. In order to address this issue, a damping function is used, which cancels the interaction energy at short and intermediate distances:

$$f_{dmp} = \frac{s_6}{1 + e^{-d\left(\frac{R_{ij}}{s_R R_r - 1}\right)}} \tag{2.31}$$

Where R_r is the sum of atomic vdW radii and $d = 20$, is a parameter that controls the "sharpness" of f_{dmp}. For PBE, $s_R = 1$ and $s_6 = 0.75$. The cutoff van der Walls radius is set at 50 Å (all the present parameters refer to VASP configuration). More dispersion terms of higher orders can be included like C_8 and C_{10}, but they are more short-ranged, and they interfere with the damping function, therefore they are not necessary at all.

The way we calculate the dispersion coefficients has its own methodology. There is the possibility that we calculate it, as the geometric mean between the atomic dispersion factors:

$$C_6^{ij} = \sqrt{C_6^i C_6^j} \tag{2.32}$$

The atomic coefficients can then be calculated based on the atomic ionization potentials I_p and the static dipole polarizabilities α_{ij} calculated theoretically. The coefficient can be given then as:

$$C_6^i = cNI_p^i\alpha^i \tag{2.33}$$

Where N has values 2, 10, 18, 36, 54, for atoms from rows 1-5 in the periodic table, and c is a proportionality constant. Note that approaching C_6^{ij} from atomic properties yields good results in systems where the atoms have similar behaviour to the free ones but may be a bad choice in the case of systems where atoms form strong bonds.[89]

2.11 Ewald summation

It is a method for computing long-range interactions in periodic systems. In this method the long-range interaction is divided in two parts: a short-range contribution and a long-range one. The short-range is calculated in real space, whereas the long range is computed using Fourier transformation. The advantage of this method is the rapid convergence of the energy compared with that of the direct summation. This means that the method has high accuracy and reasonable speed making it the standard method for computing long-range interactions. Prerequisite for it to be accurate is the charge neutrality of the system.

2.12 DFT+U

DFT dramatically fails in the prediction of electronic structure. This issue hinders the prediction of other properties including intermolecular interactions. The problems rise from the failure to describe the electron correlation accurately in the DFT scheme, due to the tendency of the xc functionals to over-delocalize valence electrons and over-stabilize metallic ground states. The reason behind this, is the inability of xc to cancel out the electronic self-interaction contained in the Hartree term. This self-interaction induces an excessive delocalization of the wave function.

Various methods have been adopted to face this issue. Hybrid functionals were formulated for this reason, to include HF exchange functionals to eliminate the double counting. This method is computationally expensive and thus, not practical for larger, more complex systems. HF method is itself unable to describe the behaviour of such strongly correlated systems like Mott insulators; metallic systems with strong correlation that are predicted to be conductors but present insulating behaviour.[90] Multi-determinant wave function is necessary, or an xc functional which will compensate for the lost correlation energy. One of the corrective approaches employed from DFT to cope for the over-localization is DFT+U. Not only it is reliable as other methods but also has a low computational cost.

The U implementation that has been used in this work is not documented anywhere in VASP manuals but here will be presented a standard method anyway[91]:

$$E_{LSDA+U} = E_{LSDA} + \frac{(\bar{U} - \bar{J})}{2} \sum_{\sigma} \left(n_{m,\sigma} - n_{m,\sigma}^{2} \right) \tag{2.34}$$

U and J themselves do not have a physical meaning, but only the term $U - J$. $\hat{n}_{\sigma} = \hat{a}_{\sigma}^{\dagger} \hat{a}_{\sigma}$ is the number of electrons occupying a particular site and n_{σ} the expectation value. The summation is performed over spin projections. m denotes the projections of the orbital moment ($m, m' = -2, -1, \dots, 2$ in the case of d electrons). $\bar{U}$ and $\bar{J}$ are the spherically averaged matrix elements of the screened Coulomb electron-electron interaction. Finally, $n_{m,\sigma}$ is the occupation number of the d state with magnetic moment m. This correction term can be understood as adding a penalty functional to the LSDA total energy expression that forces the on-site occupancy towards fully occupied or unoccupied levels, where the total number of electrons N_{σ}:

$$N_{\sigma} = \sum_{m} n_{m,\sigma} \tag{2.35}$$

2.13 Estimation of U

In this work we will compute the value of U using the linear response approach proposed by Cococcioni and Gironcoli[92]. The goal is to add an on-site (Hubbard sites) Coulomb potential to the Hamiltonian such that will fix the unnaturally delocalized d and f electrons. This method is based on a very specific effect that the self-interaction energy produced by LDA and GGA methods have on the relation of the energy with the occupancy of orbitals.

An atom in exchange with a reservoir of electrons can exchange integer number of particles with its environment. The intermediate situation with fractional number of electrons in this open atomic system is not described by a pure state but by a statistical mixture. In a system with $N + \omega$ electrons where N is integer and $0 \leq \omega \leq 1$, the total energy is given as:

$$E_{n} = (1 - \omega) E_{N} + \omega E_{N+1} \tag{2.36}$$

Where ω works as a statistical weight for the states with N and $N+1$ electrons. The total energy of the system should normally be linearly dependent on the occupancy of the system. Also, the slope should be changing discontinuously after every electron added to the system, corresponding to the electron affinity (ionization potential) of the N (N+1) electron system as shown in Figure 2.6 for the exact system. However, this linearity is not respected for LDA and GGA methods creating a non-physical curvature. This behaviour is attributed to the self-interaction.

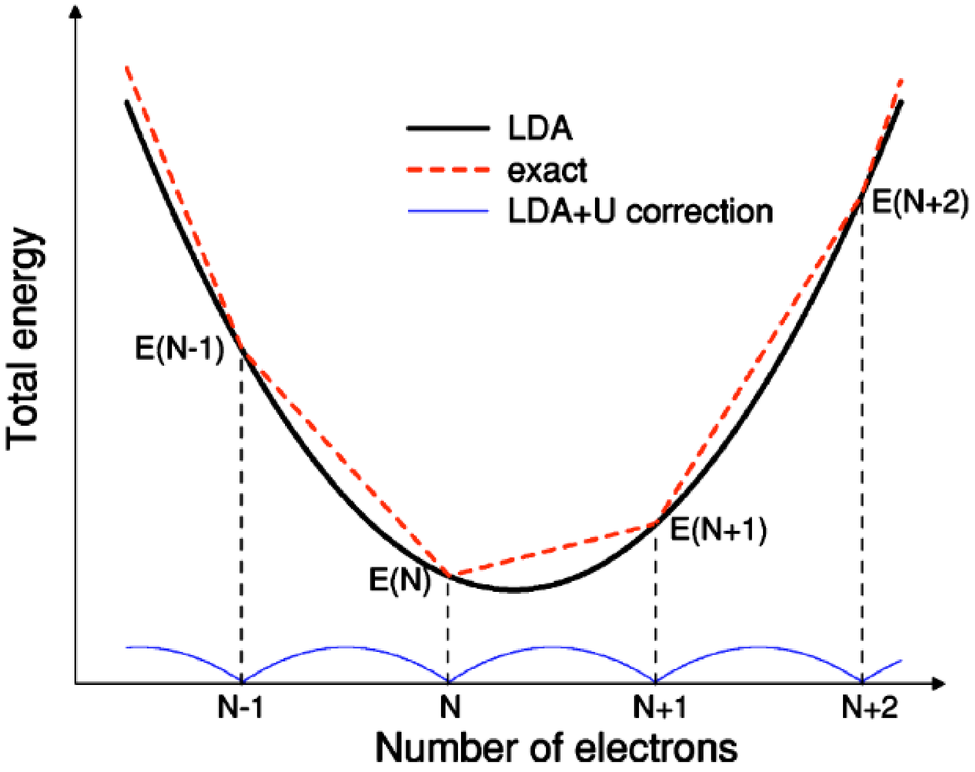

Figure 2.6: An exhibition of the open atom system total energy in relation to its occupancy is presented, calculated by LDA and compared to the exact behaviour[92]. The correction that U is supposed to apply is demonstrated with the blue line.

To treat this problem, the total energy of the system is written as a function of the localized-level occupations of the Hubbard sites:

$$E[\{q_I\}] = \min_{\mathrm{n}(\mathbf{r}),a_\mathrm{I}} \left\{ E[n(\boldsymbol{r})] + \sum_I a_I(n_I - q_I) \right\} \tag{2.37}$$

Here we use I for the atom on which we apply the potential, n_I and q_I for site occupation numbers and variations respectively and a_I are Lagrange multipliers. Naturally $E[n(\boldsymbol{r})]$ is the default energy. We therefore strive to calculate the curvature of the total energy to this variation around the unconstrained values $\left\{n_I^{(0)}\right\}$, of the occupation of one isolated site. Throughout this work, and according to the initial article, sufficiently large supercells are used to dilute the Hubbard sites, changing the on-site occupations. The curvature contains the energy cost associated with the localization of an electron on the chosen site, but non-vanishing results are included as well, because by varying the site occupation a rehybridization of the localized orbitals that happens even in the non-interacting picture of the system (with energy $E^{KS}[\{q_I\}]$), induces a non-linear change in the energy of the system. This part of the curvature that would appear both in the case of the interacting and the non-interacting band structure is subtracted from the total curvature, ending up finally with U.

$$U = \frac{\partial^2 E[\{q_I\}]}{\partial q_I^2} - \frac{\partial^2 E^{KS}[\{q_I\}]}{\partial q_I^2} \tag{2.38}$$

Using Janak's theorem[93], the second order derivative of the total energy can then be transformed into a first order derivative of the localized-level eigenvalue.

$$\begin{aligned} \frac{\partial E[\{q_J\}]}{\partial q_I} &= -a_I, & \frac{\partial^2 E[\{q_J\}]}{\partial q_I^2} &= \frac{\partial a_I}{\partial q_I} \\ \frac{\partial E^{KS}[\{q_J\}]}{\partial q_I} &= -a_I^{KS}, & \frac{\partial^2 E^{KS}[\{q_J\}]}{\partial q_I^2} &= \frac{\partial a_I^{KS}}{\partial q_I} \end{aligned} \tag{2.39}$$

In practice we use non-constrained localized orbital occupations passing to a representation where the independent variables are the a_I.

$$E[\{a_I\}] = \min_{\mathrm{n}(\mathbf{r}),\mathrm{a_I}} \left\{ E[n(\boldsymbol{r})] + \sum_I a_I n_I \right\} \tag{2.40}$$

And similarly for the non-interacting case. Variation of these functionals with respect to wavefunctions shows that the effect of the a_I is to add to the single particle potential a term where the localized potential shifts of strength a_I are applied to the localized levels associated to site I. Introducing now the interacting and non-interacting density response functions of the system with respect to these localized perturbations:

$$\chi_{IJ} = \frac{\partial^2 E}{\partial a_I \partial a_J} = \frac{\partial n_I}{\partial a_J}$$

$$\chi_{IJ}^0 = \frac{\partial^2 E^{KS}}{\partial a_I^{KS} \partial a_J^{KS}} = \frac{\partial n_I}{\partial a_J^{KS}} \tag{2.41}$$

Using the response-function language, the effective interaction parameter U associated to site I can be recast as:

$$U = +\frac{\partial a_I^{KS}}{\partial q_I} - \frac{\partial a_I}{\partial q_I} = \chi_{IJ}^0 - \chi_{IJ} \tag{2.42}$$

A final note to make is that this method neglects some important but secondary contributions to the proper calculation of this Coulomb potential for the sake of simplicity and a very clear physical interpretation.

2.14 Molecular dynamics

Experiments in a lab take into account a huge number of microstates of a system, as well as large time scales. How, thus, one aspires to extract exact properties solving Schrödinger equation for a single microstate in a single time step? Fortunately, the macroscopic properties are not very sensitive to small changes happening in the scale of particles. For instance, if we try to boil water twice retaining the same conditions, we will observe the same boiling time, although the initial atomic positions and velocities have clearly changed, forcing the trajectories to follow.

Statistical mechanics link thermodynamics to quantum mechanics, by treating a macroscopic system as a large collection of fundamental molecular units, which are free to exist in any microscopic state. However, the distribution of the systems in states is based externally forced thermodynamic conditions. Such a collection of systems with a particular set of properties we call *statistical ensemble*. A very standard ensemble is the *canonical ensemble*, which is denoted with NVT, standing for the properties remaining constant for the systems simulated, namely number of atoms (N), volume of unit cell (V) and temperature (T). Another "standard" ensemble is the microcanonical ensemble or NVE, E standing for the energy of the system. Blatantly, canonical ensemble is far more practical than the latter because it is much easier to keep the temperature throughout a system homogeneous, than its energy.

Molecular dynamics (MD), is used to extract highly accurate molecular properties by simulating the time evolution of systems, taking into account more than one state of the microscopic system. Then the value if an observable is taken as an average of points in the phase space, embodying the spirit of an experimental quantum measurement into a calculation. The practical employment of MD is based on the ergodic postulate, according to which averaging between configurations is equivalent to averaging over time. The mathematical expression of this statement follows:

$$\langle O\rangle = \frac{M}{Q}\int_{-\infty}^{\infty} dp \int_{-\infty}^{\infty} dq\, o(p,q) e^{-\frac{H(p,q)}{k_B T}} = \lim_{\tau\to\infty}\frac{1}{\tau}\int_{-\infty}^{\infty} dt\, o\big(p(t),q(t)\big) \tag{2.43}$$

Where O is an observable, p and q are the momenta and positions of atoms, t denotes time, $o(p,q)$ is the phase space function linked with the observable, H is the Hamiltonian, k_B the Boltzmann constant, T the temperature. Finally, Q is the partition function, which for a canonical ensemble is[94]:

$$Q(N,V,T) = M\int_{-\infty}^{\infty} dp \int_{-\infty}^{\infty} dq\, e^{-\frac{H(p,q)}{k_B T}} \tag{2.44}$$

M accounting for the indistinguishability of the particles belonging to the same type.

The value of MD relies on the point on which it stands between the single configuration calculation on the experiment. Particularly, when one performs a traditional single point calculation, he practically accepts that the exponential term in (2.43), which defines the weight of a single configuration in the mean value, is so large that the contributions from the rest are trivial. This crude approximation is not always valid, and this is where MD becomes valuable.

The application of MD leans on solving Newton's equations of motion for the time evolution of the system:

$$H(p,q) = V(q) + \sum_{i=1}^{3N} \frac{p_i}{2m_i} \tag{2.45a}$$

$$\dot{q} = \frac{\partial H(q,p)}{\partial p_i} = \frac{p_i}{m_i} \tag{2.45b}$$

$$\dot{p} = \frac{\partial H(q,p)}{\partial q_i} = -\frac{\partial V(q)}{\partial q_i} \tag{2.45c}$$

Where the only calculated on a quantum mechanical level is the forces between the atoms $-\frac{\partial V(q)}{\partial q_i}$. The limitation of MD appears when nuclear quantum effects, like quantum tunnelling, or zero-point vibration e.t.c. become non-negligible which is the case in low temperatures $(T < 100\ K)$. As the total energy of the Hamiltonian system is a constant of motion, if the cell parameters are not treated as dynamical variables, a standard implementation of MD generates an NVE ensemble.

As mentioned before, the control of temperature in a real system is much more realistic than the energy, consequently it would be natural to consider this case for a MD computation. There are several tools provided in modern software to control T. Nosé-Hoover is a standard one, which inserts two new terms in the Hamiltonian as:

$$H_N = \sum_{i=1}^{N} \frac{p_i}{2m_i s^2} + V(q) + \frac{p_s^2}{2M_s} + (3N+1)k_B T ln(s) \tag{2.46}$$

In this equation, in addition to the physical degrees of freedom, momenta and positions, two extras are introduced, the fictitious mass (M_s) and positions associated with a heat bath (s). The first two terms represent the kinetic and potential energy of the system while the last two, the kinetic and potential energy of the fictitious coordinate s. It has to be noted that Nosé-Hoover thermostat is nonergodic for a single harmonic oscillator. This means that the algorithm fails to generate a canonical distribution for a single harmonic oscillator.

2.15 Vienna Ab initio Simulation Package (VASP)

VASP is a computer program used for atomic scale materials modelling, e.g., electronic structure calculations and quantum-mechanical molecular dynamics, from first principles.

We use it to compute an approximate solution to the many-body Schrödinger equation, within density functional theory. In VASP, central quantities like one-electron orbitals, the electronic charge density and the local potential are expressed in plane wave basis sets. To handle the interactions between electrons and ions we use ultrasoft pseudopotentials and the projector-augmented-wave method. With VASP we use the GGA PBE functional with D2 functional to deal with the dispersion effects and calculate ground state energies of crystal systems.

We can calculate then the interaction energy E_{int} of a material A with a gas B using the formula:

$$E_{int}^{(A-B)} = E^{(A-B)} - E^{A} - E^{B} \tag{2.47}$$

Thus, having calculated the ground state of the material, the gas, and their aggregation, we can calculate their interaction energy. In the case of MD, one computes the average energy of the systems A and B and of course the complex, before performing the subtraction corresponding to (2.47).

In this work we utilize periodic PBE+D2+U for all of our calculations. The choice of PBE is based on its excellent cost-efficiency[95] and its low computational cost, which is imperative for the size of systems we study. D2 is a low cost functional used to treat the long-range interaction which is poorly estimated by PBE[84]. Its accuracy has been proven for similar systems[96]. Hubbard's potential is used to treat highly correlated transition metals.

2.16 Annex

2.16.1 Bra-ket notation

The bra-ket notation will be used in the next context. Ket, namely $|\ \rangle$, is used to denote the wavefunction of the enclosing character, whereas bra, namely $\langle\ |$, for the conjugate complex of the enclosed character. Moreover $\langle\ |\ \rangle$ is used to denote the integration of the wavefunctions of the enclosed characters over all variables, with limits depending on the range of the eigenvalues to which the eigenfunctions belong:

$$|\Psi\rangle \equiv \Psi \quad \langle\Psi| \equiv \Psi^{*} \tag{2.1$a*$}$$

$$\int \Psi^{*}\Psi d\boldsymbol{r} = \langle\Psi|\Psi\rangle \tag{2.1$b*$}$$

$$\int \Psi^{*} \boldsymbol{H} \Psi d\boldsymbol{r} = \langle \Psi | \boldsymbol{H} | \Psi \rangle \qquad (2.1c\,*)$$

Relativistic effects appear for atoms below the third period. Before that, there is no need for their inclusion. The theory will be adopted here in the absence of relativistic effects. Because of that, the electronic spin will be added now in an *ad hoc* manner, each electron having spin $\pm\frac{1}{2}$. Two states arise, one for each spin. The corresponding spin functions α and β, obey the orthonormality condition.

$$\langle \alpha | \alpha \rangle = \langle \beta | \beta \rangle = 1 \qquad (2.2a\,*)$$

$$\langle \alpha | \beta \rangle = \langle \beta | \alpha \rangle = 0 \qquad (2.2b\,*)$$

2.16.2 The Hartree-Fock method

Approximate solutions can be obtained by implementation of the variational principle, harvesting energy always higher than the real. Multiplying (2.2) with $\langle \Phi |$ and integrating, we obtain:

$$E = \frac{\langle \Phi | \boldsymbol{H} | \Phi \rangle}{\langle \Phi | \Phi \rangle} \qquad (2.3\,*)$$

We see that we can obtain the energy as the expectation value of the Hamiltonian operator. Approximating the wave function as a single Slater determinant and using the variational principle, we obtain the HF equations.

In order to produce the Slater determinant, we may use the permutation operator $\boldsymbol{A}$ on the product of the diagonal elements, which we may denote as Π.

$$\Phi = \boldsymbol{A}[\varphi_1(1)\varphi_2(2) \ldots \varphi_N(N)] = \boldsymbol{A}\Pi \qquad (2.4\,*)$$

$$A = \frac{1}{\sqrt{N!}} \sum_{p=0}^{N-1} (-1)^p \boldsymbol{P} = \frac{1}{\sqrt{N!}} \left[1 - \sum_{ij} \boldsymbol{P}_{ij} + \sum_{ijk} \boldsymbol{P}_{ijk} - \cdots \right]$$

It can be shown that A commutes with H and that A acting twice gives the same as acting once times $\sqrt{N!}$.

$$\boldsymbol{A}H = HA \tag{2.5a $*$}$$

$$\boldsymbol{AA} = \sqrt{N!}\,\boldsymbol{A} \tag{2.5b $*$}$$

Our Hamiltonian can be written as:

$$\boldsymbol{H} = \boldsymbol{T_e} + \boldsymbol{V_{e-n}} + \boldsymbol{V_{e-e}} + \boldsymbol{V_{n-n}} \tag{2.6 $*$}$$

Here e indicates electrons and n nuclei, T the kinetic energy and V the potential energy. Due to the Born-Oppenheimer approximation the kinetic energy operator of the nuclei is absent because the positions of the nuclei are fixed. In the same spirit, $\boldsymbol{V_{n-n}}$ is calculated as a constant. As for the remaining operators:

$$T_e = -\frac{1}{2}\sum_{i}^{N_{elec}} \nabla_{\mathrm{i}}^2 \tag{2.7a $*$}$$

$$V_{ne} = -\sum_{a}^{N_{nuclei}}\sum_{i}^{N_{elec}} \frac{Z_a}{|R_a - r_i|} \tag{2.7b $*$}$$

$$V_{ee} = \sum_{i}^{N_{elec}}\sum_{j>i}^{N_{elec}} \frac{1}{|r_i - r_j|} \tag{2.7c $*$}$$

$$V_{nn} = \sum_{a}^{N_{nuclei}}\sum_{b>a}^{N_{nuclei}} \frac{Z_a Z_b}{|R_a - R_b|} \tag{2.7d $*$}$$

We can classify the operators according to the number of indices.

$$\boldsymbol{h}_i = -\frac{1}{2}\nabla_i^2 - \sum_{a}^{N_{nuclei}} \frac{Z_a}{|\boldsymbol{R}_a - \boldsymbol{r}_i|} \tag{2.8a $*$}$$

$$\boldsymbol{g}_{ij} = \frac{1}{|\boldsymbol{r}_i - \boldsymbol{r}_j|} \tag{2.8b $*$}$$

$$\boldsymbol{H}_e = \sum_{i}^{N_{elec}} \boldsymbol{h}_i + \sum_{j>i}^{N_{elec}} \boldsymbol{g}_{ij} + \boldsymbol{V}_{nn} \tag{2.8c $*$}$$

Returning to $(2.6\,*)$, using $(2.7\,*)$, $(2.8\,*)$, and the orthonormality condition to equate the denominator to unity:

$$
\begin{aligned}
E &= \langle \Phi|\boldsymbol{H}|\Phi\rangle && (2.9a\,*)\\
&= \langle \boldsymbol{A}\Pi|\boldsymbol{H}|\boldsymbol{A}\Pi\rangle && (2.9b\,*)\\
&= \sqrt{N!}\,\langle \Pi|\boldsymbol{H}|\boldsymbol{A}\Pi\rangle && (2.9c\,*)\\
&= \sum_p (-1)^p\,\langle \Pi|\boldsymbol{H}|\boldsymbol{P}\Pi\rangle && (2.9d\,*)
\end{aligned}
$$

The nuclear repulsion integral can be immediately calculated.

$$\langle \Phi|\boldsymbol{V_{nn}}|\Phi\rangle = \langle \Phi|\Phi\rangle \boldsymbol{V_{nn}} = \boldsymbol{V_{nn}} \qquad (2.10\,*)$$

The one-electron operator integral for the state i becomes:

$$
\begin{aligned}
\langle \Pi|\boldsymbol{h_i}|\Pi\rangle &= \langle \varphi_1(1)\varphi_2(2)\varphi_3(3)\ldots\varphi_N(N)|\boldsymbol{h_i}|\varphi_1(1)\varphi_2(2)\varphi_3(3)\ldots\varphi_N(N)\rangle = \\
&= \langle \varphi_i(i)|\boldsymbol{h_i}|\varphi_i(i)\rangle\,\langle \varphi_1(1)|\varphi_1(1)\rangle\ldots\langle \varphi_{i-1}(i-1)|\varphi_{i-1}(i-1)\rangle\,\langle \varphi_{i+1}(i+1)|\varphi_{i+1}(i+1)\rangle \\
&\ldots\langle \varphi_N(N)|\varphi_N(N)\rangle = \langle \varphi_i(i)|\boldsymbol{h_i}|\varphi_i(i)\rangle = h_i \qquad (2.11\,*)
\end{aligned}
$$

For one-electron permutation the integrals are all zero. For two-electron permutations, regarding the states 1 and 2, and the one-electron operator:

$$
\begin{aligned}
\langle \Pi|\boldsymbol{h}_1|\boldsymbol{P}_{12}\Pi\rangle &= \langle \varphi_1(1)\varphi_2(2)\ldots\varphi_N(N)|\boldsymbol{h}_1|\varphi_2(1)\varphi_1(2)\ldots\varphi_N(N)\rangle = \\
&= \langle \varphi_1(1)|\boldsymbol{h}_1|\varphi_2(1)\rangle\langle \varphi_2(2)|\varphi_1(2)\rangle \qquad (2.12\,*)
\end{aligned}
$$

Where the overlap of two orthogonal MOs for electron 2, is zero. As for the two-electron operator there is non-zero contribution for the diagonal element:

$$
\begin{aligned}
\langle \Pi|\boldsymbol{g}_{12}|\Pi\rangle &= \langle \varphi_1(1)\varphi_2(2)\ldots\varphi_N(N)|\boldsymbol{g}_{12}|\varphi_1(1)\varphi_2(2)\ldots\varphi_N(N)\rangle = \\
&= \langle \varphi_1(1)\varphi_2(2)|\boldsymbol{g}_{12}|\varphi_1(1)\varphi_2(2)\rangle\ldots\langle \varphi_N(N)|\varphi_N(N)\rangle \\
&= \langle \varphi_1(1)\varphi_2(2)|\boldsymbol{g}_{12}|\varphi_1(1)\varphi_2(2)\rangle = J_{12} \qquad (2.13\,*)
\end{aligned}
$$

and the two index permutation elements:

$$\langle \Pi|\boldsymbol{g}_{12}|\boldsymbol{P}_{12}\Pi\rangle = \langle \varphi_1(1)\varphi_2(2) \dots \varphi_N(N)|\boldsymbol{g}_{12}|\varphi_2(1)\varphi_1(2) \dots \varphi_N(N)\rangle =$$
$$= \langle \varphi_1(1)\varphi_2(2)|\boldsymbol{g}_{12}|\varphi_2(1)\varphi_1(2)\rangle \dots \langle \varphi_N(N)|\varphi_N(N)\rangle$$
$$= \langle \varphi_1(1)\varphi_2(2)|\boldsymbol{g}_{12}|\varphi_2(1)\varphi_1(2)\rangle = K_{12} \qquad (2.14*)$$

J_{12} is the *Coulomb integral*. It represents the classic repulsion between two charge densities φ_1^2 and φ_2^2. K_{12} is the *exchange integral*, and it has no classical analogue. With these two additions we will rewrite the expression for the energy:

$$E = \sum_{i}^{N_{elec}} h_i + \sum_{i=1}^{N_{elec}} \sum_{j>i}^{N_{elec}} (J_{ij} - K_{ij}) + V_{nn}$$
$$= \sum_{i}^{N_{elec}} h_i + \frac{1}{2}\sum_{i=1}^{N_{elec}} \sum_{j=1}^{N_{elec}} (J_{ij} - K_{ij}) + V_{nn} \qquad (2.15*)$$

In the second line the condition in the sum of *j* has been replaced with ½. The minus sign before K_{ij} is due to the permutation operator. The self-interaction term J_{ii} is cancelled by K_{ii}.

We now have an expression of the energy as a function of a given set of orbitals. We now need to find a set of orbitals, made so, that it will minimize the energy. At the same time, the orbitals need to be orthonormal to each other. This is a constrained minimization and can be dealt with the *Lagrange multipliers*. The condition is that the Lagrange function will not change with a small change in the orbitals.

$$L = E - \sum_{j=1}^{N_{elec}} \lambda_{ij}\left(\langle \varphi_i|\varphi_j\rangle - \delta_{ij}\right) \qquad (2.16a*)$$

$$\delta L = \delta E - \sum_{i,j}^{N_{elec}} \lambda_{ij}\left(\langle \delta\varphi_i|\varphi_j\rangle + \langle \varphi_i|\delta\varphi_j\rangle\right) \qquad (2.16b*)$$

Now in order to have a minimization in energy we need $\delta L = 0$. The variation of the energy is written:

$$\delta E = \sum_{i}^{N_{elec}} (\langle \delta\varphi_i | \boldsymbol{h}_i | \varphi_i \rangle + \langle \varphi_i | \boldsymbol{h}_i | \delta\varphi_i \rangle)$$

$$+\frac{1}{2}\sum_{ij}^{N_{elec}} \left(\langle \delta\varphi_i | \boldsymbol{J}_j + \boldsymbol{K}_j | \varphi_i \rangle + \langle \varphi_i | \boldsymbol{J}_j + \boldsymbol{K}_j | \delta\varphi_i \rangle + \langle \delta\varphi_j | \boldsymbol{J}_i + \boldsymbol{K}_i | \varphi_j \rangle + \langle \varphi_j | \boldsymbol{J}_i + \boldsymbol{K}_i | \delta\varphi_j \rangle \right) (17 *)$$

Because the third term is equal to the fifth and the same holds for the fourth and sixth, the ½ in front of the parenthesis can be cancelled with the repeated terms. We will write the variation in terms of the *Fock operator*, F_i.

$$\delta E = \sum_{i}^{N_{elec}} (\langle \delta\varphi_i | \boldsymbol{h}_i | \varphi_i \rangle + \langle \varphi_i | \boldsymbol{h}_i | \delta\varphi_i \rangle) + \sum_{ij}^{N_{elec}} \left(\langle \delta\varphi_i | \boldsymbol{J}_j + \boldsymbol{K}_j | \varphi_i \rangle + \langle \varphi_i | \boldsymbol{J}_j + \boldsymbol{K}_j | \delta\varphi_i \rangle \right)$$

$$\delta E = \sum_{i}^{N_{elec}} (\langle \delta\varphi_i | \boldsymbol{F}_i | \varphi_i \rangle + \langle \varphi_i | \boldsymbol{F}_i | \delta\varphi_i \rangle)$$

$$\boldsymbol{F}_i = \boldsymbol{h}_i + \sum_{j}^{N_{elec}} \left(\boldsymbol{J}_j + \boldsymbol{K}_j \right) \qquad (2.18 *)$$

We now can write down the variation of the Lagrange function using the Fock matrix.

$$\delta L = \sum_{i}^{N_{elec}} (\langle \delta\varphi_i | \boldsymbol{F}_i | \varphi_i \rangle + \langle \varphi_i | \boldsymbol{F}_i | \delta\varphi_i \rangle) - \sum_{i,j}^{N_{elec}} \lambda_{ij} \left(\langle \delta\varphi_i | \varphi_j \rangle + \langle \varphi_i | \delta\varphi_j \rangle \right) \qquad (2.19 *)$$

Using the conjugate complex identities:

$$\langle \varphi | \delta\varphi \rangle = \langle \delta\varphi | \varphi \rangle^*, \qquad \langle \varphi | \boldsymbol{F} | \delta\varphi \rangle = \langle \delta\varphi | \boldsymbol{F} | \varphi \rangle^*,$$

$$\delta L = \sum_{i}^{N_{elec}} \langle \delta\varphi_i | \boldsymbol{F}_i | \varphi_i \rangle - \sum_{ij}^{N_{elec}} \lambda_{ij} \langle \delta\varphi_i | \varphi_j \rangle + \sum_{i}^{N_{elec}} \langle \delta\varphi_i | \boldsymbol{F}_i | \varphi_i \rangle^* + \sum_{ij}^{N_{elec}} \lambda_{ij} \langle \delta\varphi_j | \varphi_i \rangle^* = 0 (2.20 *)$$

The variation of either $\langle \delta\varphi_i |$ or $\langle \delta\varphi_i |^*$ should make $\delta L = 0$. Thus, the first two terms must be zero and the last two must be zero themselves. In order to make the last term look like the second, we interchange i and j in the sum, which we can do since the sum is over both the indices. That way λ_{ij} becomes λ_{ji} and $\langle \delta\varphi_j | \varphi_i \rangle^*$ becomes $\langle \delta\varphi_i | \varphi_j \rangle^*$. Subtracting from the first two the conjugate complex of the last two terms, we get:

$$\sum_{ij}^{N_{elec}} \lambda_{ij} \langle \delta\varphi_i | \varphi_j \rangle - \sum_{ij}^{N_{elec}} \lambda_{ji}^* \langle \delta\varphi_i | \varphi_j \rangle^* = \sum_{ij}^{N_{elec}} (\lambda_{ij} - \lambda_{ji}^*) \langle \delta\varphi_i | \varphi_j \rangle = 0 \qquad (2.21\,*)$$

This means that the lagrangian multipliers are terms of a Hermitian matrix. Returning to (2.23), because the first two terms are equal to zero, we can write down the final form of *Hartree-Fock equations*:

$$\boldsymbol{F}_i\, \varphi_i = \sum_{j}^{N_{elec}} \lambda_{ij}\, \varphi_j \qquad (2.22\,*)$$

The diagonalization of the matrix λ_{ij} by the operation of a unitary transformation will harvest the energy of the orbitals ($\lambda_{ii} = \varepsilon_i$) and will zero the off-diagonal elements ($\lambda_{ij} = 0$). The new orbitals that will occur are called *canonical* MOs, and denoting them as $\varphi_j{}'$ we can rewrite $(2.22\,*)$ as:

$$\boldsymbol{F}_i\, \varphi_i = \varepsilon_i\, \varphi_i' \qquad (2.23\,*)$$

The lagrangian multipliers seem to be molecular orbital energies and multiplying $(2.23\,*)$ by $\varphi_i'^*$ from the left and integrating, we can observe that they are the expectation value of the Fock operator.

$$\langle \varphi_i{}' | \boldsymbol{F}_i | \varphi_i{}' \rangle = \langle \varphi_i{}' | \varphi_i{}' \rangle \varepsilon_i = \varepsilon_i \qquad (2.24\,*)$$

The Hartree-Fock equations form a set of pseudo-eigenvalue equations as the Fock operator depends on all the occupied MOs. A specific Fock orbital can be known, only if all the other occupied MOs are known, employing iterative methods. Although the canonical MOs are convenient for solving the variational problem, the total energy depends on the total wavefunction (the Slater determinant), which is a function of the MOs. After having determined the canonical MOs we can use linear combinations of them to form other convenient functions as localized MOs, hybrid MOs e.t.c.

Skipping the primes for the MOs we can write the total energy as:

$$E = \sum_{i}^{N_{elec}} \varepsilon_i - \frac{1}{2}\sum_{ij}^{N_{elec}} \left(J_{ij} - K_{ij}\right) + V_{nn} \qquad (2.25a *)$$

$$\varepsilon_i = \langle \varphi_i | \boldsymbol{F}_i | \varphi_i \rangle = \boldsymbol{h}_i + \sum_{i}^{N_{elec}} \left(J_{ij} - K_{ij}\right) \qquad (2.25b *)$$

The total energy is not just a sum of MO energies. The Fock operator counts the electron repulson twice, which has to be corrected. Moreover, the energy calculated is not exact as the electron repulsion is computed as mean field, due to the fact that the wavefunction is treated with a single Slater determinant. The energy that is missing is called *electron correlation*, and its inclusion is very expensive computationally.

2.16.3 Basis set approximation

To express the MOs, we usually use a basis set consisted of suitable basis functions. The suitability is determined by the physics of our system, so that the basis set converges quickly as we add more elements. Also, we may choose the basis, based on the ease it offers on the calculations we meet. Often implemented basis functions are gaussians, exponentials, plane waves (for periodic systems) etc.

Each MO is expanded in terms of the basis functions χ, conventionally called atomic orbitals, although they are not solutions to the HF problem.

$$\varphi_i = \sum_{a=1}^{N_{basis}} c_{ai}\chi_a \qquad (2.26 *)$$

The HF equations may be written as:

$$\boldsymbol{F}_i \sum_{a=1}^{N_{basis}} c_{ai}\chi_a = \varepsilon_i \sum_{a=1}^{N_{basis}} c_{ai}\chi_a \qquad (2.27 *)$$

Multiplying by the left by a specific basis function and integrating yields the Roothan-Hall equations for a closed shell system, the Hartree-Fock equations in the atomic orbital basis:

$$\boldsymbol{FC} = \boldsymbol{SC\varepsilon} \qquad (2.28a*)$$

$$F_{\alpha\beta} = \langle \chi_\alpha | \boldsymbol{F} | \chi_\beta \rangle \qquad (2.28b*)$$

$$S_{\alpha\beta} = \langle \chi_\alpha | \chi_\beta \rangle \qquad (2.28c*)$$

The whole formalism can be rewritten for the basis functions, but the principles are the same so this step will be skipped.

2.16.4 Restricted and unrestricted Hartree-Fock

The Slater determinant is written in terms of spin-orbitals, the products of spatial orbitals and spin functions (α and β). If there are no restrictions on the form of the spatial orbitals, the trial wavefunction is an *Unrestricted Hartree-Fock* (UHF) wavefunction. If the system under consideration has an even number of electrons and a singlet type wavefunction (closed shell system), the restriction that each spatial orbital should have two electrons, one with α and one with β spin, is made. Such a wavefunction is known as *Restricted Hartree-Fock* (RHF). For open-shell systems, a UHF treatment leads to well-defined orbital energies, which may be interpreted as ionization potentials. Open shell systems can also be described by restricted type wavefunctions where the special part of the doubly occupied orbitals is forced to be the same and this is known as *Restricted Open-shell Hartree Fock* (ROHF). For a ROHF wavefunction, it is not possible to choose a unitary transformation that makes the matrix of the Lagrange multipliers diagonal, and orbital energies from ROHF wavefunction are consequently not uniquely defined (and cannot be equated to ionization potentials by a Koopman-type argument).[84]

The UHF wavefunction allows different special orbitals for the two electrons in an orbital. As restricted type wavefunctions put constrains on the variational parameters, the energy of a UHF wavefunction is always lower than or equal to a corresponding R(O)HF type wavefunction. Whether for closed shell systems the two possibilities would not make much of a change, in the case of a doublet state, if the single electron has an α spin electron, it will interact in a different manner with other α spin electrons than with β. Thus, the different orbitals should have the freedom to change independently. In UHF description, however, the wavefunction is not an eigenfunction of the $\boldsymbol{S}^2$ operator, unless equal to the RHF description, where $\boldsymbol{S}^2$ the squared operator of the total electron spin. This means that a singlet UHF wavefunction may also contain contributions from higher lying sates (triplet, quintet, e.t.c.).

2.16.5 Self-consistent field

The Roothan-Hall equations have to be solved iteratively since the Fock matrix depends on its solutions. The iteration process is:

1. Calculate all one- and two-electron integrals.
2. Generate a suitable start guess for the MO coefficients.
3. Form the initial density matrix.
4. Form the Fock matrix.
5. Diagonalize the Fock matrix. The eigenvectors contain the new MO coefficients.
6. Form the new density matrix. If it is sufficiently close to the previous density matrix the SCF is done, otherwise go to 4.

There are still some hidden spots in the procedure. Its convergence is not guaranteed. The energy that one will reach is not certainly the global minimum. In fact, it can even be a maximum or a saddle point. Can the number of iterations until convergence be reduced? Does the most efficient method depend on the size of the system and/or the computer? There are various methods to face these topics, but these are very technical details for the purposes of this work.

3. A systematic DFT screening of cationic faujasite-type zeolites for the adsorption of NO, NO_2 and H_2O

Abstract

The limitation of NO and NO_2 (NO_x) emissions out of exhaust gases released from diesel engines in confined environments requires efficient adsorbents. Since NO_x species are present in trace amounts (50-1000 ppm) in exhaust gases, and always co-exist with a large content of H_2O (2 - 12wt%), adsorbents need to be highly selective to trap NO_x over H_2O. To this end, periodic density functional theory (DFT) calculations in combination with dispersion corrections have been used for a systematic screening of monovalent and divalent cation-exchanged faujasite zeolites. The present work investigates the effect of the cation nature and Si/Al ratios (1.4; 2.43; 23; 47), on the adsorption selectivity of faujasite towards NO and NO_2 against H_2O. Alkali and alkali-earth metals Li(I), Na(I), K(I), Rb(I), Cs(I) and Ca(II), Ba(II), as well as monovalent and divalent transition metals Cu(I), Ag(I), and Zn(II), Pt(II), Pd(II), Cu(II), Fe(II), Co(II), Ni(II) embedded in faujasites, have been explored for their ability to capture NO and NO_2. Bond activation of adsorbed gases has also been checked for the most promising materials to assess the tendency of these gases to further react with the adsorption site. Bader charges and charge density difference calculations were carried out for the most effective faujasite structures to assess the bond formation between materials and adsorbed gases. Much weaker interaction energies were predicted for Y vs X faujasites, which is in favour of the material's regeneration. Cu(I) and Fe (II) based Y zeolites (Si/Al = 2.43) were identified as the most attractive candidates. Nevertheless, iron strongly activated the bonds of NO_2 upon adsorption raising doubts about its implementation with faujasite. This is the first time that such a large screening of cationic zeolites has been performed for a separation topic using DFT calculations. In the specific case of NO_x / H_2O separation, the present work helped to exclude most of the zeolites explored from future theoretical or experimental investigations, highlighting the potential of Cu(I)Y and the promising selectivity that Fe(II) can bestow on a zeolite.

Keywords: DFT, NO, NO_2, H_2O, interaction energy, Bader charges, charge density difference, charge transfer, Si/Al ratio, Faujasite, porous material, transition metals, alkaline metals,

alkaline-earth metals, diesel, PNA.

3.1 Introduction

Anthropogenic NO_x (NO and NO_2) sources include biomass burning, fossil fuel and biofuel combustion, and N-fertilized soil emissions.[1,2] At the environmental level, NO_x even present in trace amounts are known to deteriorate atmospheric chemistry, air quality and climate. NO_x are not major greenhouse gases themselves, but they may modify the latter's concentration through complex chemical processes.[1] Looking at the atmospheric chemistry, oxidation of NO produces NO_2 which favours the formation of tropospheric O_3. Although O_3 is known to be a greenhouse gas, it is also a precursor of OH radicals, which determine the atmospheric lifetime of other pollutants such as methane, many volatile organic compounds (VOCs) and carbon monoxide.[97]

At the human level, repeated NO_2 exposure increases the asthmatic response of individuals.[3] Moreover, long-term exposure to particulate matter and NO_2 from car exhausts has been linked to the development of heart failure.[4] According to a 2011 EU survey,[6] non-road diesel engines contribute to 7.3% of the total NO_x emissions. Non-road diesel fumes are especially harmful to humans working in confined environments. EU directive 2017/164 limits NO and NO_2 exposures per 8 hours (a full-time working day) to 2 and 0.5 ppm, respectively.[7] Several strategies exist to handle the strict NO_x limits in lean-burn automotive emissions.

Currently *NO_x storage reduction* (NSR),[11,12] and *selective catalytic reduction* (SCR)[13,14] are the main catalytic treatments for the neutralization of NO_2. These solutions can be very effective. SCR in particular can reach almost 100% NO_x conversion into harmless N_2.[13] However, these catalytic treatments require high temperatures (above 200°C) to be efficient, which limits their application for vehicles subjected to discontinuous operation and consequently, to many cold starts.

To this end, an effective adsorbent is needed for the low-temperature selective capture of NO and NO_2 in the presence of water. A fine balance between high adsorption selectivity and easy regeneration is desired. This separation has been based on the thermodynamic selectivity throughout the literature. Pt/Pd promoted oxide-traps (CeO_2, ZnO_2, WO_3) subjected to NO_x containing gas streams have managed to reduce the outlet NO_x concentration[31,32]. However, these oxides are prone to sulphur poisoning which deteriorates their structural properties and obstructs their iterating operation. Zeolites were later tested promoted by Pt/Pd, and not only they were found to work selectively but also to be resilient to sulphur poisoning and regenerable[35,36,98]. They were successful in reducing NO_x from a gas stream either by passively trapping them at low temperatures and releasing them at higher ones, giving rise to the *passive NO_x adsorbers* (PNA)[31–33,35,99], or by catalysing their neutralization at the same time, bearing the *cold start concept* catalysts[19,30,100]. As Pt and Pd are expensive, this work is part of a bigger cause to find cheaper alternatives to these precious metals for the construction of a PNA based on the framework of faujasite.

NO_x always co-exists with large amounts of H_2O, which may reach up to 12 wt% of diesel exhaust gases,[101] and can inhibit NO_x adsorption through competition for active adsorption sites. NO_x concentration ranges between 50 and 1000 ppm[102], i.e. 100-2000 times lower than the water content. Therefore, the desired zeolitic adsorbents need to be highly selective for NO_x in comparison to water. To this end, we strive to identify efficient and selective materials for NO_x adsorption in the presence of water. These materials should be able to support diesel exhaust gas pipe conditions of the non-road vehicles, namely they should be hydrothermally and chemically stable, water insoluble, and highly NO_x selective.

In the present work, periodic density functional theory was employed to achieve a systematic screening of various faujasite (FAU) formulations regarding their NO_x/H_2O affinity. These formulations vary from the nature of the cation they are promoted by, as well as from the Si/Al ratio (i.e., cation loading). Indeed, the electron structure of the cation is decisive considering its reactivity, and consequently its affinity towards the NO_x/H_2O. [51,95,103] As the separation in hand is challenging, several cations needed to be considered. On the other hand, lowering the Si/Al ratio increases the cation loading of the zeolite. Cations affect the stabilization of an adsorbed gas even from a distance due to non-bonding interactions[51,95,103]. Since the presence of cations determines the existence of adsorption sites but also has strong effect on the structural properties of the zeolite, their abundancy is imperative for the adsorption capacity. These criteria motivated the exploration of such low Si/Al ratios, but also the framework of faujasite, which can retain its crystallinity in so high Al content.

Two sets of cations have been considered as follows: $monovalent\,(M) = \{Li, Na, K, Rb, Cs, Cu, Ag\}$ and $divalent\,(D) = \{Ba, Ca,\ Zn,\ Cu,\ Pt,\ Pd, Fe, Co, Ni\}$. Their adsorption energies for NO_x and H_2O were calculated at 0 K. The Si/Al ratios implemented in this work are 47 and 23 for isolated cation cells, 2.43 for Y zeolite and 1.4 for X zeolite. FAU has been chosen for its potential to easily incorporate a large panel of cations. FAU has been used in the past for the selective trapping of gases in general, but also for more relevant investigations like catalytic NO reduction.[104–107] DFT has proven its efficiency and usefulness regarding the prediction of adsorption energies for a range of gases on zeolites.[108–110] The accuracy and efficiency of specific functionals for the determination of molecular interactions has been commented elsewhere[84,95] but the point is that some of them can really stand up to the challenge of producing accurate results for gas-solid interactions, avoiding time and money consuming experiments.

3.2 Methods and models

3.2.1 Computational methods

DFT calculations were performed using the Vienna Ab initio Simulation Package (VASP).[111] The Pedrew Burke Ernzerhof (PBE) exchange-correlation functional in the generalized gradient approximation (GGA) was used.[87] The electron-ion interactions were described using the projector augmented plane wave (PAW) method, and the Kohn-Sham equations were solved self-consistently until the energy difference between the cycles was lower than 10^{-6} eV.[112] The plane wave cut-off energy was set at 450 eV. A Gaussian smearing with $\sigma = 0.1$ eV was applied to the band occupations in order to improve the total energy convergence. The atomic positions were optimized until the force differences between two successive ionic steps were no more than 0.02 eV Å^{-1}. The sampling of the Brillouin zone was limited to the Γ-point. Due to the local nature of the GGA, dispersion corrections were added separately in order to accurately simulate the adsorption process.[95,113] Grimme's D2 scheme was used, where the dispersion interactions were modelled as an atom-pairwise correction. The C_6 coefficients were defined for each atomic species independently of the system.[89,114] In a previous work, it was found that different dispersion correction methods of various complexity (D2, TS/HI – standing for Tkatchenko-Scheffler scheme with iterative Hirshfeld partitioning – and FI/MBD – standing for many-body dispersion with its fractionally ionic (FI)[115–117]) lead to similar results for NO_x and H_2O adsorption on isolated monovalent exchanged FAU, namely Si/Al: 47. The structures considered there have chemical environments akin to the ones used in this work.[96] Hence we have selected the D2 method for this work as it is less costly. Only in the case of FeY, MBD, which is a more sophisticated correction, has been used to cross-evaluate the results obtained with D2.

Hubbard's potential U is an add-on to conventional GGA, used to treat the inadequate description of strongly correlated systems.[118,119] The U values used in this work, calculated for the transition metals in similar environments, were equal to 6.0, 4.5 and 5.9 eV for Fe, Co and

Ni, respectively.[120]

The interaction energy ($\varDelta E_{int}$) at 0 K is determined in 4 steps: 1) The atomic positions and the zeolitic cell parameters are relaxed according to the convergence conditions given above. 2) The relaxed cell parameters are used to optimize the atomic positions of the isolated gases. 3) Placing a relaxed gas close to the desired adsorption site of a zeolite, we relax the atomic positions of the adduct, zeolite-gas. 4) The energy of the interaction is calculated as:

$$\varDelta E_{int} = E_{FAU-X} - E_{FAU} - E_X \tag{3.1}$$

where E_{FAU-X} expresses the energy of the gas/FAU adduct, E_{FAU}, the energy of the material, and E_X the energy of the gas.[95] These energies are associated to the relaxed structures of steps 3, 1 and 2 respectively.

To shed light on the nature of the bonds formed between the gases and the most effective zeolite structures, induced Bader charges[121–125] and charge density differences due to adsorption were calculated. Bader charges were first calculated for the complex Q_{FAU-X}, the zeolite, Q_{FAU}, and the gas, Q_X, and their differences gave the charge difference due to adsorption $\varDelta Q$ as:

$$\varDelta Q = Q_{FAU-X} - Q_{FAU} - Q_X \tag{3.2}$$

Correspondingly, the charge density difference $\Delta\rho$ was calculated as:

$$\varDelta \rho = \rho_{FAU-X} - \rho_{FAU} - \rho_X \tag{3.3}$$

3.2.2 Faujasite structure

The siliceous structure of FAU crystallizes within the Fd-3m symmetry space group.[126] FAU consists of a sequence of TO_4 where T is an abbreviation for the tetrahedrally coordinated Si and Al atoms – Si(IV) and Al(III) – linked together by oxygen atoms. Their assembly makes a crystal structure. It is uniform, regular, and ordered. In the present study, a primitive rhombohedral cell (1/4 of the conventional cell) was used to reduce the computational effort (Figure 3.1). The lattice parameters of the primitive cell after relaxation at the PBE+D2 level of theory were $a \approx b \approx c \approx 17$ Å and $\alpha \approx \beta \approx \gamma \approx 60^{\circ}$ and the unit cell volume$\approx 3\,800$ Å^3. The exact values of the relaxed cell parameters for different cation-exchanged zeolite structures are shown in Table 3.SI of the supporting information.

FAU comprises hexagonal prisms (D6R), sodalite cages and large supercages with a diameter of about 11 Å (International Zeolite Association 2017) (Figure 3.1). The D6R comprises two six membered rings (6MR), where the T atoms of the two rings are bridged through an O atom forming a second type of ring: a 4-membered one (4MR). The sodalite cage is constructed out of eight 6MR, always linked by 4MR.[127] Figure 3.1, not only summarizes these structural elements but also presents the cationic sites.

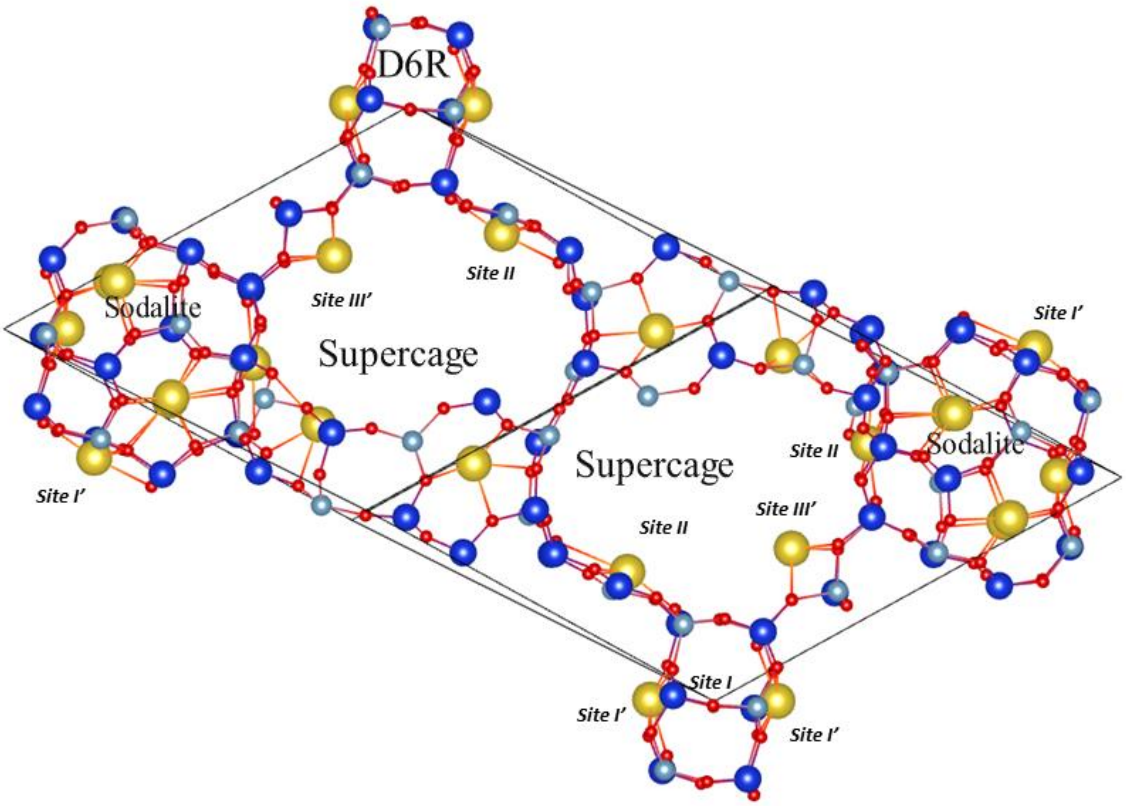

Figure 3.1: The rhombohedral cell of a Na-X zeolite is depicted. Its three types of cavities are illustrated, namely the hexagonal prism or D6R (double 6-membered rings), the sodalite cage and the supercage. The adsorption sites are also included (SI and SI' in the centre and on the facet of a D6R respectively, SII on the facet of a 6MR of a sodalite towards the supercage and SIII' on the facet of a 4MR of either a D6R or a sodalite facing towards the supercage). Si atoms are coloured in blue, O in red, Al in lightblue and sodium cations in yellow.

The openings of the sodalite cage (Figure 3.1) do not allow most of the molecules to enter, but tiny ones like dihydrogen,[48] except on higher loadings.[49,50] On the contrary, supercage gives access to bigger molecules as well. As depicted in Figure 3.1, we identify 4 kinds of sites. Site I' is on the facet of a 6MR belonging to a D6R. A cation occupying this site will always face a sodalite cage and is inaccessible to the gases. The same holds for the cations located in site I which are enclosed in the centre of a D6R. Cations located on site II are placed on a 6MR facet of the sodalite and are accessible to the gases, as they face the supercage. Finally, cations located on site III' are placed on a 4MR, a facet that might belong either to a sodalite or to a 6MR and has access to the supercage. Based on this analysis we only carry out adsorptions on sites accessible from the supercage namely, site II and III.

The negative charge due to the Al/Si substitutions must be compensated by the addition of a cation. The chemical formula of a FAU mesh is the following:

$$M_{x/m}{}^{m+}\left[(AlO_2)_x\,(SiO_2)_y\right] \tag{3.4}$$

where x and y represent the number of Al and Si atoms, respectively, thus, x + y stands for the number of tetrahedral atoms in the framework. As one can observe the number of O atoms of the structure is $2(x+y)$. Finally, M stands for the extraframework metals compensating for the charge lost after each replacement of Si with Al. m stands for the charge, therefore, the number of the metals should be equal to x/m, so that the charge that they donate to the framework is equal to the one that has been lost.

The sequences of T atoms are not randomly set. According to Löwenstein's rule two AlO_4^- tetrahedra should be interspersed with at least one SiO_4. In this work we favour Al – Si – Si – Al sequences over Al – Si – Al whenever possible, as – in principle – dispersing the negative charge stabilizes the system.

The Si/Al ratios considered in this work were: $\{47, 2.43\,, 1.4\}$ for monovalent and $\{23, 2.43\,, 1.4\}$ for divalent cation exchanged cells. Faujasites with Si/Al ratios of 1.4 and 2.43 are denoted as X and Y zeolites, respectively. In addition, pure silica cell was used.

To achieve realistic zeolite structures, the cation distributions within the considered Y and X zeolites were drawn from T. Frising and P. Leflaive's research where they gathered the preferred occupation sites of several compensating cations from previous syntheses.[128] Figure 3.2 summarizes the site occupation, cation loading, and Si/Al of each structure. For the monovalent cations M, where $M = \{Li, Na, K, Rb, Cs, Ag, Cu(I)\}$ a full exchange was applied during the modelling of the majority of these systems[129–135] with the exception of Rb and Cs for which only partial exchange was experimentally demonstrated.[128] Due to their large size, it was revealed that these two cations tend to avoid the occupation of sodalite and D6R (sites I and I')[136–138]. Instead, sodium atom is located on these sites and Rb and Cs occupy only sites II and III'. Subsequently, the generalized molecular formula (3.4) for these monovalent cations incorporated in the FAU is given as follows: For Si/Al = 47 the single cation was placed on site II being the most stable site over all others.[139] For the primitive cell where $x + y = 96$, we obtain $MAlSi_{47}O_{96}$. In the same spirit, for MY, where Si/Al = 2.43 and taking into consideration that Rb and Cs cells are partially exchanged, we get $Na_xM_{14-x}Al_{14}Si_{34}O_{96}$, where $x = 6$ for Rb and Cs, and 0 otherwise. Finally, for MX we get $Na_xM_{20-x}Al_{20}Si_{28}O_{96}$, applying the same values for x as in the case of MY.

As for the divalent cations, where $D = \{Ca, Ba, Zn, Pt, Pd, Cu(II), Fe, Co, Ni\}$. T. Frising and P. Leflaive have shown in their excellent review that divalent cations present a fussy behaviour regarding the site occupation compared to that of monovalent. Not all of them prefer the same sites and neither achieve the same exchange rate. Figure 3.2 summarizes the site occupation, cation loading, and Si/Al of each structure. Utilizing (3.4) for the primitive cell where $x + y = 96$: If Si/Al = 23 with only one divalent cation located at site II, we obtain the molecular formula $DAl_2Si_{46}O_{96}$. For Y, two molecular formulas were used: $D_7Al_{14}Si_{34}O_{96}$ for Ca, Ba, Zn, and Cu(II) where a full exchange was achievable and divalent cations occupied site II, I and I', and $D_6Na_2Si_{34}O_{96}$ for the rest. Both were inspired by previously synthesised structures.[128,140–148]. The fully exchanged structures contain three divalent cations in sodalites and four on site II, while the partially exchanged cell contains two divalent and two Na cations in sodalites and four divalent cations on site II. Finally, X zeolite cells were divided into four groups. The only fully exchanged cells were experimentally found achievable for Cu(II) and Ca(II) with the molecular formula $D_{10}Al_{20}Si_{28}O_{96}$. The partially exchanged structures are the ones of Fe(II), with the molecular formula $Na_6Fe_7Al_{20}Si_{28}O_{96}$, the cell of Co, with the molecular formula $Na_4Co_8Al_{20}Si_{28}O_{96}$, and finally, the cell of Ni, with the molecular formula $Na_6Ni_7Al_{20}Si_{28}O_{96}$. It is noted that BaX, ZnX, PtX and PdX were not investigated because they do not occupy site III',[128] thus their interaction energies are expected to resemble the Y cases.

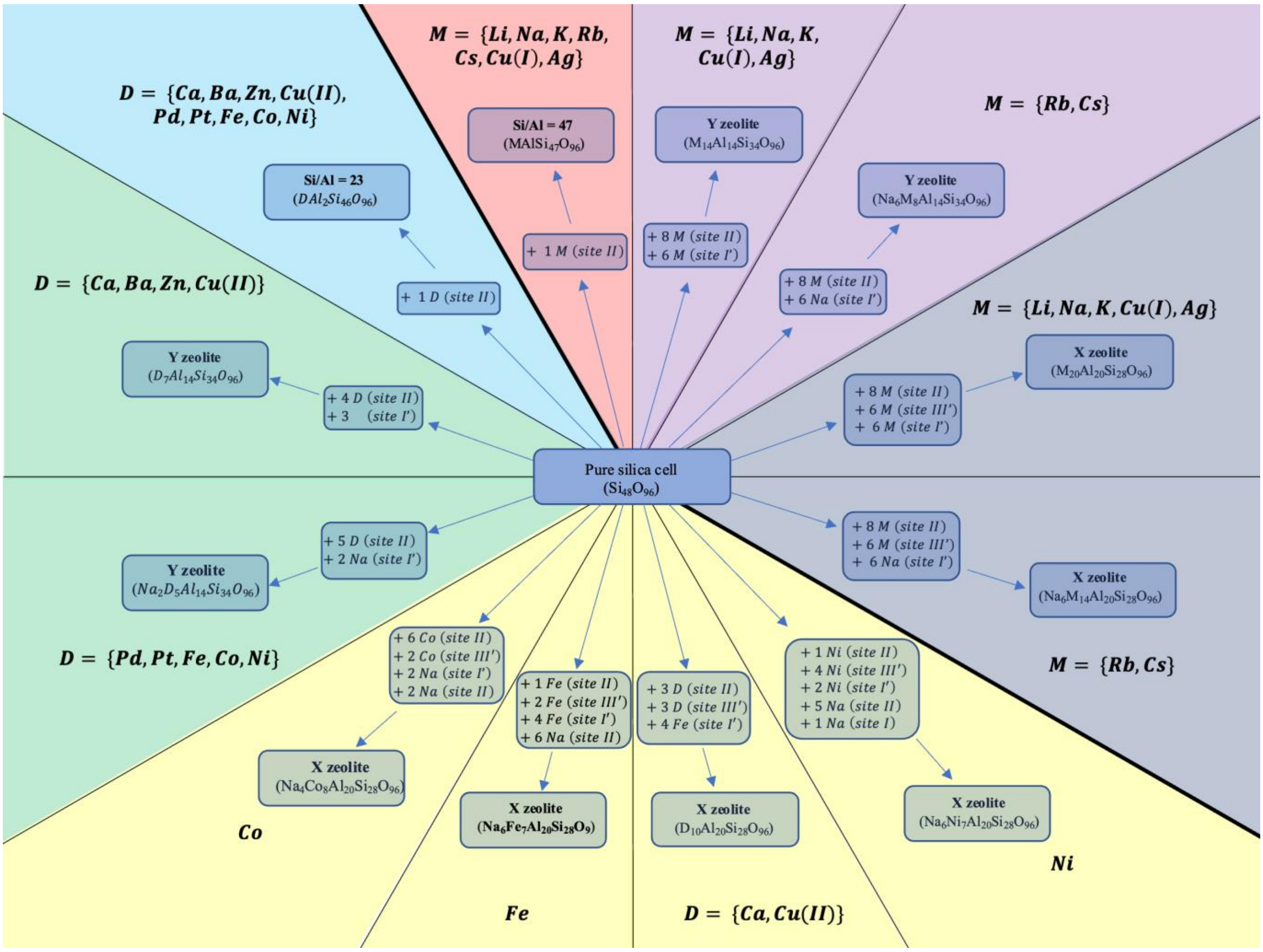

Figure 3.2: The site occupation, cation loading, and Si/Al of the sites considered are presented. Lines separate each kind of structure based on site occupation and cation loading. Thick lines separate monovalent from divalent structures. Colours separate the different Si/Al ratios. The arrows illustrate how introduction of cations leads from the pure silica cell to each kind of structure.

3.3 Results

3.3.1 Adsorption screening for the monovalent cations

As mentioned earlier, three different Si/Al ratios have been investigated for monovalent cation embedded cells in the present study: 47 (isolated cation cell), 2.43 (Y zeolite), or 1.4 (X zeolite). Adsorption energies determined for NO, NO_2 and H_2O on FAU zeolites are presented in Table 3.1 and illustrated in Figure 3.3. Results obtained for Si/Al = 47 structure at the

PBE+D2 level of theory were extracted from a previous work[96] and they are compared here with the present results. Adsorption energies for pure silica cell were equal to -19.1, -17.9 and -27.5 kJ/mol for NO, NO_2 and H_2O respectively.

Table 3.1: Adsorption energies (kJ/mol) of H_2O, NO and NO_2 computed for the three different investigated Si/Al ratios. Data for Si/Al = 47 is taken from Hessou et al and are underlined.[96] The numbers marked with bold refer to cross adsorption (adsorption between site II and III').

Si/Al ratio	Gases	Li^+	Na^+	K^+	Rb^+	Cs^+	Cu^+	Ag^+
47	NO	-32.4	-24.8	-19.1	-22.7	-20.3	-121.8	-73.5
	NO_2	-38.2	-30.7	-29.3	-21.7	-20.1	-81.8	-54.9
	H_2O	-80.5	-64.0	-64.4	-58.5	-61.6	-86.3	-84.7
2.43 (Y)	NO	-32.9	-27.8	-12.9	-27.4	-33.1	-117.4	-82.7
	NO_2	-34.7	-33.3	-11.6	-25.2	-34.3	-122.7	-36.0
	H_2O	-77.8	-73.1	-72.8	-72.5	-73.7	-80.4	-67.3
1.4 (X)	NO	-41.4	**-38.6**	**-47.1**	**-60.8**	**-59.7**	-173.0	-77.7
	NO_2	**-53.9**	**-73.2**	**-99.6**	**-131.9**	**-123.3**	**-255.2**	**-164.2**
	H_2O	-106.6	-105.9	-96.4	**-89.1**	**-114.0**	-137.5	-113.8

For structures with Si/Al = 47, all alkaline cations presented much higher affinity for water than for NO_x (Figure 3.3a). Remarkably, Cu(I) shows a great preference for NO over water with an energy difference of 35.5 kJ/mol, but NO_2 does not follow this trend. Similar adsorption energy was reported in a previous work for NO adsorption in Cu(I) embedded chabazite on site II using the PBE+D2 level of theory harvesting an interaction energy of -123.4 kJ/mol, very similar to ours at -117.4kJ/mol.[149]

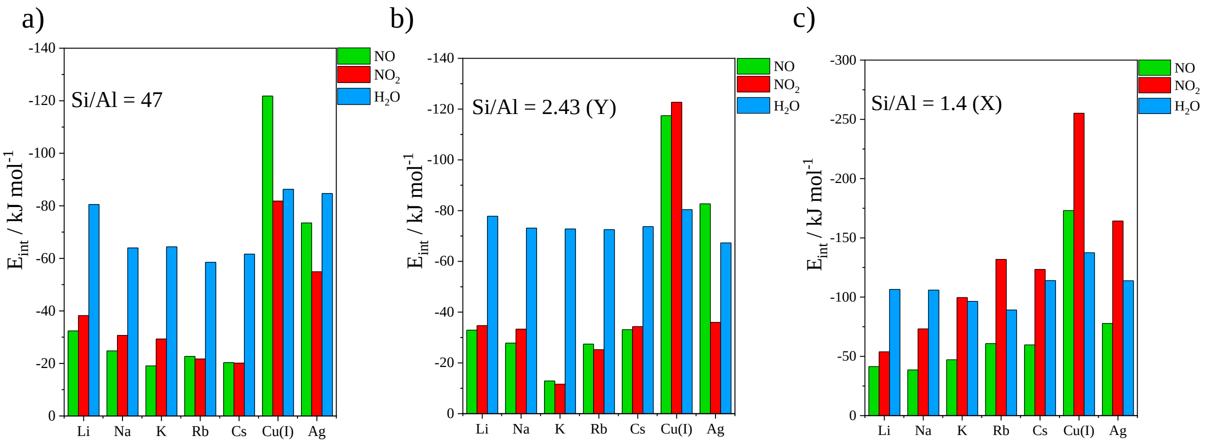

Figure 3.3: Interaction energies computed at the PBE+D2 level of theory for NO, NO_2, and H_2O adsorption on a) isolated monovalent cation embedded faujasite (Si/Al = 47), b) Y zeolite (Si/Al = 2.43) and c) X zeolite (Si/Al = 1.4).

For Y structures (Figure 3.3b), all alkaline atoms exhibit a stronger interaction with H_2O than with NO_x. Cu(I) showed a much higher adsorption energy for NO and NO_2 than for H_2O with differences at 37.0 kJ/mol and 117.3 kJ/mol, respectively. Hessou et al. (2018)[96] reported similar results for all cations. Adsorption configurations are illustrated in Figures 3.4a-f, depicting the adsorbed gases on Na of the alkali group and on Cu(I) of the transition metal group incorporated in Y zeolite. The adsorption on the other cations is illustrated in Figure 3.SI of the supporting information. NO and NO_2 were adsorbed on Na with a distance of 2.60 and 2.53 Å respectively (Figure 3.4a and c). Water stayed closer to the cation, at 2.40 Å (Figure 3.4e). For adsorption on Cu(I), NO and NO_2 were connected with lengths of 1.79 and 1.88 Å respectively (Figure 3.4b and d), while water remained at 1.93 Å. The latter even formed a H-bond with the 6MR oxygen with a length equal to 1.75 Å (Figure 3.4f). The shorter distances observed with Cu(I) support the stronger affinity of Cu(I) for NO_x than water, especially considering the longer covalent radius of N by comparison with O. The opposite behaviour was observed for alkaline cations, which formed stronger interactions with water.

Finally, for X structure (Si/Al = 1.4), the results are depicted on Figure 3.3c and Table 3.1. The adsorption energies were highly increased in comparison to results obtained for Si/Al = 47 and 2.43. For water, this was systematically observed on alkaline gas exchanged X zeolite. This is attributed to the formation of stabler (shorter) H-bonds with the framework which are favoured in the curvy topology of site III' much more than the relatively flat of site II, used for 47 and Y. NO_2 adsorption was also strongly enhanced in the cases of X zeolite. As cross-adsorption between site II and site III' is particularly strong for NO_2, it leads to higher binding energies than water as opposed to zeolite Y. This is exemplified by KX with a difference of 3.2 kJ/mol, RbX with a difference of 42.8 kJ/mol, and CsX with a difference of 9.4 kJ/mol, but not by Na^+ and Li^+, which consistently favour water over NO_2. Similarly, the interaction with NO was strongly enhanced on zeolite X due to cross-adsorption between site II and site III', as shown in Table 3.1, but overall, the simulated trends were similar to those observed for Y. In short, Cu(I) appeared once again to be selective towards NO_x as interaction energies with NO and NO_2 remained 35.5 kJ/mol and 117.7 kJ/mol higher than with water, respectively.

Adsorption configurations of gases adsorbed on X are shown in Figures 3.5a-f, for the representative cations Na (from the group of alkaline cations) and Cu(I) (from the monovalent transition metals). NO and NO_2, were both cross adsorbed by site II and site III' with similar interaction distances, above 2.4 Å (Figure 3.5a and c), while water formed a shorter interaction at 2.30 Å with the cation, and two H-bonds at 1.82 Å and 2.02 Å strongly stabilizing the complex (Figure 3.5e). As for Cu(I), NO was adsorbed on site III' with an interacting distance of 1.79 Å (Figure 3.5b), and NO_2 got cross adsorbed by site III' and site II with lengths of 1.88 and 1.86 Å respectively (Figure 3.5d). In this figure especially, Cu^+ migration was very clearly observed, by comparison with its position in Figure 3.5b and f. This is a known phenomenon that occurs in zeolites, to stabilize the complex.[132] Finally, water is adsorbed on Cu(I) with a length of 1.91 Å and a H-bond of 1.71 Å.

In summary, it appears that structures with Si/Al = 47 and 2.43 share common binding patterns. Their big difference regards Cu(I), which differently from 47, it behaves selectively towards NO_2, when incorporated in Y. This selectivity is driven by non-bonding interactions between the closest O atom of NO_2 to the 6MR, with the atoms of the 6MR. In regard to X zeolite, all interaction energies became much higher due to cross adsorption and the interaction of gases with site III' as expected.[139,149,150] While only selected adsorption configurations are shown here, the whole of the results are presented in supporting information, at Figures 3.SIII.

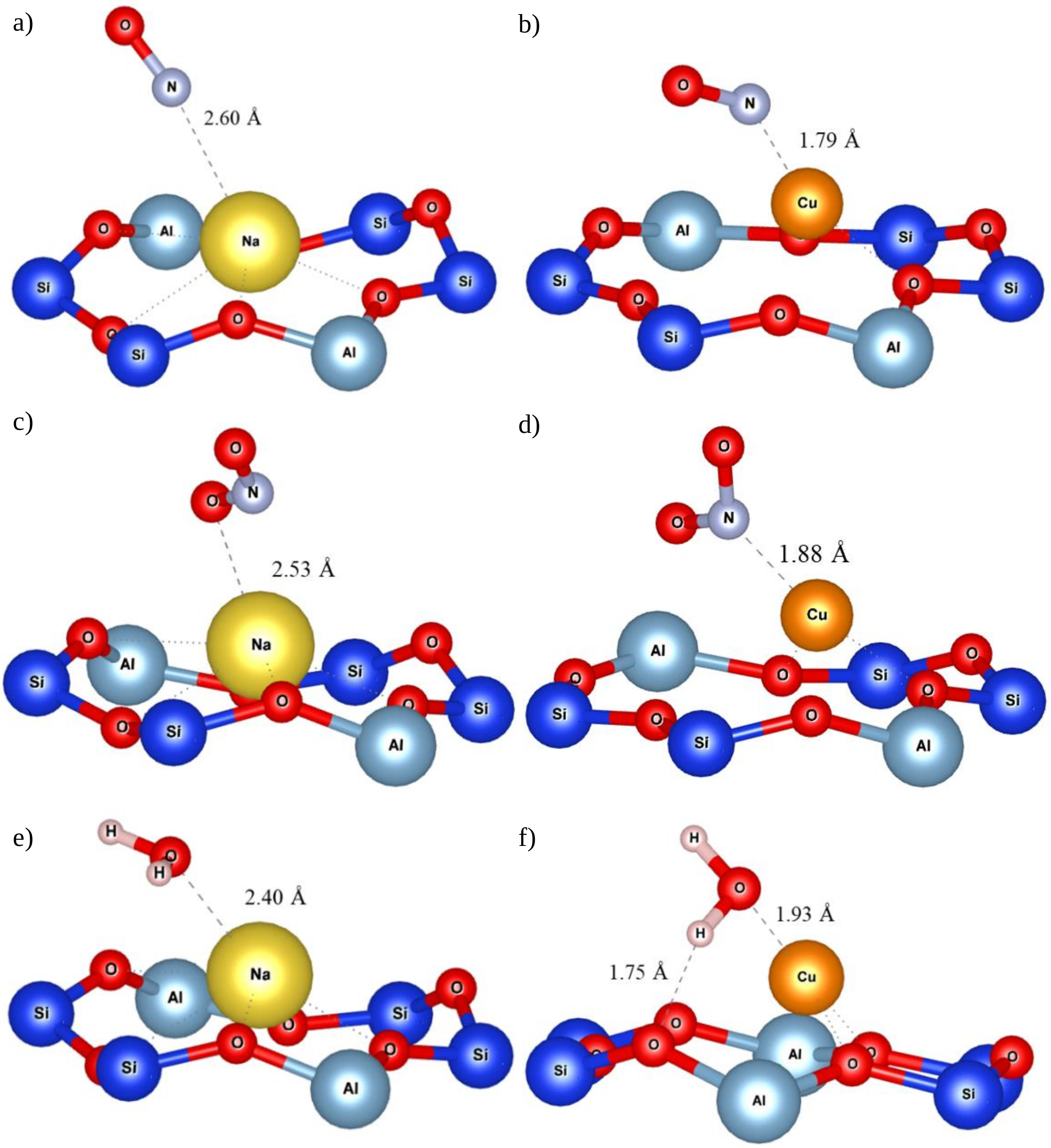

Figure 3.4: Na and Cu(I) embedded Y adsorption configurations of NO (a and b respectively), NO_2 (c and d respectively) and H_2O (e and f respectively). The cations are located on site II.

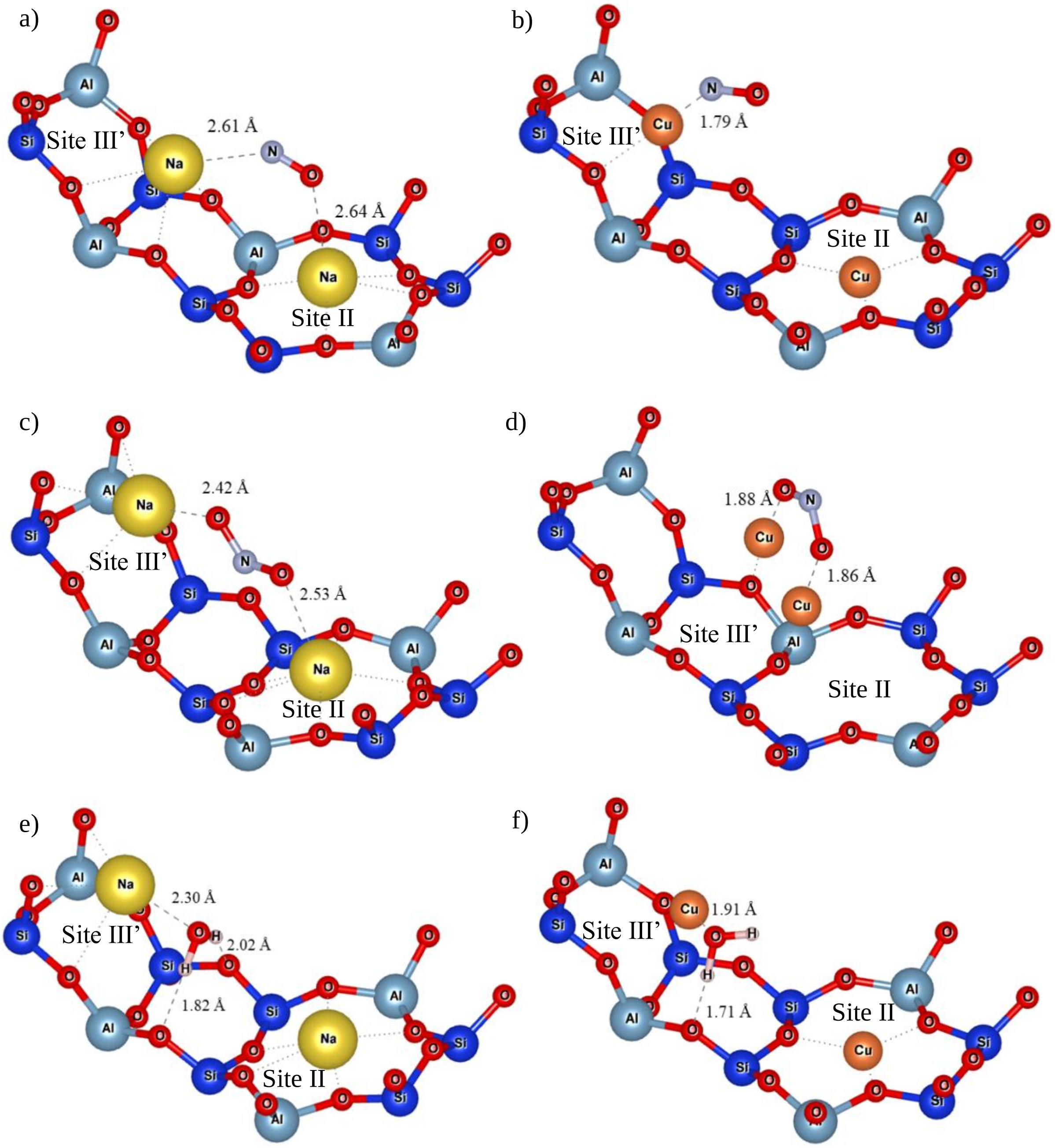

Figure 3.5: Na and Cu(I) embedded X adsorption configurations of NO (a and b respectively), NO_2 (c and d respectively) and H_2O (e and f respectively). Strong migration was observed in the case of adsorption of NO_2 on Cu(I)X, both for copper located on site II and site III'.

3.3.2 Adsorption screening for the divalent cations

Adsorption energies determined for NO, NO_2 and H_2O on divalent cation embedded cells are reported in Table 3.2 and illustrated in Figure 3.6.

Table 3.2: Adsorption energies of gases over divalent cation exchanged cells. Numbers marked in bold refer to cross adsorption. No calculations have been done for Ba, Zn, Pt and Pd, supported by X, as according to the literature, the cationic distribution was expected to give similar results to Y.

Si/Al ratio (zeolite)	Gases	Ca^{2+}	Ba^{2+}	Zn^{2+}	Pt^{2+}	Pd^{2+}	Cu^{2+}	Fe^{2+}	Co^{2+}	Ni^{2+}
23	NO	-41.7	-31.3	-49.4	-79.6	-108.6	-130.6	-207.0	-130.3	-82.3
	NO_2	-46.0	-31.7	-49.5	-24.2	-39.3	-39.1	-147.2	-68.7	-59.0
	H_2O	-108.9	-77.3	-111.0	-17.9	-28.4	-90.6	-114.4	-116.9	-120.5
2.43 (Y)	NO	-46.5	-40.1	-55.9	-114.4	-110.5	-103.8	-246.6	-185.5	-157.0
	NO_2	-60.9	-77.0	-64.6	-24.8	-49.4	-29.4	-192.4	-102.6	-72.5
	H_2O	-110.6	-119.1	-108.8	-31.5	-24.6	-77.0	-143.8	-131.9	-111.1
1.4 (X)	NO	-56.8					-147.6	-257.5	-215.9	-185.1
	NO_2	**-152.5**					-66.0	**-232.6**	-240.2	**-133.4**
	H_2O	-139.4					-134.4	-146.6	-157.5	-167.4

The results for the structures with Si/Al = 23 are depicted in Figure 3.6a. NO/NO_2 were more strongly adsorbed than H_2O on Pt and Pd by 61.7/80.2 and 6.3/10.9 kJ/mol, respectively. Moreover, NO and NO_2 were selectively adsorbed compared to H_2O on Fe, with interaction energy differences of 92.6 and 32.8 kJ/mol respectively. Alkaline earth cations (Ca, Ba) and Zn showed a stronger affinity for water than for NO_x. Although the remaining metals (Cu(II), Co(II) and Ni(II)) showed preference for NO, they displayed poor affinity for NO_2. Daouli et al[151] performed a cation screening for isolated cation-embedded faujasite using periodic PBE, U = 4.0 for Fe^{2+} and the Tkatchenko–Scheffler scheme with iterative Hirshfeld partitioning (TS/HI), for dispersion corrections. Their findings are similar to ours for Ca, Ba, Zn and Cu^{2+}, but they differ significantly for Pt and Pd. Differently from us, they predicted that Fe is not selective.

The results concerning Y zeolite, are depicted in the histogram of Figure 3.6b. The alkaline earths and Zn behaved hydrophilically, as observed previously on structures with Si/Al = 23. Interaction energies of NO and NO_2 on PdY exceeded that of water by 85.9 and 24.8 kJ/mol, respectively. Fe also appeared to be selective towards NO and NO_2, with binding energies exceeding that of water by 102.8 and 48.6 kJ/mol, respectively. Pt, Cu(II), CoY and NiY were poor candidates. Göltl and co-workers[57] have used a regression analysis model to determine the adsorption energies of NO and CO on different zeolite rings. Their results regarding 6MR (which we also used for Si/Al = 23 and 2.43 (Y)), with the same Al distribution as ours, for Cu^{2+}(-103.3 kJ/mol), Co^{2+} (-172.2 kJ/mol) and Ni^{2+} (-167.8 kJ/mol), were consistent with our results for Y. Conversely, their result for Fe^{2+} (-181.0 kJ/mol) was less negative than ours. This difference is attributed to the zeolite they use (SSZ-13), which imposes a different coordination to the cations.

Adsorption configurations of Ca (representing alkaline earth metals) and Fe (representing divalent transition metals) on Y are presented in Figures 3.7a-f, while all the rest are provided in the ESI (Figure 3.SII). NO and NO_2 were bound to CaY with distances of 2.59 Å and 2.35 Å (Figure 7a and c), water staying at a distance of 2.37 Å (Figure 3.7e). NO and NO_2 were adsorbed at approximately the same distance from Fe, at 1.67 and 1.68 Å respectively (Figure 3.7b and d), much closer than water which stayed 1.98 Å away from Fe. These results are in line with the interaction energies which indicated a higher affinity of Fe for NO_x than for water. It is noticeable that H_2O did not form any H-bonds when adsorbed on divalent cations (unlike with monovalent cation-exchanged Y).

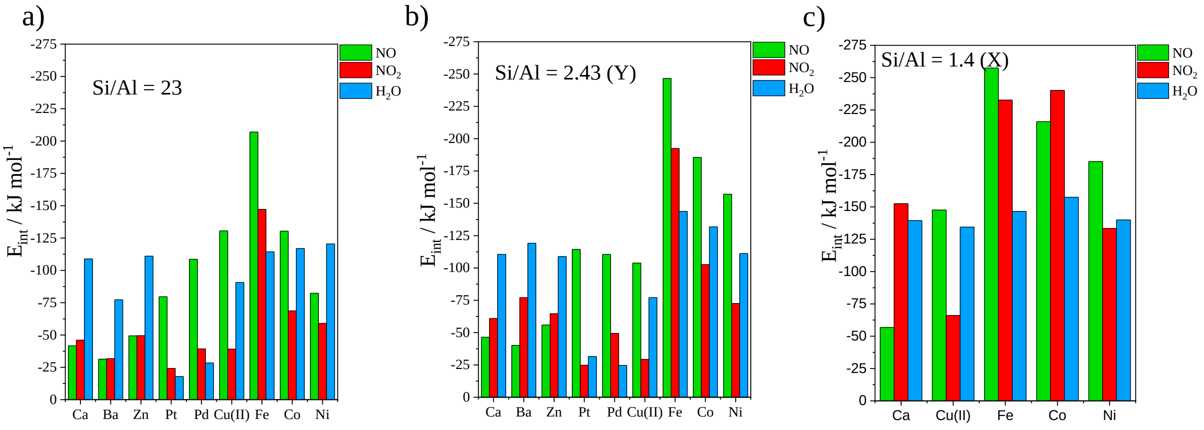

Figure 3.6: Interaction energies computed at the PBE+D2 level of theory for NO, NO_2, and H_2O adsorption on a) isolated divalent cation embedded faujasite (Si/Al = 23), b) Y zeolite (Si/Al = 2.43) and c) X zeolite (Si/Al = 1.4).

Regarding X zeolite, adsorption energy values were overall higher than for Y and 23 (Figure 3.6c). CaX showed similar affinities for NO_2 and H_2O, which are higher than for NO. PtX and PdX are exceptionally selective, interacting more strongly with NO/NO_2 than H_2O by 147.0/99.6 kJ/mol and 113.4/51.9 kJ/mol, respectively. Furthermore, Fe^{2+} and Co^{2+} appeared to be selective for both nitrogen oxides, yielding differences between NO/NO_2 and H_2O, equal to 110.9/86.0 kJ/mol, and 58.4/86.0kJ/mol respectively. Finally, Cu^{2+} and Ni^{2+}, were found to be selective for NO but not for NO_2.

Adsorption configurations of gases on DX are given in Figures 3.8a-f and Figure 3.SIV. NO is adsorbed on Ca of site III' with an interacting distance of 2.48 Å (Figure 3.8a), quite shorter than the value calculated for site II (2.59 Å). NO_2 showed a different behaviour being cross-adsorbed, at equal distances from the Ca atoms (~2.4 Å) of site II and site III' (Figure 3.8c). Water remained 2.28 Å away from Ca, forming two H-bonds with lengths 1.70 and 1.80 Å with the framework (Figure 3.8e). The formation of 2 H-bonds tightened the adsorption of water on site III', as we observe in Figure 3.6c. Considering Fe, NO formed a tight connection of length 1.65 Å with the cation on site III' (Figure 3.8b). NO_2 was adsorbed by iron on site III' through both its N and O atoms with distances of 1.93 and 1.84 Å respectively, bringing also its second oxygen at 2.71 Å from Na on site II (Figure 3.8d). Water was linked with Fe, with a separating distance of 1.95 Å (Figure 3.8f) – far longer than NO_x, which is in accordance with its smaller binding energy. However, the interaction of water with the framework was further enhanced through one H-bond of 1.59 Å.

Overall, the cation distribution significantly affected the separation capability of the faujasites. Although the adsorption took place on site II both for Si/Al = 23 and Y structures, their interaction energies were often dissimilar. In contrast, adsorption energies on monovalent cation-embedded 47 and Y were similar. X zeolite interactions were much stronger than Y and 23, as we should expect, based on the less stable attach of the cations to the 4MR. The possibility of cross-adsorption with increased NO_2 loading is studied in the last part of the ESI. Calculations were carried out for CaX, NiX and FeX, and they show that cross-adsorption is not prevented by the presence of a second NO_2 in the vicinity of the cross-adsorbed one. On the contrary it is adsorbed as well.

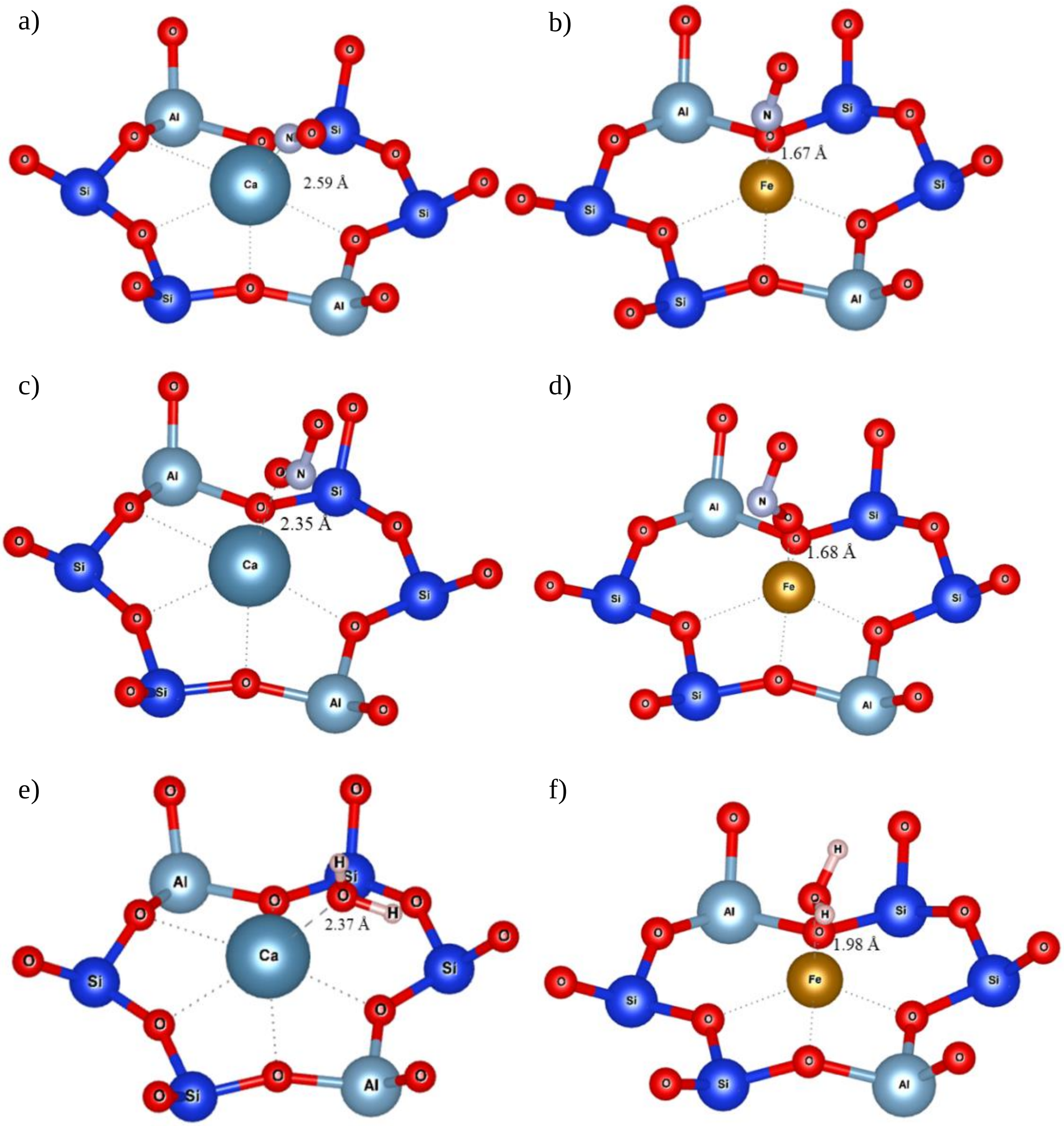

Figure 3.7: Ca and Fe embedded Y adsorption configurations of NO (a and b respectively), NO_2 (c and d respectively) and H_2O (e and f respectively). The cations are located on site II.

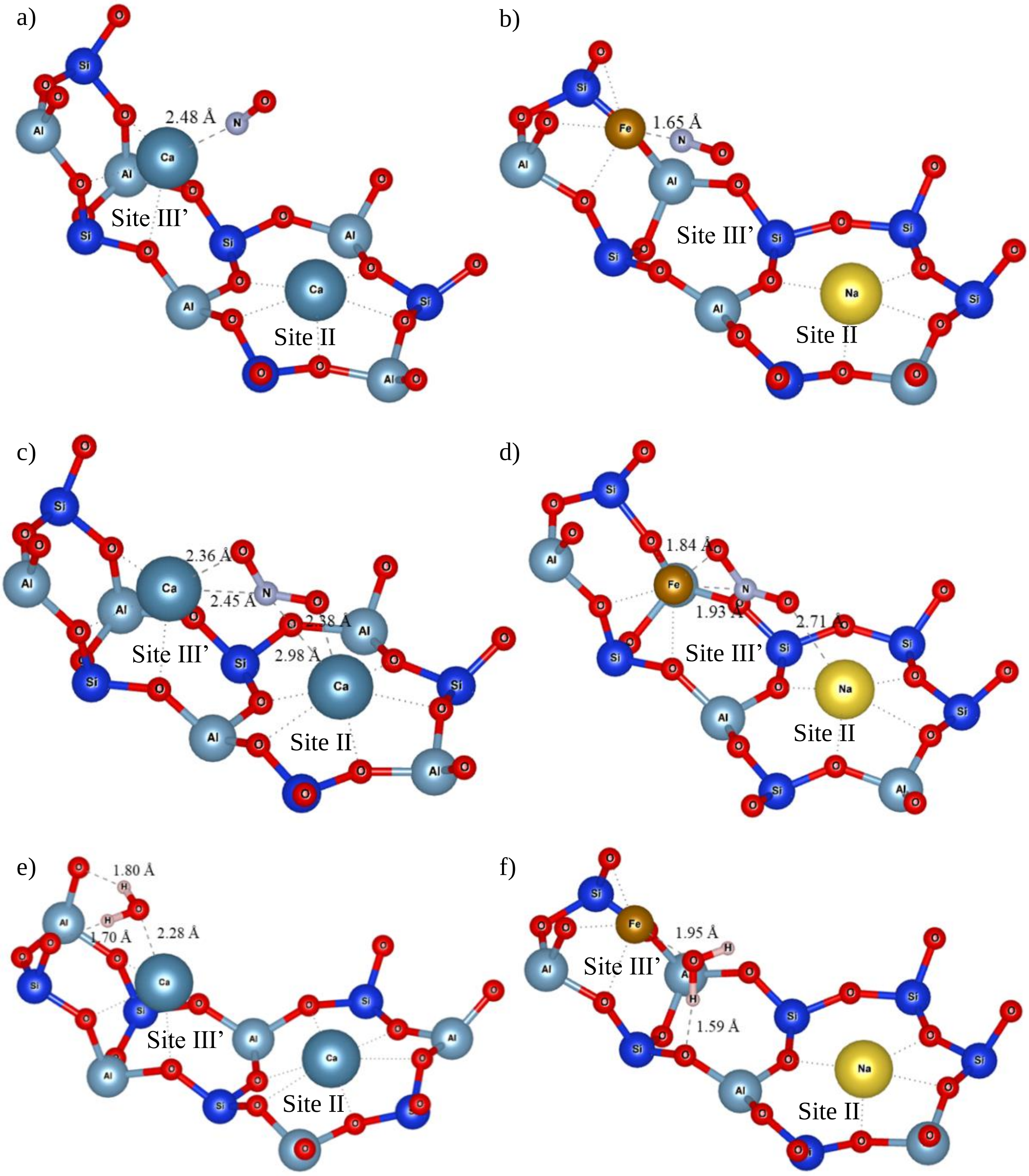

Figure 3.8: Ca and Fe embedded X adsorption configurations of NO (a and b respectively), NO$_2$ (c and d respectively) and H$_2$O (e and f respectively). Cross adsorptions were observed in both cases for NO$_2$.

3.4 Discussion

All the adsorption data computed for Y and X are gathered in Figure 3.9 for the identification of the best structures according to their thermodynamic selectivity for NO_x over water. Figure 3.9's upper right square i.e., with x and y values > 0 contains the selective materials, namely materials where both the interaction energies of NO and NO_2 are in absolute value higher than that of water. According to this graph, the selective materials are Cu(I)Y, PdY, FeY, Cu(I)X, PtX, PdX, FeX and CoX.

3.4.1 Identification of the best selective materials

The next step was to determine the best cation/zeolite pair. As observed by comparing Figures 3.3, and 3.6, adsorption energies were almost always higher for X than for Y zeolites. Consequently, the regeneration criterion favours Y. Moreover, X is known to be much more hydrophilic[152] than Y, which makes it less stable in the presence of high levels of water.[153] Therefore, Y zeolite is the preferred candidate between the two zeolites.

The best compensating metals for Y were Cu(I), Pd and Fe(II). Palladium presents high selectivity, but its high cost and low availability calls for alternative options. On the other hand, both Cu(I) and Fe(II) showed great selectivity (especially iron) and are both cheap and abundant. Consequently, Cu^+ and Fe^{2+} embedded on Y are the most suitable cations for our application. In order to cross-evaluate results obtained with the D2 level of theory, the adsorption energies of FeY with NO, NO_2, and H_2O were re-calculated using the MBD level of theory for dispersion interactions. The resulting adsorption energies were, -210.5, -157.1 and -104.2 kJ/mol, for NO, NO_2 and H_2O, respectively, in agreement with the order of D2.

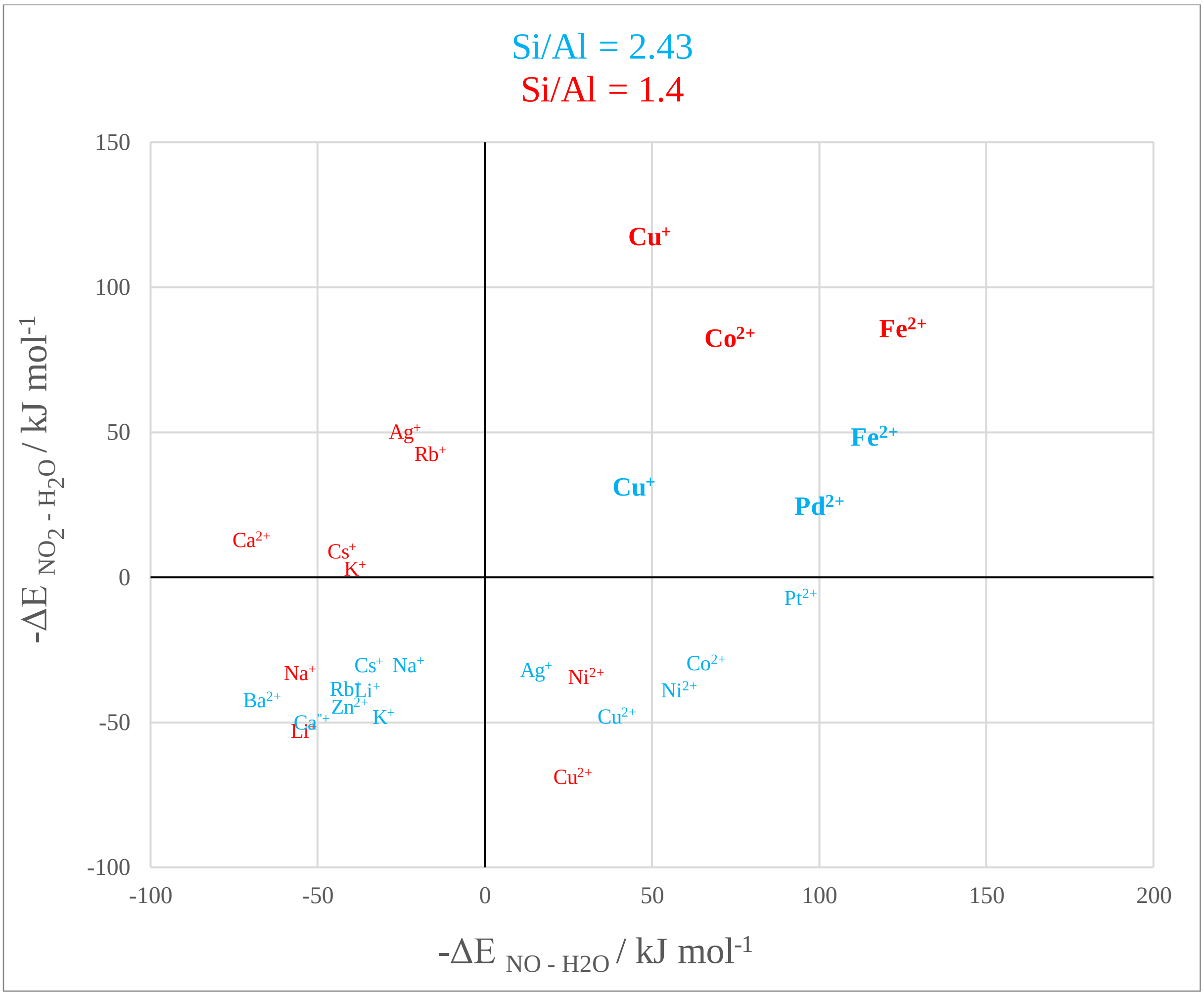

Figure 3.9: This map contains all the results of adsorptions on Y (blue colour) and X (red colour). The axes represent the subtractions of the interaction energies between H_2O and NO (x) and H_2O and NO_2 (y). The up and right corner contains the selective cations.

3.4.2 Bond and regeneration analysis and formation of by-products assessment for Cu(I) and Fe(II)

It is imperative for the application that the material is able to regenerate after the operational hours. Thus, it is important to know if during the adsorption the gases have their intramolecular bonds stretched. We use the term *bond activation* to call the extensive bond stretching. We interpret bond stretching as a tendency of the gas adsorbed, to further react leading to the formation of by-products. It is possible that these by-products will hinder the regeneration of the material rendering it practically useless after its operational hours. The bond stretching can be measured by a subtraction of the intramolecular bond lengths of the gases before and after the adsorption. This analysis is carried out only for the most prominent structures Cu(I)Y and

FeY and the results are presented in Table 3.3. Moreover, Bader charge transfers (Table 3.4) and charge density differences (Figure 3.10), that occurred due to the adsorption, were calculated to rationalize the bond elongations. The aforementioned calculations have also been performed for Pd, Pt, Co and Ni promoted Y, during the treatment of NO_2, only, and they are provided in the supporting information (Tables 3.SIV & 3.SVI, Figure 3.SXI) for comparison.

Table 3.3: The initial intramolecular bond lengths of NO, NO_2 and H_2O are given along with the induced changes due to adsorption on Cu(I)Y and FeY (Si/Al = 2.43) in Å. The values in brackets correspond to the stretching with respect to the initial bond length in percentages.

Gas species concerned	NO	NO_2		H_2O	
Bond	N-O	O1-NO	O2-NO	H1-OH	H2-OH
Initial length (Å)	1.17	1.23	1.23	0.97	0.97
Cu(I)Y (Å)	0.02 (2%)	0.08 (7%)	0.02 (2%)	0.03 (3%)	0.00 (0%)
FeY (Å)	0.00 (0%)	0.31 (26%)	-0.04 (-3%)	0.00 (0%)	0.01 (1%)

Table 3.4: Bader charge differences due to adsorptions of the gases H_2O, NO and NO_2 calculated for the systems Cu(I)Y and FeY.

Complex	Atom	Charge Difference
Cu-NO	O	0.042
	N	-0.254
	Cu(I)	0.144
$Cu – N – O_2$	O1	-0.156
	O2	-0.134
	N	-0.204
	Cu(I)	0.102
Cu-H_2O	O1	-0.006
	H1	0.053
	H2	0.037
	Cu(I)	-0.016
Fe-NO	O	0.092

	N	-0.169
	Fe	0.072
Fe – O1 – N | O2	O1	-0.370
	O2	-0.021
	N	0.040
	Fe	0.233
Fe-H_2O	O	-0.004
	H1	0.083
	H2	0.049
	Fe	0.065

3.4.2.1 {Cu(I), Fe} Y– N – O

In the case of NO, only minor bond changes are computed. Accounting for Cu(I), N – O bond is slightly stretched by 0.02 Å (2%) (Table 3.3) by comparison with the initial bond, followed by a Bader charge transfer of -0.254 e to N, a shortage of 0.042 e on O and of 0.144 e on Cu (Table 3.4). The angle Cu – N – O is computed at 140°.

Nitrosyl ligands of transition metals are known to be bent.[154] As the angle becomes more bent, nitrosyls are expected to behave as NO^-. They donate electron charge through σ-donation and accept it back through π-backdonation, the latter being more prominent. To accept electrons, monovalent copper will have to make a *sd* hybridization. Then they are returned to NO due to π-backdonation. Figure 3.10a depicts clearly the rehybridization of Cu orbitals based on a charge density difference before and after adsorption. Upon accepting charge according to Bader population analysis, NO fills its antibonding $\pi_{2p}{}^*$ orbital thus reducing the N – O bond order. The breaking of symmetry of NO's $\pi^*_{2p_x}$ and $\pi^*_{2p_y}$ is followed by a charge accumulation perpendicular to the plane Cu – N – O. The orbitals created have a contribution from the *sd* hybrids of Cu and the antibonding π of NO leading to a π-backdonation.

We treat the adsorption on Fe in a similar manner. No bond elongation is found in this case (Table 3.3). Bader charges of 0.092, -0.169 and 0.072 e were distributed on Fe, N and O respectively (Table 3.4). The charge flow towards NO is now approximately 1/3 of that calculated for Cu(I). A Fe – N – O angle of 166° is predicted.

It is notable that, in agreement with the literature, the smaller charge transfer to NO from Fe than from Cu(I), is accompanied with a smaller deviation of the M – N – O angle from linearity. We observe clearly from the charge density difference (figure 3.10b) the depopulation of the orbital between N and O, due to σ-donation. We can also observe the rehybridization of the iron's orbitals with a strong $3d_{z^2}$ character, for the formation of a charge accumulation between N and Fe. The π-backdonation balances almost perfectly the donation to Fe leaving N with a small charge.

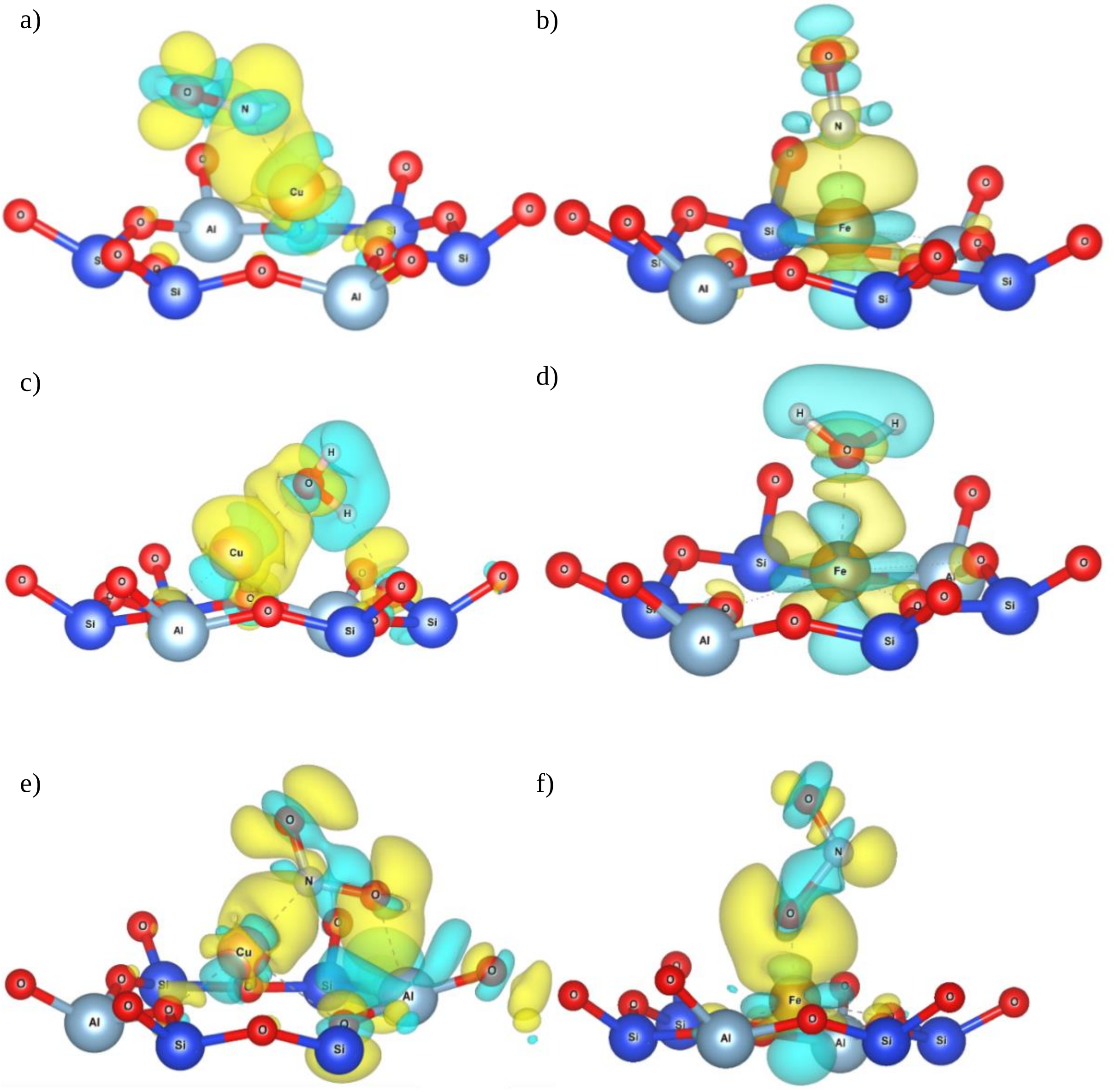

Figure 3.10: Charge density differences that occurred during the adsorption of NO on a) Cu(I)Y and b) FeY, of H_2O on c) Cu(I)Y and d) FeY and of NO_2 on e) Cu(I)Y and f) FeY. The isosurfaces have a density 0.002 e/a_0^3.

3.4.2.2 {Cu(I), Fe} Y– O – H_2

Moving to H_2O, we once again predict insignificant bond activation. When adsorbed on Cu(I) the bond changes of 0.03 (3%) and 0.00 Å (0%) were computed (table 3.3). Slight Bader charge transfers of -0.006 e to O and -0.016 e to Cu(I) and deficits of 0.053 and 0.037 e were attributed to the H atoms (table 3.4). This discrepancy between the H atoms can be straightforwardly attributed to a formation of a H-bond for one of them as indicated by the configuration in figure 3.10c.

Strong polarization of the charge density of water is predicted, towards O, increasing its already strong dipole moment. This leads to strong induction and electrostatic forces connecting it to Cu. Adding up the Bader charges of water though, we see that there is charge transfer from it to the material and more specifically to Cu(I). The presence of the positive Cu(I) and the H-bond formed, further pushes electron charge towards water's O. The charge difference figure 3.10c highlights excellently all the aspects discussed and reveals a charge accumulation between O and Cu. The latter will have to undergo a *sd* hybridization to accept this charge as its 3d orbitals are full. This is clearly shown as a yellow shell around Cu in figure 3.10c.

As for Fe, a similar approach could be taken. Negligible bond stretching was computed equal to 0.00 (0%) and 0.01 Å (1%) (table 3.3) for the two O – H bonds. Bader charge transfer of -0.004 e was attributed to O and 0.083, 0.049 and 0.065 e moved from H1, H2 and Fe respectively (table 3.4). This charge difference between the H atoms is well illustrated in the charge density difference in figure 3.10d.

The same reasoning as for Cu can be adopted here too. Iron favours the perpendicular adsorption and water is unable to form H-bonds. The nucleophilic attack of O on Fe should be more plausible now as Fe has available d orbitals to accept a σ-donation. On the other hand, the charge transfer is mitigated due to oxygen's strong electronegativity. The charge-dipole interaction is now stronger than before. Figure 3.10d reveals a charge redistribution of iron's orbitals during the adsorption, like the one we observed for NO. Charge density is pushed from H atoms towards O to feed the bond with Fe.

3.4.2.3 NO_2

A special treatment was made for NO_2. Differently from the other two gasses, NO_2 does not adsorb always through a particular atom. Moreover, the interaction energies are sometimes close between adsorption through N and O.

To provide a more complete bond stretching analysis, we study how the bonds of NO_2 evolve in different potential wells with particularly prominent depth. For this reason, we consider the adsorption when NO_2 adsorbs: 1) through N while O atoms remain away (M – N – O2), 2) through O1 while N and O2 are ordered parallelly to the 6MR (M – O1 – N – O2) and 3) through O1 while N and O2 are ordered perpendicularly to the 6MR (M – O1 – N | O2). We provide bond length elongations, Bader charge transfers and charge density differences in tables SIV, SVI and Figure SXI respectively, for all these adsorption modes but we comment in the text only the data associated to the stablest configurations.

3.4.2.3.1 Cu(I)Y– N – O_2

Upon adsorption on Cu(I) through N, NO_2 shows low bond activation. Elongations of 0.08 (7%) and 0.02 (2%) Å are computed for the N – O bonds of NO_2 (table 3.3). These findings are supported by Bader charge transfers of -0.156 and -0.134 e on O1 and O2 respectively (table 3.4). In addition, N received -0.204 and Cu 0.102 e. The difference between the O atoms is evident from the adsorption mode as one O approaches one Al atom of the ring. The interaction energy calculated for this adsorption mode was equal to -122.7 kJ/mol.

As shown from figure 3.10e, charge flows towards NO_2. It also highlights how polarization induced from the presence of the O of NO_2, upon the charge of O and Al of the 6MR, forces them to rehybridize their orbitals resulting in some non-bonding attraction. This induction will motivate a secondary flow of charge towards the O of NO_2 that remains close to the 6MR, disclosing the difference mentioned above. This physical interaction between O and the atoms of the 6MR, further stabilizes the adsorption. A *sd* hybridization will enable Cu to accept charge from the antibonding LUMO of NO_2 due to the favourable arrangement of the complex, but π-backdonation dominates. This is proven by the bond elongations and the Bader charge transfers which imply the increased occupation of the antibonding LUMO of NO_2.

3.4.2.3.2 FeY– O1 – N | O2

Next, we move to the perpendicular adsorption on Fe (Fe – O1 – N | O2). We found very similar bonding characteristics to the parallel mode. Exactly the same elongations are predicted as before namely, 0.31 (26%) and -0.04 (-3%) Å (table 3.3). The Bader charge transfers are -0.370 and -0.021 e to the O atoms, 0.040 e to N and 0.233 e to Fe (table 3.4). The interaction energy calculated at -192.4 kJ/mol, is only 0.1 kJ/mol larger than the parallel.

Table SVI reveals strong charge transfer only in the cases of Cu(I), Co and Fe. The big difference between Cu(I) and the other two cations is its filled *d* subshell. Therefore, σ-donation, which destabilizes the gas, is seriously obstructed for Cu(I). The charge transfer from Cu(I) to NO_2 results to be high because there is no competition between π-backdonation and σ-donation. On the other hand, Co and Fe have unfilled *d* orbitals, and are prone to both electron donation phenomena. We can realize the σ-donation for Fe and Co, in Figure 3.SXI, from the charge deficit between N and O. This charge deficit is not observed in the case of Cu(I) according to same figures.

To conclude, we believe that, differently from FeY, adsorption on Cu(I)Y should not impose any troubling bond activation to any of the gases. NO and H_2O remained inactive at all instances. The intramolecular bonds of NO_2 were slightly extended upon adsorption on Cu(I) reaching an extension of 7%. In the case of Fe, the two adsorption modes through O were equivalent, both accounting for the interaction energy, but also the bond O1 – N elongation of 26%.

The alarming stretching of NO_2 during adsorption on FeY, regarding the most prominent configurations suggests that the formation of by-products is possible. Despite this downside, Fe^{2+} showed notable selectivity and its implementation as an extraframework cation by a different zeolite could lead to smaller interaction energies and bond activations. To better understand the regeneration potential of a zeolite, future studies should be focused on the forces that determine the balance between σ-donation and π-backdonation. We showed that when both happen at the same time, the regenerability of the material is put in jeopardy.

3.5 Conclusions

The goal of this study was to screen the adsorption capability of NO_x in the presence of H_2O on a series of FAU with different cations and Si/Al ratios using periodic PBE+D2. The purpose was to identify a zeolite which can be applied in vehicles working in closed-spaced environments, trap exhaust gas NO_x in ambient temperatures and release them at higher ones. High temperatures will enable catalysts to operate efficiently and transform NO_x into harmless N_2, protecting the health of workers that are exposed to the air pollutants. Furthermore, this material has to be regenerable, so that it can be used several times. Pt/Pd promoted zeolites have been successfully implemented in the past, but due to their high cost, we search for alternatives. For this investigation, faujasites promoted by the monovalent cations Li, Na, K, Rb, Cs, Cu and Ag and the divalent Ca, Ba, Zn, Cu, Pt, Pd, Fe, Co, and Ni were tested. Based primarily on the thermodynamic selectivity and secondarily on the availability and price of the materials FeY and Cu(I)Y were identified as the best candidates for this application. These two formulations have further been explored using Bader charge analysis and charge density differences to shed light on charge transfer and bond stretching upon adsorption. Quite a significant change for the N – O1 bond of NO_2 was measured while adsorbed on Fe(II)Y (26%), suggesting that it is possibly prone to further chemical reactions.

This is the first screening of such a significant size regarding the selective trapping of NO_x against water. The only structure that made it through the screening of selectivity and regenerability was Cu(I)Y. Nonetheless, Fe(II) showed excellent selectivity, and due to its low price and high availability, its implementation as an extraframework cation should by tested by other zeolites too. To better understand the regeneration potential of a zeolite, future studies should be focused on the forces that determine the balance between σ-donation and π-backdonation. We showed that when both happen at the same time, the regenerability of the material is put in jeopardy.

Acknowledgements

This work was granted access to the HPC resources of TGCC under the allocation 2022-A0120810433 made by GENCI. This work is partially funded by the French National Research Agency NOA Project (ANR-20-CE08-0024).

3.6 A systematic DFT screening of cationic faujasite-type zeolites for the adsorption of NO, NO_2 and H_2O

Electronic Supplementary Information

Table 3.SI: Parameters of the cells used. The matrix of the cell parameters is 3X3 as seen below.

Cell	axis	X	Y	Z
LiY	X	17.48279984	0.028468534	-0.010319501
	Y	8.840644478	15.10530102	0.001263263
	Z	8.953000395	5.186455266	14.30151694

NaY	X	17.83194901	-1.22E-04	-0.028527718
	Y	8.891369642	15.20535001	-0.012376228
	Z	9.008870912	5.331352808	14.47801799
KY	X	17.88242991	0.013399027	-0.022310091
	Y	8.969844509	15.21942585	-0.006752499
	Z	9.046752553	5.32724579	14.54203205
RbY	X	17.8220724	0.017842701	-0.028852805
	Y	8.872341967	15.25630517	-0.016960456
	Z	9.019747107	5.323323404	14.46825396
CsY	X	17.79319373	0.026282437	-0.030084551
	Y	8.847363736	15.23561722	-0.016684936
	Z	9.012119865	5.319173337	14.44479319
CuIY	X	17.69461509	0.005533381	-0.015061614
	Y	8.906587859	15.17316108	-0.00268668
	Z	8.949985666	5.22394246	14.37118436
AgY	X	17.82524546	0.023009813	-0.028088024
	Y	8.880991429	15.32137819	0.005711805
	Z	8.958022677	5.31230187	14.54800329
CaY	X	17.56170831	0.131723813	0.103303089
	Y	8.878751494	15.34634733	0.003723999
	Z	8.891002006	5.141876132	14.47215009
BaY	X	17.65739619	0.197592615	0.157008324
	Y	8.983397819	15.558916	0.022902052
	Z	9.001210744	5.22787995	14.55107451
ZnY	X	17.4541068	0.122307802	0.222089139
	Y	8.815425302	15.13138704	0.158866791
	Z	8.931016264	5.157649615	14.44206101
CuIIY	X	17.30853447	0.144358639	0.312544215
	Y	8.760911454	15.11543416	0.166930556
	Z	8.936631394	5.120753288	14.46748513
PdY	X	17.62329264	0.230506831	0.10947841
	Y	8.994678643	15.35556634	0.049814261
	Z	8.954558123	5.218480772	14.53710812
PtY	X	17.53141983	0.291843634	0.070306227
	Y	8.999833178	15.40006848	0.01764803
	Z	8.893854019	5.24300261	14.48522903

FeY	X	17.50640945	0.390115192	0.205316363
	Y	9.073682875	15.44158663	0.063068069
	Z	9.021402311	5.267918167	14.34289535
CoY	X	17.58637875	0.294444132	0.14215959
	Y	9.032084866	15.29525744	0.106447387
	Z	8.981756115	5.257715159	14.41576421
NiY	X	17.3893343	0.293164911	0.141810096
	Y	8.933382807	15.18903178	0.151598882
	Z	8.882548702	5.264660529	14.55657155
LiX	X	17.20779103	-0.099117749	-0.033554342
	Y	8.338860954	15.21910813	-0.067090683
	Z	8.313796344	4.775980281	14.42869594
NaX	X	17.50382636	-0.131349582	0.0169997
	Y	8.455522484	15.37393218	0.051261406
	Z	8.490991148	4.903275144	14.71353001
KX	X	17.86417227	0.102227913	0.085683286
	Y	8.836784935	15.54315865	0.17768206
	Z	8.789938477	5.123316737	14.81413347
RbX	X	17.76150318	-0.067543852	0.020097229
	Y	8.842103836	15.48536092	-0.102119503
	Z	8.868095283	5.141645087	14.61398294
CsX	X	17.50088428	0.345714795	0.220266252
	Y	8.082573939	15.56428608	0.212631853
	Z	8.054974766	4.932908444	14.77715554
CuIX	X	17.62051503	-0.010132539	0.114160925
	Y	8.617120596	15.29570477	0.107523483
	Z	8.662434278	4.927601359	14.64341397
AgX	X	17.81225847	0.054675081	0.009557503
	Y	8.758736933	15.47997897	0.009327313
	Z	8.789320613	5.027229698	14.70153928
CaX	X	17.61194975	0.263403809	0.371209908
	Y	8.624573607	15.46104291	0.20133009
	Z	8.909050686	5.125985862	14.85135332
CuIIX	X	17.67742153	0.177255785	0.353225077
	Y	8.579003098	15.52226593	0.264419036
	Z	8.899130319	5.185531733	14.38814033

PdX	X	17.83957706	0.249977681	0.180537079
	Y	8.719619091	15.56567803	0.032198283
	Z	8.853928903	5.080695317	14.48579026
PtX	X	17.825907	0.184276319	0.170238245
	Y	8.656290352	15.45583077	0.082535494
	Z	8.820879476	5.076330333	14.51127437
FeX	X	17.78957072	0.185862305	0.002613992
	Y	8.639262577	15.43725461	0.030610093
	Z	8.661412834	5.097080758	14.42098654
CoX	X	17.57506741	0.280839684	0.089658921
	Y	8.621063543	15.4326837	0.017277895
	Z	8.65751587	5.074782613	14.30456417
NiX	X	17.72344761	0.234706778	-0.236718482
	Y	8.651499869	15.66373621	-0.104939962
	Z	8.442070368	5.164781487	14.17715624

Table 3.SII: Stretching induced to the intramolecular bonds of the gases during the adsorptions over the different Y and X cation-exchanged faujasites.

Gas species concerned	NO	NO_2		H_2O	
Bond	N-O	O1-NO	O2-NO	H1-OH	H2-OH
Initial length (Å)	1.17	1.21	1.21	0.97	0.97
LiY	0.00	-0.01	0.01	0.00	0.01
NaY	0.00	0.02	-0.01	0.01	0.00
KY	0.00	0.01	0.01	0.02	0.00
RbY	0.00	0.01	0.01	0.01	0.01
CsY	0.00	0.01	0.01	0.01	0.01
Cu(I)Y	**0.02 (2%)**	**0.08 (7%)**	**0.02 (2%)**	**0.03 (3%)**	**0.00 (0%)**
AgY	0.00	0.01	0.01	0.00	0.02
CaY	-0.01	0.05	0.00	0.00	0.01
BaY	0.00	0.02	0.03	0.02	0.02
ZnY	0.00	0.06	0.00	0.01	0.00
Cu(II)Y	-0.02	0.02	-0.01	0.01	0.03

PdY	-0.01	0.00	0.00	0.01	0.01
PtY	0.00	0.00	0.01	0.01	0.01
FeY	**0.00 (0%)**	**-0.04 (3%)**	**0.31 (26%)**	**0.00 (0%)**	**0.01 (1%)**
CoY	-0.01	-0.05	0.35	0.02	0.01
NiY	-0.01	0.03	-0.01	0.01	0.01
LiX	-0.01	0.02	0.02	0.02	0.01
NaX	0.00	0.03	0.02	0.01	0.03
KX	0.02	0.04	0.05	0.02	0.02
RbX	0.03	0.04	0.06	0.02	0.03
CsX	0.02	0.04	0.05	0.04	0.01
Cu(I)X	0.02	0.07	0.07	0.04	0.00
AgX	0.01	0.05	0.07	0.03	0.01
CaX	0.00	0.05	0.06	0.04	0.03
CuII(X)	-0.01	0.04	0.00	0.01	0.07
PdX	0.00	0.01	0.03	0.03	0.01
PtX	0.00	0.03	0.03	0.03	0.04
FeX	0.01	0.14	0.01	0.06	0.00
CoX	-0.01	0.07	0.07	0.02	0.04
NiX	-0.01	0.09	0.05	0.01	0.05

Table 3.SIII: Intramolecular bonds of the gases during the adsorptions over the different Y and X cation-exchanged faujasites.

Gas species concerned	NO	NO2		H2O	
Bond	N-O	O1-NO	O2-NO	H1-OH	H2-OH
Initial length (Å)	1.17	1.21	1.21	0.97	0.97
LiY	1.17	1.20	1.22	0.97	0.98
NaY	1.17	1.23	1.20	0.98	0.97
KY	1.17	1.22	1.22	0.99	0.97
RbY	1.17	1.22	1.22	0.98	0.98
CsY	1.17	1.22	1.22	0.98	0.98
Cu(I)Y	**1.19**	**1.29**	**1.23**	**1.00**	**0.97**
AgY	1.17	1.22	1.22	0.97	0.99
CaY	1.16	1.26	1.21	0.97	0.98
BaY	1.17	1.23	1.24	0.99	0.99
ZnY	1.17	1.27	1.21	0.98	0.97
Cu(II)Y	1.15	1.23	1.20	0.98	1.00
PdY	1.16	1.21	1.21	0.98	0.98
PtY	1.17	1.21	1.22	0.98	0.98
FeY	**1.17**	**1.17**	**1.52**	**0.97**	**0.98**
CoY	1.16	1.16	1.56	0.99	0.98
NiY	1.16	1.24	1.20	0.98	0.98
LiX	1.16	1.23	1.23	0.99	0.98
NaX	1.17	1.24	1.23	0.98	1.00
KX	1.19	1.25	1.26	0.99	0.99
RbX	1.20	1.25	1.27	0.99	1.00
CsX	1.19	1.25	1.26	1.01	0.98
Cu(I)X	1.19	1.28	1.28	1.01	0.97
AgX	1.18	1.26	1.28	1.00	0.98
CaX	1.17	1.26	1.27	1.01	1.00
CuII(X)	1.16	1.25	1.21	0.98	1.04
PdX	1.17	1.22	1.24	1.00	0.98

PtX	1.17	1.24	1.24	1.00	1.01
FeX	1.18	1.35	1.22	1.03	0.97
CoX	1.16	1.28	1.28	0.99	1.01
NiX	1.16	1.30	1.26	0.98	1.02

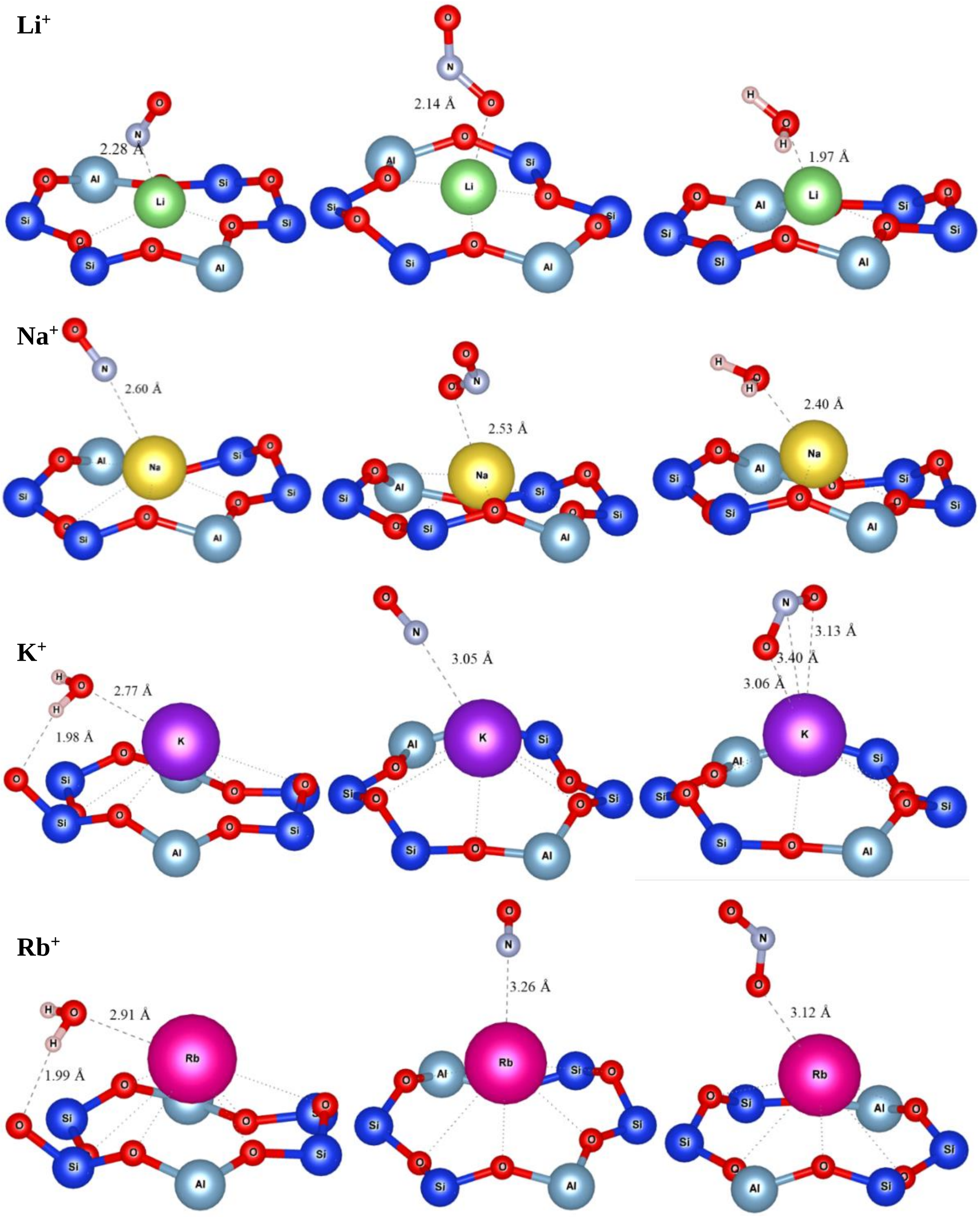
Li+
2.28 Å
2.14 Å
1.97 Å
Na+
2.60 Å
2.53 Å
2.40 Å
K+
2.77 Å
1.98 Å
3.05 Å
3.13 Å
3.40 Å
3.06 Å
Rb+
2.91 Å
1.99 Å
3.26 Å
3.12 Å

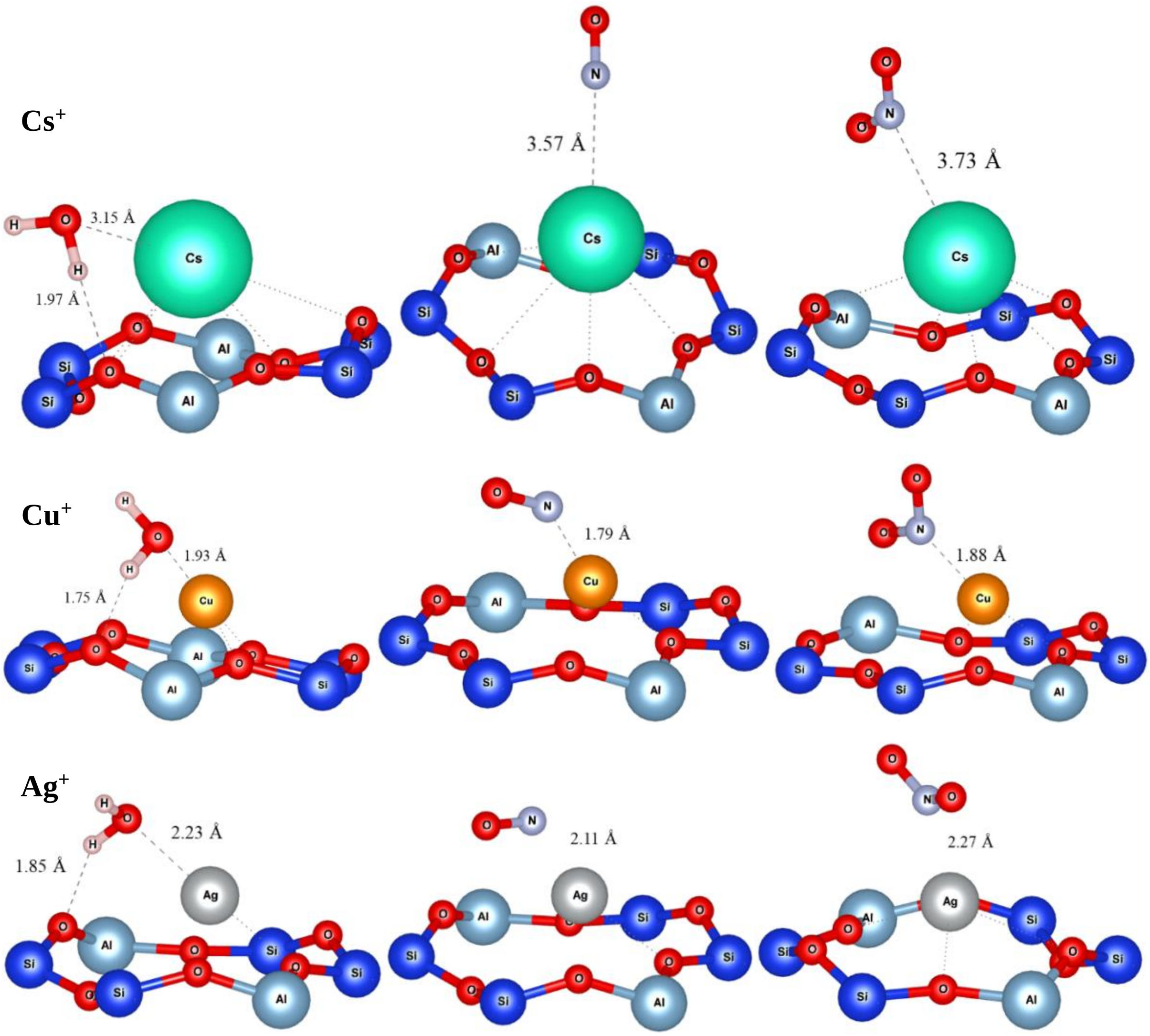

Figure 3.SI: Adsorption modes of the gases (H_2O: left, NO: middle, and NO_2: right) over the different Y monovalent cation-exchanged faujasites.

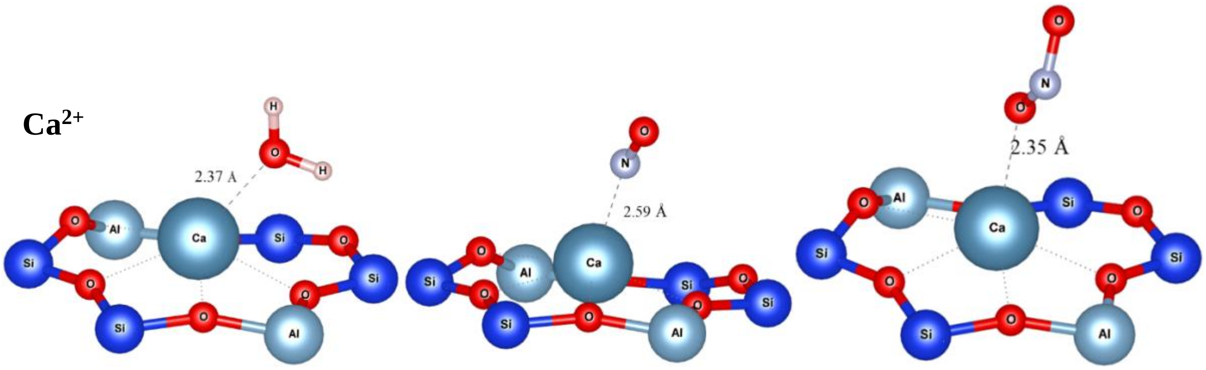

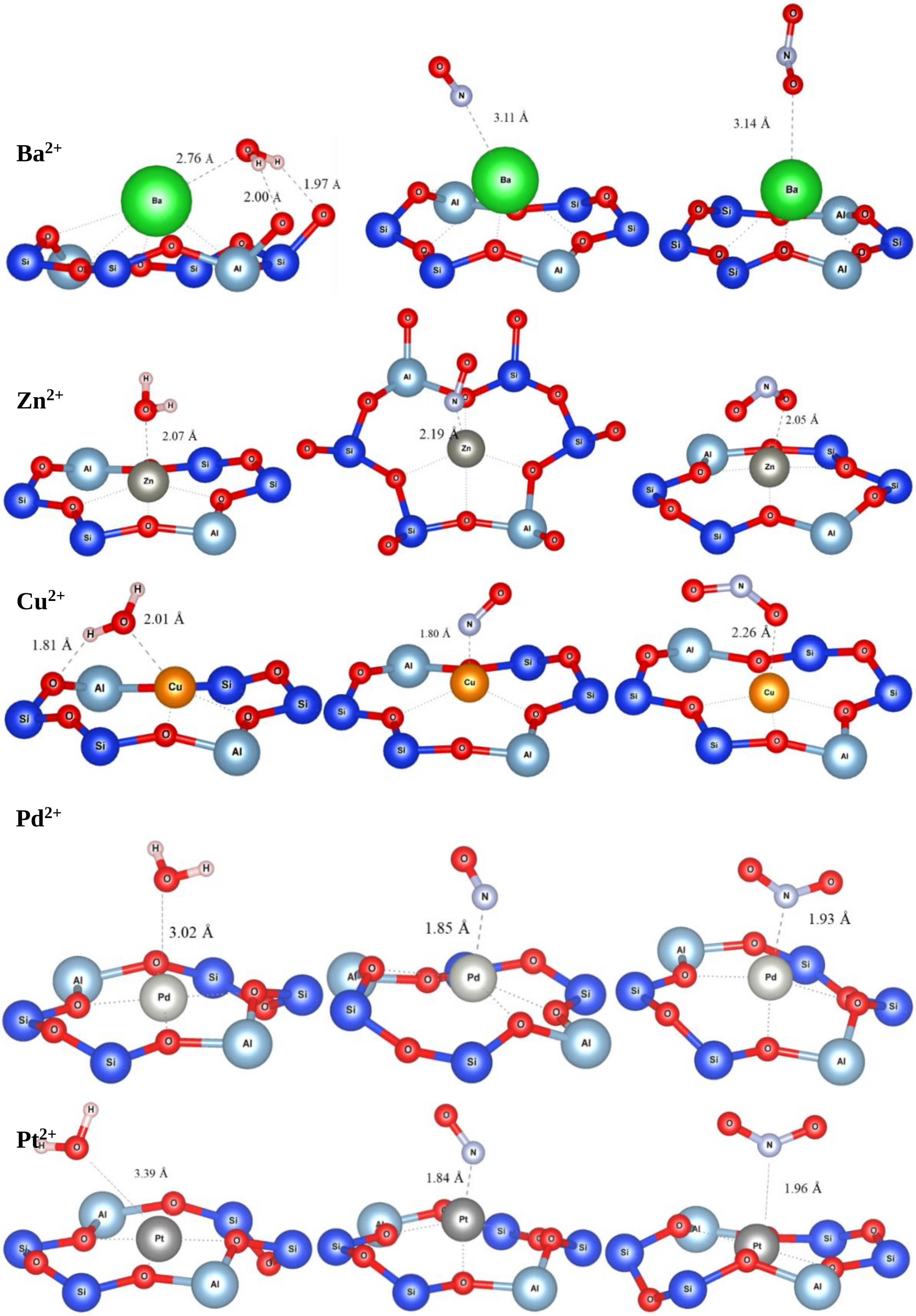
Ba^{2+}
2.76 Å
2.00 Å
1.97 Å
3.11 Å
3.14 Å
Zn^{2+}
2.07 Å
2.19 Å
2.05 Å
Cu^{2+}
1.81 Å
2.01 Å
1.80 Å
2.26 Å
Pd^{2+}
3.02 Å
1.85 Å
1.93 Å
Pt^{2+}
3.39 Å
1.84 Å
1.96 Å

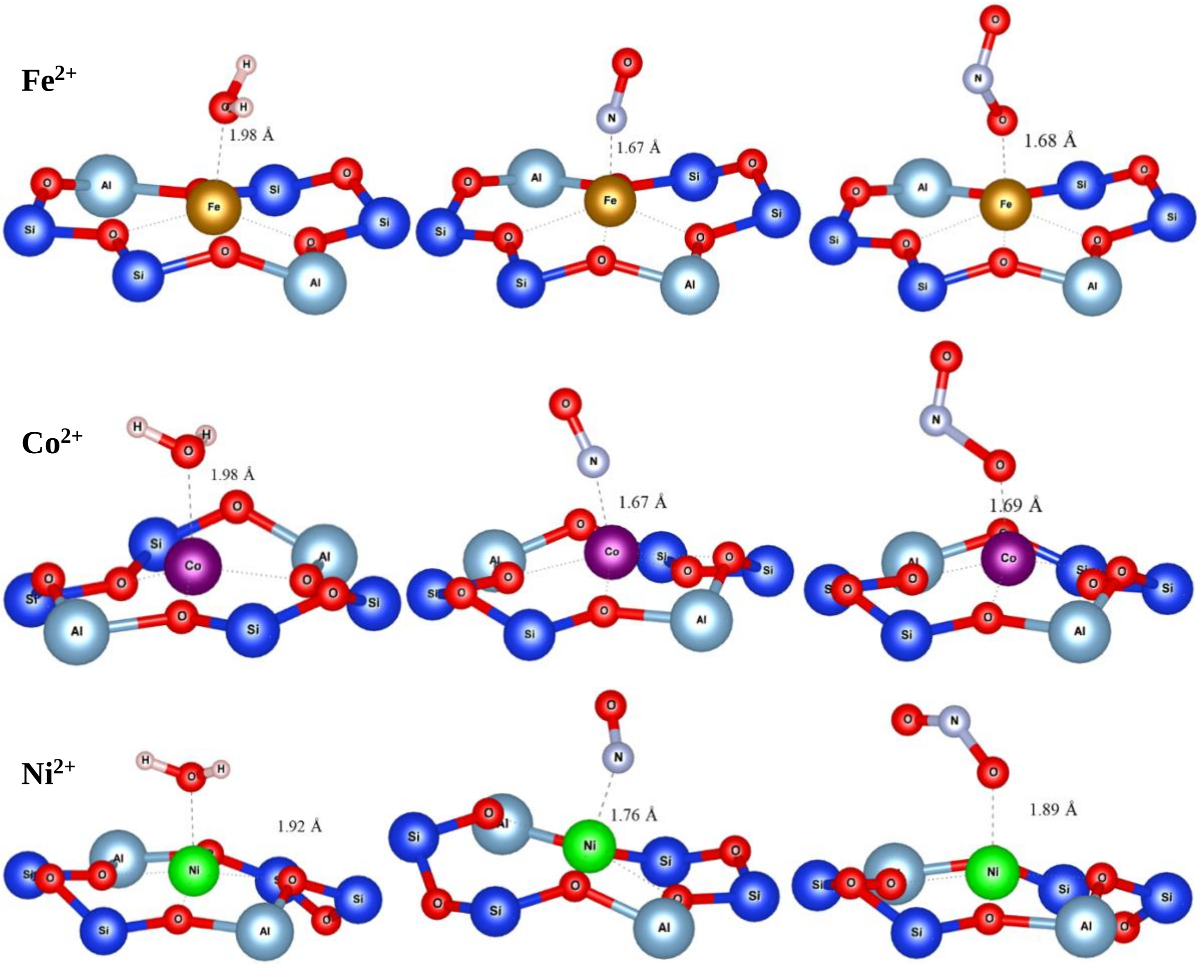

Figure 3.SII: Adsorption modes of the gases (H_2O: left, NO: middle, and NO_2: right) over the different Y divalent cation-exchanged faujasites.

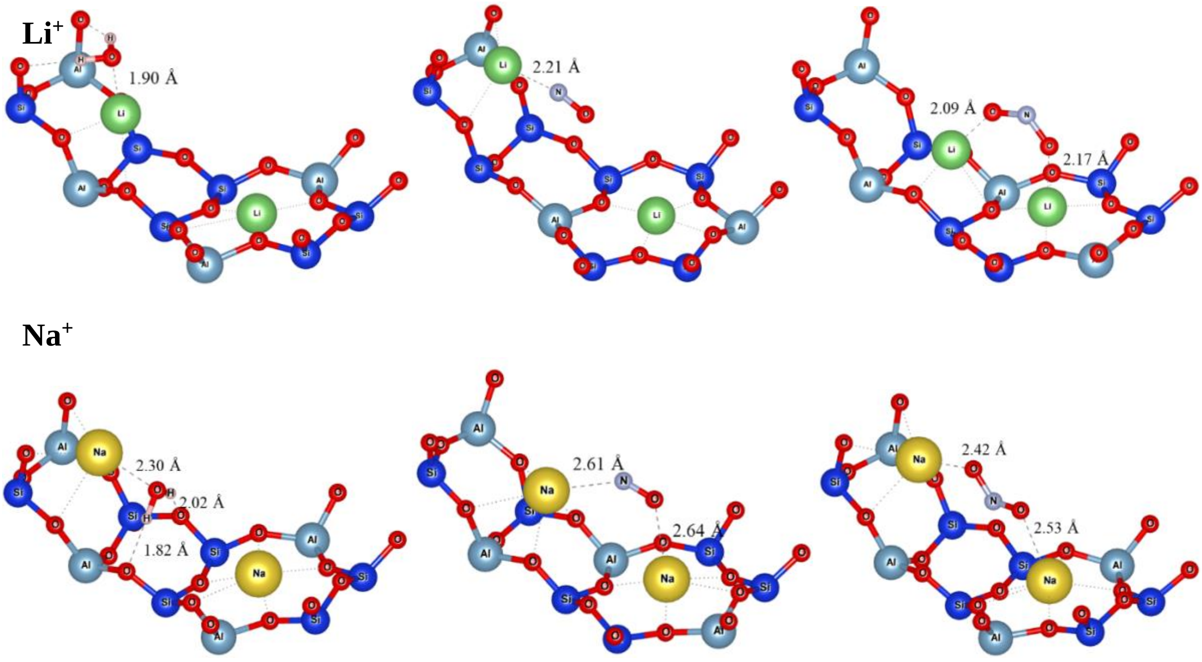

K$^+$

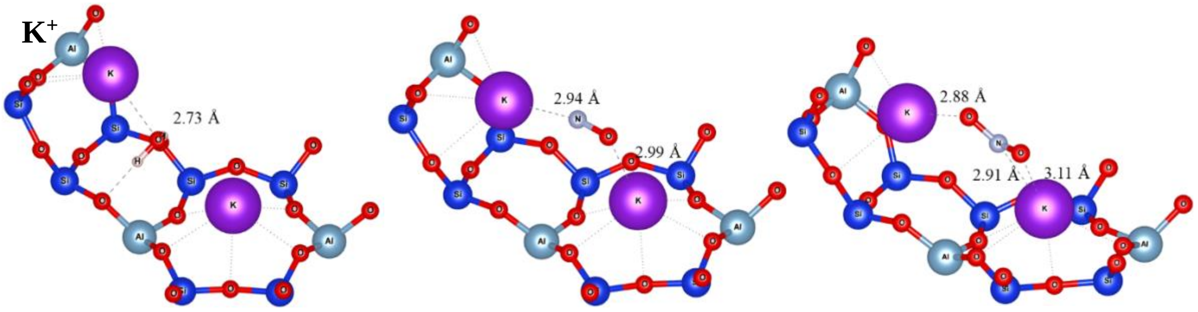
2.73 Å
2.94 Å
2.99 Å
2.88 Å
2.91 Å
3.11 Å
K
N
H
Si
Al

Rb$^+$

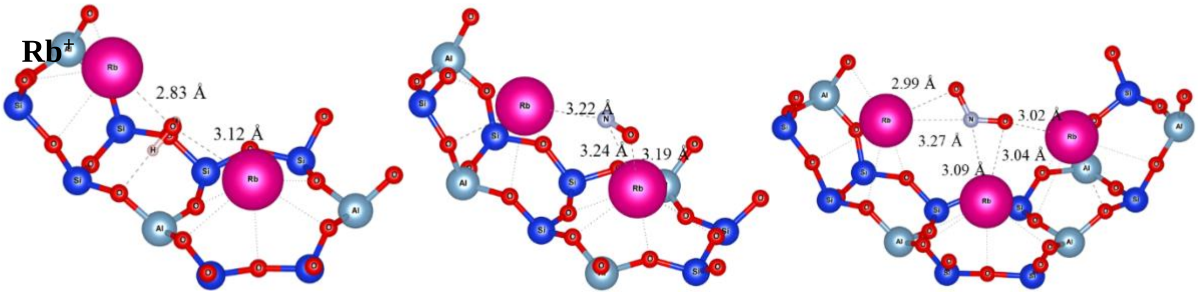
2.83 Å
3.12 Å
3.22 Å
3.24 Å
3.19 Å
2.99 Å
3.02 Å
3.27 Å
3.09 Å
3.04 Å
Rb
N
H
Si
Al

Cs$^+$

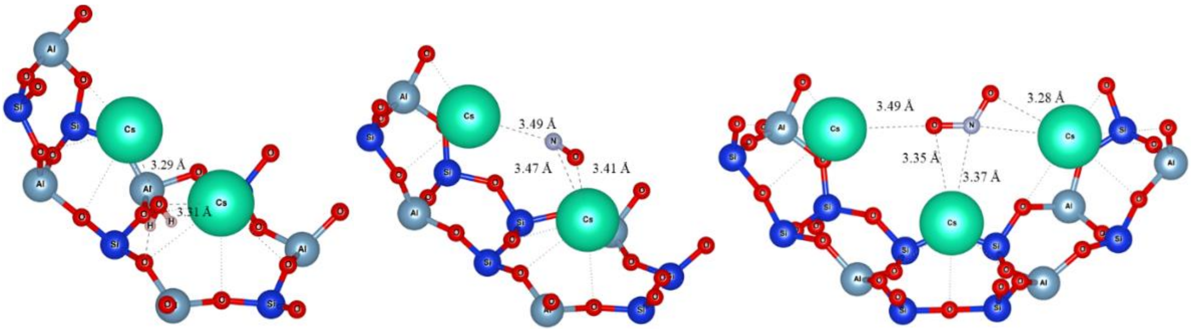
3.29 Å
3.31 Å
3.49 Å
3.47 Å
3.41 Å
3.49 Å
3.28 Å
3.35 Å
3.37 Å
Cs
N
H
Si
Al

Cu$^+$

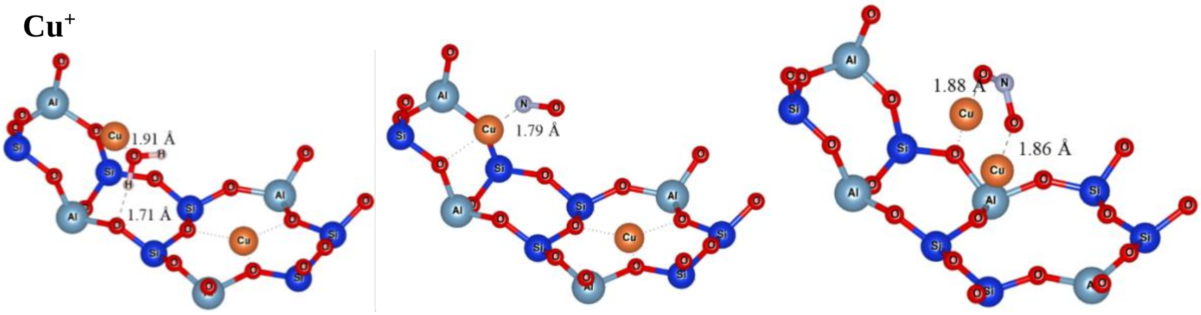
1.91 Å
1.71 Å
1.79 Å
1.88 Å
1.86 Å
Cu
N
H
Si
Al

Ag$^+$

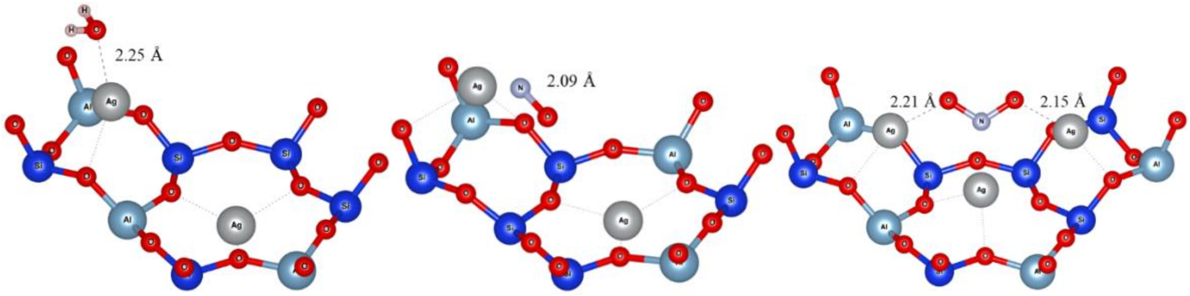

Figure 3.SIII: Adsorption modes of the gases (H_2O: left, NO: middle, and NO_2: right) over the different X monovalent cation-exchanged faujasites.

Ca^{2+}

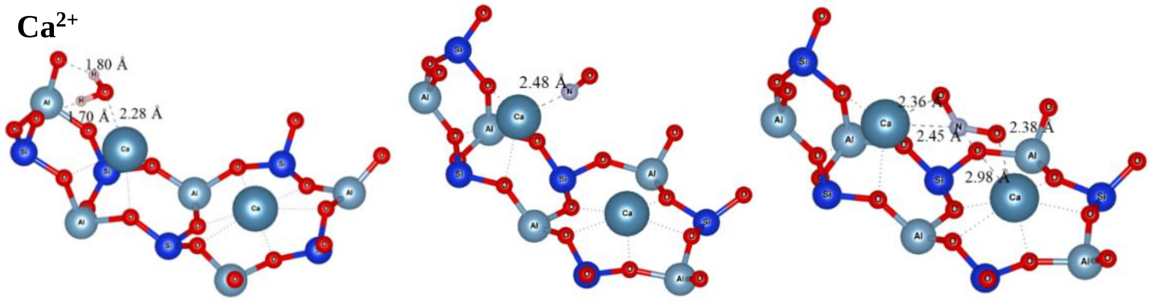

Cu^{2+}

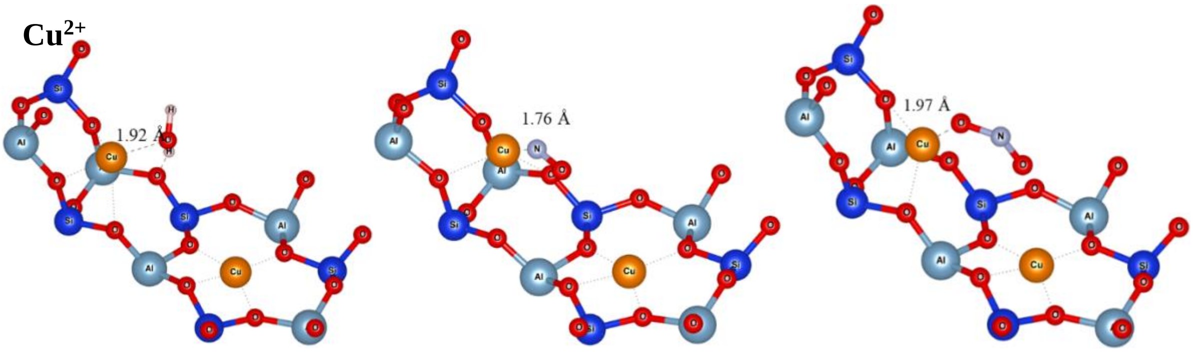

Fe^{2+}

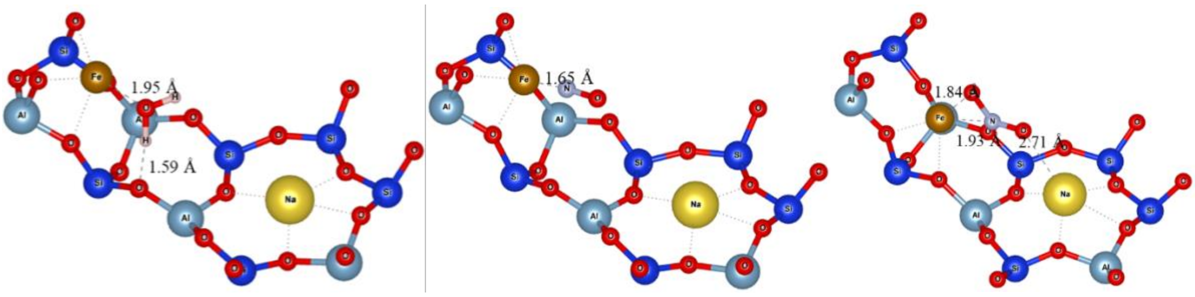

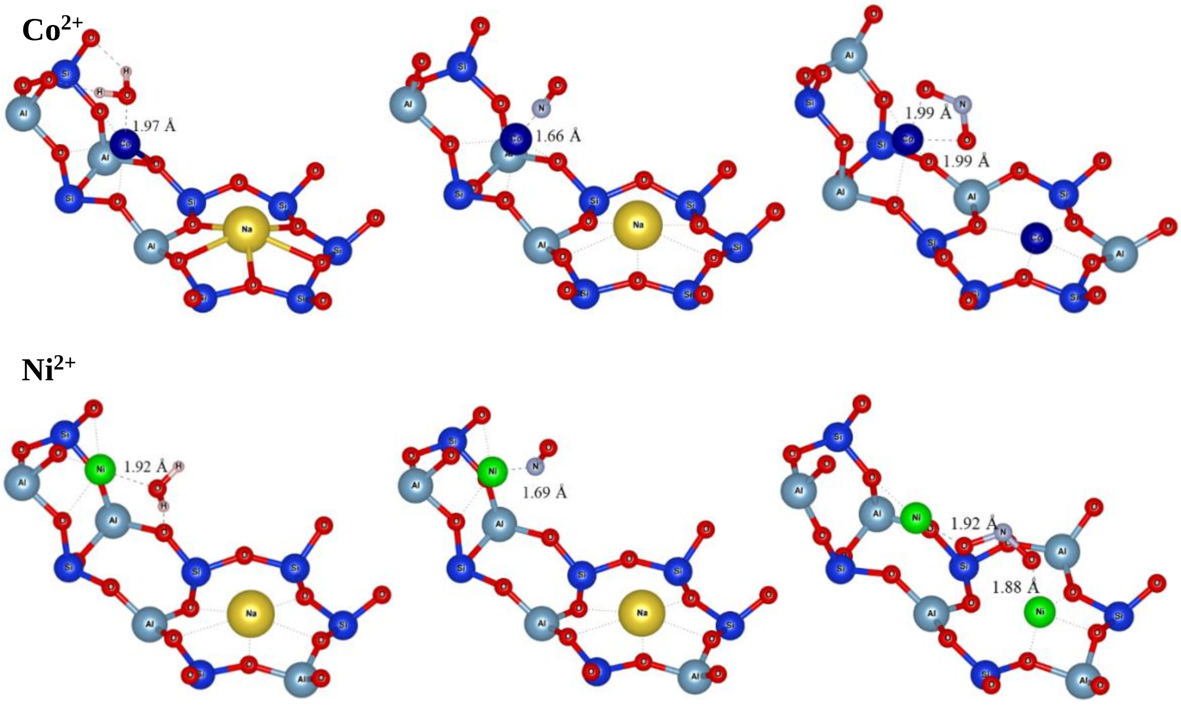

Figure 3.SIV: Adsorption modes of the gases (H_2O: left, NO: middle, and NO_2: right) over the different X divalent cation-exchanged faujasites.

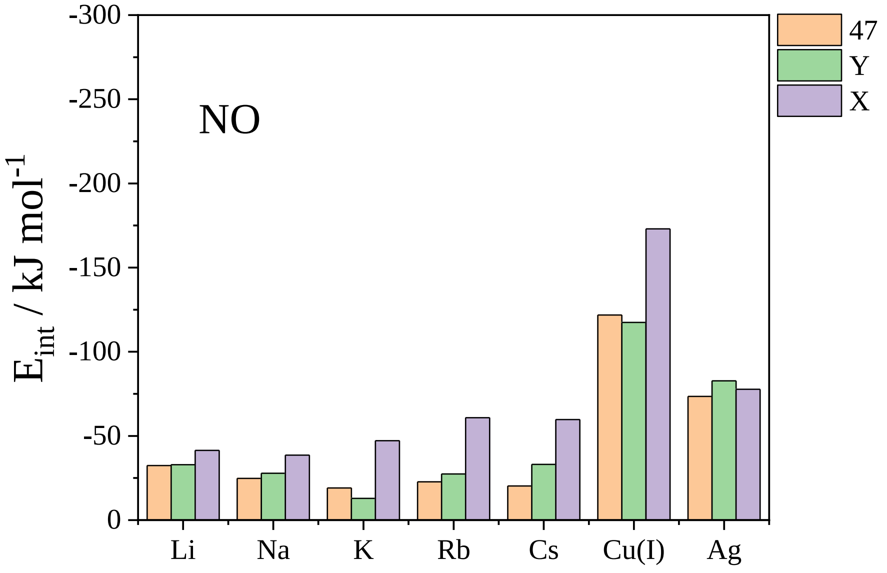

Figure 3.SV: Interaction energies computed at the PBE+D2 level of theory for NO on monovalent cation embedded faujasite with Si/Al = {47, 2.43, 1.4}.

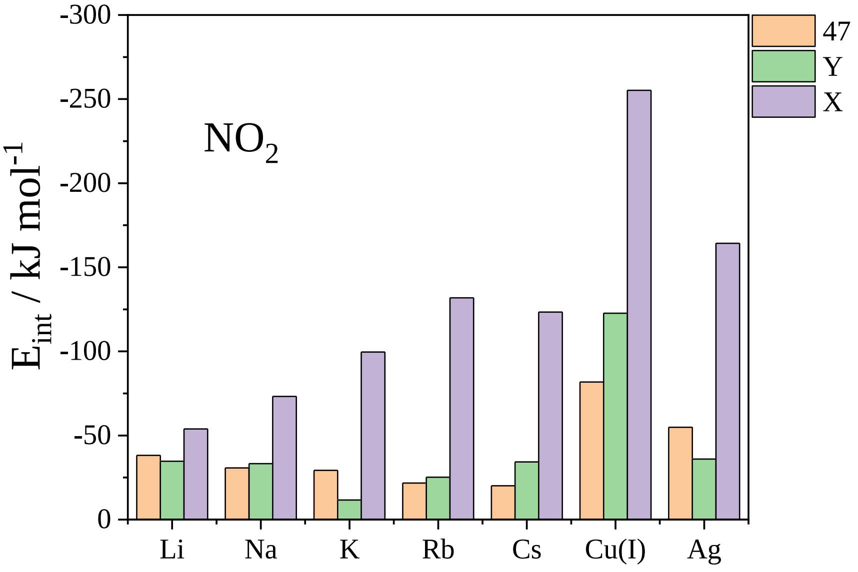

Figure 3.SVI: Interaction energies computed at the PBE+D2 level of theory for NO_2 on monovalent cation embedded faujasite with Si/Al = {47, 2.43, 1.4}.

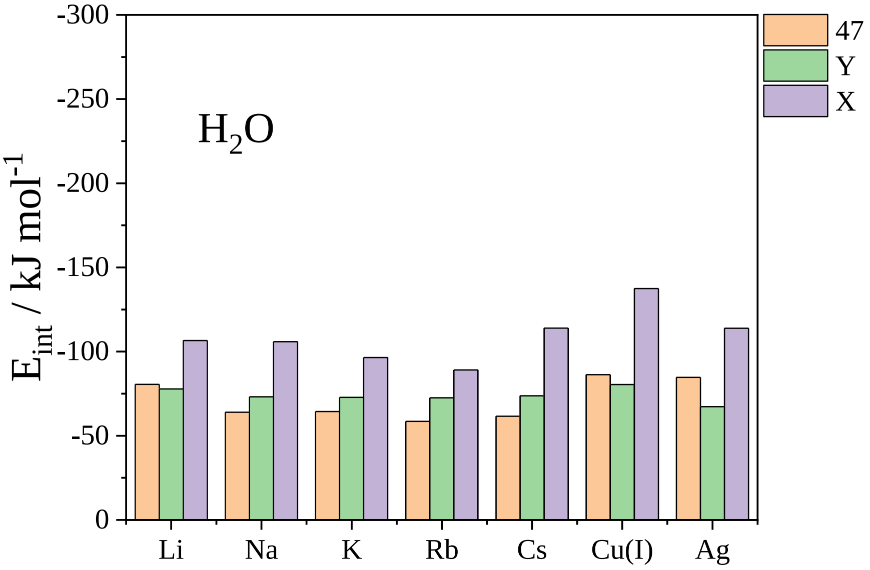

Figure 3.SVII: Interaction energies computed at the PBE+D2 level of theory for H_2O on monovalent cation embedded faujasite with Si/Al = {47, 2.43, 1.4}.

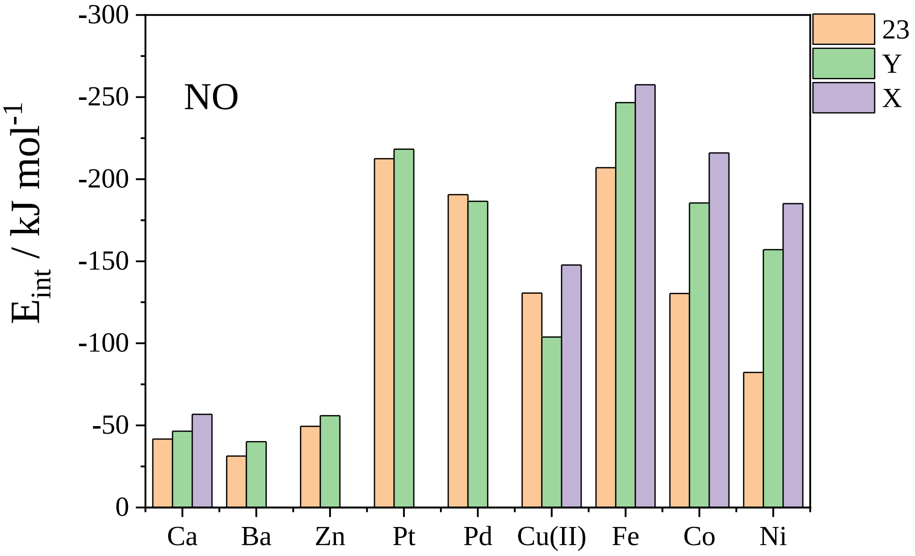

Figure 3.SVIII: Interaction energies computed at the PBE+D2 level of theory for NO on divalent cation embedded faujasite with Si/Al = {23, 2.43, 1.4}.

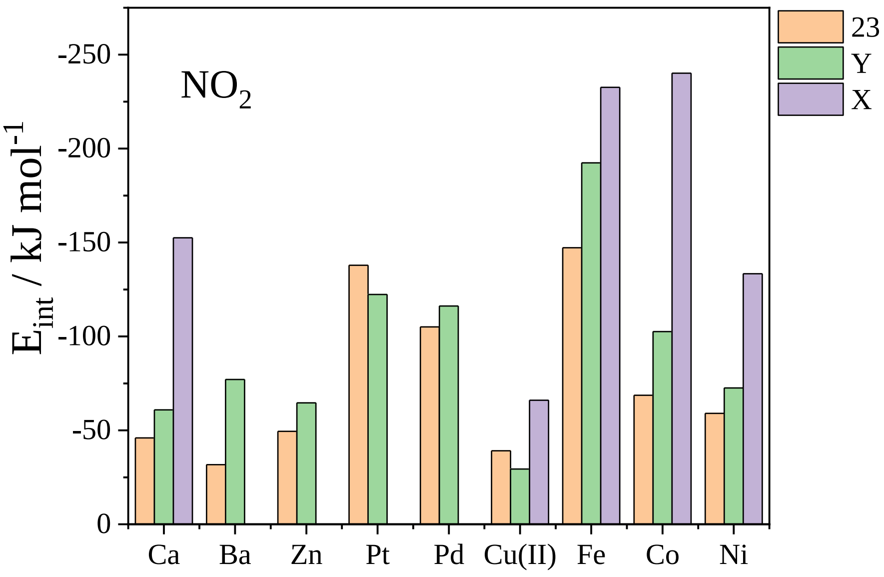

Figure 3.SIX: Interaction energies computed at the PBE+D2 level of theory for NO_2 on divalent cation embedded faujasite with Si/Al = {23, 2.43, 1.4}.

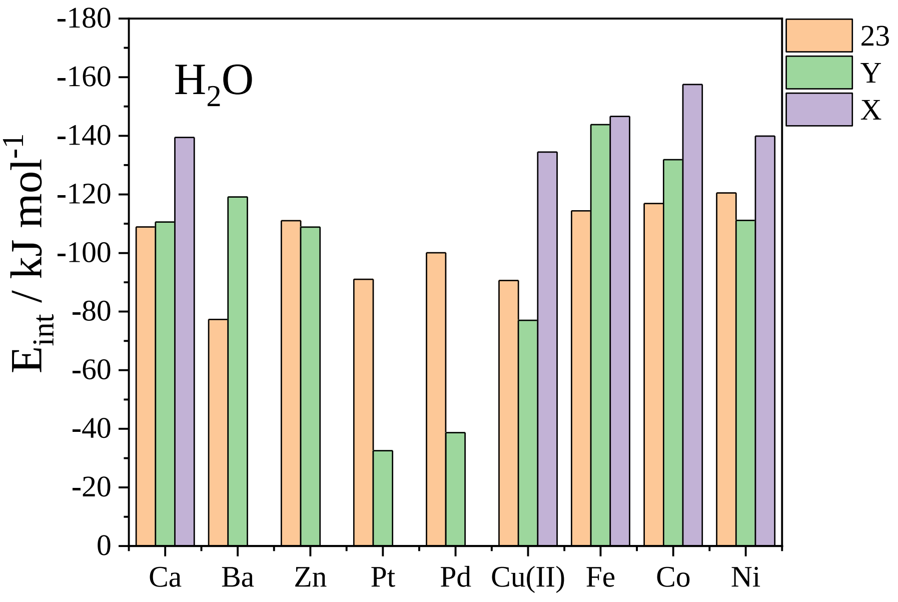

Figure 3.SX: Interaction energies computed at the PBE+D2 level of theory for H_2O on divalent cation embedded faujasite with Si/Al = {23, 2.43, 1.4}.

Table 3.SIV: The induced intramolecular bond changes of NO_2 due to its adsorption on Cu(I)Y, PdY, PtY, FeY, CoY and NiY (Si/Al = 2.43), are presented. The configurations considered are 1: through N (M – N – O2), 2: through O1 while N and O2 are ordered perpendicularly to the 6MR (M – O1 – N | O2) and 3: through O1 while N and O2 are ordered parallelly to the 6MR (M – O1 – N – O2). The values in brackets correspond to the stretching with respect to the initial bond length in percentages. In the second line we also include the interaction energy that complemented these configuration modes.

Gas species concerned	M – N – O_2		M – O1 – N – O2		M – O1 – N | O2	
Bond	O1-NO	O2-NO	O1-NO	O2-NO	O1-NO	O2-NO
Cu(I)Y (Å)	**0.08 (7%)** **(-122.7)**	**0.02 (2%)**	0.08 (7%) (-88.4)	0.01 (1%)	0.10 (8%) (-96.1)	0.01 (1%)
PdY (Å)	**0.01** **(-120.8)**	**0.01**	Not Stable	Not Stable	Not Stable	Not Stable
PtY (Å)	**0.01** **(-137.6)**	**0.01**	Not Stable	Not Stable	Not Stable	Not Stable

FeY (Å)	0.11 (9%) (-173.6)	-0.01 (-1%)	0.31 (26%) (-192.3)	-0.04 (-3%)	**0.31 (26%)** **(-192.4)**	**-0.04 (-3%)**
CoY (Å)	0.02 (-94.7)	0.02	0.07 (-94.7)	0.00	**0.35** **(-102.6)**	**-0.05**
NiY (Å)	0.01 (-71.4)	0.01	**0.03** **(-72.5)**	**-0.01**	0.08 (-64.8)	-0.01

Table 3.SV: The intramolecular bonds of NO_2 after its adsorption on Cu(I)Y, PdY, PtY, FeY, CoY and NiY (Si/Al = 2.43), are presented. The configurations considered are 1: through N (M – N – O2), 2: through O1 while N and O2 are ordered perpendicularly to the 6MR (M – O1 – N | O2) and 3: through O1 while N and O2 are ordered parallelly to the 6MR (M – O1 – N – O2). The values in brackets correspond to the stretching with respect to the initial bond length in percentages.

Gas species concerned	M – N – O_2		M – O1 – N – O2		M – O1 – N | O2	
Bond	O1-NO	O2-NO	O1-NO	O2-NO	O1-NO	O2-NO
Cu(I)Y (Å)	**1.28 (7%)**	**1.23 (2%)**	1.29	1.22	1.31	1.22
PdY (Å)	**1.22**	**1.22**	Not Stable	Not Stable	Not Stable	Not Stable
PtY (Å)	**1.22**	**1.22**	Not Stable	Not Stable	Not Stable	Not Stable
FeY (Å)	1.32	1.20	1.52	1.17	**1.52 (26%)**	**1.17 (-3%)**
CoY (Å)	1.23	1.23	1.28	1.21	**1.56**	**1.16**
NiY (Å)	1.22	1.22	**1.24**	**1.20**	1.29	1.20

Table 3.SVI: Bader charge differences due to adsorptions of NO_2 calculated for the systems Cu(I)Y, PdY, PtY, FeY, CoY and NiY. The configurations considered are 1: through N (M – N – O2), 2: through O1 while N and O2 are ordered perpendicularly to the 6MR (M – O1 – N | O2) and 3: through O1 while N and O2 are ordered parallelly to the 6MR (M – O1 – N – O2).

Cation	config	Atom	Charge Difference
Cu(I)	– N – O_2	O1	-0.156
		O2	-0.134
		N	-0.204
		Cu(I)	0.102
	– O1 – N | O2	O1	-0.292
		O2	-0.137
		N	-0.075
		Cu(I)	0.110
	– O1 – N – O2	O1	-0.254
		O2	-0.179
		N	-0.017
		Cu(I)	0.159
Pd	– N – O_2	O1	-0.010
		O2	-0.036
		N	-0.087
		Pd	0.083
	– O1 – N | O2	O1	Not Stable
		O2	
		N	
		Pd	
	– O1 – N – O2	O1	Not Stable
		O2	
		N	
		Pd	

Pt	$– N – O_2$	O1	-0.044
		O2	0.001
		N	-0.108
		Pt	0.113
	– O1 – N | O2	O1	Not Stable
		O2	
		N	
		Pt	
	– O1 – N – O2	O1	Not Stable
		O2	
		N	
		Pt	
Fe	$– N – O_2$	O1	-0.218
		O2	-0.048
		N	-0.156
		Fe	0.196
	– O1 – N | O2	O1	-0.370
		O2	-0.021
		N	0.040
		Fe	0.233
	– O1 – N – O2	O1	-0.369
		O2	-0.050
		N	0.055
		Fe	0.227
Co	$– N – O_2$	O1	-0.045
		O2	-0.034
		N	-0.149
		Co	0.038
	– O1 – N | O2	O1	-0.334
		O2	0.017
		N	0.086

		Co	0.165
	– O1 – N – O2	O1	-0.212
		O2	-0.046
		N	-0.007
		Co	0.096
Ni	– N – O_2	O1	0.010
		O2	0.008
		N	-0.097
		Ni	0.007
	– O1 – N | O2	O1	-0.158
		O2	0.017
		N	0.031
		Ni	0.121
	– O1 – N – O2	O1	-0.085
		O2	0.055
		N	0.024
		Ni	0.053

Table 3.SVII Magnetic moments of the zeolites before and after the adsorption.

System	Before	NO	N-O2	O1-N-O2	O1-N|O2	H_2O
Cu(I)Y	0.00	1.00	0.63	0.52	0.53	0.00
PdY	0.00	0.00	0.00	Not Stable	Not Stable	0.00
PtY	0.00	0.00	0.97	Not Stable	Not Stable	0.00
FeY	24.00 (6*4)	23.00	25.00	25.00	25.00	24.00
CoY	17.97 (6*3)	16.95	17.94	18.00	18.92	17.97
NiY	11.7 (6*2)	10.74	11.43	12.70	11.04	11.76

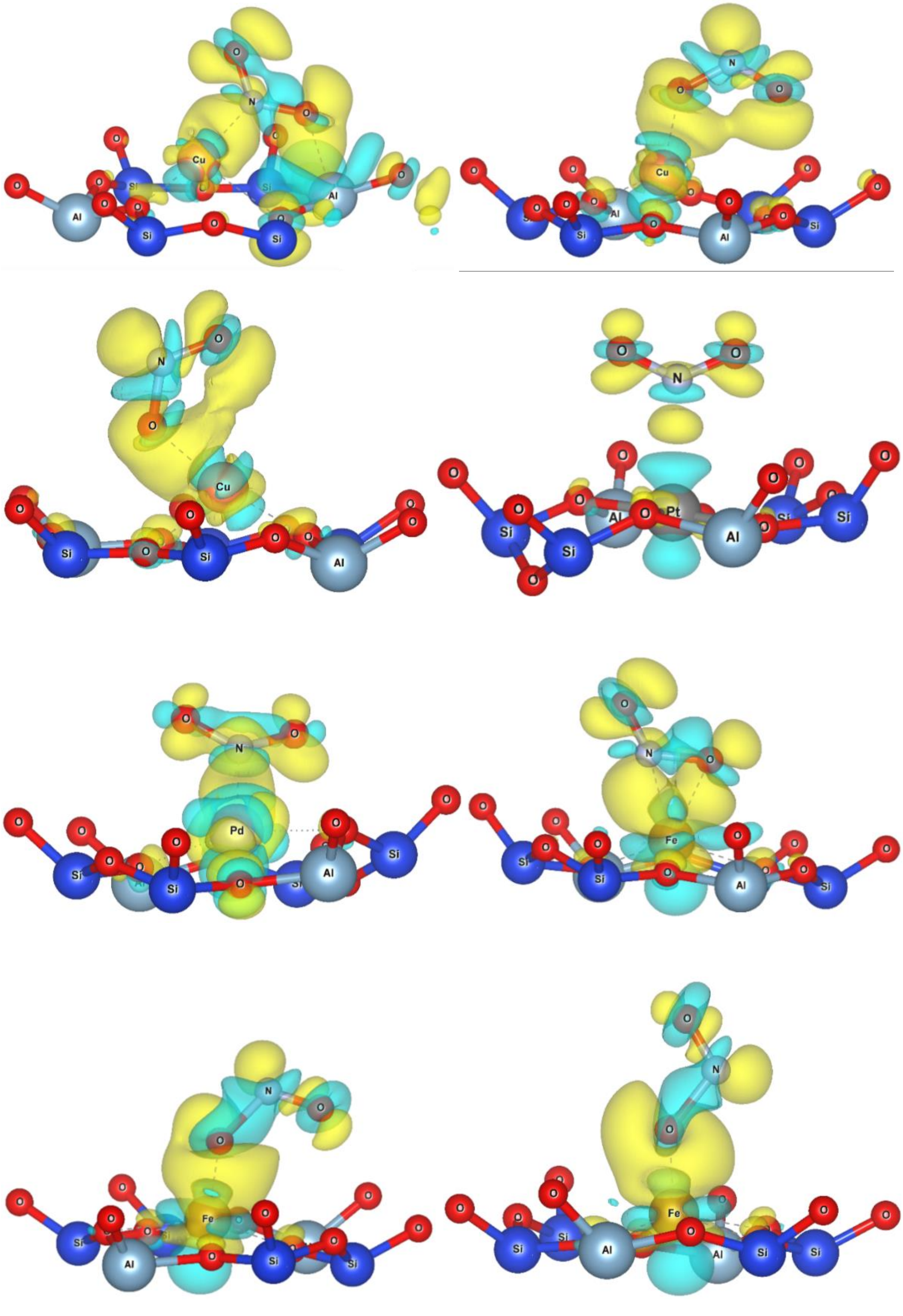
O
N
O
Cu
Si
Al
Cu
Pt
Pd
Fe
Fe
Fe

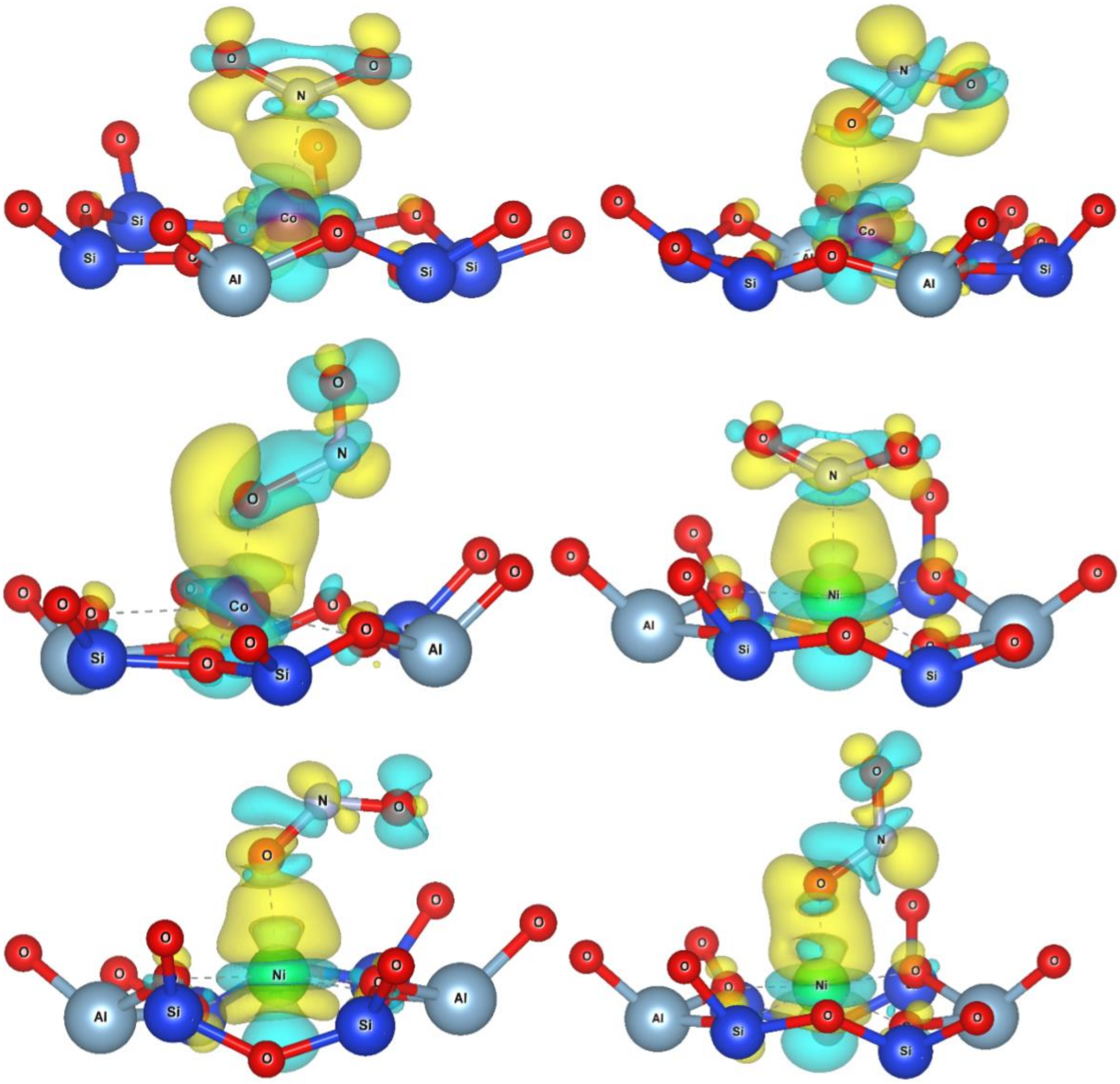

Figure 3.SXI: Charge density differences that occurred during the adsorption NO_2 on Cu(I)Y, PtY, PdY, FeY, CoY, NiY through 3 different modes: 1: through N (M – N – O2), 2: through O1 while N and O2 are ordered perpendicularly to the 6MR (M – O1 – N | O2) and 3: through O1 while N and O2 are ordered parallelly to the 6MR (M – O1 – N – O2). The isosurfaces have a density 0.002 e/a_0^3.

The check whether increased NO_2 coverage will affect the possibility of cross-adsorption in X zeolite, we performed a series of geometry optimization calculations: Starting with relaxed NO_2 cross-adsorption geometries and placing a second NO_2 close to one of the two adsorption sites, we checked whether the adsorption of the second NO_2 is possible, and if it will obstruct the cross-adsorption of the first. Calculations were carried out for Ca, Fe and Ni promoted X zeolite. The adsorption modes are displayed in Figure 3.SXII.

In the case of Ca, we study the cross adsorption between two Ca cations, representing alkaline earth metals. When the second NO_2 was placed close to site III', it adsorbed successfully, while the first NO_2 molecule stayed cross-adsorbed. When the second NO_2 was placed close to site II, its adsorption was prevented by steric affects, between the two NO_2 molecules. An overall interaction energy of -192.9 kJ/mol is associated with the simultaneous adsorption of the two gases.

FeX cross-adsorption occurred between one Fe and one Na cation, namely between a transition metal in site III' and an alkali metal in site II. The presence of a second NO_2 gas did not prevent the cross-adsorption of the first. Two configurations were obtained dependent on whether the second NO_2 was adsorbed on a) site III' Fe or, b) on site II Na. These two adsorption configurations are associated with interaction energies of -333.1 and -266.5 kJ/mol, respectively.

In the case of Ni, we studied the cross adsorption between two Ni cations, namely between two transition metals. The first NO_2 molecule stayed cross-adsorbed, when the second was placed near site II or site III'. The second, adsorbed by both site II and site III', one at a time, giving rise to interaction energies of -138.3 and 230.0 kJ/mol, respectively.

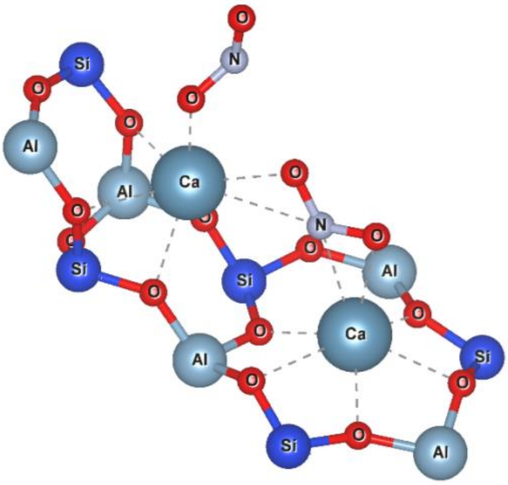

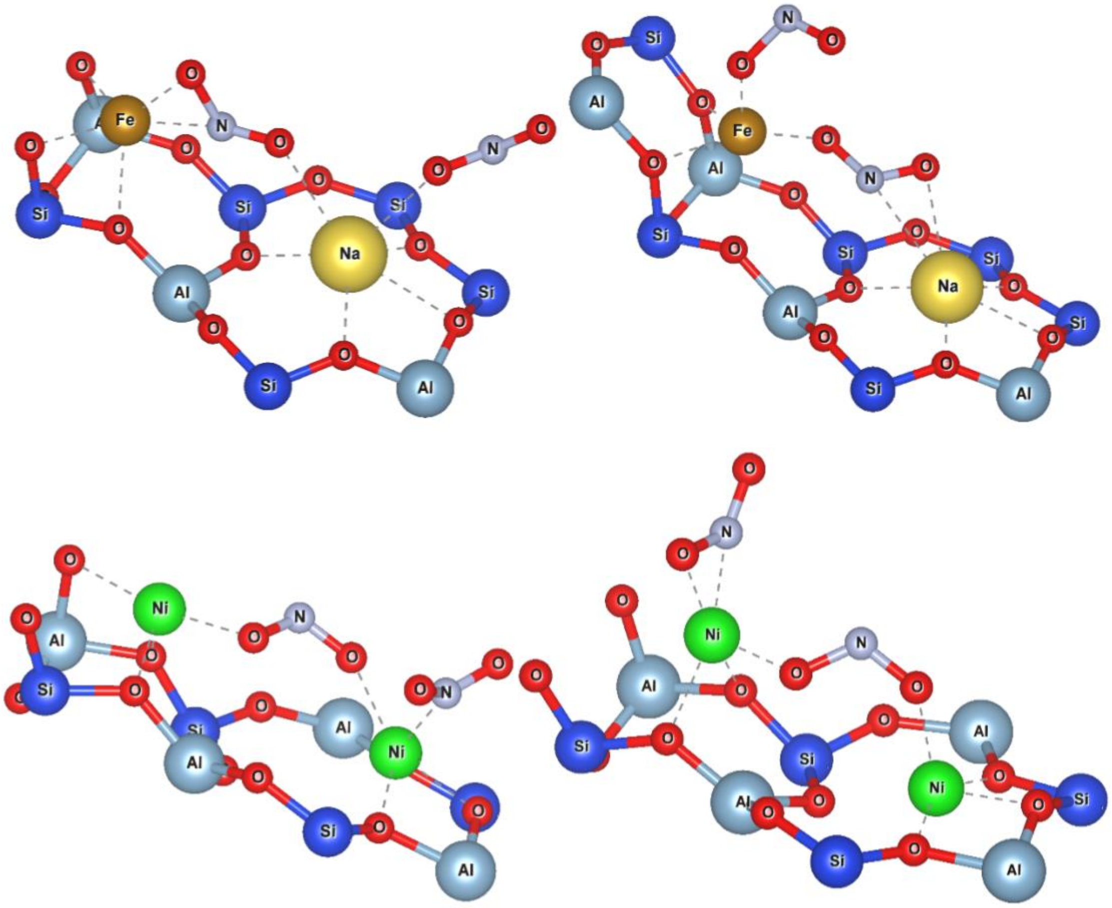

Figure 3.SXII: Adsorption of 2 NO_2 molecules on the same sites of X zeolite. One NO_2 molecule stays always cross-adsorbed, while the second adsorbs by either a site II or a site III' cation.

4. Computational study of iron zeolites for selective capture of NO_x and CO against H_2O and CO_2

Abstract

NO, NO_2, CO, CO_2 and H_2O interaction energies with Fe^{2+} supporting chabazite, and mordenite with various Si/Al ratios were calculated at the periodic Perdew-Burke-Ernzerhof level of theory. Single-configuration calculations were initially performed. The Si/Al ratio sets of {11, 5, 3} and {23, 11, 5} were chosen for chabazite, and mordenite respectively. Both materials exhibit thermodynamic preference for NO and NO_2 over H_2O and CO_2. Molecular dynamics simulations at 300 K for Si/Al = 3 Fe-chabazite show NO, NO_2 and CO, adsorption upon Fe, even in the presence H_2O molecules. Radial distribution function was employed to depict the effect of steam on the attachment of NO, NO_2 and CO to the transition metal, under certain conditions. CO_2 co-adsorption was neglected in our study due to its low interaction energy. Bond elongation after adsorption was studied to account for the regeneration of the substrate. In this respect, Bader charges and charge density differences were calculated to rationalize the elongations. Most importantly, low Si/Al ratios improve the affinity for NO and NO_2 and favour the regenerability.

Keywords: NOx, carbon monoxide, carbon dioxide, water, iron, chabazite, mordenite, Si/Al, DFT, molecular dynamics, radial distribution function, interaction energy

4.1. Introduction

Nitrogen dioxide and nitric oxide (NO_x) are dangerous air pollutants with serious environmental and human health consequences[1–4,97]. Among sources of NO_x, diesel engine vehicles operating discontinuously through the day[155], like in construction sites, constitute a major threat for workers, especially in confined spaces lacking ventilation. *Institut National de Recherche et de Sécurité* (INRS) has devoted a project on the limitation of NO_x emissions to ameliorate the quality of working conditions for these people.

European union (EU) regulations have been set to reduce the ceiling of NO_x emissions giving rise to technological adaptations on vehicles. In its effort to reduce air pollutant emissions, Europe published in 2014 Euro stage VI regulation, a series of new directives concerning the exhaust gases. According to them, NO_x fumes from diesel vehicles cannot surpass the limit of 80 mg/km, a decrease of 56% from Euro V[156,157]. EU directive 2017/164 limits NO and NO_2 exposures per 8 hours (a full-time working day) to 2 and 0.5 ppm, respectively[157]. To meet these restrictions, several technologies have been proposed.

Catalytic treatment is the main method to reduce NO_x emissions. The two major representatives are *NO_x storage reduction* (NSR)[11,12] and *selective catalytic reduction* (SCR)[13,14]. At maximum efficiency, SCR can reach almost 100% NO_x conversion to harmless N_2. However, high catalytic performances demand temperatures higher than 200 °C. Since construction site operating vehicles work discontinuously through the day, they are subjected to many cold starts. On a gasoline engine, a three-way catalyst (TWC) component located close to the engine-out position reaches its operating temperature quite quickly. On the contrary, diesel engines produce lower-temperature exhaust gases showing extended cold starts, thus jeopardizing the low-temperature NO_x removal process[23–25].

The solution to low temperature de-NO_x consists in using materials capable of low temperature NO_x adsorption, on the basis of thermodynamic selectivity. Two major categories of materials have been used for this purpose. The first one comprises *passive NO_x adsorbers* (PNA), which trap NO_x at low temperatures and release them at higher temperatures, without reacting with them [31–33,35,99] . The second one comprises *cold start concept* (CSC) catalysts, which catalyse NO_x conversion during their capture, further enhancing the performance of the system[19,30,158]. Successful candidates include oxides such as CeO_2, ZrO_2, WO_3. Combinations of them achieved even greater physicochemical properties, not possible by a pure oxide[31,32]. These materials were promoted by transition metals, Pt and Pd being the most prominent among them for the application. They are highly efficient for low temperature NO_x reduction, even in the presence of steam, a strong NO_x inhibitor [31] (with NO_x concentration of 350–1000 ppm and H_2O content of about 10%[18,19]). However, these oxide-based materials are notoriously sensitive to sulphur poisoning due to the presence of sulphur oxides in the diesel exhaust gases, which degrades the catalysts.

Zeolites not only have been employed to address this issue with great efficiency, but also have showed excellent behaviour when promoted by Pd/Pt for the low-temperature NO_x removal. In realistic conditions, zeolites display high storage efficiencies combined with significant resistance to sulphur poisoning[35,36,98]. Furthermore, studies have assessed the efficiency of zeolites with various cationic loadings[36–39,159]. Indeed, measuring the Pt-group-cation/NO_x occupation ratio, revealed that loadings < 1 wt% perform far more cost-efficiently.

It is possible however that transition metals belonging to other groups perform better in higher loadings. Furthermore, the stabilization of divalent cations in zeolites requires low Si/Al ratios[160], resulting in much higher loadings. Hence, the increased cation-linked cost requires the exploration of cheap substitutes for Pd and Pt.

Recent theoretical studies on cation exchanged zeolites have identified some promising low-cost candidates for low temperature NO_x removal. Using *density functional theory* (DFT) to study the thermodynamic selectivity and regenerability of faujasite with Si/Al = 47, Hessou et al.[96] proposed Cu^I as a valid choice. In a similar study, Daouli et al.[161] found that Pt^{2+} and Pd^{2+} supporting faujasite, with Si/Al = 23, exhibit much higher affinity for NO_x than for H_2O[162].

Fe^{2+} exchanged zeolites have been used in the past for various applications. Sun et al.[163] used Fe exchanged ZSM-5 for the catalytic decomposition of N_2O. They identified various ferrous species with cationic or oligomeric nature, but high Fe^{2+} concentration was observed after a high temperature treatment in He at 1173 K. Panov et al.[164] used Fe-ZSM-5 for the room-temperature oxidation of hydrocarbons. Iron exchange is perfectly feasible as demonstrated by SCR of NO_x with a variety of zeolites such as MOR, BEA, CHA, ZSM-5[165–168].

Using DFT, the present work assesses the performances of mordenite and chabazite zeolites supporting divalent iron for low temperature NO_x and CO adsorption, versus water and CO_2. Si/Al ratios of 23, 11 and 5, as well as 11, 5 and 3, were implemented for mordenite and chabazite respectively, for investigating microscopic phenomena affecting the adsorption process at 0 K. *Molecular dynamics* (MD), a cutting-edge technique was also employed on the most favourable structure to harvest reference results at operando conditions.

4.2. Methods and models

4.2.1. Computational details

Periodic DFT calculations were implemented through *Vienna Ab Initio Simulation Package* (VASP) [111,112,169–171] with the projected augmented wave (PAW) method. Perdew-Burke-Ernzerhof (PBE) functional[87] – a particularly efficient representative of the generalized gradient approximation (GGA) – was chosen for the simulations. Grimme D2[89,172–174] long-range dispersion correction was employed as a complement to GGA[95,113]. In particular was validated by Hessou et al.[96] over systems akin to ours. The dispersion contributions which account for a small percentage of the interaction energy, range from 15 to 30 kJ/mol (see SI).

The Kohn-Sham equations were solved self-consistently until the energy difference between two consecutive cycles was less than 10^{-7} eV. For fixed cell parameters, as in similar systems[58,96,161,175], the plane wave energy cut-off was set at 450 eV. The latter was raised to 1000 eV when the cell parameters were treated as dynamical variables. The reciprocal space was modelled with one k-point at the gamma point of the Brillouin zone. A gaussian smearing of $\sigma = 0.1$ eV was applied to the band occupations to improve the total energy convergence. The atomic positions were optimized until the force differences between ionic steps were within 0.02 eV $Å^{-1}$ per atom.

GGA is the lowest acceptable level of DFT to describe the electron structure of systems with chemical bonds[84]. Its adequacy is severely challenged during the modelling of strongly correlated d and f orbitals of transition metals. Hubbard's on-site potential (U) is introduced to treat the unphysical delocalization of the electrons occupying these orbitals[92,118]. In this work we use a linear response method to calculate optimal U values for adequately sparse transition metals in chabazite and mordenite structures. The values obtained were 3.0 eV and 3.5 eV for mordenite and chabazite respectively and were adopted for all the calculations on Fe atom. U in VASP was set-up with LDAUTYPE=3, setting J=1. The single configuration interaction energy between gas and zeolite was computed in the supermolecular approach by the subtraction:

$$\Delta E_{int} = E_{FAU-X} - E_{FAU} - E_X \tag{4.1},$$

where E_{FAU-X} expresses the energy of the aggregation of the gas with the material, E_{FAU}, the energy of the material, and E_X the energy of the gas[95]. Correspondingly, utilization of MD for the calculation of interaction energy was done by replacing the variables in (1) with their averages over a time interval of 50 ps. A time step of 1fs was used.

$$\Delta E_{int} = \langle E_{FAU-X} \rangle - \langle E_{FAU} \rangle - \langle E_X \rangle \tag{4.2}$$

A key point to account for the regeneration of the material is based on the intramolecular bond elongations of the gases due to their adsorption. These elongations are rationalized by their association to induced Bader charge transfers[121–125] and charge density differences. Bader charges were first calculated for the relaxed complex (Q_{FAU-X}), the zeolite omitting the gas, (Q_{FAU}), and the gas omitting the zeolite (Q_X), and their subtraction gave the charge difference due to adsorption ΔQ as:

$$\Delta Q = Q_{FAU-X} - Q_{FAU} - Q_X \tag{4.3},$$

due to the corresponding adsorptions. Likewise, the electron density difference $\Delta\rho$ is defined as:

$$\Delta\rho = \rho_{FAU-X} - \rho_{FAU} - \rho_X \tag{4.4}$$

4.2.2 Structures

Zeolites are aluminosilicate porous materials comprising 4-coordinated Si and Al atoms bridged with 2-coordinated oxygens, forming solids with various ring-like arrangements. The aperture sizes of the rings are typically described by the number of tetrahedrally coordinated (T-atoms) Si and Al belonging in it. For instance, a ring composed of 4 T-atoms (and hence 4 O atoms too), is described as a 4-membered ring (4MR). Zeolites are classified according to their maximum aperture size into small- (≤ 8 MR), medium- (≤ 10 MR), large- (≤ 12 MR) and ultra large-pore ones. The introduction of Al atoms in the framework is accompanied by one electron deficit, which will be covered by a cation. This way, the appearance of 2 Al atoms in a close distance can be neutralized by the electron donation that an iron atom will introduce, appearing as a Fe^{2+} species.

Chabazite and mordenite zeolitic models were built by replacing Si with Al atoms in a manner that Lowenstein rule is respected (two Al atoms cannot be bridged by only an O atom). Al atoms were close enough to iron cations, so that the latter exist in the form Fe^{2+}.[160] Thus, the adsorptions sites are characterized by the nature of the cation, the shape and size of the pore, and the Al distribution around the cation.

The unit cells used, were taken from the studies of Bučko et al[176] and Rey et al[177]. A low Si/Al ratio favours the presence of divalent-Fe in the framework of operando systems[36]. Al distributions with high stability were implemented on the zeolites. The Si/Al ratios that have been considered for the purely Fe-supporting chabazite throughout this study are 11, 5 and 3 giving rise to loadings of 3.7, 7.2 and 11.0 wt%. Regarding mordenite, the achievable Si/Al ratios of 23, 11 and 5 were explored[160,178,179], with the first two structures carrying solely Fe, and the last one, Na too, giving the possibility for further testing. These formulations led to the loadings of 1.9, 3.7 and 3.7 wt%.

4.2.2.1 Chabazite

Chabazite is a naturally abundant small-pored zeolite. It consists of double 6-membered rings (D6R), forming prisms, which are themselves connected by 8MRs as shown in Figure 4.1. Large volume spaces are formed, called *supercages*, which are of utter importance to this application, due to the accessibility they offer to the gases, through the sufficiently wide 8MR. Two locations are adopted for the localization of cations in chabazite throughout this study. They are based on the combination of high stability and availability offered: The first one in the middle of the six membered ring with at least 2 Al atoms in the ring, called site-II, and the second one in the 8MR, called site-IV. The unit cells used have a rhombohedral symmetry with $\alpha \approx \beta \approx \gamma \approx 60°$.

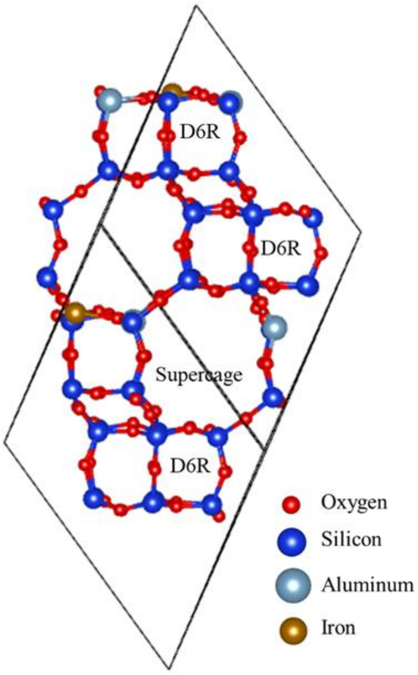

Figure 4.1: A representation of chabazite with Si/Al = 11. The names of the basic structural units are provided on-site.

4.2.2.2 Mordenite

Mordenite is an abundant material belonging to the category of large-pore zeolites. Its channel-based structure is composed of 3 fundamental units (see Figure 4.2): An 8MR elliptical ring, which, when extended transversely, gives rise to the *side channel* (SC), a 5MR generating the *side pocket* (SP) in a similar way to SC, and – the most important part – a 12MR generating the *main channel* (MC). The cations are settled in the structure by checking: the stability of the resulting structures as well as their relevance to the application. The main channel, being the most spacious channel hosts the majority of the gas stream[59], and is consequently the most interesting for our investigation. The cations are hosted on ellipsoid 6MRs that offer the highest stability between the available choices[58,180], as shown in Figure 4.2. The ratio of 23 considers only one cation on a ring with the stablest possible Al distribution, where the Al atoms retain a minimum distance of 3 T-atoms (configuration 1-4). 11 and 5, additionally to the adsorption site of 23, contain a ring with Al atoms staying at a minimum distance of 2-T atoms (configuration 1-3). According to our findings small reduction in stability is translated into a slight increase of the interaction energy between the gas and the cation. The unit cells used for mordenite are slightly distorted tetragonal.

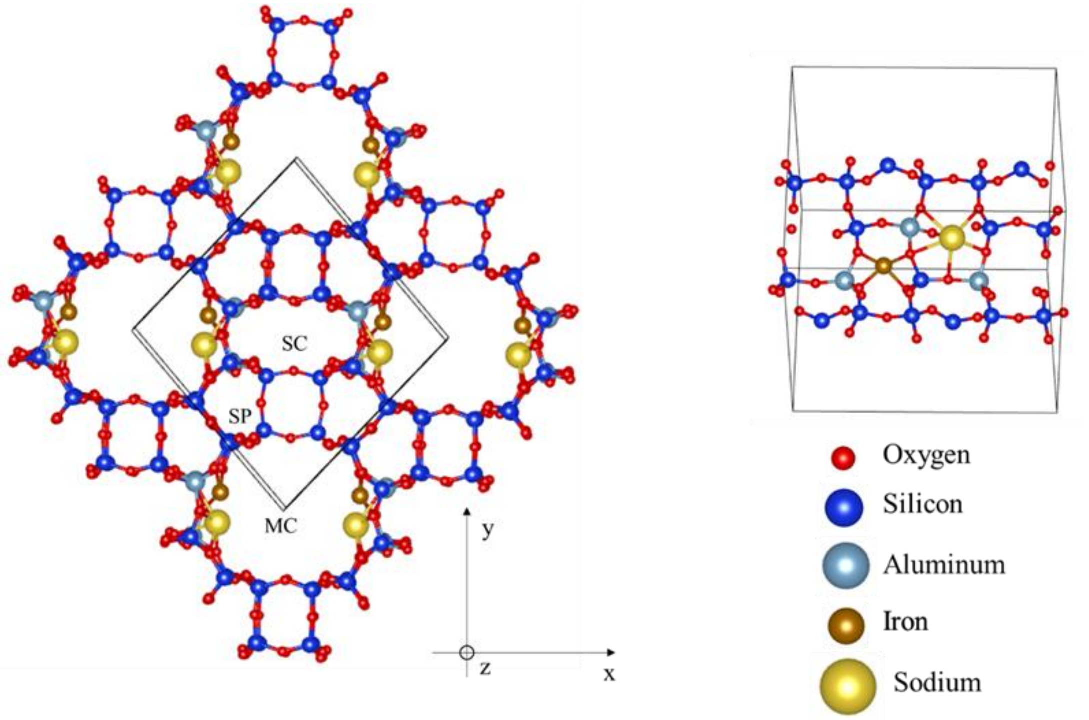

Figure 4.2: A representation of mordenite with Si/Al = 5, with the channels noted with labels is presented on the left side, from a x-y plane perspective. Three different channels are available: SC, with an opening of 8 tetrahedral atoms, SP with 5 and MC with 12, being the most spacious, thus the most interesting for us. The smaller figure on the right side depicts the inner of the main channel, highlighting iron in a 6MR, 1-3 configuration.

NO_2 requires special treatment due to its large size compared to the other gases. Indeed, when two cations are close enough, NO_2 can be adsorbed by both at the same time, a phenomenon which we define *cross-adsorption*. Cross-adsorption occurs in the cases of MOR with Si/Al = 5, and CHA, with Si/Al = 5 and 3. Furthermore, when CHA with Si/Al = 3 is considered, we can have 2 kinds of cross-adsorption: 1) Between a site-II and a site-IV Fe, and 2) between two site-IV cations.

4.3. Results

4.3.1 Adsorption screening for mordenite

The thermodynamic selectivity of mordenite structures with Si/Al of 23, 11 and 5 has been assessed for NO_x and CO over H_2O and CO_2. Aluminium distributions 1-3 and 1-4 (see structures section) have also been assessed.

Interaction energies of gases with mordenite are presented in Table 4.1 and Figure 4.3. Interaction patterns are as follows: 1) the preferred adsorbate is always NO; 2) the second one is NO_2 except for Si/Al = 23, where water is more tightly adsorbed than NO_2; 3) close adsorption energies are observed for CO and H_2O, except for Si/Al = 23 and Si/Al = 5 with Al distribution 1-4; 4) the weakest adsorption deals with CO_2. Since interaction energies of CO_2 are the lowest ones, we tend to exclude CO_2, and focus on H_2O considering the material selectivity.

Indeed, NO_x are preferred over water for all geometries apart from the one where Si/Al = 23. Considering 1-4 configurations, Si/Al = 11 showed positive results, with NO and NO_2 surpassing water's interaction energy by 104.1 and 29.2 kJ/mol respectively, while CO stayed barely below, by 1.1 kJ/mol. Likewise, regarding Si/Al = 5, NO and NO_2 overcome water by 89.8 and 33.4 kJ/mol respectively, while CO stayed behind by 28.3 kJ/mol. NO_2 showed increased affinities for Si/Al = 5, compared to the other cells by ≈ 20 kJ/mol. This difference is attributed to the cross-adsorption between Fe and Na cations.

Table 4.1: Total interaction energies for gas adsorption on Mordenite with Si/Al ratio of 23, 11, or 5, and 1-3 or 1-4 Al distributions (Energy / kJ/mol).

	NO	NO_2	CO	H_2O	CO_2
23-(1-3)	-220.3	-138.6	-106.6	-145.1	-54.6
11-(1-3)	-217.7	-140.9	-103.5	-104.6	-51.6
11-(1-4)	-212.3	-137.6	-93.5	-108.4	-39.2
5-(1-3)	-216.5	-160.1	-98.4	-126.7	-45.9
5-(1-4)	-211.4	-162.8	-92.8	-101.6	-46.7

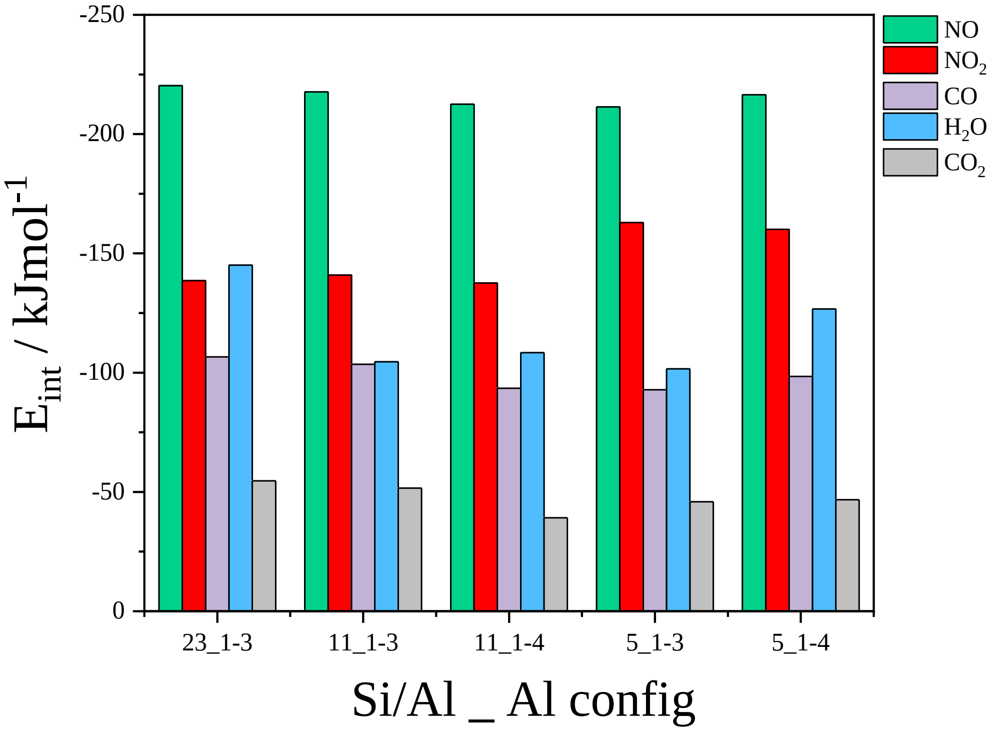

Figure 4.3: Interaction energies computed at the PBE+D2+U level of theory of NO, NO_2, CO, H_2O and CO_2 on Fe-MOR. The adsorption sites considered, are characterized by Si/Al = {23, 11, 5}, 6MR topology, and Al distributions 1-3 and 1-4.

4.3.2 Adsorption screening for chabazite

Three structures have been considered for chabazite, corresponding to the Si/Al ratios of 11, 5 and 3. For each of these unit cells adsorptions of NO, NO_2, CO, H_2O and CO_2 have been performed, and the interaction energy has been calculated according to equation (1). The size of NO_2 is large enough to allow adsorption between two cations at the same time, calling for special treatment for structures with ratios of 5 and 3.

The interaction energies are presented on Table 4.2 and Figure 4.4. Once again, the most obvious patterns are the following: 1) NO is always the most preferred; 2) CO_2 is the least preferred; 3) CO is the last but CO_2; 4) NO_2 is the second most preferred on site II but H_2O takes its place while site-IV is considered. Adsorption between two different cations enables NO_2 to enhance its affinity towards the zeolite, even overcoming water in the case of adsorption between two site-IV located cations. For the remaining manuscript, CO_2 will be neglected because of its low interaction energy, compared to the other gases.

For Si/Al = 11, both NO and NO_2 adsorb with a higher interaction energy than water by 87.2 kJ/mol and 11.6 kJ/mol respectively. CO, on the other hand, adsorbs less tightly than water by 24.2 kJ/mol. For Si/Al = 5, in regard to site-II, the findings follow the same trend as before, with NO and NO_2 staying 93.5 and 11.1 kJ/mol over water and CO 13.2 below it (the differences are depicted as absolute values). In the case of site-IV, only NO remains higher than water by 38.5 kJ/mol, NO_2 and CO staying below by 46.3 and kJ/mol 67.9 kJ/mol. One can observe that in comparison to site II, the differences have globally moved by approximately 50 kJ/mol, in favour of water. Finally, for Si/Al = 3, the same trends hold. For site-II, NO and NO_2 overcame the interaction of water by 83.6 and 17.3 kJ/mol respectively while CO stayed below by 24.3 kJ/mol. For site-IV, NO was once again the only one to overcome water by 27.3 kJ/mol, leaving NO_2 and CO lower by H_2O by 58.0 and 73.6 kJ/mol.

Cross-adsorption enabled a sharper adsorption of NO_2 in respect to water. The structure with Si/Al = 5, contains two Fe atoms close to each other (one on site-II and one on site-IV), and Si/Al = 3 contains three, giving rise to two new different adsorption configurations for NO_2: Bridged 1) between site-II and site-IV (cross-II-IV), and 2) between two different site-IV (cross-IV-IV). In the case of Si/Al = 5 only cross-II-IV is possible, which presented higher interaction energy than the corresponding site-II by 57.7 kJ/mol and lower for site-IV by 20.7 kJ/mol. As for Si/Al = 3, cross-II-IV appeared again with an interaction energy higher than both site-II and site-IV by 28.7 and 6.6 kJ/mol respectively. On the contrary, cross-IV-IV adsorption energy was quite increased compared to site-IV. This configuration surpassed even water in adsorption energy by 5.3 kJ/mol.

Table 4.2: Total interaction energies of the gases with the cations on site II (denoted as II), IV (denoted as IV) and areas between two of them (denoted as II-IV and IV-IV). (Energy / kJ/mol).

	NO	NO_2	CO	H_2O	CO_2
11_{II}	-194.5	-118.9	-83.1	-107.3	-40.5
5_{II}	-188.3	-105.9	-81.6	-94.8	-37.5
5_{IV}	-227.7	-142.9	-121.3	-189.2	-80.0
5_{II-IV}		-163.6			-69.4
3_{II}	-184.3	-117.0	-76.4	-100.7	-34.6
3_{IV}	-224.4	-139.1	-123.5	-197.1	-66.5
3_{II-IV}		-145.7			-73.7
3_{IV-IV}		-202.4			-51.0

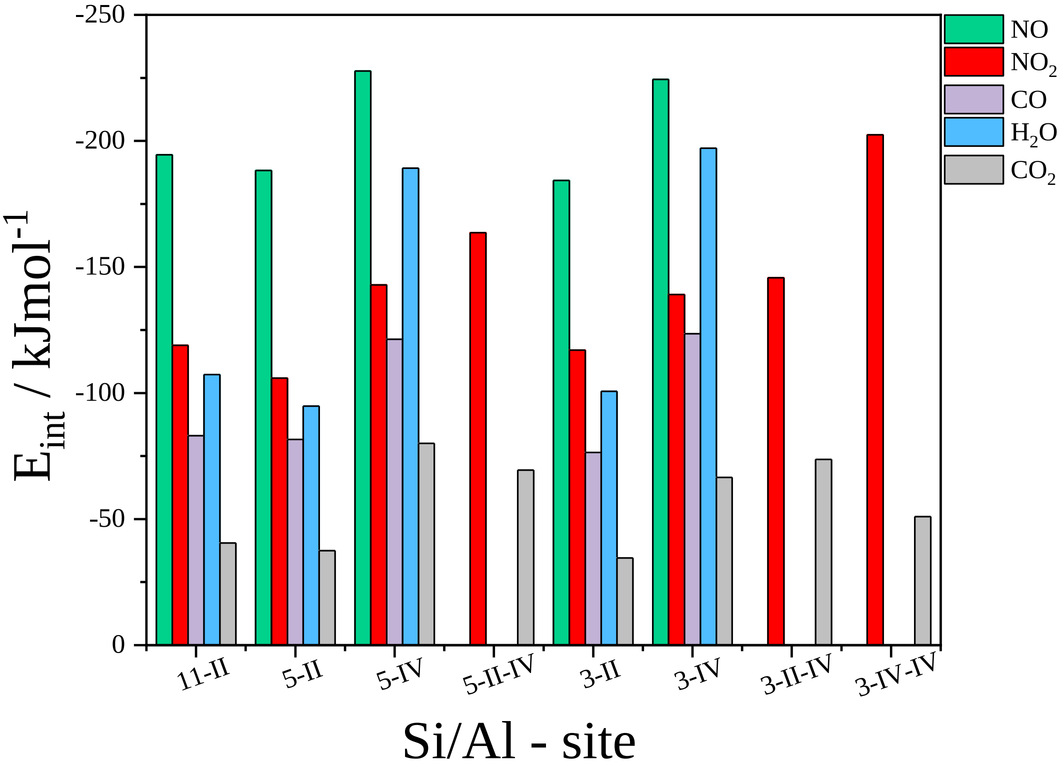

Figure 4.4: Interaction energies computed at the PBE+D2+U level of theory of NO, NO_2, CO, H_2O and CO_2 on divalent iron embedded CHA, considering cations on site-II (denoted as II), IV (denoted as IV) and areas between two of them (denoted as II-IV and IV-IV).

4.3.3 Molecular dynamics for chabazite with Si/Al = 3

Ab-initio molecular dynamics is employed to harvest accurate energy results and shed light on the impact of steam on the trapping efficiency. Lower Si/Al ratios are more interesting for low-temperature NO_x adsorption, as they contain more cations and higher chances for Al atoms to be close to each other, permitting the stabilization of Fe^{2+}. Hence, Si/Al = 3 was chosen for that study. The initial positions of the gases, where on site-II. This guess was made, because, if the gases were placed randomly, they would adsorb on site-IV, due to the stronger interaction. On the contrary, placing them on site-II, may reveal, whether the gases will spontaneously migrate to site-IV.

The mean distance between cation and adsorbed gas was calculated, by a radial distribution function (RDF). As point of reference for the location of the gas, we used the location of C for CO, N for NO and N for NO_2. This distance was also calculated in the presence of n = 0, 1, 2, 3 and 4 H_2O molecules according to Figures 4.3, 4.4 and 4.5.

RDFs illustrate that the presence of steam does not affect the adsorptions of NO and CO. The peaks exhibit similar shape and height independently of the number of water molecules involved. An exception is observed in the case of NO_2, when two water molecules were considered. In this case, a secondary peak is depicted owing to a short-termed migration of NO_2 from site-II to site-IV.

The RDF of NO_2 is not presented when n = 0, as the gas escaped the bond barrier, impelled by the attraction of the cations on site-IV. The presence of water does not repel NO_2 away from site-II. On the contrary, water molecules screen the attractive potential of site-IV, due to their presence around the cations, forcing NO_2 to stay on site-II.

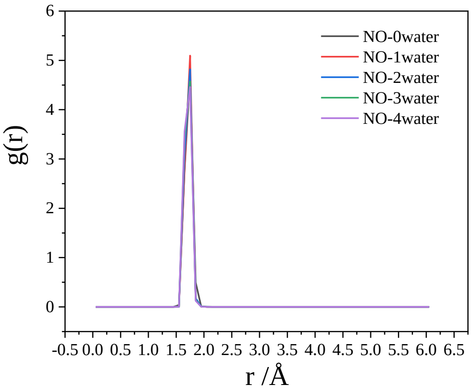

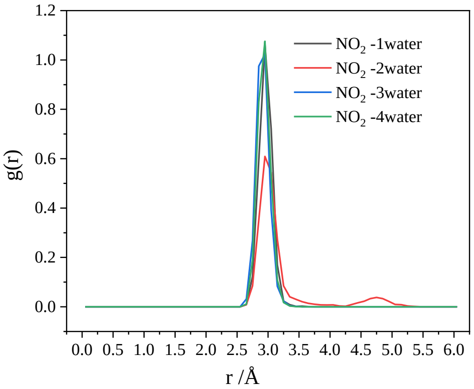

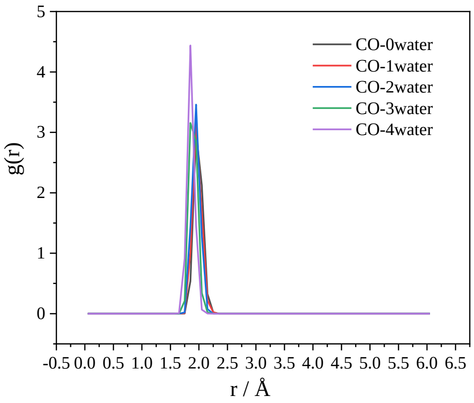

Figures 4.3, 4.4 and 4.5: RDFs between site-II Fe and {NO, NO_2, CO} respectively, in the presence of n = 0, 1, 2, 3 and 4 H_2O molecules. Isolated NO_2 RDF is omitted as it escapes site-II Fe.

The interaction energies obtained with molecular dynamics, which are gathered on Table 4.3, agree with the ones obtained with certain single configuration DFT calculations, proving the latter's worth. Dealing with CO, we found an interaction energy of -72.4 kJ/mol, in close agreement with the interaction energy on site-II. For H_2O, we found -189.0 kJ/mol, which agrees with site-IV adsorption. For NO, the interaction energy of -172.6 kJ/mol suggests that static DFT gives a slight overestimation, though agrees with site-II adsorption. Finally, NO_2 adsorption energy agrees with the cross-IV-IV value.

Table 4.3: The interaction energies calculated by MD, for the isolated gases at 298 K (at the corresponding site). (Energy / kJ/mol).

Si/Al	Gas	ΔE_{int}
3	NO	-172.6 (site-II)
	NO_2	-201.8 (cross-IV-IV)
	CO	-72.4 (site-II)
	H_2O	-189.0 (site IV)

4.4. Discussion

4.4.1 Thermodynamic assessment

The thermodynamic separation criterion is fulfilled by most of the cases considered above. Regarding CHA, site-II Fe exhibits stronger affinity for NO_x than for H_2O. Moreover, two closely located Fe^{2+}, which occupy site-IV can cross adsorb NO_2, leading once again to stronger adsorptions than water. Overall, NO is always preferred over water. Similar trends were found for MOR. NO is always preferred over water and NO_2 in all cases but 23_1-3. High Al concentrations favour NO_2 selectivity, offering the possibility of cross-adsorption. It needs to be pointed out that the high affinity for NO is itself an excellent finding of ours. The concentration of NO_x in the SCR section of the exhaust during cold starts, is mainly NO. Moreover, CO reduces NO_2 to NO, further shifting their chemical equilibrium. Because of that, several experimental studies have used only NO in the gas stream for the evaluation of PNAs[19,30,39,98].

Mordenite with Si/Al = 23 shows a high affinity relatively to the cells with Si/Al = 11 and 5. This excessive hydrophilicity of 23 is attributed to the H-bond that H_2O forms with the O atoms of the cell. This H-bond formation is prohibited in the other cells because of the deformation that the extra cations apply on the channel. Moreover, the introduction of Na atoms, close to Fe, strongly enhanced the selectivity of MOR towards NO_2. To sum up, high Al concentration favours the thermodynamic selectivity of NO_x for both MOR and CHA.

Despite molecular dynamics calculations are not suitable for mordenite, because of their high computational cost, chabazite gave strong evidence that our static DFT results are trustworthy. The RDFs further support the idea that NO_x resist water's competition for the adsorption sites, at least when there are several cations in the vicinity, which is expected in low-silica solids.

4.4.2. Bonding and regeneration analysis

The reoccupation of the adsorbent is crucial for the application in low-temperature NO_x capture. The adsorption of the gases is possible to catalyse the formation of by-products, which might lead to degradation of the zeolite. To challenge this possibility, we calculated the intramolecular bond elongation of the gases after adsorption. The latter phenomenon is rationalized while combined with Bader charge transfers and charge density differences due to adsorption. To perform this study, we used the cells with the lowest Si/Al ratios as they are the most interesting for the case of Fe(II), according to the analysis in 4.4.1.

Following ligand field theory[181] (LFT) on the adsorption site complexes, one can make predictions on the reordering of the d orbitals of Fe. When Fe is placed in the 6MR of CHA-3, it is 4-fold coordinated. If we treat the – O – groups as ligands according to Figure 4.5, we can notice that 1) The ligands are on on-plane; 2) The shape of the plane is between the square and the trigonal; 3) One O atom is much more distant from Fe than the others (2.18 Å). According to the LFT, it is sure that $d_{x^2-y^2}$ and d_{xy} orbitals are the most unstable due to the repulsions from the other ligands. Then, d_{z^2} follows, being more affected from the azimuthal ligands than d_{xz}, d_{yz}, due to its "donut" part. However, the difference between the last three orbitals, is predicted to be small, thus, their simultaneous occupation is not impossible according to molecular orbital theory. The adsorption of the gases provokes structural changes on Fe but does not change its coordination number to the plane. Then, when the ligand approaches Fe perpendicularly to the plane, the energy of the d_{z^2} orbital is increased due to the repulsion with the gas' electrons.

The Fe coordination on MOR clearly resembles a square plane. The square plane coordination predicted by LFT was analysed already for the 6MR of CHA-3 and it is the same for the 6MR of MOR-5.

Regarding the 8MR Fe on CHA-3, there is a pseudo-planar coordination, albeit slightly perturbed. Not only the fourth ligand of the square plane is missing in this case, but also the ligands are not placed exactly on a plane. As a consequence, we cannot make a prediction based on the LFT in this case. Two perspectives are provided in Figures 4.5c and 4.5d, depicting site IV.

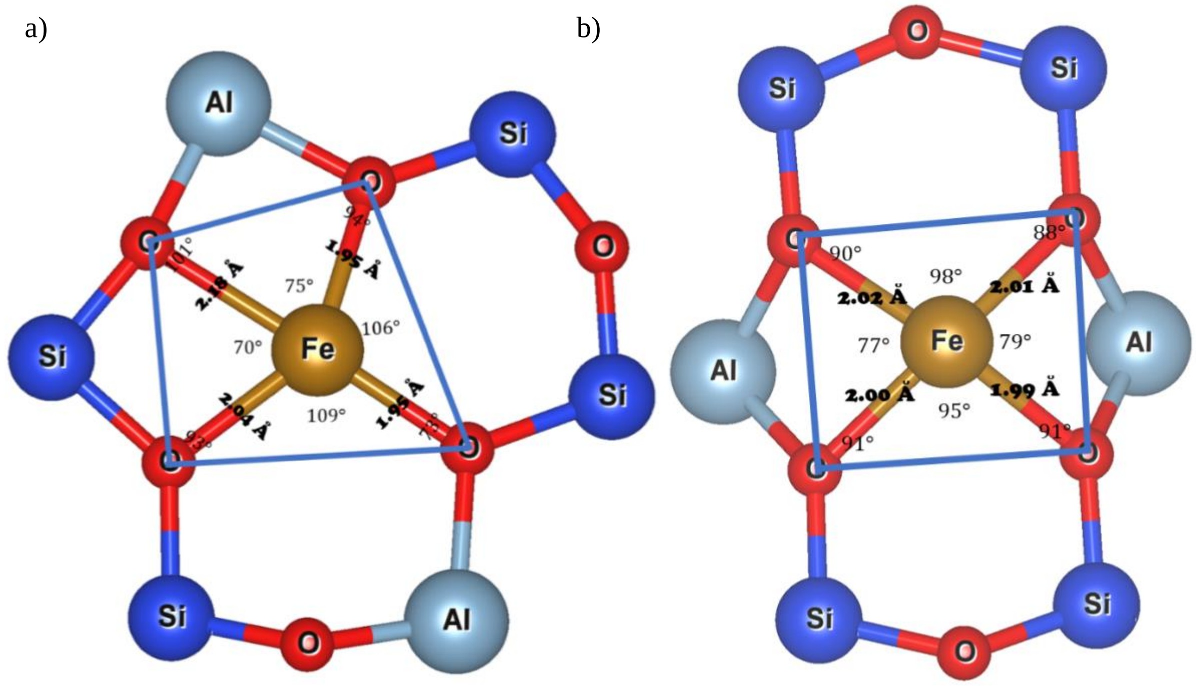

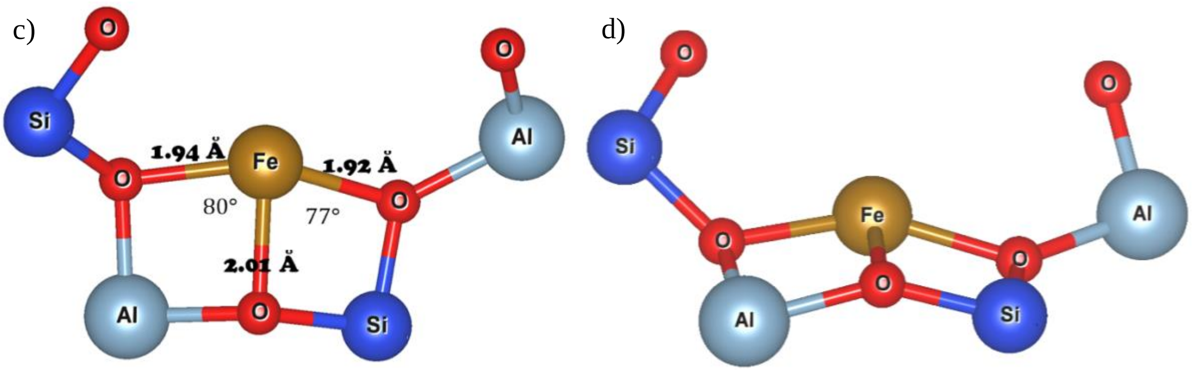

Figure 4.5: Fe placed a) on the 6MR of CHA-3, b) on the 6MR of MOR, c) and d) on the 8MR of CHA-3. Two figures are given for the 8-MR to illustrate the slightly perturbed plane.

Table 4.4: Bond elongations due to adsorption are reported for NO_x, CO and H_2O over both MOR and CHA with Si/Al equal to 5 and 3 respectively. The configurations treated for MOR are always over Fe with Al distributions 1-4, and for CHA, the ones obtained from MD calculations.

Gas species concerned	NO	NO_2		CO	H_2O	
Bond	N-O	O1-NO	O2-NO	C-O	H1-OH	H2-OH
Initial length (Å)	1.17	1.21	1.21	1.144	0.97	0.97
$Fe^{(II)}$ MOR-5 (Å)	0.00 (0%)	0.14 (12%)	0.00 (0%)	0.00 (0%)	0.00 (0%)	0.01 (1%)
$Fe^{(II)}$ CHA-3 (Å)	0.00 (0%)	0.07 (6%)	0.07 (6%)	0.00 (0%)	0.07 (7%)	0.01 (1%)

Table 4.5: Bader charge differences attributed to the adsorption of the gases on MOR with Si/Al = 5 on the left, and CHA with Si/Al = 3 on the right. The adsorptions for MOR have been performed on 1-4 site for all cases, but for CHA the locations are the same as for the MD calculations,

Mordenite	Atom	Charge Difference
Fe-NO	O	0.12
	N	-0.25
	Fe	0.00

Chabazite	Atom	Charge Difference
Fe-NO	O	0.09
	N	-0.20
	Fe	0.09

Fe-NO_2	O1	-0.24	Fe-NO_2	O1	-0.27
	O2	-0.19		O2	-0.25
	N	-0.04		N	-0.05
	Fe	0.05		Fe1	0.16
				Fe2	0.19
Fe-CO	O	0.07	Fe-CO	O	0.06
	C	-0.12		C	-0.09
	Fe	0.02		Fe	0.01
Fe-H_2O	O	-0.03	Fe-H_2O	O	-0.11
	H1	0.04		H1	0.10
	H2	0.05		H2	0.09
	Fe	-0.02		Fe	0.05

4.4.2.1 Fe-MOR-NO

NO adsorbs on the 6MR of MOR in a slightly bent configuration (see Figure 4.SIII). No bond stretching is predicted for N – O (Table 4.4). Bader charge transfers of 0.12, -0.25 and 0.00 e are distributed on O, N and Fe respectively (Table 4.5). A charge transfer of -0.13 e is predicted for NO. The interaction energy associated with this adsorption mode is -211.4 kJ/mol.

It is known from the literature that, the more bent the adsorption mode of nitrosyls, the more significant the adoption of NO^- character[182], as very recently shown in our previous study[162]. The insignificant charge transfer predicted in this case, is in line with this rule. Figure 4.6a depicts the Fe d_{z^2} depopulation, which is attributed to the expected increase in energy, according to the LFT discussion. A charge excess is depicted for d_{xz} and d_{yz}, which now, are far more stable than d_{z^2}. The empty d_{z^2} is available for σ-donation by the HOMO-1 of NO, which is allowed by arrangement of the atoms in space. Similarly, the electron-rich d_{xz} and d_{yz} donate charge to the antibonding LUMO of NO through π-backdonation. The degeneracy of the two LUMO is lifted due to the slight bent of NO. A series of new bonding orbitals is now permitted between d_{z^2} and HOMO-1, and d_{xz}/d_{yz} and $\pi^*_{p_x}/\pi^*_{p_y}$. The balance between σ-donation and π-backdonation ends up with a slight charge transfer on NO.

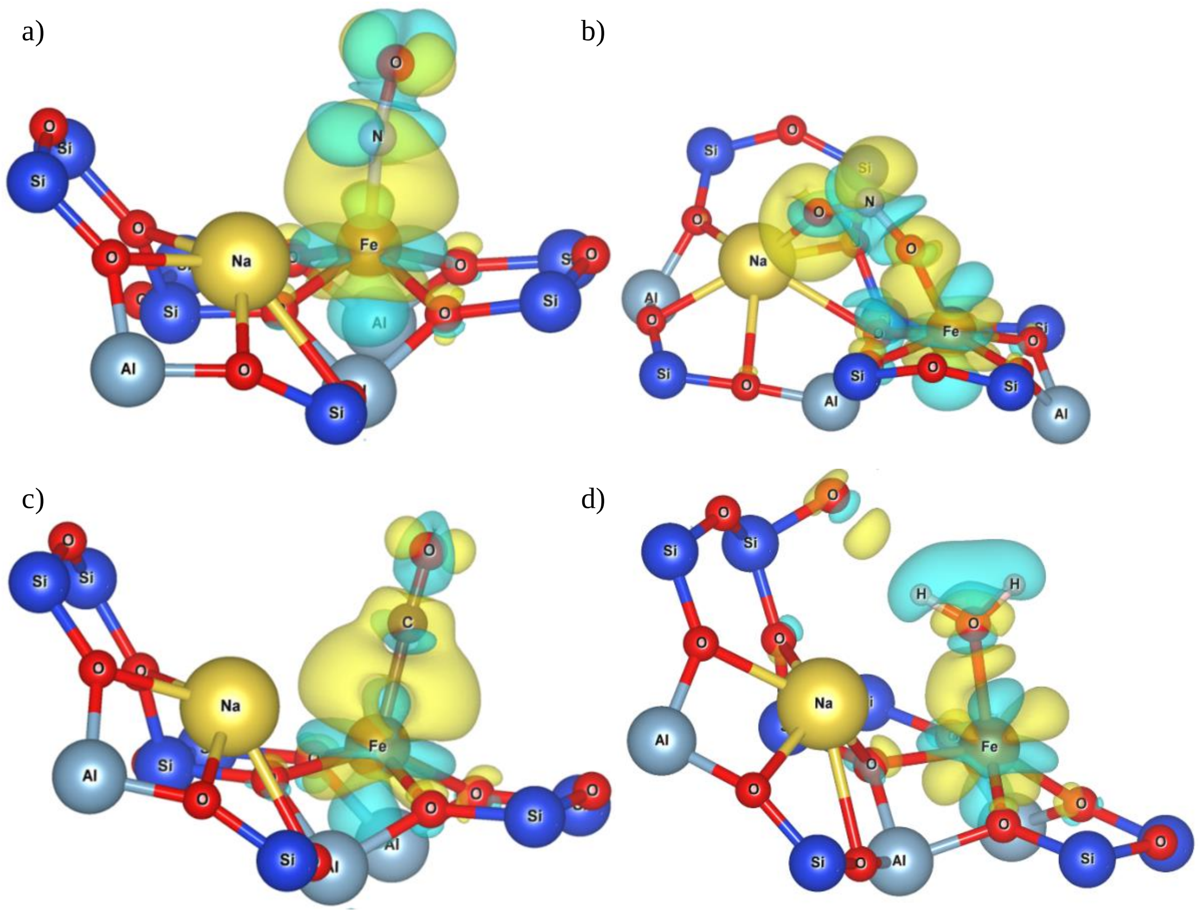

Figure 4.6: The charge density differences that occurred during the adsorption on FeMOR-5, of a) NO, b) NO_2, c) CO and d) H_2O. The isosurfaces have a density of 0.002 e/Å^3.

4.4.2.2 Fe-MOR-NO_2

NO_2 adsorbs on both Fe and Na simultaneously (see Figure 4.SIII). Bond stretching of 0.14 (12%) and 0.00 (0%) (Table 4.4) is calculated for N – O1 and N – O2 respectively. Bader charge transfers of -0.24, -0.19, -0.04 and 0.05 e (Table 4.5) are distributed to O1, O2, N and Fe respectively. A charge transfer of -0.47 e is predicted for NO_2. The interaction energy associated with this adsorption mode is -162.8 kJ/mol.

NO_2 has its HOMO semi-occupied, similar to NO. NO_2 can accept e^- by its LUMO, and donate by its HOMO-1, through π-backdonation and σ-donation respectively. NO_2 approaches Fe from a bent angle, limiting the destabilization of d_{z^2}. The N – O1 bond is less activated in this case than during single cation adsorptions[162]. The non-bonding interaction of O2, with Na, polarizes the electron density of NO_2, increasing the interaction energy. Figure 4.6b depicts all these phenomena.

4.4.2.3 Fe-MOR-CO

The adsorption of CO on MOR occurred perpendicularly to the 6MR of MOR (see Figure 4.SIII). Thus, it is not affected by the presence of Na cations. The O – C was not stretched at all. Bader charge transfers of 0.07, -0.12 and 0.02 e were calculated for O, C and Fe respectively. A very small transfer of -0.05 is predicted for CO due to the adsorption. The interaction energy associated with this mode is -92.8 kJ/mol.

The bond angle Fe – C – O is almost linear, with small deviations due to steric effects. The electron configuration of CO is very similar to NO. Yet, CO is closed-shell with a significant band gap opening. Thus, the formation of the bonds between d_{xz}/d_{yz} and $\pi^*_{p_x}/\pi^*_{p_y}$ are hindered. This is the reason of the small interaction energy compared to NO. For the same reason, the π-backdonation is less significant for CO.

4.4.2.4 Fe-MOR-H_2O

According to Table 4.4, elongation of 0.00 (0%) and 0.01 (1%) Å is predicted for H1 – O and H2 – O. Bader charge transfers of -0.03, 0.04, 0.05 and -0.02 e are distributed to O, H1, H2 and Fe (Table 4.5). Charge is transferred towards Fe, due to water being unable to accept e^- charge.

H_2O adsorbs on Fe through O, forming an acute angle with the 6MR (see Figure 4.SIII). As this angle tends to 45° the formation of a H-bond with the framework becomes possible. However, the bond between the d_{z^2} and the HOMO of water, keeps the latter in a perpendicular conformation, preventing the H-bond formation. At the same time, repulsions between the electron density of H_2O and d_{z^2}, destabilize the latter, resulting in depopulation of d_{z^2} and population of d_{xz}/d_{yz}.

4.4.2.5 Fe-CHA(SII)-NO

NO adsorbs in a slightly bent mode on the 6MR of CHA-3 (see Figure 4.SIII). No bond stretching is predicted for N – O (Table 4.4). Bader charge transfers of 0.09, -0.20 and 0.09 e are distributed on O, N and Fe respectively (Table 4.5). The sum of -0.11 e is transferred on NO. The interaction energy associated with this adsorption mode is -184.3 kJ/mol. The smaller interaction compared to MOR, is attributed to the stabler coordination that the ring of CHA permits. Figure 4.7a reveals the same charge density difference characteristics as the adsorption on MOR-5.

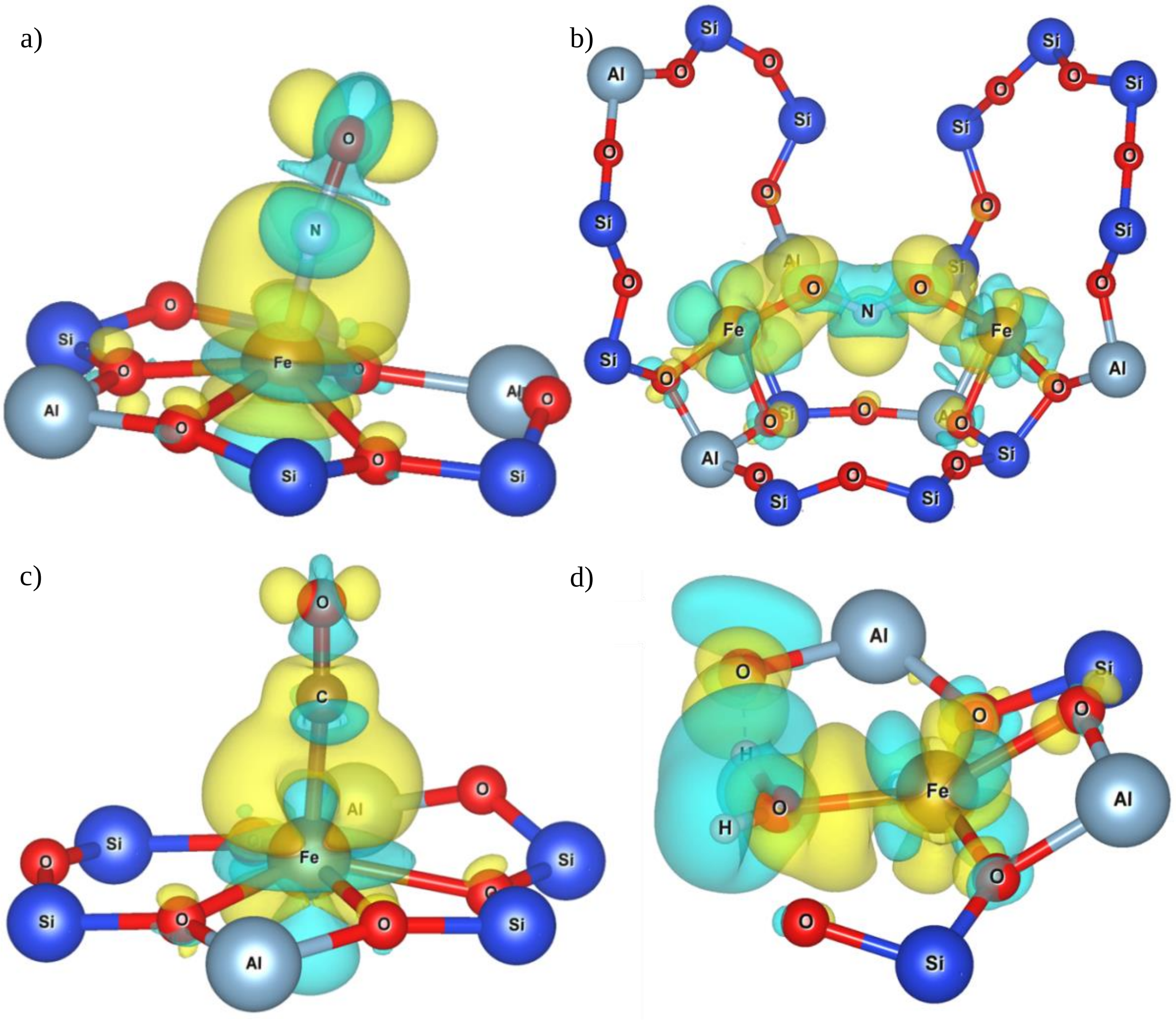

Figure 4.7: The charge density differences that occurred during the adsorption on FeCHA-3, of a) NO, b) NO_2, c) CO, and d) H_2O. The isosurfaces have a density of 0.002 e/Å^3.

4.4.2.6 Fe-CHA(SIV-SIV)-NO_2

The cross-adsorption of NO_2 between two site-IV Fe cations is presented on Figure 4.SIII. Bond stretching of 0.07 Å (6%) is predicted for both N – O1 and N – O2. Bader charge transfers of -0.27, -0.25 and -0.05 were distributed on O1, O2 and N, while Fe1 and Fe2 obtained 0.16 and 0.19 e. A strong interaction of -202.4 kJ/mol is associated with this sorption.

Figure 4.7b illustrates the charge density difference that occurs during the adsorption of

NO2 between two site IV placed Fe. Unlike adsorption on MOR, the adsorption of NO_2 induces depopulation of d_{xz} and d_{yz} and not d_{z^2}. In fact, the shape of the newly formed orbitals reveals strong contribution of the LUMO of NO_2, but the identity of the d orbitals around Fe is not clarified by the charge density difference representation given in Figure 4.7b. The confinement of the gas between the cations prevents the strong activation of the NO_2 bonds.

4.4.2.7 Fe-CHA(SII)-CO

No bond elongation is predicted for the adsorption of CO on the 6MR of CHA-3. Bader charge transfers of 0.06, -0.09 and 0.01 e are distributed on O, C and Fe. The very low charge transfer is the result of the weak π-backdonation to its LUMO. The interaction energy of this adsorption is equal to -76.4 kJ/mol. The bonding analysis is omitted, being the same as the one associated with MOR-5.

4.4.2.8 Fe-CHA(SII)-H_2O

The adsorption of H2O on site-IV of CHA-3 is presented in Figure 4.SIII. The O – H1 and O – H2 were stretched by 0.07 (7%) and 0.01 (1%) Å, respectively. Bader charge transfers of -0.11, 0.10, 0.09 and 0.05 were distributed on O, H1, H2 and Fe, respectively. The interaction energy of -197.1 kJ/mol was calculated for this mode.

Like in the case of NO_2, adsorption of H_2O induces increase of the d_{z^2} population and depopulation of another clover shaped orbital. As the ligands are not distributed on the edges of a perfectly planar geometry, $d_{x^2-y^2}$ orbital is not oriented along the bonds. The limited repulsion felt by d_{z^2} after the adsorption, increases its population. In addition, charge density leaves the H atoms of water transfers towards the space between the gas and the cation. The H-bond formed with the O atom of the framework, induces a charge reorientation around the O atom and enhances the polarization of water. All of these aspects are illustrated on Figure 4.7d.

4.5 Conclusion

To sum up, we provided promising results on the implementation of Fe^{2+} – supporting chabazite and mordenite as PNA. The study is based on static PBE+D2+U at O K and state-of-the-art ab-initio molecular dynamics at 297 K. The low-price of the studied zeolites as well as of Fe might render these materials worthy substitutes for the, up to now best, nonetheless extremely expensive, Pt^{2+} and Pd^{2+}. The current findings call for the synthesis of these solids and their actual testing as PNA.

To conclude, the bond stretching calculations reveal weak intramolecular bond activations on the gases. In the past it was predicted that adsorption of NO_2 on Fe^{2+} promoted Y zeolite, causes serious N – O1 activation. In this study, we reveal that the extended bond stretching is not present in the cases of cross-adsorption. This is a very consequential finding, which restores the interest of Fe^{2+} promoted zeolites, as PNA candidates.

4.6 Computational study of iron zeolites for selective capture of NO_x and CO against H_2O and CO_2

Electronic Supplementary Information

23

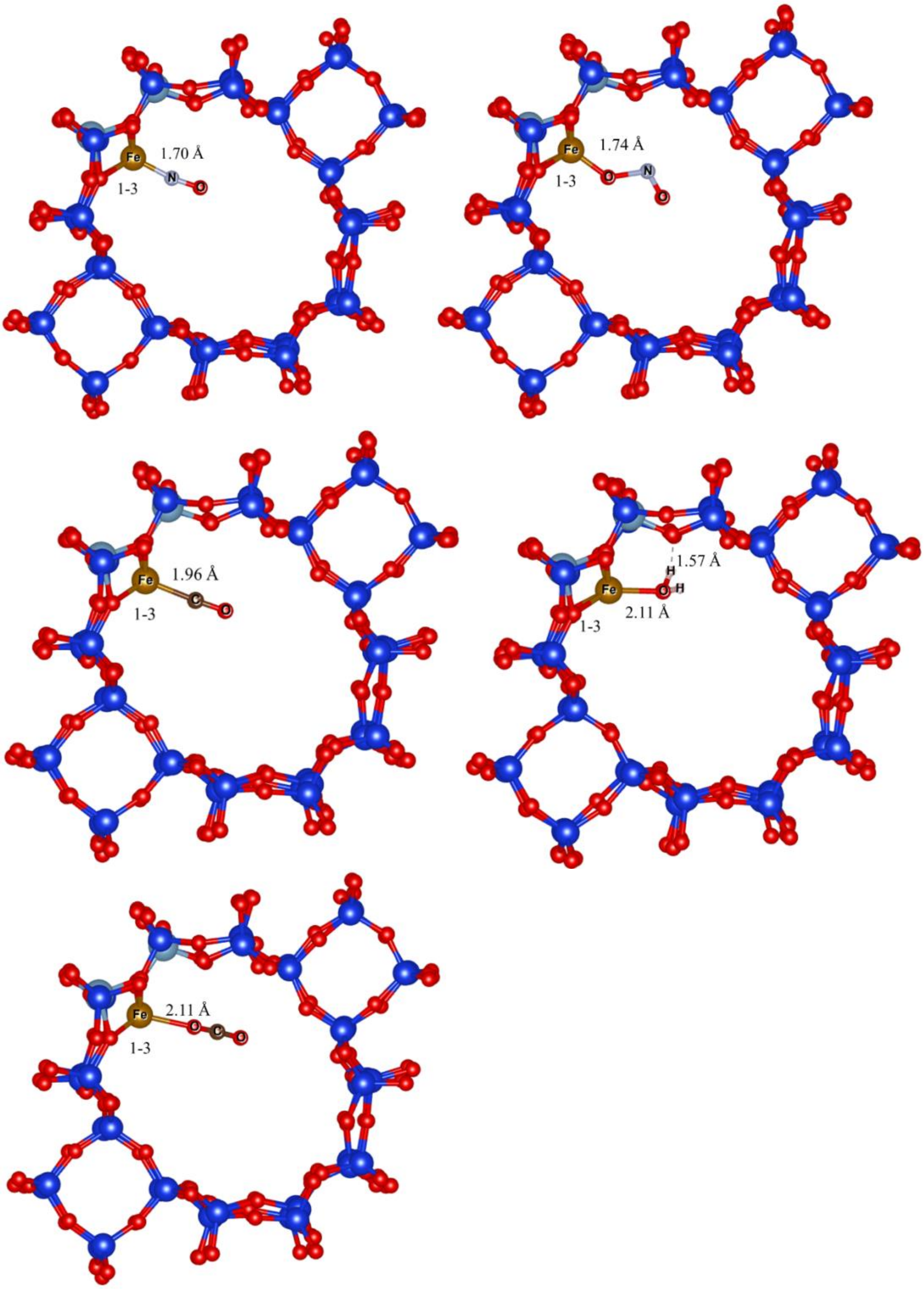

Figure 4.SI: Adsorption modes of the gases NO, NO_2, CO, H_2O, CO_2, over Fe-MOR-23. The Al distribution of the ring and the bond length are also mentioned.

11

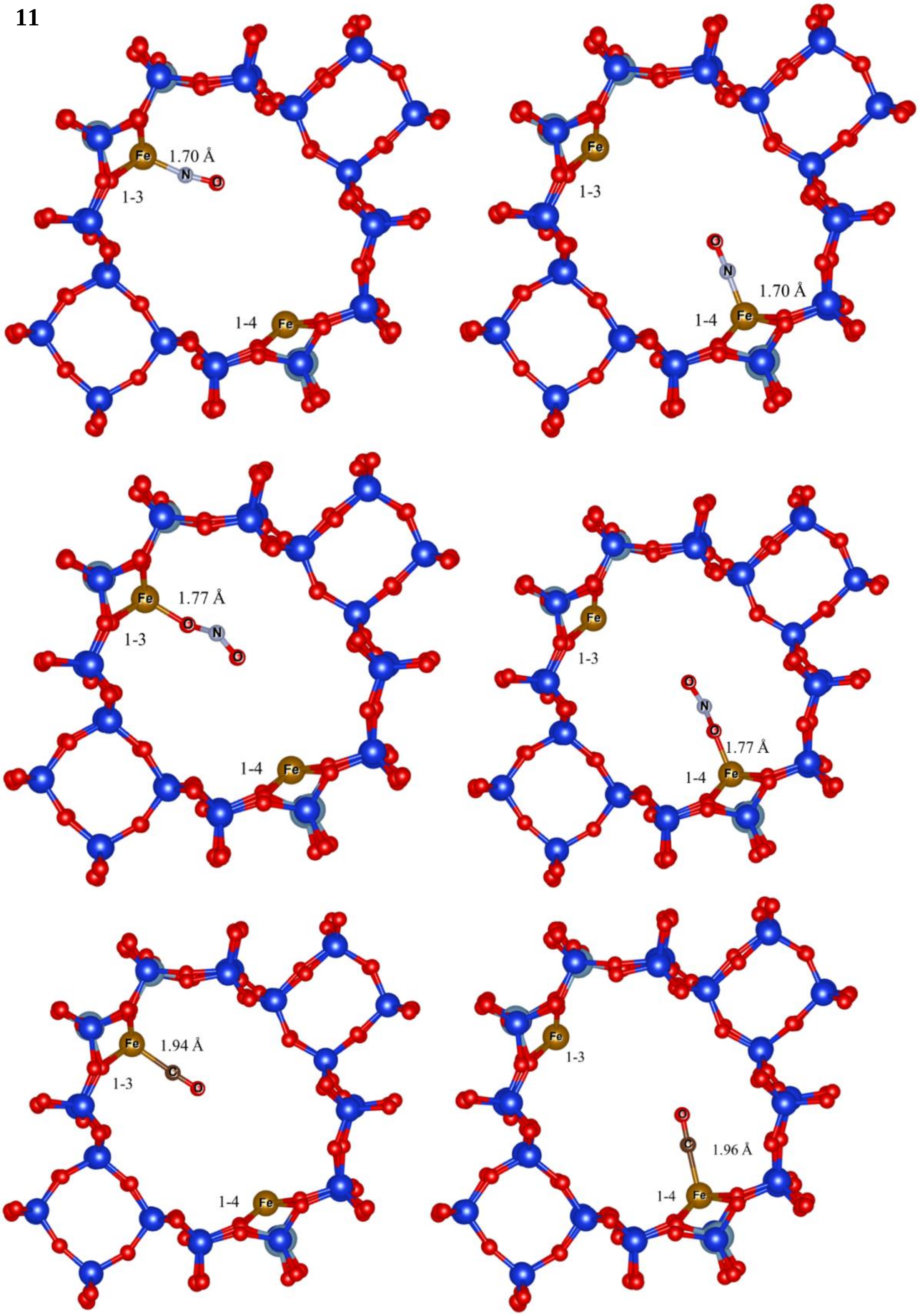

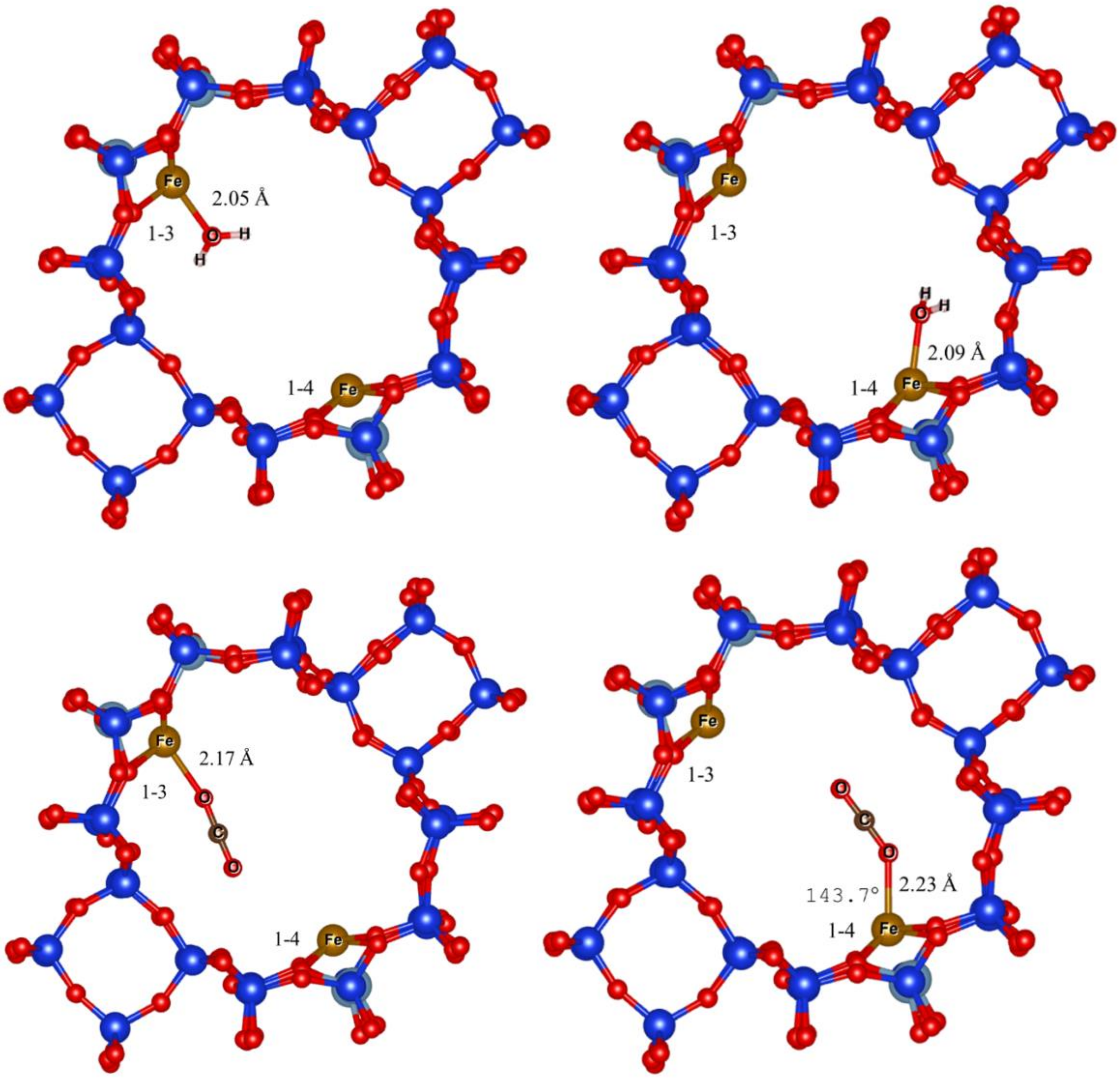

Figure 4.SII: Adsorption modes of the gases NO, NO_2, CO, H_2O, CO_2, over Fe-MOR-11. The Al distribution of the rings and the bond length are also mentioned.

5

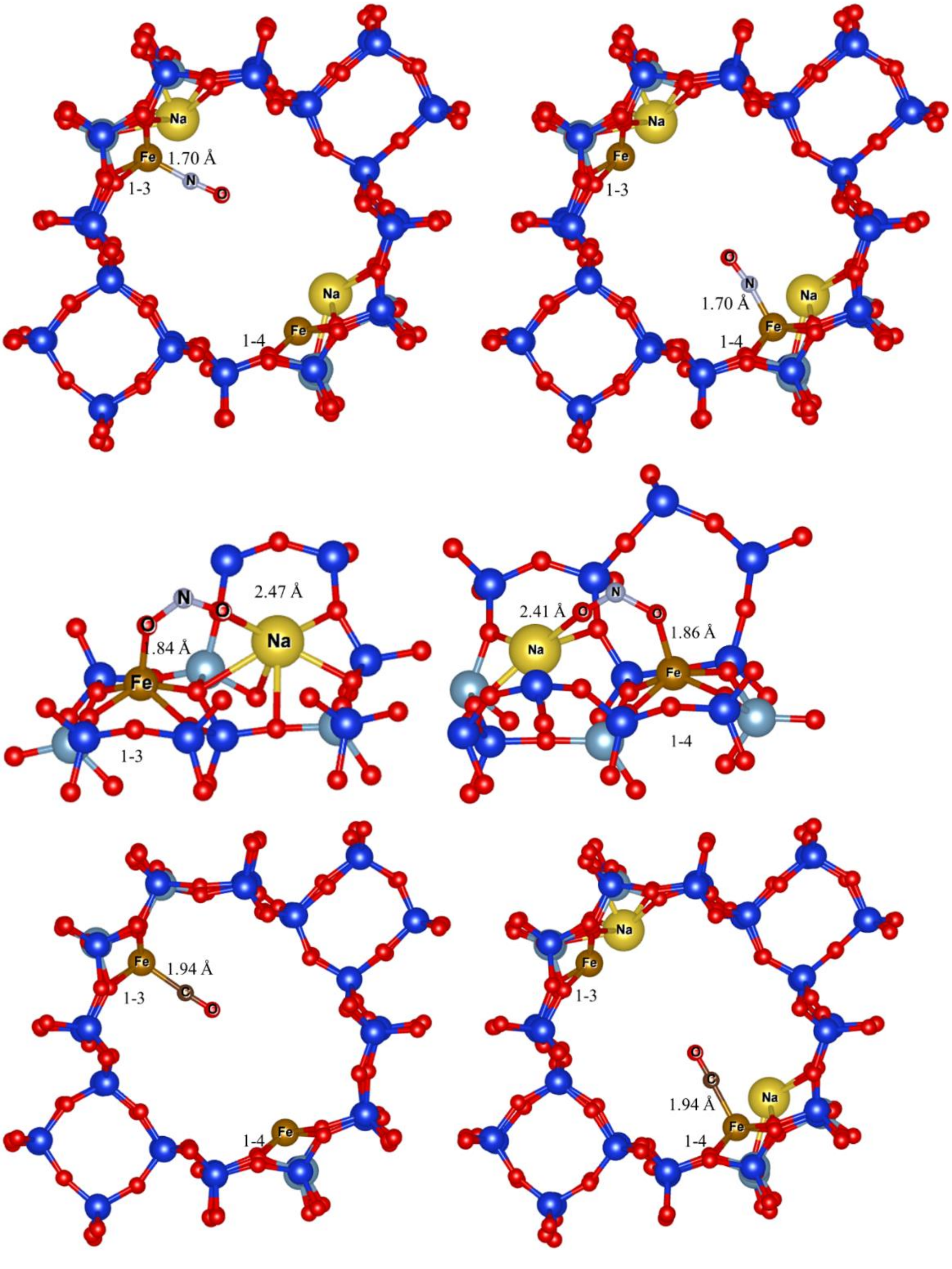
Na
Fe
1.70 Å
N
O
1-3
Na
Fe
1-4
Na
Fe
1-3
O
N
1.70 Å
Na
Fe
1-4
N
O
2.47 Å
O
Na
1.84 Å
Fe
1-3
N
2.41 Å
O
O
1.86 Å
Na
Fe
1-4
Fe
1.94 Å
C
O
1-3
1-4
Fe
Na
Fe
1-3
O
C
1.94 Å
Na
Fe
1-4

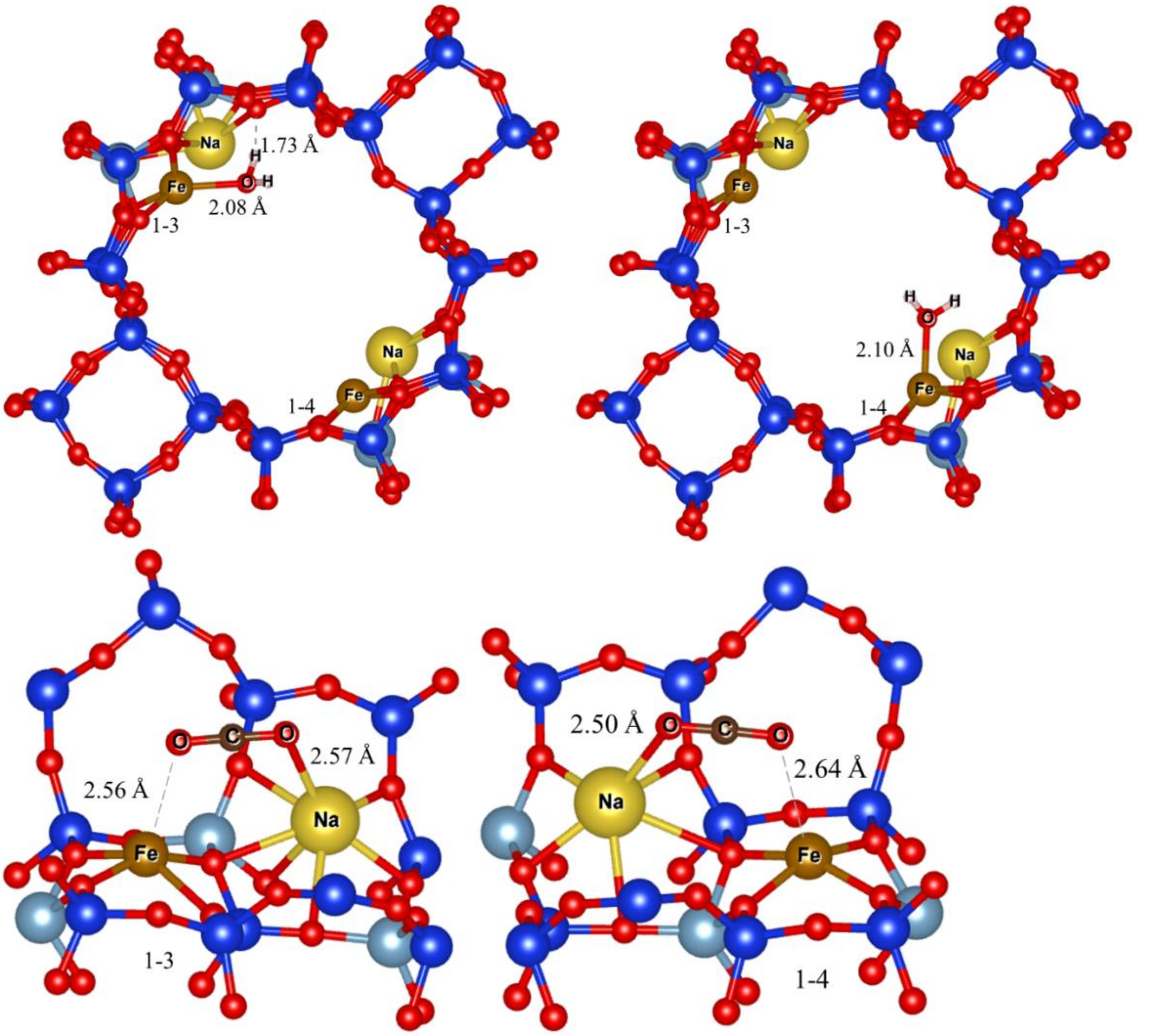

Figure 4.SIII: Adsorption modes of the gases NO, NO_2, CO, H_2O, CO_2, over Fe-MOR-5. CO_2 and NO_2 were adsorbed by two cations at the same time, thus an alternative perspective is provided for them. The Al distribution of the rings and the bond length are also mentioned.

11

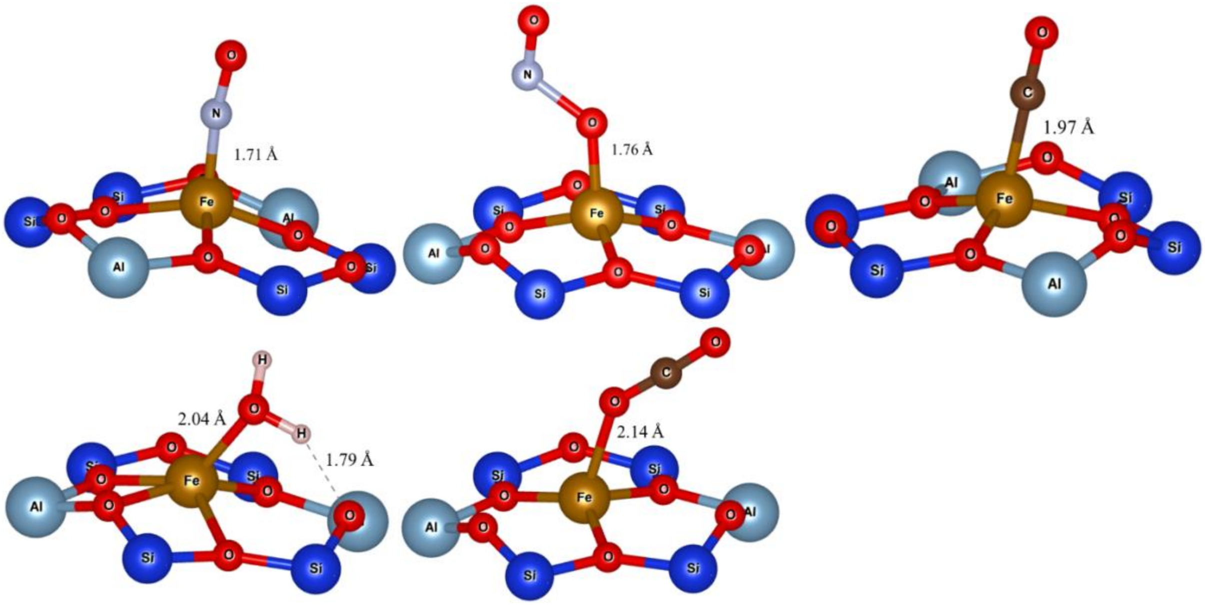

Figure 4.SIV: Adsorption modes of the gases NO, NO_2, CO, H_2O, CO_2, over Fe-CHA-11 on the 6MR. The bond length is also mentioned.

5

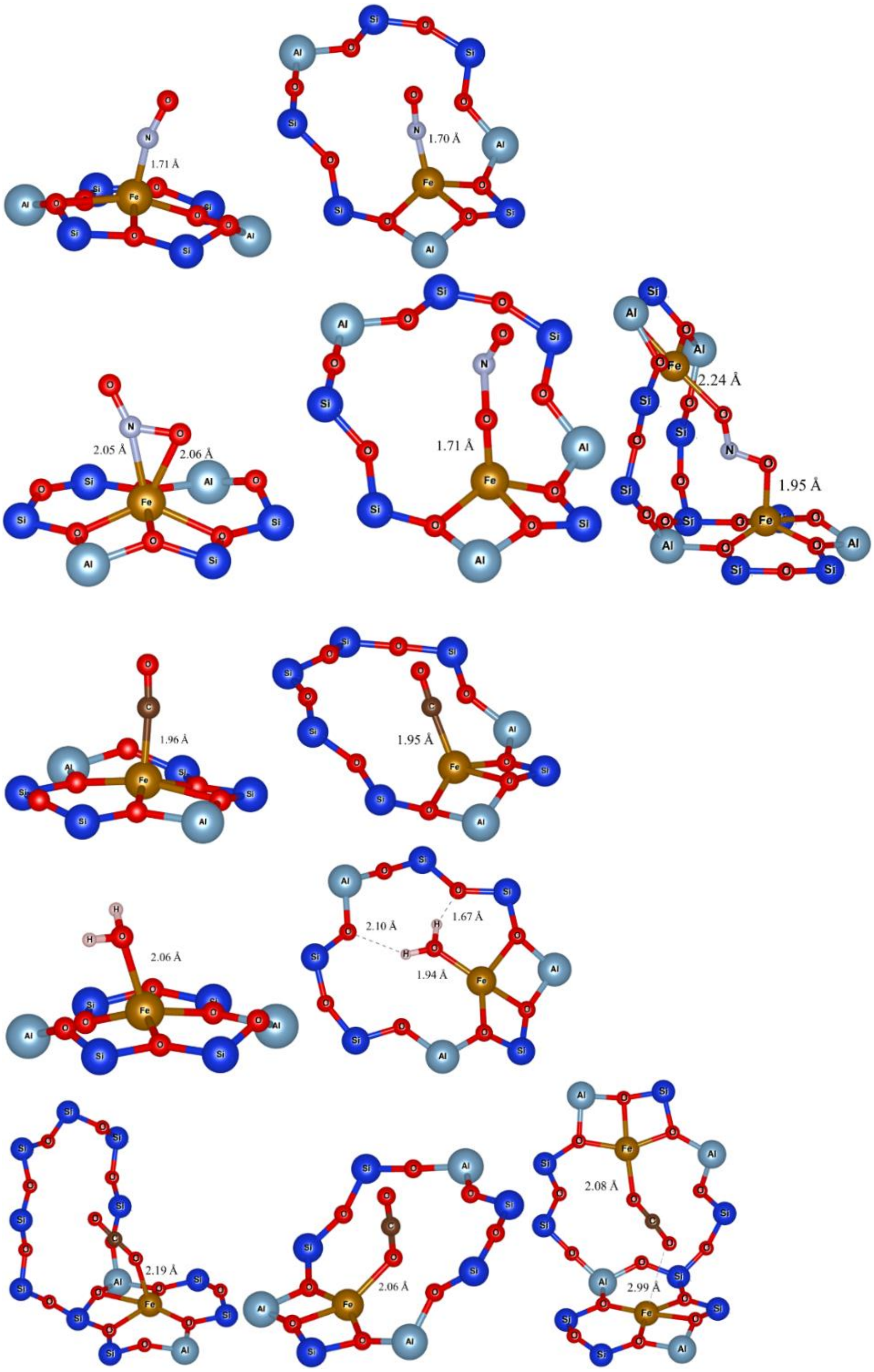

Figure 4.SV: Adsorption modes of the gases NO, NO_2, CO, H_2O, CO_2, over Fe-CHA-5 on the 6MR and 8MR. Cross adsorptions are feasible for the dioxides. The bond length is also mentioned.

3

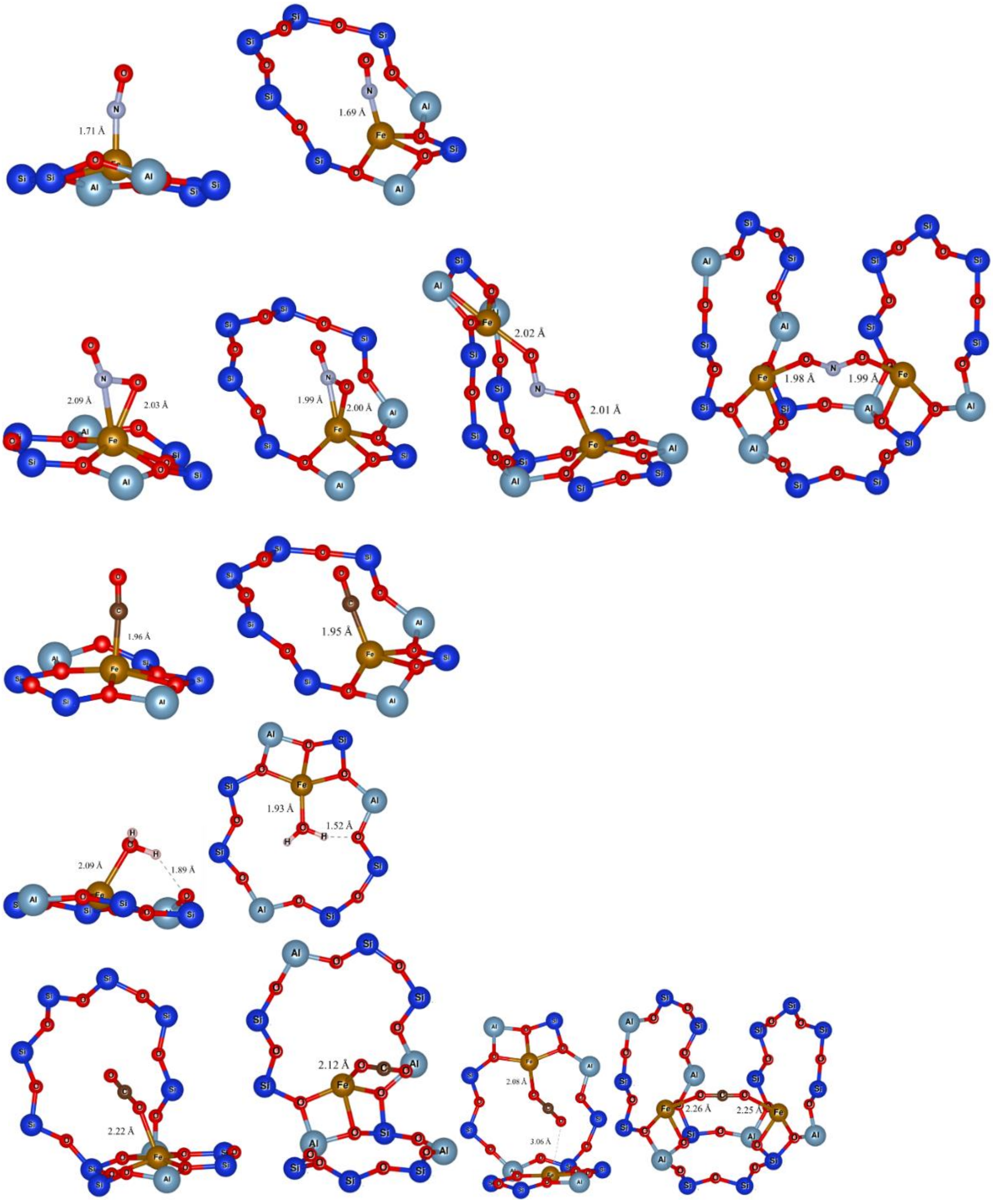

Figure 4.SVI: Adsorption modes of the gases NO, NO_2, CO, H_2O, CO_2, over Fe-CHA-5 on the 6MR and 8MR. Cross adsorptions are feasible for the dioxides. The bond length is also mentioned.

5. Adsorption of NO and NO_2 on Pure and Transition Metal-Promoted Amorphous Silica Surfaces

5.1. Introduction

NO_x air pollutants (NO and NO_2) coming from human activity constitute a serious threat to the atmospheric balance and human health. They can worsen the condition of asthmatic and allergic individuals if inhaled systematically, as well as disturb the normal functioning of the respiratory system[3]. Moreover, NO_x strongly affect the concentration of greenhouse gases in the atmosphere through complex chemical processes[1]. NO_x inhalation is especially harmful for people working in closed spaces, without ventilation.[3,183] The current study is part of a greater project of *Institut national de recherche et de sécurité* (INRS), opting to limit NO_x emissions from diesel engine exhaust gases.

Methods to limit NO_x emissions are already available and well known. *NO_x storage reduction* (NSR)[11,12], and *selective catalytic reduction* (SCR)[13,14], are the two major technologies used for NO_x abatement. NSR and SCR can achieve exceptionally high conversions to harmless N_2. However, at temperatures below 200 °C, the catalysts do not work efficiently. Diesel engines that work discontinuously through the day undergo a series of cold starts, ending up with long periods where NO_x are free to be released[19,24,25].

Low-temperature (< 200 °C) NO_x traps have been designed, which release the latter when the temperature is high enough for the catalysts to be efficient, the *passive NO_x adsorbers* (PNA)[30]. PNAs have to be chemically inert in the operational temperature range of the diesel exhaust gases, and in high humidity, as well as low-cost to be suitable for production in an industrial scale. Silica based materials are exceptional PNA candidates because not only they fulfil the aforementioned conditions, but also, they have tuneable gas affinities. The tuning can be achieved by introducing cations with different electronic configurations.

Hessou et al. employed DFT to calculate the interaction energy of a series of monovalent cations promoted faujasite, with NO_x and H_2O[96]. Daouli et al. did the same but for divalent exchanged faujasite[161]. Among the cations they explored, they singled out Cu^+, Pt^{2+} and Pd^{2+} as selective towards NO_x. *Cold start concept* catalysts (CSC), combine the utility of PNA with low-temperature catalytic activity, presenting quite satisfying performances[19,158]. Both PNA and CSC have been found to achieve significant NO_x abatement.[19,158]

In this DFT study we investigate the potential of amorphous silica embedded with transition metals as passive NO_x and CO adsorber, based on their difference in interaction energy with H_2O and CO_2. Amorphous silica is one of the most widely used supports for transition metals, combining high mechanical resistance, potential for chemical modification and dielectric strength[65–69]. Amorphous silica pore sizes are not standard, but they exhibit distributions strongly favouring medium sizes[70–72]. Their smaller pore diameters compared to the large-pored faujasite, translates into lower diffusion rates of the adsorbed gases[73,75,184]. Transition metals can be grafted in amorphous silica as monomers, dimers or clusters[65]. Among the transition metal nanoparticles that are grafted in amorphous silica, there are sizes and shapes with particularly high stability[76–78].

Currently, periodic DFT is used to assess the trapping efficiency and selectivity of Ni, Co, Fe and Cu^+ clusters supported on amorphous silica and compare it to bare silica matrix. The $magic\ number\ n = 13$ (icosahedron)[77,78,185] is used throughout this study for the transition metal clusters, as a highly stable species, supported amorphous silica with a silanol density of $3.3\ OH/nm^2$, which was previously synthesized[65,79,80]. This is the first time to study theoretically a) transition metal clusters for the abatement of diesel-fume NO_x and CO and b) amorphous silica as substrate for this purpose.

5.2. Computational methods

Our periodic spin polarized density functional theory calculations were performed using the Vienna ab initio simulation package (VASP-5.4) code[186] based on the projector augmented wave method[187] with an energy cutoff of 450 eV. The Perdew, Burke, and Ernzerhof (PBE) functional[188] was employed to account for the exchange correlation, in conjunction with the rotationally invariant PBE+U approach[189,190] as available in VASP. The U and J Hubbard parameters were set to 3.0 eV and 0.9 eV, respectively, to describe correctly the on-site Coulomb repulsion of the $3d$-states in transition metals (Iron, Cobalt, Nickel, and Copper)[191,192]. The structural, electronic, and magnetic properties of the transition metal clusters that are available in the literature, are well reproduced by these parameter values[193–197] The weak van der Waals interactions are taken into account within the Grimme's D2 approach as implemented within VASP[198,199].

To separate the periodically repeated slab, a vacuum of 20 Å was used along the crystallographic *c* direction. We used only the Γ point for the integration of the first Brillouin zone because of the large system size. The convergence threshold of the difference of the Kohn–Sham self-consistent total energy was set to 10^{-6} eV. For the structural optimizations, we relaxed all the atomic positions of the considered molecules, transition metal clusters, and the first silica surface plane, while the other planes are frozen. The force criterion on all relaxed atoms was fixed to 0.03 eV/Å.

5.3. Results & discussion

5.3.1 Geometrical models

The amorphous silica surface considered in the present work was modelled by Comas-Vives via a dehydroxylation of an entire hydroxylated surface of 402 atoms per periodic super cell. The typical silanol density of 3.3 is the result of various synthesis pathways of mesoporous silica under vacuum conditions at 200°[200–205]. The surface used in this work, was modelled with a super cell of 375 atoms; 46 hydrogen, 227 oxygen, and 102 silicon atoms[206].

The transition metal (Fe, Co, Ni, and Cu) clusters have been modelled with 13 atoms and adopt the D_{3d} symmetry[207,208]. The small magic cluster number of 13 was also adopted for other nanoparticles such as Ga and Pt. This model exhibits a high dynamic stability and corresponds to the size of experimentally observed transition metal nanoparticles on SBA-15. In previous works, Gueddida et al. have studied the adsorption mechanism of Fe, Co, Ni, and Cu species with different forms (monomers, dimers, clusters) on various silica surfaces with different silanol density ranged between 1.1 and 7.2 OH per nm^2. They identified the most stable (energetically) adsorption configuration for each heterogeneous catalyst. The Ni_{13} clusters are energetically more stable than those of Fe_{13}, Co_{13}, and Cu_{13}, which is in good agreement with the experimental observations[191,192]. Therefore, for the supported amorphous silica surfaces, we used the corresponding stable adsorption structures.

5.3.2 Adsorption sites

Three possible adsorption sites of both NO and NO_2 molecules are considered: (1) on the silica surface, (2) on the top of the transition metal clusters, or (3) at the interface transition-metal-clusters@silica-surface. The 3.3 amorphous silica surface displays all possible adsorption silanol sites such as geminal, vicinal, isolated, nest-1, and nest-2, as shown in Figure 5.1. The geminal silanol group is defined as two OH groups bonded to the same silicon atom. The vicinal one is defined as a pair of silanols belonging to tetrahedra that share a common oxygen vertex. The two silicon atoms of the vicinal site are separated by an oxygen atom so that the two hydroxyl groups (SiOH) are separated by less than ~ 3 Å. A single SiOH group is called an isolated silanol when the distance to the closest SiOH groups is more than ~ 3.3 Å, so that it cannot be involved in a mutual hydrogen bond with the adsorbate. Nest-1 site is composed of a vicinal and an isolated silanol, while the nest-2 site is composed of a geminal silanol and an isolated silanol. Several geometrical structures of the grafted NO and NO2 molecules on the pure and the supported transition metal cluster silica surfaces were systematically investigated in order to find the most favourable adsorption configurations. For all systems, calculations were started from reasonable estimations for two interaction modes (flat or perpendicular O interactions).

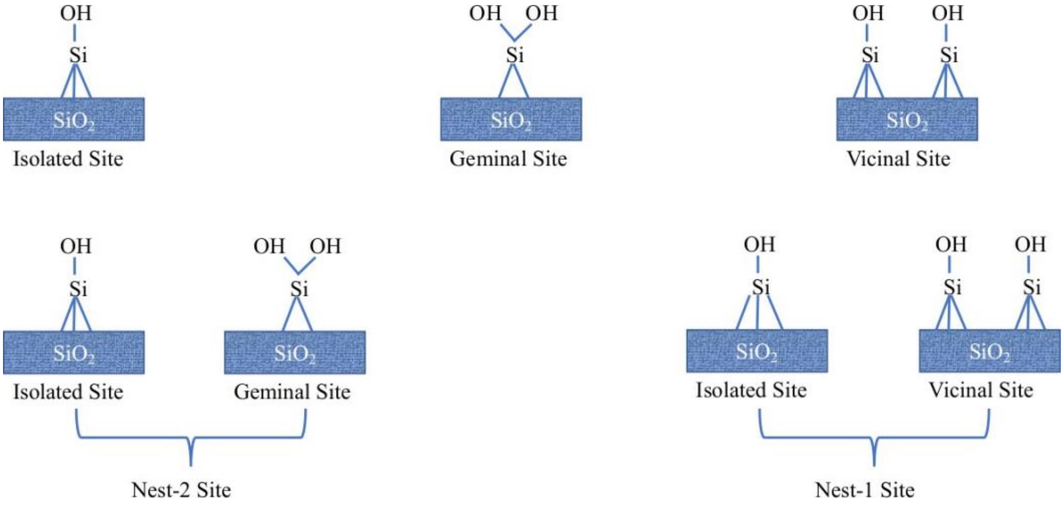

Figure 5.1: Different silanol sites existing on the considered amorphous silica surface SiO_2-3.3: geminal, vicinal, isolated, nest-1 and nest-2.

The corresponding interaction energies are given by:

$$\Delta E = E_{sys} - E_{mol} - E_{surf} \tag{5.1}$$

where E_{surf} is the total PBE+U+D2 energy of the pure or the supported silica surface, E_{mol} is the total PBE+U+D2 energy of NO or NO_2 molecule, and E_{sys} is that of the total system

(Molecule@pure/supported-silica-surface). In order to minimize the numerical errors, these energies were computed using the same super cell.

5.3.3. Pure 3.3 silica surface

Table 5.1 shows the computed PBE+D2 adsorption energies of the most configurations of NO and NO_2 on pure amorphous silica surface SiO_2-3.3 via perpendicular and flat O-interaction modes. Our calculations show that the NO molecule prefers flat adsorptions on nest-1, vicinal, nest-2, and geminal sites, with energy values of -71 kJ/mol, -95 kJ/mol, -74 kJ/mol, and -66 kJ/mol, respectively, while on the isolated site, NO is adsorbed through the perpendicular O-interaction mode with an adsorption energy of -90 kJ/mol.

Table 1: PBE+D2 computed adsorption energy of the most stable configuration of NO, and NO_2 on amorphous silica surface with a silanol density of 3.3 OH/nm^2. The blue-coloured values represent the maximum interaction energies of each molecule.

Molecule	Interaction mode	Isolated	Nest-1	Vicinal	Nest-2	Geminal
NO	Perp O-int	-90	-66	-65	-65	-64
	Flat O-int	-65	-71	-95	-74	-66
NO_2	Perp O-int	-66	-79	-75	-70	
	Flat O-int	-67	-78	-77	-79	-71

Similarly, NO_2 favours the flat O-interaction over all silanol sites with adsorption energies of -67 kJ/mol on the isolated site, -78 kJ/mol on the nest-1 site, -77 kJ/mol on the vicinal site, -79 kJ/mol on the nest-2 silanol site, and -71 kJ/mol on the geminal one. The perpendicular and flat O-interaction modes for NO on nest-1 are associated with similar adsorption energies, of -79 and -78 kJ/mol, respectively. We found that NO prefers vicinal silanol site via the flat O-interaction mode with a strong adsorption energy of -95 kJ/mol. A very close adsorption energy of -90 kJ/mol was also observed for the interaction of NO with the isolated silanol site through the perpendicular O-interaction mode. The adsorption of NO_2, on nest-1 and nest-2 silanol sites is associated with equal interaction energies of -79 kJ/mol. To conclude, we found that the maximum interaction energy of NO on the silica surface is higher than that of NO_2 by 16 kJ/mol, as pointed out on table 5.1, by the implementation of blue coloured values.

Table 5.2**:** Most stable configurations (in kJ/mol) computed within the PBE+U+D2 approximation for the interaction of NO and NO_2 on the supported Fe_{13}, Co_{13}, Ni_{13} and Cu_{13} silica surfaces (at the interface M_{13}@silica and on the top of the transition metal cluster).

Molecule	Interaction mode	Isolated	Nest-1	Vicinal	Nest-2	Geminal
NO	Perp O-int	-90	-66	-65	-65	-64
	Flat O-int	-65	-71	-95	-74	-66
NO_2	Perp O-int	-66	-79	-75	-70	
	Flat O-int	-67	-78	-77	-79	-71

5.3.4 Pure vs Supported 3.3 silica surfaces

Table 5.3 and Figure 5.3 show a comparison between the computed adsorption energies of the most stable adsorption modes of NO, NO_2, CO, CO_2 and H_2O, on pure and supported silica surfaces. The most stable adsorption energy of NO is found to be -95 kJ/mol on pure silica surface, and -273 kJ/mol, -269 kJ/mol, -269 kJ/mol, and -221 kJ/mol at the interfaces (Fe_{13}, Co_{13}, Ni_{13} and Cu_{13})@silica, respectively. Regarding NO_2, the adsorption energy of the most stable interaction structure is found to be 79 kJ/mol for pure silica surface, -339 kJ/mol at the interface Fe_{13}@silica, -327 kJ/mol at the interface Co_{13}@silica, -286 kJ/mol at the interface Ni_{13}@silica, and -274 kJ/mol at the interface Cu_{13}@silica. Both NO and NO_2 are more strongly adsorbed at the interface M_{13}@silica than at the pure silica surface. We found that the adsorption energy of nitrogen monoxide on the pure silica surface is 16 kJ/mol higher than that of nitrogen dioxide. At the interfaces M_{13}@silica, the adsorption energies of NO_2 are 66 kJ/mol, 58 kJ/mol, 17 kJ/mol, and 53 kJ/mol higher than those of the NO, for Fe_{13}, Co_{13}, Ni_{13} and Cu_{13}, respectively. Conversely, we found that carbon dioxide is more adsorbed on the pure silica surface rather the carbon monoxide with an energy difference of 10 kJ/mol, and it is less absorbed than carbon monoxide at the interface M_{13}@silica with energy differences of 62 kJ/mol for Fe_{13}@silica, 76 kJ/mol for Co_{13}@silica, 146 kJ/mol for Ni_{13}@silica, and 163 kJ/mol for Cu_{13}@silica. Water is also strongly adsorbed at the interface M_{13}@silica (with an adsorption energy of -136 kJ/mol for Fe_{13}@silica, -139 kJ/mol for Co_{13}@silica, -165 kJ/mol for Ni_{13}@silica, and -150 kJ/mol for Cu_{13}@silica) rather than the pure silica surface with energy differences ranging between 66 kJ/mol and 95 kJ/mol. The adsorption energy order of the inhibiting molecules on the pure silica surface is: $H_2O > CO_2 > CO$, while at the interface M_{13}@silica, it is, $CO > H_2O > CO_2$. We found that the adsorption of CO, CO_2 and water molecules compared to those of nitrogen mono- and dioxide compounds are negligible at the Fe_{13}@silica, Co_{13}@silica, Ni_{13}@silica, and Cu_{13}@silica interfaces, while on the pure amorphous silica surface, the adsorption energy of water is expected to be major compared to that of NO_2.

Table 5.3: PBE+U+D2 calculated adsorption energy of the most stable configurations of NO, NO_2, CO, and H_2O on pure and supported amorphous silica surfaces with a silanol density of 3.3 OH/nm^2.

	SiO_2-3.3	Fe_{13}@SiO_2	Co_{13}@SiO_2	Ni_{13}@SiO_2	Cu_{13}@SiO_2
NO	-95	-273	-269	-269	-221
NO_2	-79	-339	-327	-286	-274
CO	-12	-185	-177	-232	-191
CO_2	-22	-122	-101	-86	-28
H_2O	-70	-136	-139	-165	-150

Adsorption of NO

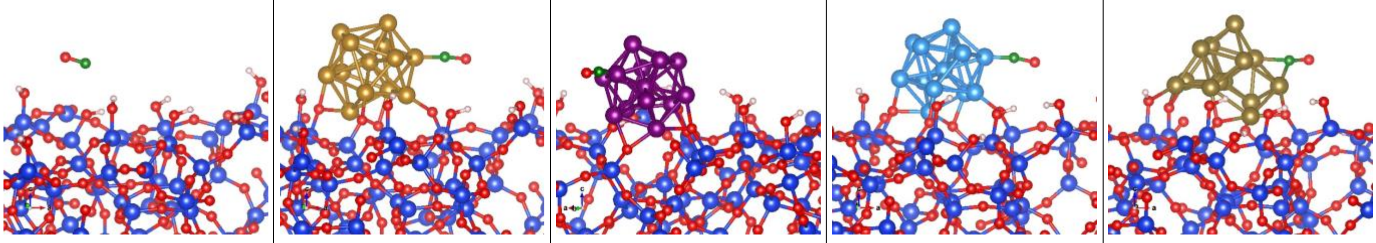

(a) SiO_2 (b) Fe_{13}@SiO_2 (c) Co_{13}@SiO_2 (d) Ni_{13}@SiO_2 (e) Cu_{13}@SiO_2

Adsorption of NO_2

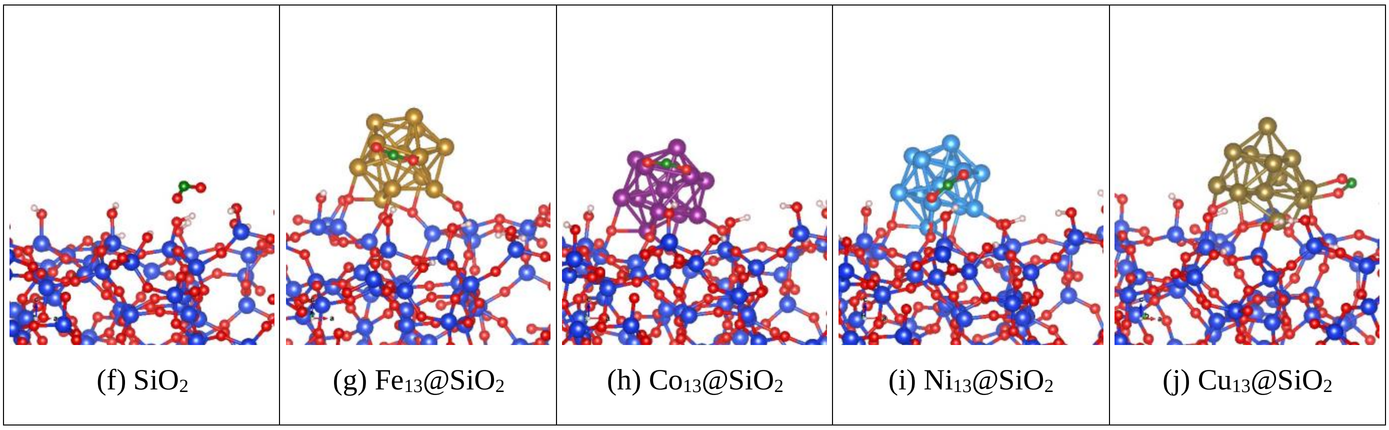

(f) SiO_2 (g) Fe_{13}@SiO_2 (h) Co_{13}@SiO_2 (i) Ni_{13}@SiO_2 (j) Cu_{13}@SiO_2

Figure 5.2: The optimized structures of the most stable configuration of the NO (upper panels) and the NO_2 (lower panels) molecules over pure silica and different heterogeneous catalysts (Fe_{13}@silica, Co_{13}@silica, Ni_{13}@silica, and Cu_{13}@silica).

Figure 5.2 shows the most stable interaction structures of nitrogen mono- and dioxide molecules over pure amorphous silica surface and the different heterogeneous catalysts (Fe_{13}, Co_{13}, Ni_{13}, and Cu_{13})@silica. For pure silica surface, the equilibrium N–O interatomic distance is found to be 1.17 Å for nitrogen monoxide and ranged between 1.21 Å and 1.22 Å for nitrogen dioxide. These distances are quite similar to those calculated for the isolated nitrogen mono- and dioxide molecules. However, for nitrogen dioxide, a slight variation is observed on the $O\widehat{N}O$ bond angle from 133.33 ° for isolated molecule to 132.90 ° for the adsorbed one. At the interface M_{13}@silica, we found that NO preferably adsorbs on the transition metal clusters through N, except for the copper cluster, where the nitrogen atom is bonded to two Cu as shown in Figure 5.2e. The equilibrium M–N distances (with M = Fe, Co, Ni, and Cu) are found to be 1.68 Å, 1.64 Å, 1.62 Å, and 1.93 Å, respectively. We observe that these distances are similar for iron, cobalt, and nickel clusters, but strongly different for the copper cluster. These differences are also observed on the equilibrium N–O distances, which are found to be 1.19 Å for Fe_{13}@silica and Co_{13}@silica, 1.18 Å for Ni_{13}@silica, and 1.23 Å for Cu_{13}@silica. The N–O stretching is slightly influenced by the clusters and ranges between 0.02 Å and 0.06 Å compared to those of the isolated molecule. Our results show that NO_2 forms two bonds with the transition metal cluster through its oxygen atoms. The M–O equilibrium distances were found to be [1.98, 1.98] Å for Fe_{13}@silica, [1.94, 1.95] Å for Co_{13}@silica, [1.92, 1.97] Å for Ni_{13}@silica, and [1.98, 2.03] for Cu_{13}@silica, while the N–O bond lengths are, [1.28, 1.28] Å, [1.28, 1.29] Å, [1.27, 1.28] Å, and [1.26, 1.28] Å, respectively. The intramolecular bond stretching of NO_2 due to the adsorption on the metal clusters ranges between 0.05 Å and 0.08 Å. This effect is clearly observed on the $O\widehat{N}O$ bond angles, which are found to be 115.2 Å for Fe_{13}@silica, 115.9 ° for Co_{13}@silica, 117.2 ° for Ni_{13}@silica, and 117.8 ° for Cu_{13}@silica, with a standard variation ranged between 15.6 ° and 18.1 °.

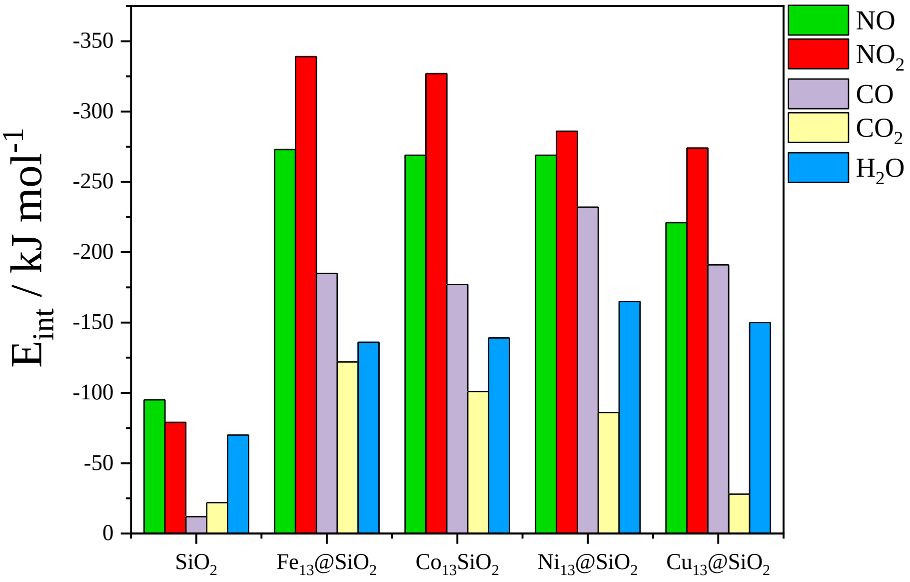

Figure 5.3: PBE+U+D2 calculated adsorption energy of the most stable configurations of NO, NO_2, CO, and H_2O on pure and supported amorphous silica surfaces.

5.4. Conclusions

In this work, we have studied the interaction of nitrogen mono- and dioxide molecules, water and carbon mono- dioxide inhibiting molecules with pure and supported amorphous silica surfaces using periodic spin-polarized density functional theory calculations. For the heterogeneous catalysts, we have used the most stable clusters (Fe_{13}, Co_{13}, Ni_{13}, and Cu_{13}), as determined previously by Gueddida et al, supported on the amorphous silica surface with a silanol density of 3.3 OH/nm^2. Pure amorphous SiO_2-3.3 and supported transition metal cluster-silica surfaces were investigated systematically using the PBE+U+D2 for the adsorption of NO, NO_2, CO, CO_2 and H_2O, SiO_2-3.3 at different adsorption sites by perpendicular and flat interaction modes. Our results show that both nitrogen mono- and dioxide molecules prefer the adsorption at the interface M_{13}@silica. We found that the adsorption energy of NO@silica is 16 kJ/mol higher than that of NO_2@silica, while at the interface M_{13}, the NO_2 adsorption energies are 66 kJ/mol, 58 kJ/mol, 17 kJ/mol, and 53 kJ/mol higher than that of NO energy values, for Fe_{13}@silica, Co_{13}@silica, Ni_{13}@silica, and Cu_{13}@silica interfaces. Our calculations show also that the inhibiting molecules prefer to accommodate at the interface M_{13}@silica. For pure silica surface, the adsorption energies of the inhibiting molecules are found in the following order: $H_2O > CO_2 > CO$, while at the interface M_{13}@silica, $CO > H_2O > CO_2$. We found that the adsorption of CO, CO_2 and water molecules compared to those of nitrogen mono- and dioxide compounds are negligible at the

M_{13}@silica interfaces, while on the pure amorphous silica surface, the adsorption of water molecule is expected to be major compared to the NO_2 adsorption energy.

Future plans include the estimation of charge transfer and intramolecular bond elongation of the gases, that happen during the adsorption, as well as experimental assessment of our most prominent candidates.

General conclusion

The purpose of this project is the assessment of materials for their ability to separate NO, NO_2, and CO from a gas stream rich in water. The separation is based on the stronger affinity of the gases to porous materials. Both the static and the molecular dynamics approaches of density functional theory are implemented, on the PBE level of theory. Grimme's D2 functional is used to treat the dispersion corrections. Hubbard's potential is used to treat the strongly correlated d orbitals of the 3rd row transition metals.

During the first step of the dissertation, the large-porous faujasite was investigated to identify the most selective cations towards NO_x. The monovalent cations Li, Na, K, Rb, Cs, Cu, Ag and the divalent Ca, Ba, Zn, Cu, Pt, Pd, Fe, Co and Ni were placed on the adsorption sites of faujasite, and several possible adsorption modes were tested. The influence of the Si/Al ratio was also evaluated, using the ratios, 47, 23, 2.43 and 1.4. The static DFT approach was adopted during this study, at the PBE+D2+U level of theory. The thermodynamic selectivity and the regeneration of the material were investigated, placing Cu(I) and Fe(II) at the centre of interest.

In the second step, chabazite and mordenite were investigated as alternatives to faujasite, for the low-temperature NO_x and CO adsorption, against H_2O and CO_2, to support the highly selective and cheap Fe(II). Chabazite was picked as a representative of small porous zeolites with great adsorption capacity potential and mordenite as a channel-based zeolite. Three different Si/Al ratios were tested. PBE+D2+U functional was implemented in a static fashion, to assess the thermodynamic selectivity of the materials investigated. Fe(II) promoted chabazite with the lowest Si/Al evaluated (= 3) was chosen as a very interesting candidate, for further testing through molecular dynamics calculations. The latter calculation showed that the presence of 1, 2, 3 and 4 water molecules does not hinder the adsorption of NO_x and CO. Moreover, this study showed that adsorption of NO_2 through many cations at the same time prevents its intramolecular bonds' elongation that happens during the interaction. Consequently, low-Si/Al ratios present excellent findings when it comes to the thermodynamic selectivity and the regeneration of the material, as far as DFT is concerned.

In the last study of this dissertation, clusters of the transition metals Fe, Co and Cu, were incorporated onto amorphous silica surfaces with a stable silanol density ($3.3\ OH/nm^2$). These materials were tested as low-temperature NO_x and CO adsorbers against H_2O and CO_2, through static PBE+D2+U at 0 K. The results showed that all the transition metals present highly selective options. Further study is planned, towards the desorption capability of these materials, through the charge transfer and the intramolecular bond elongation of the gases during their adsorption. In addition, experiments are planned to complete this study.

The investigation of passive NO_x adsorbers is ongoing. Zeolitic frameworks were explored theoretically in this work, and the prevailing ones will be studied experimentally too. Fe^{2+} promoted faujasite chabazite and mordenite were currently proven to be selective towards NO_x in many cases. Their experimental implementation is already planned. The synthesis of low Si/Al zeolites retaining their structural characteristics is imperative to combine numerous adsorption sites with vast surface areas. Consequently, LTA zeolite is an attractive candidate due to its ability to reach exceptionally low Si/Al ratios, and its study is also planned for the future. Activated carbon-based materials have also been studied for low-temperature NO_x abatement. Their activity is based on the oxidation of NO to NO_2 in the presence of O_2, NO_2 being able to adsorb on the surface. However, the interest on this material is probably limited as it promotes high concentrations of the corrosive NO_2, hampering the regeneration. UiO-66, a metal organic framework representative, promoting adverse transition metals revealed excellent results concerning its selectivity. It was also favoured due to its inherent regeneration capability to form much weaker interactions with the gases than zeolites. Hence, its synthesis is also in progress and thermodynamic separation tests will be carried out soon. Other metal organic frameworks are investigated in theoretical and experimental level too. Although zeolites tend to have worse regenerability than MOFs, they are still interesting due to their much lower price. The combination of selectivity, regenerability and cost will determine the final choice for the trap.

To conclude, this dissertation screened a series of porous materials supporting transition metals, using periodic DFT, towards the design of a low-temperature selective NO_x adsorber. It highlighted the prominence of several candidates and shed light on the bonding characteristics between the trap and the gases. It also studied the regenerability of the trap through the formation of by-products during the adsorption of the gases, which can lead to the degradation of the former. Future plans include the further investigation of the transition metal clusters as regarding their regenerability, as well as the experimental application of the best candidates. Furthermore, chabazite and mordenite are about to be synthesised and tested using the lowest possible Si/Al ratios as indicated by DFT calculations.

References

(1) Jain, A. K.; Tao, Z.; Yang, X.; Gillespie, C. Estimates of Global Biomass Burning Emissions for Reactive Greenhouse Gases (CO, NMHCs, and NO_x) and CO_2. *J. Geophys. Res.* **2006**, *111* (D6), D06304. https://doi.org/10.1029/2005JD006237.

(2) Jaeglé, L.; Steinberger, L.; Martin, R. V.; Chance, K. Global Partitioning of NOx Sources Using Satellite Observations: Relative Roles of Fossil Fuel Combustion, Biomass Burning and Soil Emissions. *Faraday Discuss.* **2005**, *130*, 407. https://doi.org/10.1039/b502128f.

(3) Strand, V.; Svartengren, M.; Rak, S.; Barck, C.; Bylin, G. Repeated Exposure to an Ambient Level of NO₂ Enhances Asthmatic Response to a Nonsymptomatic Allergen Dose. *European Respiratory Journal* **1998**, *12* (1), 6–12. https://doi.org/10.1183/09031936.98.12010006.

(4) Atkinson, R. W.; Carey, I. M.; Kent, A. J.; van Staa, T. P.; Anderson, H. R.; Cook, D. G. Long-Term Exposure to Outdoor Air Pollution and Incidence of Cardiovascular Diseases: *Epidemiology* **2013**, *24* (1), 44–53. https://doi.org/10.1097/EDE.0b013e318276ccb8.

(5) Ye, C.; Heard, D. E.; Whalley, L. K. Evaluation of Novel Routes for NO_x Formation in Remote Regions. *Environ. Sci. Technol.* **2017**, *51* (13), 7442–7449. https://doi.org/10.1021/acs.est.6b06441.

(6) *Nitrogen oxides (NOx) emissions — European Environment Agency*. https://www.eea.europa.eu/data-and-maps/indicators/eea-32-nitrogen-oxides-nox-emissions-1/assessment.2010-08-19.0140149032-3 (accessed 2020-09-02).

(7) Lebouvier, A.; Fresnet, F.; Fabry, F.; Boch, V.; Rohani, V.; Cauneau, F.; Fulcheri, L. Exhaust Gas Fuel Reforming of Diesel Fuel by Nonthermal Arc Discharge for NO_x Trap Regeneration Application. *Energy Fuels* **2011**, *25* (3), 1034–1044. https://doi.org/10.1021/ef101674r.

(8) Al-Qurashi, K.; Zhang, Y.; Boehman, A. L. Impact of Intake CO2 Addition and Exhaust Gas Recirculation on NOx Emissions and Soot Reactivity in a Common Rail Diesel Engine. *Energy Fuels* **2012**, *26* (10), 6098–6105. https://doi.org/10.1021/ef201120f.

(9) Jacobs, T.; Assanis, D. N.; Filipi, Z. The Impact of Exhaust Gas Recirculation on Performance and Emissions of a Heavy-Duty Diesel Engine; 2003; pp 2003-01–1068. https://doi.org/10.4271/2003-01-1068.

(10) Ladommatos, N.; Abdelhalim, S. M.; Zhao, H.; Hu, Z. The Dilution, Chemical, and Thermal Effects of Exhaust Gas Recirculation on Diesel Engine Emissions - Part 1: Effect of Reducing Inlet Charge Oxygen; 1996; p 961165. https://doi.org/10.4271/961165.

(11) Castoldi, L.; Lietti, L.; Bonzi, R.; Artioli, N.; Forzatti, P.; Morandi, S.; Ghiotti, G. The NO_x Reduction by CO on a Pt–K/Al_2O_3 Lean NO_x Trap Catalyst. *J. Phys. Chem. C* **2011**, *115* (4), 1277–1286. https://doi.org/10.1021/jp106753g.

(12) Büchel, R.; Strobel, R.; Baiker, A.; Pratsinis, S. E. Flame-Made Pt/K/Al2O3 for NO x Storage–Reduction (NSR) Catalysts. *Top Catal* **2009**, *52* (13–20), 1799–1802. https://doi.org/10.1007/s11244-009-9334-x.

(13) *Steam: Its Generation and Use*, 41. ed., 1. print.; Kitto, J. B., Ed.; Babcock & Wilcox: Barberton, Ohio, 2005.

(14) Latha, H. S.; Prakash, K. V.; Veerangouda, M.; Maski, D.; Ramappa, K. T. A Review on SCR System for NOx Reduction in Diesel Engine. *Int.J.Curr.Microbiol.App.Sci* **2019**, *8* (04), 1553–1559. https://doi.org/10.20546/ijcmas.2019.804.180.

(15) Chen, L.; Li, J.; Ge, M. Promotional Effect of Ce-Doped V_2O_5-WO_3/TiO_2 with Low Vanadium Loadings for Selective Catalytic Reduction of NO_x by NH_3. *J. Phys. Chem. C* **2009**, *113* (50), 21177–21184. https://doi.org/10.1021/jp907109e.

(16) Shan, Y.; Du, J.; Zhang, Y.; Shan, W.; Shi, X.; Yu, Y.; Zhang, R.; Meng, X.; Xiao, F.-S.; He, H. Selective Catalytic Reduction of NO *x* with NH3: Opportunities and Challenges of Cu-Based Small-Pore Zeolites. *National Science Review* **2021**, *8* (10), nwab010. https://doi.org/10.1093/nsr/nwab010.

(17) *Glossary | Publications and Other Information | BTSC*. https://web.archive.org/web/20080218094403/http://www.brownfieldstsc.org/glossary.cfm?q=1 (accessed 2020-10-07).

(18) Kašpar, J.; Fornasiero, P.; Hickey, N. Automotive Catalytic Converters: Current Status and Some Perspectives. *Catalysis Today* **2003**, 31.

(19) Chen, H.-Y.; Mulla, S.; Weigert, E.; Camm, K.; Ballinger, T.; Cox, J.; Blakeman, P. Cold Start Concept (CSC^{TM}): A Novel Catalyst for Cold Start Emission Control. *SAE Int. J. Fuels Lubr.* **2013**, *6* (2), 372–381. https://doi.org/10.4271/2013-01-0535.

(20) Woo, S.-Y.; Lee, H.-S.; Ji, H.; Kim, Y.-D. Adsorption Isotherm Model for Analyzing the Adsorption Characteristics of Water Vapor to Commercially Available Silica Gel Adsorbents for Adsorption Desalination Applications. *J. Chem. Eng. Data* **2021**, *66* (2), 1144–1156. https://doi.org/10.1021/acs.jced.0c00927.

(21) Li, G.; Xiao, P.; Xu, D.; Webley, P. A. Dual Mode Roll-up Effect in Multicomponent Non-Isothermal Adsorption Processes with Multilayered Bed Packing. *Chemical Engineering Science* **2011**, *66* (9), 1825–1834. https://doi.org/10.1016/j.ces.2011.01.023.

(22) *Equilibria | Dynamic Sorption, Breakthrough Curve Measurement, mixSorb, dynaSorb BT*. https://www.dynamicsorption.com/dynamic-sorption-method/equilibria/ (accessed 2022-12-11).

(23) Ball, D.; Zammit, M.; Wuttke, J.; Buitrago, C. Investigation of LEV-III Aftertreatment Designs. *SAE Int. J. Fuels Lubr.* **2011**, *4* (2), 1–8. https://doi.org/10.4271/2011-01-0301.

(24) Millo, F.; Vezza, D. Characterization of a New Advanced Diesel Oxidation Catalyst with Low Temperature NO $_x$ Storage Capability for LD Diesel; 2012; pp 2012-01–0373. https://doi.org/10.4271/2012-01-0373.

(25) Henry, C.; Langenderfer, D.; Yezerets, A.; Ruth, M.; Chen, H.-Y.; Hess, H.; Naseri, M. Passive Catalytic Approach to Low Temperature NOx Emission Abatement. **2011**, 12.

(26) *Lean-burn nox catalyst/nox trap system - Patent US-5727385-A - PubChem*. https://pubchem.ncbi.nlm.nih.gov/patent/US-5727385-A (accessed 2022-12-05).

(27) *Method for converting exhaust gases from a diesel engine using nitrogen oxide absorbent - Patent US-6182443-B1 - PubChem*. https://testpubchem.ncbi.nlm.nih.gov/patent/US-6182443-B1 (accessed 2022-12-05).

(28) *Method and apparatus for NOx abatement in lean gaseous streams - Patent US-6471924-B1 - PubChem*. https://testpubchem.ncbi.nlm.nih.gov/patent/US-6471924-B1 (accessed 2022-12-05).

(29) Rajaram, R. R.; Chen, H.-Y.; Liu, D. Cold Start Catalyst and Its Use in Exhaust Systems. US20150158023A1, June 11, 2015. https://patents.google.com/patent/US20150158023A1/en (accessed 2022-12-03).

(30) Gu, Y.; Epling, W. S. Passive NOx Adsorber: An Overview of Catalyst Performance and Reaction Chemistry. *Applied Catalysis A: General* **2019**, *570*, 1–14. https://doi.org/10.1016/j.apcata.2018.10.036.

(31) Ji, Y.; Xu, D.; Bai, S.; Graham, U.; Crocker, M.; Chen, B.; Shi, C.; Harris, D.; Scapens, D.; Darab, J. Pt- and Pd-Promoted CeO $_2$ –ZrO $_2$ for Passive NOx Adsorber Applications. *Ind. Eng. Chem. Res.* **2017**, *56* (1), 111–125. https://doi.org/10.1021/acs.iecr.6b03793.

(32) Ji, Y.; Bai, S.; Xu, D.; Qian, D.; Wu, Z.; Song, Y.; Pace, R.; Crocker, M.; Wilson, K.; Lee, A.; Harris, D.; Scapens, D. Pd-Promoted WO3-ZrO2 for Low Temperature NOx Storage. *Applied Catalysis B: Environmental* **2020**, *264*, 118499. https://doi.org/10.1016/j.apcatb.2019.118499.

(33) Ryou, Y.; Lee, J.; Lee, H.; Kim, C. H.; Kim, D. H. Effect of Sulfur Aging and Regeneration on Low Temperature NO Adsorption over Hydrothermally Treated Pd/CeO2 and Pd/Ce0.58Zr0.42O2 Catalysts. *Catalysis Today* **2017**, *297*, 53–59. https://doi.org/10.1016/j.cattod.2017.06.035.

(34) Hernández-Giménez, A. M.; Lozano-Castelló, D.; Bueno-López, A. Effect of CO2, H2O and SO2 in the Ceria-Catalyzed Combustion of Soot under Simulated Diesel Exhaust Conditions. *Applied Catalysis B: Environmental* **2014**, *148–149*, 406–414. https://doi.org/10.1016/j.apcatb.2013.11.029.

(35) Chen, H.-Y.; Collier, J. E.; Liu, D.; Mantarosie, L.; Durán-Martín, D.; Novák, V.; Rajaram, R. R.; Thompsett, D. Low Temperature NO Storage of Zeolite Supported Pd for Low Temperature Diesel Engine Emission Control. *Catal Lett* **2016**, *146* (9), 1706–1711. https://doi.org/10.1007/s10562-016-1794-6.

(36) Ryou, Y.; Lee, J.; Cho, S. J.; Lee, H.; Kim, C. H.; Kim, D. H. Activation of Pd/SSZ-13 Catalyst by Hydrothermal Aging Treatment in Passive NO Adsorption Performance at Low Temperature for Cold Start Application. *Applied Catalysis B: Environmental* **2017**, *212*, 140–149. https://doi.org/10.1016/j.apcatb.2017.04.077.

(37) Lee, J.; Ryou, Y.; Cho, S. J.; Lee, H.; Kim, C. H.; Kim, D. H. Investigation of the Active Sites and Optimum Pd/Al of Pd/ZSM–5 Passive NO Adsorbers for the Cold-Start Application: Evidence of Isolated-Pd Species Obtained after a High-Temperature Thermal Treatment. *Applied Catalysis B: Environmental* **2018**, *226*, 71–82. https://doi.org/10.1016/j.apcatb.2017.12.031.

(38) Ryou, Y.; Lee, J.; Lee, H.; Kim, C. H.; Kim, D. H. Effect of Various Activation Conditions on the Low Temperature NO Adsorption Performance of Pd/SSZ-13 Passive NOx Adsorber. *Catalysis Today* **2019**, *320*, 175–180. https://doi.org/10.1016/j.cattod.2017.11.030.

(39) Zheng, Y.; Kovarik, L.; Engelhard, M. H.; Wang, Y.; Wang, Y.; Gao, F.; Szanyi, J. Low-Temperature Pd/Zeolite Passive NO $_x$ Adsorbers: Structure, Performance, and Adsorption Chemistry. *J. Phys. Chem. C* **2017**, *121* (29), 15793–15803. https://doi.org/10.1021/acs.jpcc.7b04312.

(40) Murata, Y.; Morita, T.; Wada, K.; Ohno, H. NOx Trap Three-Way Catalyst (N-TWC) Concept: TWC with NOx Adsorption Properties at Low Temperatures for Cold-Start Emission Control. *SAE International Journal of Fuels and Lubricants* **2015**, *8* (2), 454–459.

(41) Mihai, O.; Trandafilović, L.; Wentworth, T.; Torres, F. F.; Olsson, L. The Effect of Si/Al Ratio for Pd/BEA and Pd/SSZ-13 Used as Passive NOx Adsorbers. *Top Catal* **2018**, *61* (18–19), 2007–2020. https://doi.org/10.1007/s11244-018-1017-z.

(42) Adil, K.; Belmabkhout, Y.; Pillai, R. S.; Cadiau, A.; Bhatt, P. M.; Assen, A. H.; Maurin, G.; Eddaoudi, M. Gas/Vapour Separation Using Ultra-Microporous Metal–Organic Frameworks: Insights into the Structure/Separation Relationship. *Chem. Soc. Rev.* **2017**, *46* (11), 3402–3430. https://doi.org/10.1039/C7CS00153C.

(43) Shang, S.; Wen, C.; Yang, C.; Tian, Y.; Wang, C.; Shang, J. The Low-Temperature NO2 Removal by Tailoring Metal Node in Porphyrin-Based Metal-Organic Frameworks. *Science of The Total Environment* **2021**, *801*, 149710. https://doi.org/10.1016/j.scitotenv.2021.149710.

(44) Gopalsamy, K.; Wahiduzzaman, M.; Daouli, A.; Badawi, M.; Maurin, G. Computational Exploration of a Metal(II) Catecholate-Functionalized UiO-66 Nanoporous Metal–Organic Framework for Effective NO $_x$ Capture. *ACS Appl. Nano Mater.* **2022**, *5* (10), 15123–15132. https://doi.org/10.1021/acsanm.2c03284.

(45) Jensen, S.; Tan, K.; Feng, L.; Li, J.; Zhou, H.-C.; Thonhauser, T. Porous Ti-MOF-74 Framework as a Strong-Binding Nitric Oxide Scavenger. *J. Am. Chem. Soc.* **2020**, *142* (39), 16562–16568. https://doi.org/10.1021/jacs.0c02772.

(46) Smith, J. V. Topochemistry of Zeolites and Related Materials. 1. Topology and Geometry. *Chem. Rev.* **1988**, *88* (1), 149–182. https://doi.org/10.1021/cr00083a008.

(47) Paolucci, C.; Parekh, A. A.; Khurana, I.; Di Iorio, J. R.; Li, H.; Albarracin Caballero, J. D.; Shih, A. J.; Anggara, T.; Delgass, W. N.; Miller, J. T.; Ribeiro, F. H.; Gounder, R.; Schneider, W. F. Catalysis in a Cage: Condition-Dependent Speciation and Dynamics of Exchanged Cu Cations

in SSZ-13 Zeolites. *J. Am. Chem. Soc.* **2016**, *138* (18), 6028–6048. https://doi.org/10.1021/jacs.6b02651.

(48) Bordiga, S.; Garrone, E.; Lamberti, C.; Zecchina, A.; Areán, C. O.; Kazansky, V. B.; Kustov, L. M. Comparative IR-Spectroscopic Study of Low-Temperature H_2 and CO Adsorption on Na Zeolites. *J. Chem. Soc., Faraday Trans.* **1994**, *90* (21), 3367–3372. https://doi.org/10.1039/FT9949003367.

(49) Abrioux, C.; Coasne, B.; Maurin, G.; Henn, F.; Jeffroy, M.; Boutin, A. Cation Behavior in Faujasite Zeolites upon Water Adsorption: A Combination of Monte Carlo and Molecular Dynamics Simulations. *J. Phys. Chem. C* **2009**, *113* (24), 10696–10705. https://doi.org/10.1021/jp902274t.

(50) Nour, Z.; Berthomieu, D.; Yang, Q.; Maurin, G. A Computational Exploration of the CO Adsorption in Cation-Exchanged Faujasites. *J. Phys. Chem. C* **2012**, *116* (46), 24512–24521. https://doi.org/10.1021/jp305145s.

(51) Sun, M.; Gu, Q.; Hanif, A.; Wang, T.; Shang, J. Transition Metal Cation-Exchanged SSZ-13 Zeolites for CO2 Capture and Separation from N2. *Chemical Engineering Journal* **2019**, *370*, 1450–1458. https://doi.org/10.1016/j.cej.2019.03.234.

(52) Akporiaye, D. E.; Dahl, I. M.; Mostad, H. B.; Wendelbo, R. Aluminum Distribution in Chabazite: An Experimental and Computational Study. *J. Phys. Chem.* **1996**, *100* (10), 4148–4153. https://doi.org/10.1021/jp952189k.

(53) Guo, Y.; Sun, T.; Gu, Y.; Liu, X.; Ke, Q.; Wei, X.; Wang, S. Rational Synthesis of Chabazite (CHA) Zeolites with Controlled Si/Al Ratio and Their $CO_2/CH_4/N_2$ Adsorptive Separation Performances. *Chem. Asian J.* **2018**, *13* (21), 3222–3230. https://doi.org/10.1002/asia.201800930.

(54) Solans-Monfort, X.; Branchadell, V.; Sodupe, M.; Zicovich-Wilson, C. M.; Gribov, E.; Spoto, G.; Busco, C.; Ugliengo, P. Can Cu^+-Exchanged Zeolites Store Molecular Hydrogen? An Ab-Initio Periodic Study Compared with Low-Temperature FTIR. *J. Phys. Chem. B* **2004**, *108* (24), 8278–8286. https://doi.org/10.1021/jp0486651.

(55) Civalleri, B.; Ferrari, A. M.; Llunell, M.; Orlando, R.; Mérawa, M.; Ugliengo, P. Cation Selectivity in Alkali-Exchanged Chabazite: An Ab Initio Periodic Study. *Chem. Mater.* **2003**, *15* (21), 3996–4004. https://doi.org/10.1021/cm0342804.

(56) Smith, L. J.; Eckert, H.; Cheetham, A. K. Site Preferences in the Mixed Cation Zeolite, Li,Na-Chabazite: A Combined Solid-State NMR and Neutron Diffraction Study. *J. Am. Chem. Soc.* **2000**, *122* (8), 1700–1708. https://doi.org/10.1021/ja992882b.

(57) Göltl, F.; Müller, P.; Uchupalanun, P.; Sautet, P.; Hermans, I. Developing a Descriptor-Based Approach for CO and NO Adsorption Strength to Transition Metal Sites in Zeolites. *Chem. Mater.* **2017**, *29* (15), 6434–6444. https://doi.org/10.1021/acs.chemmater.7b01860.

(58) Ayadi, T.; Badawi, M.; Cantrel, L.; Lebègue, S. Rational Approach for an Optimized Formulation of Silver-Exchanged Zeolites for Iodine Capture from First-Principles Calculations. *Mol. Syst. Des. Eng.* **2022**, *7* (5), 422–433. https://doi.org/10.1039/D1ME00149C.

(59) Chibani, S.; Chebbi, M.; Lebègue, S.; Cantrel, L.; Badawi, M. Impact of the Si/Al Ratio on the Selective Capture of Iodine Compounds in Silver-Mordenite: A Periodic DFT Study. *Phys. Chem. Chem. Phys.* **2016**, *18* (36), 25574–25581. https://doi.org/10.1039/C6CP05015H.

(60) Porta, A.; Pellegrinelli, T.; Castoldi, L.; Matarrese, R.; Morandi, S.; Dzwigaj, S.; Lietti, L. Low Temperature NOx Adsorption Study on Pd-Promoted Zeolites. *Top Catal* **2018**, *61* (18–19), 2021–2034. https://doi.org/10.1007/s11244-018-1045-8.

(61) Zhang, W.-X.; Yahiro, H.; Iwamoto, M. Reversible and Irreversible Adsorption of Nitrogen Monoxide on Cobalt Ion-Exchanged ZSM-5 and Mordenite Zeolites at 273-523 K. *J. CHEM. SOC. FARADAY TRANS.* **1995**, *91*.

(62) van laak, A. N. C.; Gosselink, R. W.; Sagala, S. L.; Meeldijk, J. D.; de Jongh, P. E.; de Jong, K. P. Alkaline Treatment on Commercially Available Aluminum Rich Mordenite. *Applied Catalysis A: General* **2010**, *382* (1), 65–72. https://doi.org/10.1016/j.apcata.2010.04.023.

(63) Gili, M. B. Z.; Conato, M. T. Synthesis and Characterization of Mordenite-Type Zeolites with Varying Si/Al Ratio. *Mater. Res. Express* **2018**, *6* (1), 015515. https://doi.org/10.1088/2053-1591/aae8db.

(64) Khalil, U.; Muraza, O. Microwave-Assisted Hydrothermal Synthesis of Mordenite Zeolite: Optimization of Synthesis Parameters. *Microporous and Mesoporous Materials* **2016**, *232*, 211–217. https://doi.org/10.1016/j.micromeso.2016.06.016.

(65) Gueddida, S.; Lebègue, S.; Badawi, M. Interaction between Transition Metals (Co, Ni, and Cu) Systems and Amorphous Silica Surfaces: A DFT Investigation. *Applied Surface Science* **2020**, *533*, 147422. https://doi.org/10.1016/j.apsusc.2020.147422.

(66) Goldsmith, B. R.; Peters, B.; Johnson, J. K.; Gates, B. C.; Scott, S. L. Beyond Ordered Materials: Understanding Catalytic Sites on Amorphous Solids. *ACS Catal.* **2017**, *7* (11), 7543–7557. https://doi.org/10.1021/acscatal.7b01767.

(67) Guesmi, H.; Gryboś, R.; Handzlik, J.; Tielens, F. Characterization of Molybdenum Monomeric Oxide Species Supported on Hydroxylated Silica: A DFT Study. *Phys. Chem. Chem. Phys.* **2014**, *16* (34), 18253–18260. https://doi.org/10.1039/C4CP02296C.

(68) Kamutzki, F.; Schneider, S.; Barowski, J.; Gurlo, A.; Hanaor, D. A. H. Silicate Dielectric Ceramics for Millimetre Wave Applications. *Journal of the European Ceramic Society* **2021**, *41* (7), 3879–3894. https://doi.org/10.1016/j.jeurceramsoc.2021.02.048.

(69) Siodla, T.; Sobczak, I.; Ziolek, M.; Tielens, F. Theoretical and Experimental Insight into Zinc Loading on Mesoporous Silica. *Microporous and Mesoporous Materials* **2018**, *256*, 199–205. https://doi.org/10.1016/j.micromeso.2017.08.008.

(70) Ji, G.; Gao, X.; Smart, S.; Bhatia, S. K.; Wang, G.; Hooman, K.; da Costa, J. C. D. Estimation of Pore Size Distribution of Amorphous Silica-Based Membrane by the Activation Energies of Gas Permeation. *Processes* **2018**, *6* (12), 239. https://doi.org/10.3390/pr6120239.

(71) Krivak, T. G.; Jones, L. E. Amorphous Precipitated Silica Having a Low Proportion of Small Pores. US5911963A, June 15, 1999. https://patents.google.com/patent/US5911963A/en (accessed 2022-12-04).

(72) Calderon V, S.; Ribeiro, T.; Farinha, J. P. S.; Baleizão, C.; Ferreira, P. J. On the Structure of Amorphous Mesoporous Silica Nanoparticles by Aberration-Corrected STEM. *Small* **2018**, *14* (40), 1802180. https://doi.org/10.1002/smll.201802180.

(73) Mu, D.; Liu, Z.-S.; Huang, C.; Djilali, N. Determination of the Effective Diffusion Coefficient in Porous Media Including Knudsen Effects. *Microfluid Nanofluid* **2008**, *4* (3), 257–260. https://doi.org/10.1007/s10404-007-0182-3.

(74) Forse, A. C.; Colwell, K. A.; Gonzalez, M. I.; Benders, S.; Torres-Gavosto, R. M.; Blümich, B.; Reimer, J. A.; Long, J. R. Influence of Pore Size on Carbon Dioxide Diffusion in Two Isoreticular Metal–Organic Frameworks. *Chem. Mater.* **2020**, *32* (8), 3570–3576. https://doi.org/10.1021/acs.chemmater.0c00745.

(75) Zech, A.; de Winter, M. A Probabilistic Formulation of the Diffusion Coefficient in Porous Media as Function of Porosity. *Transp Porous Med* **2022**. https://doi.org/10.1007/s11242-021-01737-5.

(76) Kabir, M.; Mookerjee, A.; Bhattacharya, A. K. Structure and Stability of Copper Clusters: A Tight-Binding Molecular Dynamics Study. *Phys. Rev. A* **2004**, *69* (4), 043203. https://doi.org/10.1103/PhysRevA.69.043203.

(77) WeiJun Hu; LiangMo Mei; Hua Li. Simulation of Ground State Structure of Nickel Clusters ($n \leq 40$). *Solid State Communications* **1996**, *100* (2), 129–131. https://doi.org/10.1016/0038-1098(96)00396-1.

(78) Xie, Z.; Ma, Q.-M.; Liu, Y.; Li, Y.-C. First-Principles Study of the Stability and Jahn–Teller Distortion of Nickel Clusters. *Physics Letters A* **2005**, *342* (5–6), 459–467. https://doi.org/10.1016/j.physleta.2005.05.067.

(79) Blin, J. L.; Carteret, C. Investigation of the Silanols Groups of Mesostructured Silica Prepared Using a Fluorinated Surfactant: Influence of the Hydrothermal Temperature. *J. Phys. Chem. C* **2007**, *111* (39), 14380–14388. https://doi.org/10.1021/jp072369h.

(80) Zhuravlev, L. T. Concentration of Hydroxyl Groups on the Surface of Amorphous Silicas. *Langmuir* **1987**, *3* (3), 316–318. https://doi.org/10.1021/la00075a004.

(81) Gueddida, S.; Badawi, M.; Lebègue, S. Grafting of Iron on Amorphous Silica Surfaces from *Ab Initio* Calculations. *J. Chem. Phys.* **2020**, *152* (21), 214706. https://doi.org/10.1063/5.0007128.

(82) *Unit Cell, Primitive Cell and Wigner-Seitz Cell | Physics in a Nutshell*. https://www.physics-in-a-nutshell.com/article/5/unit-cell-primitive-cell-and-wigner-seitz-cell (accessed 2022-12-20).

(83) Lee, J. G. *Computational Materials Science: An Introduction*, Second edition.; CRC Press, Taylor & Francis Group, CRC Press is an imprint or the Taylor & Francis Group, an informa business: Boca Raton, 2017.

(84) Jensen, F. *Introduction to Computational Chemistry*, 2nd ed.; John Wiley & Sons: Chichester, England ; Hoboken, NJ, 2007.

(85) Hohenberg, P.; Kohn, W. Inhomogeneous Electron Gas. *Phys. Rev.* **1964**, *136* (3B), B864–B871. https://doi.org/10.1103/PhysRev.136.B864.

(86) Kohn, W.; Sham, L. J. Self-Consistent Equations Including Exchange and Correlation Effects. *Phys. Rev.* **1965**, *140* (4A), A1133–A1138. https://doi.org/10.1103/PhysRev.140.A1133.

(87) Perdew, J. P.; Burke, K.; Ernzerhof, M. Generalized Gradient Approximation Made Simple. *Phys. Rev. Lett.* **1996**, *77* (18), 3865–3868. https://doi.org/10.1103/PhysRevLett.77.3865.

(88) Grimme, S. Density Functional Theory with London Dispersion Corrections. *WIREs Comput Mol Sci* **2011**, *1* (2), 211–228. https://doi.org/10.1002/wcms.30.

(89) Grimme, S. Semiempirical GGA-Type Density Functional Constructed with a Long-Range Dispersion Correction. *J. Comput. Chem.* **2006**, *27* (15), 1787–1799. https://doi.org/10.1002/jcc.20495.

(90) Tolba, S. A.; Gameel, K. M.; Ali, B. A.; A.Almossalami, H.; Allam, N. K. *The DFT+U: Approaches, Accuracy, and Applications*; IntechOpen, 2018. https://doi.org/10.5772/intechopen.72020.

(91) Dudarev, S. L.; Botton, G. A.; Savrasov, S. Y.; Humphreys, C. J.; Sutton, A. P. Electron-Energy-Loss Spectra and the Structural Stability of Nickel Oxide: An LSDA⁒U Study. 5.

(92) Cococcioni, M.; de Gironcoli, S. Linear Response Approach to the Calculation of the Effective Interaction Parameters in the LDA + U Method. *Phys. Rev. B* **2005**, *71* (3), 035105. https://doi.org/10.1103/PhysRevB.71.035105.

(93) Janak, J. F. Proof That $\frac{\ensuremath{\partial}E}{\ensuremath{\partial}{n}_{i}}=\ensuremath{\epsilon}$ in Density-Functional Theory. *Phys. Rev. B* **1978**, *18* (12), 7165–7168. https://doi.org/10.1103/PhysRevB.18.7165.

(94) Tuckerman, M. E. *Statistical Mechanics: Theory and Molecular Simulation*, Illustrated edition.; Oxford University Press: Oxford ; New York, 2010.

(95) Stone, A. J. *The Theory of Intermolecular Forces*, 2nd ed.; Clarendon Press: Oxford, 1997.

(96) Hessou, E. P.; Kanhounnon, W. G.; Rocca, D.; Monnier, H.; Vallières, C.; Lebègue, S.; Badawi, M. Adsorption of NO, NO2, CO, H2O and CO2 over Isolated Monovalent Cations in Faujasite Zeolite: A Periodic DFT Investigation. *Theor Chem Acc* **2018**, *137* (12), 161. https://doi.org/10.1007/s00214-018-2373-2.

(97) Amann, M.; Derwent, D.; Forsberg, B.; Hänninen, O.; Hurley, F.; Krzyzanowski, M.; de Leeuw, F.; Liu, S.; Mandin, C.; Schneider, J.; Schwarze, P.; Simpson, D. *Health Risks of Ozone from Long-Range Transboundary Air Pollution*; WHO Regional Office for Europe: DK-2100 Copenhagen Ø, Denmark, 2008.

(98) Chen, H.-Y.; Collier, J. E.; Liu, D.; Mantarosie, L.; Durán-Martín, D.; Novák, V.; Rajaram, R. R.; Thompsett, D. Low Temperature NO Storage of Zeolite Supported Pd for Low Temperature Diesel Engine Emission Control. *Catal Lett* **2016**, *146* (9), 1706–1711. https://doi.org/10.1007/s10562-016-1794-6.

(99) Ji, Y.; Bai, S.; Crocker, M. Al2O3-Based Passive NOx Adsorbers for Low Temperature Applications. *Applied Catalysis B: Environmental* **2015**, *170–171*, 283–292. https://doi.org/10.1016/j.apcatb.2015.01.025.

(100) Rajaram, R. R.; Chen, H.-Y.; Liu, D. Cold Start Catalyst and Its Use in Exhaust Systems. US20150158023A1, June 11, 2015. https://patents.google.com/patent/US20150158023A1/en (accessed 2023-03-03).

(101) *What Are Diesel Emissions*. https://dieselnet.com/tech/emi_intro.php (accessed 2022-06-15).

(102) *Gaseous Emissions*. https://dieselnet.com/tech/emi_gas.php (accessed 2022-06-15).

(103) Yang, R. T. Zeolites and Molecular Sieves. In *Adsorbents: Fundamentals and Applications*; John Wiley & Sons, Ltd: New Jersey, 2003; pp 157–190. https://doi.org/10.1002/047144409X.ch7.

(104) Ayadi, T.; Badawi, M.; Cantrel, L.; Lebègue, S. Rational Approach for an Optimized Formulation of Silver-Exchanged Zeolites for Iodine Capture from First-Principles Calculations. *Mol. Syst. Des. Eng.* **2022**, *7* (5), 422–433. https://doi.org/10.1039/D1ME00149C.

(105) Delahay, G.; Kieger, S.; Tanchoux, N.; Trens, P.; Coq, B. Kinetics of the Selective Catalytic Reduction of NO by NH3 on a Cu-Faujasite Catalyst. *Applied Catalysis B: Environmental* **2004**, *52* (4), 251–257. https://doi.org/10.1016/j.apcatb.2004.04.008.

(106) Delahay, G.; Coq, B.; Kieger, S.; Neveu, B. The Origin of N2O Formation in the Selective Catalytic Reduction of NOx by NH3 in O2 Rich Atmosphere on Cu-Faujasite Catalysts. *Catalysis Today* **1999**, *54* (4), 431–438. https://doi.org/10.1016/S0920-5861(99)00206-0.

(107) Khalil, I.; Jabraoui, H.; Maurin, G.; Lebègue, S.; Badawi, M.; Thomas, K.; Maugé, F. Selective Capture of Phenol from Biofuel Using Protonated Faujasite Zeolites with Different Si/Al Ratios. *J. Phys. Chem. C* **2018**, *122* (46), 26419–26429. https://doi.org/10.1021/acs.jpcc.8b07875.

(108) Speybroeck, V. V.; Hemelsoet, K.; Joos, L.; Waroquier, M.; Bell, R. G.; Catlow, C. R. A. Advances in Theory and Their Application within the Field of Zeolite Chemistry. *Chem. Soc. Rev.* **2015**, *44* (20), 7044–7111. https://doi.org/10.1039/C5CS00029G.

(109) Khalil, I.; Jabraoui, H.; Lebègue, S.; Kim, W. J.; Aguilera, L.-J.; Thomas, K.; Maugé, F.; Badawi, M. Biofuel Purification: Coupling Experimental and Theoretical Investigations for Efficient Separation of Phenol from Aromatics by Zeolites. *Chemical Engineering Journal* **2020**, *402*, 126264. https://doi.org/10.1016/j.cej.2020.126264.

(110) Hessou, E. P.; Jabraoui, H.; Khalil, I.; Dziurla, M.-A.; Badawi, M. Ab Initio Screening of Zeolite Y Formulations for Efficient Adsorption of Thiophene in Presence of Benzene. *Applied Surface Science* **2021**, *541*, 148515. https://doi.org/10.1016/j.apsusc.2020.148515.

(111) Kresse, G.; Hafner, J. Ab Initio Molecular Dynamics for Liquid Metals. *Phys. Rev. B* **1993**, *47* (1), 558–561. https://doi.org/10.1103/PhysRevB.47.558.

(112) Kresse, G.; Joubert, D. From Ultrasoft Pseudopotentials to the Projector Augmented-Wave Method. *Phys. Rev. B* **1999**, *59* (3), 1758–1775. https://doi.org/10.1103/PhysRevB.59.1758.

(113) Strømsheim, M. D.; Kumar, N.; Coriani, S.; Sagvolden, E.; Teale, A. M.; Helgaker, T. Dispersion Interactions in Density-Functional Theory: An Adiabatic-Connection Analysis. *J. Chem. Phys.* **2011**, *135* (19), 194109. https://doi.org/10.1063/1.3660357.

(114) Grimme, S. Accurate description of van der Waals complexes by density functional theory including empirical corrections. *Journal of Computational Chemistry* **2004**, *25* (12), 1463–1473. https://doi.org/10.1002/jcc.20078.

(115) Tkatchenko, A.; DiStasio, R. A.; Car, R.; Scheffler, M. Accurate and Efficient Method for Many-Body van Der Waals Interactions. *Phys. Rev. Lett.* **2012**, *108* (23), 236402. https://doi.org/10.1103/PhysRevLett.108.236402.

(116) Ambrosetti, A.; Reilly, A. M.; DiStasio, R. A.; Tkatchenko, A. Long-Range Correlation Energy Calculated from Coupled Atomic Response Functions. *The Journal of Chemical Physics* **2014**, *140* (18), 18A508. https://doi.org/10.1063/1.4865104.

(117) Bučko, T.; Lebègue, S.; Hafner, J.; Ángyán, J. G. Improved Density Dependent Correction for the Description of London Dispersion Forces. *J. Chem. Theory Comput.* **2013**, *9* (10), 4293–4299. https://doi.org/10.1021/ct400694h.

(118) Anisimov, V. I.; Zaanen, J.; Andersen, O. K. Band Theory and Mott Insulators: Hubbard U Instead of Stoner I. *Phys. Rev. B* **1991**, *44* (3), 943–954. https://doi.org/10.1103/PhysRevB.44.943.

(119) Zaanen, J.; Jepsen, O.; Gunnarsson, O.; Paxton, A. T.; Andersen, O. K.; Svane, A. What Can Be Learned about HighTc from Local Density Theory? *Physica C: Superconductivity* **1988**, *153–155*, 1636–1641. https://doi.org/10.1016/0921-4534(88)90436-4.

(120) Lan, G.; Song, J.; Yang, Z. A Linear Response Approach to Determine Hubbard U and Its Application to Evaluate Properties of Y2B2O7, B = Transition Metals 3d, 4d and 5d. *Journal of Alloys and Compounds* **2018**, *749*, 909–925. https://doi.org/10.1016/j.jallcom.2018.03.336.

(121) Bader, R. F. W. Atoms in Molecules. *Accounts of Chemical Research* **1985**, *18*, 7.

(122) Tang, W.; Sanville, E.; Henkelman, G. A Grid-Based Bader Analysis Algorithm without Lattice Bias. *J. Phys.: Condens. Matter* **2009**, *21* (8), 084204. https://doi.org/10.1088/0953-8984/21/8/084204.

(123) Sanville, E.; Kenny, S. D.; Smith, R.; Henkelman, G. Improved Grid-Based Algorithm for Bader Charge Allocation. *J. Comput. Chem.* **2007**, *28* (5), 899–908. https://doi.org/10.1002/jcc.20575.

(124) Henkelman, G.; Arnaldsson, A.; Jónsson, H. A Fast and Robust Algorithm for Bader Decomposition of Charge Density. *Computational Materials Science* **2006**, *36* (3), 354–360. https://doi.org/10.1016/j.commatsci.2005.04.010.

(125) Yu, M.; Trinkle, D. R. Accurate and Efficient Algorithm for Bader Charge Integration. *The Journal of Chemical Physics* **2011**, *134* (6), 064111. https://doi.org/10.1063/1.3553716.

(126) Baur, W. H. On the Cation and Water Positions in Faujasite1. *American Mineralogist* **1964**, *49* (5–6), 697–704.

(127) *Database of Zeolite Structures*. http://www.iza-structure.org/databases/ (accessed 2022-06-16).

(128) Frising, T.; Leflaive, P. Extraframework Cation Distributions in X and Y Faujasite Zeolites: A Review. *Microporous and Mesoporous Materials* **2008**, *114* (1–3), 27–63. https://doi.org/10.1016/j.micromeso.2007.12.024.

(129) Porcher, F.; Souhassou, M.; Dusausoy, Y.; Lecomte, C. The Crystal Structure of a Low-Silica Dehydrated NaX Zeolite. *European Journal of Mineralogy* **1999**, *11*, 333–344. https://doi.org/10.1127/ejm/11/2/0333.

(130) Eulenberger, G. R.; Shoemaker, D. P.; Keil, J. G. Crystal Structures of Hydrated and Dehydrated Synthetic Zeolites with Faujasite Aluminosilicate Frameworks. I. The Dehydrated Sodium, Potassium, and Silver Forms. *J. Phys. Chem.* **1967**, *71* (6), 1812–1819. https://doi.org/10.1021/j100865a040.

(131) Herden, H.; Einicke, W.-D.; Schöllner, R.; Mortier, W. J.; Gellens, L. R.; Uytterhoeven, J. B. Location of Li-Ions in Synthetic Zeolites X and Y. *Zeolites* **1982**, *2* (2), 131–134. https://doi.org/10.1016/S0144-2449(82)80014-6.

(132) Palomino, G. T.; Bordiga, S.; Zecchina, A.; Marra, G. L.; Lamberti, C. XRD, XAS, and IR Characterization of Copper-Exchanged Y Zeolite. *J. Phys. Chem. B* **2000**, *104* (36), 8641–8651. https://doi.org/10.1021/jp000584r.

(133) Hutson, N. D.; Yang, R. T. Structural Effects on Adsorption of Atmospheric Gases in Mixed Li,Ag–X-Zeolite. *AIChE J.* **2000**, *46* (11), 2305–2317. https://doi.org/10.1002/aic.690461121.

(134) Zhu, L.; Seff, K. Cation Crowding in Zeolites. Reinvestigation of the Crystal Structure of Dehydrated Potassium-Exchanged Zeolite X. *J. Phys. Chem. B* **2000**, *104* (38), 8946–8951. https://doi.org/10.1021/jp000710r.

(135) Zhu, L.; Seff, K. Cation Crowding in Zeolites. Reinvestigation of the Crystal Structure of Dehydrated Potassium-Exchanged Zeolite X. *J. Phys. Chem. B* **2001**, *105* (48), 12221–12222. https://doi.org/10.1021/jp0133844.

(136) Marra, G. L.; Fitch, A. N.; Zecchina, A.; Ricchiardi, G.; Salvalaggio, M.; Bordiga, S.; Lamberti, C. Cation Location in Dehydrated Na−Rb−Y Zeolite: An XRD and IR Study. *J. Phys. Chem. B* **1997**, *101* (50), 10653–10660. https://doi.org/10.1021/jp971747n.

(137) Kirschhock, C. E. A.; Hunger, B.; Martens, J.; Jacobs, P. A. Localization of Residual Water in Alkali-Metal Cation-Exchanged X and Y Type Zeolites. *J. Phys. Chem. B* **2000**, *104* (3), 439–448. https://doi.org/10.1021/jp9919112.

(138) Norby, P.; Poshni, F. I.; Gualtieri, A. F.; Hanson, J. C.; Grey, C. P. Cation Migration in Zeolites: An in Situ Powder Diffraction and MAS NMR Study of the Structure of Zeolite Cs(Na)−Y during Dehydration. *J. Phys. Chem. B* **1998**, *102* (5), 839–856. https://doi.org/10.1021/jp9730398.

(139) Rejmak, P.; Sierka, M.; Sauer, J. Theoretical Studies of Cu(I) Sites in Faujasite and Their Interaction with Carbon Monoxide. *Phys. Chem. Chem. Phys.* **2007**, *9* (40), 5446–5456. https://doi.org/10.1039/B710051E.

(140) Yeom, Y. H.; Jang, S. B.; Kim, Y.; Song, S. H.; Seff, K. Three Crystal Structures of Vacuum-Dehydrated Zeolite X, $M_{46}Si_{100}Al_{92}O_{384}$, M = Mg^{2+}, Ca^{2+}, and Ba^{2+}. *J. Phys. Chem. B* **1997**, *101* (35), 6914–6920. https://doi.org/10.1021/jp970907s.

(141) Peapples-Montgomery, P. B.; Seff, K. Synthesis of Fully Dehydrated Fully Zinc(2+)-Exchanged Zeolite Y and Its Crystal Structure Determined by Pulsed-Neutron Diffraction. *J. Phys. Chem.* **1992**, *96* (14), 5962–5965. https://doi.org/10.1021/j100193a058.

(142) Maxwell, I. E.; Boer, J. J. D.; Downing', R. S. Zeolite Catalysts for the Cyclodimerization of Butadiene. *Journal of Catalysis* **1980**, *61*, 10.

(143) Bergeret, G.; Gallezot, P.; Imelik, B. X-Ray Study of the Activation, Reduction, and Reoxidation of Palladium in Y-Type Zeolites. *J. Phys. Chem.* **1981**, *85* (4), 411–416. https://doi.org/10.1021/j150604a020.

(144) Lee, S. H.; Kim, Y.; Seff, K. Crystal Structure of Partially Pd^{2+}-Exchanged Zeolite X Dehydrated in Oxygen at 400 °C. Formation of Linear Pd_2O_3 Clusters Proposed To Be $HO{-}Pd^{IV}{-}O{-}Pd^{IV}{-}OH$ in $(Pd^{2+})_{14}(HOPdOPdOH^{4+})_8(Na^+)_{32}{-}Si_{100}Al_{92}O_{384}$. *J. Phys. Chem. B* **2000**, *104* (11), 2490–2494. https://doi.org/10.1021/jp993092r.

(145) Pearce, J. R.; Mortier, W. J.; Uytterhoeven, J. B.; Lunsford, J. H. Crystallographic Study of the Distribution of Cations in Y-Type Zeolites Containing FeII and FeIII. *J. Chem. Soc., Faraday Trans. 1* **1981**, *77* (4), 937–946. https://doi.org/10.1039/F19817700937.

(146) Bae, D.; Seff, K. Structures of Cobalt(II)-Exchanged Zeolite X. *Microporous and Mesoporous Materials* **1999**, *33* (1–3), 265–280. https://doi.org/10.1016/S1387-1811(99)00146-8.

(147) Simpson, H. D.; Steinfink, H. X-Ray Diffraction Study of the Zeolite Complex m-Dichlorobenzene-Nickel Faujasite. *J. Am. Chem. Soc.* **1969**, *91* (23), 6225–6229. https://doi.org/10.1021/ja01051a003.

(148) Bae, D.; Seff, K. Crystal Structure of Zeolite X Nickel(II) Exchanged at PH 4.3 and Partially Dehydrated, Ni2(NiOH)35(Ni4AlO4)2(H3O)46Si101Al91O384. *Microporous and Mesoporous Materials* **2000**, *40* (1–3), 219–232. https://doi.org/10.1016/S1387-1811(00)00184-0.

(149) Göltl, F.; Hafner, J. Structure and Properties of Metal-Exchanged Zeolites Studied Using Gradient-Corrected and Hybrid Functionals. III. Energetics and Vibrational Spectroscopy of Adsorbates. *The Journal of Chemical Physics* **2012**, *136* (6), 064503. https://doi.org/10.1063/1.3676410.

(150) Rejmak, P.; Broclawik, E.; Góra-Marek, K.; Radoń, M.; Datka, J. Nitrogen Monoxide Interaction with Cu(I) Sites in Zeolites X and Y: Quantum Chemical Calculations and IR Studies. *J. Phys. Chem. C* **2008**, *112* (46), 17998–18010. https://doi.org/10.1021/jp8042686.

(151) Daouli, A.; Hessou, E. P.; Monnier, H.; Dziurla, M.-A.; Hasnaoui, A.; Maurin, G.; Badawi, M. Adsorption of NO, NO2 and H2O in Divalent Cation Faujasite Type Zeolites: A Density

Functional Theory Screening Approach. *Physical Chemistry Chemical Physics* **2022**, *24* (25), 15565–15578.

(152) Wang, C.; Guo, H.; Leng, S.; Yu, J.; Feng, K.; Cao, L.; Huang, J. Regulation of Hydrophilicity/Hydrophobicity of Aluminosilicate Zeolites: A Review. *Critical Reviews in Solid State and Materials Sciences* **2021**, *46* (4), 330–348. https://doi.org/10.1080/10408436.2020.1819198.

(153) Zhang, L.; Chen, K.; Chen, B.; White, J. L.; Resasco, D. E. Factors That Determine Zeolite Stability in Hot Liquid Water. *J. Am. Chem. Soc.* **2015**, *137* (36), 11810–11819. https://doi.org/10.1021/jacs.5b07398.

(154) Lamberti, C.; Zecchina, A.; Groppo, E.; Bordiga, S. Probing the Surfaces of Heterogeneous Catalysts by in Situ IR Spectroscopy. *Chem. Soc. Rev.* **2010**, *39* (12), 4951–5001. https://doi.org/10.1039/C0CS00117A.

(155) Monnier, H. Réflexions pour une approche intégrée de la prévention des risques chimiques.

(156) Williams, M.; Minjares, R. A Technical Summary of Euro 6/VI Vehicle Emission Standards.

(157) *Commission Directive (EU) 2017/164 of 31 January 2017 Establishing a Fourth List of Indicative Occupational Exposure Limit Values Pursuant to Council Directive 98/24/EC, and Amending Commission Directives 91/322/EEC, 2000/39/EC and 2009/161/EU (Text with EEA Relevance.)*; 2017; Vol. 027. http://data.europa.eu/eli/dir/2017/164/oj/eng (accessed 2022-03-06).

(158) Rajaram, R. R.; Chen, H.-Y.; Liu, D. Cold Start Catalyst and Its Use in Exhaust Systems. US20150158023A1, June 11, 2015. https://patents.google.com/patent/US20150158023A1/en (accessed 2022-12-03).

(159) Jones, S.; Ji, Y.; Crocker, M. Ceria-Based Catalysts for Low Temperature NO x Storage and Release. *Catalysis Letters* **2016**, *146*. https://doi.org/10.1007/s10562-016-1704-y.

(160) Dědeček, J.; Sobalík, Z.; Wichterlová, B. Siting and Distribution of Framework Aluminium Atoms in Silicon-Rich Zeolites and Impact on Catalysis. *Catalysis Reviews* **2012**, *54* (2), 135–223. https://doi.org/10.1080/01614940.2012.632662.

(161) Daouli, A.; Hessou, E.; Monnier, H.; marie-antoinette, D.; Hasnaoui, A.; Maurin, G.; Badawi, M. Adsorption of NO, NO2 and H2O in Divalent Cation Faujasite Type Zeolites: A Density Functional Theory Screening Approach. *Physical Chemistry Chemical Physics* **2022**. https://doi.org/10.1039/D2CP00553K.

(162) Karamanis, I.; Daouli, A.; Monnier, H.; Dziurla, M.-A.; Maurin, G.; Badawi, M. A Systematic DFT Screening of Cationic Faujasite-Type Zeolites for the Adsorption of NO, NO2 and H2O. *Molecular Systems Design & Engineering* **2023**. https://doi.org/10.1039/D3ME00044C.

(163) Sun, K.; Xia, H.; Hensen, E.; Vansanten, R.; Li, C. Chemistry of N2O Decomposition on Active Sites with Different Nature: Effect of High-Temperature Treatment of Fe/ZSM-5. *Journal of Catalysis* **2006**, *238* (1), 186–195. https://doi.org/10.1016/j.jcat.2005.12.013.

(164) Rodkin, M. A.; Sobolev, V. I.; Dubkov, K. A.; Watkins, N. H.; Panov, G. I. Room-Temperature Oxidation of Hydrocarbons over FeZSM-5 Zeolite. In *Studies in Surface Science and Catalysis*; Elsevier, 2000; Vol. 130, pp 875–880. https://doi.org/10.1016/S0167-2991(00)81069-1.

(165) Feng, X.; Keith Hall, W. FeZSM-5: A Durable SCR Catalyst for NOxRemoval from Combustion Streams. *Journal of Catalysis* **1997**, *166* (2), 368–376. https://doi.org/10.1006/jcat.1997.1530.

(166) He, C.; Wang, Y.; Cheng, Y.; Lambert, C. K.; Yang, R. T. Activity, Stability and Hydrocarbon Deactivation of Fe/Beta Catalyst for SCR of NO with Ammonia. *Applied Catalysis A: General* **2009**, *368* (1–2), 121–126. https://doi.org/10.1016/j.apcata.2009.08.020.

(167) Hamoud, H. I.; Valtchev, V.; Daturi, M. Selective Catalytic Reduction of NOx over Cu- and Fe-Exchanged Zeolites and Their Mechanical Mixture. *Applied Catalysis B: Environmental* **2019**, *250*, 419–428. https://doi.org/10.1016/j.apcatb.2019.02.022.

(168) Gao, F.; Zheng, Y.; Kukkadapu, R. K.; Wang, Y.; Walter, E. D.; Schwenzer, B.; Szanyi, J.; Peden, C. H. F. Iron Loading Effects in Fe/SSZ-13 NH $_3$ -SCR Catalysts: Nature of the Fe Ions and

Structure–Function Relationships. *ACS Catal.* **2016**, *6* (5), 2939–2954. https://doi.org/10.1021/acscatal.6b00647.

(169) Kresse, G.; Furthmüller, J. Efficiency of Ab-Initio Total Energy Calculations for Metals and Semiconductors Using a Plane-Wave Basis Set. *Computational Materials Science* **1996**, *6* (1), 15–50. https://doi.org/10.1016/0927-0256(96)00008-0.

(170) Kresse, G.; Furthmüller, J. Efficient Iterative Schemes for Ab Initio Total-Energy Calculations Using a Plane-Wave Basis Set. *Phys. Rev. B* **1996**, *54* (16), 11169–11186. https://doi.org/10.1103/PhysRevB.54.11169.

(171) Kresse, G.; Hafner, J. Norm-Conserving and Ultrasoft Pseudopotentials for First-Row and Transition Elements. *J. Phys.: Condens. Matter* **1994**, *6* (40), 8245. https://doi.org/10.1088/0953-8984/6/40/015.

(172) Bučko, T.; Hafner, J.; Lebègue, S.; Ángyán, J. G. Improved Description of the Structure of Molecular and Layered Crystals: Ab Initio DFT Calculations with van Der Waals Corrections. *J. Phys. Chem. A* **2010**, *114* (43), 11814–11824. https://doi.org/10.1021/jp106469x.

(173) Grimme, S.; Antony, J.; Ehrlich, S.; Krieg, H. A Consistent and Accurate Ab Initio Parametrization of Density Functional Dispersion Correction (DFT-D) for the 94 Elements H-Pu. *J. Chem. Phys.* **2010**, *132* (15), 154104. https://doi.org/10.1063/1.3382344.

(174) Kerber, T.; Sierka, M.; Sauer, J. Application of Semiempirical Long-Range Dispersion Corrections to Periodic Systems in Density Functional Theory. *Journal of Computational Chemistry* **2008**, *29* (13), 2088–2097. https://doi.org/10.1002/jcc.21069.

(175) Ayadi, T.; Lebègue, S.; Badawi, M. *Ab Initio* Molecular Dynamics Investigation of the Co-Adsorption of Iodine Species with CO and H_2O in Silver-Exchanged Chabazite. *Phys. Chem. Chem. Phys.* **2022**, *24* (40), 24992–24998. https://doi.org/10.1039/D2CP02267B.

(176) Bučko, T.; Hafner, J. The Role of Spatial Constraints and Entropy in the Adsorption and Transformation of Hydrocarbons Catalyzed by Zeolites. *Journal of Catalysis* **2015**, *329*, 32–48. https://doi.org/10.1016/j.jcat.2015.04.015.

(177) Rey, J.; Gomez, A.; Raybaud, P.; Chizallet, C.; Bučko, T. On the Origin of the Difference between Type A and Type B Skeletal Isomerization of Alkenes Catalyzed by Zeolites: The Crucial Input of Ab Initio Molecular Dynamics. *Journal of Catalysis* **2019**, *373*, 361–373. https://doi.org/10.1016/j.jcat.2019.04.014.

(178) Nenoff, T. M.; Rodriguez, M. A.; Soelberg, N. R.; Chapman, K. W. Silver-Mordenite for Radiologic Gas Capture from Complex Streams: Dual Catalytic CH3I Decomposition and I Confinement. *Microporous and Mesoporous Materials* **2014**, *200*, 297–303. https://doi.org/10.1016/j.micromeso.2014.04.041.

(179) Borisenko, V. E.; Gaponenko, S. V.; Gurin, V. S.; Filonov, A. B. *Physics, Chemistry And Application Of Nanostructures: Reviews And Short Notes To Nanomeeting '99*; World Scientific, 1999.

(180) Chibani, S.; Medlej, I.; Lebègue, S.; Ángyán, J. G.; Cantrel, L.; Badawi, M. Performance of CuII-, PbII-, and HgII-Exchanged Mordenite in the Adsorption of I2, ICH3, H2O, CO, ClCH3, and Cl2: A Density Functional Study. *ChemPhysChem* **2017**, *18* (12), 1642–1652. https://doi.org/10.1002/cphc.201700104.

(181) Muller, U. *Inorganic Structural Chemistry*, 2nd edition.; John Wiley & Sons Inc.: New Jersey, 2006.

(182) Lamberti, C.; Zecchina, A.; Groppo, E.; Bordiga, S. Probing the Surfaces of Heterogeneous Catalysts by in Situ IR Spectroscopy. *Chem. Soc. Rev.* **2010**, *39* (12), 4951–5001. https://doi.org/10.1039/C0CS00117A.

(183) Atkinson, R. W.; Carey, I. M.; Kent, A. J.; van Staa, T. P.; Anderson, H. R.; Cook, D. G. Long-Term Exposure to Outdoor Air Pollution and Incidence of Cardiovascular Diseases: *Epidemiology* **2013**, *24* (1), 44–53. https://doi.org/10.1097/EDE.0b013e318276ccb8.

(184) Forse, A. C.; Colwell, K. A.; Gonzalez, M. I.; Benders, S.; Torres-Gavosto, R. M.; Blümich, B.; Reimer, J. A.; Long, J. R. Influence of Pore Size on Carbon Dioxide Diffusion in Two Isoreticular

Metal–Organic Frameworks. *Chem. Mater.* **2020**, *32* (8), 3570–3576. https://doi.org/10.1021/acs.chemmater.0c00745.

(185) Borisova, S. D.; Rusina, G. G.; Chulkov, E. V. Structure and Vibrational Properties of Cobalt Clusters (n ≤ 20). *Phys. Solid State* **2010**, *52* (4), 838–843. https://doi.org/10.1134/S106378341004027X.

(186) Kresse, G.; Furthmüller, J. Efficiency of Ab-Initio Total Energy Calculations for Metals and Semiconductors Using a Plane-Wave Basis Set. *Computational Materials Science* **1996**, *6* (1), 15–50. https://doi.org/10.1016/0927-0256(96)00008-0.

(187) Blöchl, P. E. Projector Augmented-Wave Method. *Phys. Rev. B* **1994**, *50* (24), 17953–17979. https://doi.org/10.1103/PhysRevB.50.17953.

(188) Perdew, J. P.; Burke, K.; Ernzerhof, M. Generalized Gradient Approximation Made Simple. *Phys. Rev. Lett.* **1996**, *77* (18), 3865–3868. https://doi.org/10.1103/PhysRevLett.77.3865.

(189) Anisimov, V. I.; Aryasetiawan, F.; Lichtenstein, A. I. First-Principles Calculations of the Electronic Structure and Spectra of Strongly Correlated Systems: The LDA+ U Method. *J. Phys.: Condens. Matter* **1997**, *9* (4), 767. https://doi.org/10.1088/0953-8984/9/4/002.

(190) Bengone, O.; Alouani, M.; Blöchl, P.; Hugel, J. Implementation of the Projector Augmented-Wave LDA+U Method: Application to the Electronic Structure of NiO. *Phys. Rev. B* **2000**, *62* (24), 16392–16401. https://doi.org/10.1103/PhysRevB.62.16392.

(191) Gueddida, S.; Badawi, M.; Lebègue, S. Grafting of Iron on Amorphous Silica Surfaces from *Ab Initio* Calculations. *J. Chem. Phys.* **2020**, *152* (21), 214706. https://doi.org/10.1063/5.0007128.

(192) Gueddida, S.; Lebègue, S.; Badawi, M. Interaction between Transition Metals (Co, Ni, and Cu) Systems and Amorphous Silica Surfaces: A DFT Investigation. *Applied Surface Science* **2020**, *533*, 147422. https://doi.org/10.1016/j.apsusc.2020.147422.

(193) WeiJun Hu; LiangMo Mei; Hua Li. Simulation of Ground State Structure of Nickel Clusters (n ≤ 40). *Solid State Communications* **1996**, *100* (2), 129–131. https://doi.org/10.1016/0038-1098(96)00396-1.

(194) Kabir, M.; Mookerjee, A.; Bhattacharya, A. K. Structure and Stability of Copper Clusters: A Tight-Binding Molecular Dynamics Study. *Phys. Rev. A* **2004**, *69* (4), 043203. https://doi.org/10.1103/PhysRevA.69.043203.

(195) Xie, Z.; Ma, Q.-M.; Liu, Y.; Li, Y.-C. First-Principles Study of the Stability and Jahn–Teller Distortion of Nickel Clusters. *Physics Letters A* **2005**, *342* (5–6), 459–467. https://doi.org/10.1016/j.physleta.2005.05.067.

(196) Borisova, S. D.; Rusina, G. G.; Chulkov, E. V. Structure and Vibrational Properties of Cobalt Clusters (n ≤ 20). *Phys. Solid State* **2010**, *52* (4), 838–843. https://doi.org/10.1134/S106378341004027X.

(197) Kim, E.; Mohrland, A.; Weck, P. F.; Pang, T.; Czerwinski, K. R.; Tománek, D. Magic Numbers in Small Iron Clusters: A First-Principles Study. *Chemical Physics Letters* **2014**, *613*, 59–63. https://doi.org/10.1016/j.cplett.2014.08.056.

(198) Grimme, S. Semiempirical GGA-Type Density Functional Constructed with a Long-Range Dispersion Correction. *J. Comput. Chem.* **2006**, *27* (15), 1787–1799. https://doi.org/10.1002/jcc.20495.

(199) Bučko, T.; Hafner, J.; Lebègue, S.; Ángyán, J. G. Improved Description of the Structure of Molecular and Layered Crystals: Ab Initio DFT Calculations with van Der Waals Corrections. *J. Phys. Chem. A* **2010**, *114* (43), 11814–11824. https://doi.org/10.1021/jp106469x.

(200) Zhuravlev, L. T. Concentration of Hydroxyl Groups on the Surface of Amorphous Silicas. *Langmuir* **1987**, *3* (3), 316–318. https://doi.org/10.1021/la00075a004.

(201) Legrand, A. P. *The Surface Properties of Silicas*; John Wiley: Chichester, 1998.

(202) Blin, J. L.; Carteret, C. Investigation of the Silanols Groups of Mesostructured Silica Prepared Using a Fluorinated Surfactant: Influence of the Hydrothermal Temperature. *J. Phys. Chem. C* **2007**, *111* (39), 14380–14388. https://doi.org/10.1021/jp072369h.

(203) Tielens, F.; Gervais, C.; Lambert, J. F.; Mauri, F.; Costa, D. *Ab Initio Study of the Hydroxylated Surface of Amorphous Silica: A Representative Model*. ACS Publications. https://doi.org/10.1021/cm8001173.

(204) Gierada, M.; Petit, I.; Handzlik, J.; Tielens, F. Hydration in Silica Based Mesoporous Materials: A DFT Model. *Phys. Chem. Chem. Phys.* **2016**, *18* (48), 32962–32972. https://doi.org/10.1039/C6CP05460A.

(205) Berro, Y.; Gueddida, S.; Bouizi, Y.; Bellouard, C.; Bendeif, E.-E.; Gansmuller, A.; Celzard, A.; Fierro, V.; Ihiawakrim, D.; Ersen, O.; Kassir, M.; El Haj Hassan, F.; Lebegue, S.; Badawi, M.; Canilho, N.; Pasc, A. Imprinting Isolated Single Iron Atoms onto Mesoporous Silica by Templating with Metallosurfactants. *Journal of Colloid and Interface Science* **2020**, *573*, 193–203. https://doi.org/10.1016/j.jcis.2020.03.095.

(206) Comas-Vives, A. Amorphous SiO2 Surface Models: Energetics of the Dehydroxylation Process, Strain, Ab Initio Atomistic Thermodynamics and IR Spectroscopic Signatures. *Phys. Chem. Chem. Phys.* **2016**, *18* (10), 7475–7482. https://doi.org/10.1039/C6CP00602G.

(207) Ciotonea, C.; Mazilu, I.; Dragoi, B.; Catrinescu, C.; Dumitriu, E.; Ungureanu, A.; Alamdari, H.; Petit, S.; Royer, S. Confining for Stability: Heterogeneous Catalysis with Transition Metal (Oxide) Nanoparticles Confined in the Secondary Pore Network of Mesoporous Scaffolds. *ChemNanoMat* **2017**, *3* (4), 233–237. https://doi.org/10.1002/cnma.201700014.

(208) Ciotonea, C.; Dragoi, B.; Ungureanu, A.; Catrinescu, C.; Petit, S.; Alamdari, H.; Marceau, E.; Dumitriu, E.; Royer, S. Improved Dispersion of Transition Metals in Mesoporous Materials through a Polymer-Assisted Melt Infiltration Method. *Catal. Sci. Technol.* **2017**, *7* (22), 5448–5456. https://doi.org/10.1039/C7CY00963A.